Title

A Multiscale Study of the Interface Behavior between Sand and Snakeskin-inspired Surfaces and Pile Shafts

Permalink

https://escholarship.org/uc/item/3x012233

Author

O'Hara, Kyle

Publication Date

2022

Peer reviewed|Thesis/dissertation

A Multiscale Study of the Interface Behavior between Sand and Snakeskin-inspired Surfaces and Pile Shafts

By

KYLE O'HARA
DISSERTATION

Submitted in partial satisfaction of the requirements for the degree of

DOCTOR OF PHILOSOPHY

in

Civil Engineering

in the

OFFICE OF GRADUATE STUDIES

of the

UNIVERSITY OF CALIFORNIA

DAVIS

Approved:

_____
Alejandro Martinez, Chair

_____
Jason T. DeJong

_____
Ross W. Boulanger

Committee in Charge

2023

To my family and my friends

Table of Contents

Table of Figures

ix

Table of Tables

Abstract

A Multiscale Study of the Interface Behavior between Sand and Snakeskin-inspired Surfaces and Pile Shafts

The interface between the soil and structural material is the region where load is transferred for many geosystems, including deep foundations, soil nails, modified soil earth walls, and tunnel walls. Specifically, the frictional resistances generated by piles depend on a number of factors, such as the sand density and friction angle, effective stress acting on the pile surface, and the surface roughness of the pile. Certain types of piles shafts may benefit from resistances that are different in one direction of loading compared to the other, including reaction piles that generate lower installation resistance compared to the pullout resistance or offshore foundations subjected to tensile bias loading during a storm surge. Engineering the surface of such foundations to produce a directionally-dependent shaft resistance could result in a reduction of the required installation depth, and therefore reducing material and installation costs.

A pile shaft that results in directionally-dependent resistances may be designed by structuring the shaft surface with asymmetric asperities similar to a ratchet. In order to narrow the parametric space of possible solutions, a bioinspired approach was employed in this work. Biogeotechnics has gained traction as a field in recent years due to its utility in providing efficient solutions to engineering problems based on designs already existing in nature. A number of morphologies exhibit directional-dependent resistances, including the ventral scales of snakes, which were considered in these studies. Particularly, cranial shearing is induced when the scales are displaced against the soil, resulting in mobilization of larger frictional resistances. In contrast, caudal shearing is induced when the scales are displaced with the soil, resulting in smaller frictional

resistances. A number of geometric profiles based on the ventral scales of snakes were used to study pile shaft interface behavior, both as planar surfaces in laboratory interface shear testing and as piles with custom-machined surfaces.

Constant normal stiffness (CNS) laboratory interface shear testing on sand was performed on reference rough, smooth, and snakeskin-inspired surfaces to study the interface shear at the unit resistance level under both monotonic and cyclic loading, while centrifuge pile load testing was performed to assess the analogous field-scale behavior in terms of installation and pullout resistances as well as stability under cyclic loading. The CNS laboratory tests showed that the snakeskin-inspired surfaces mobilized directional-dependent shear resistances under monotonic loading, which generally agreed with results from the pile shaft resistances measuring during installation and pullout. The laboratory tests also showed that the failure envelopes associated with the snakeskin-inspired surfaces were nonlinear compared to reference rough and smooth surfaces. Potential mechanisms underlying this trend were investigated using particle image velocimetry and it was found that the trend is correlated with the shear strains at the interface at different normal stress conditions.

Pile load tests were conducted on internally instrumented piles with reference rough, smooth, and snakeskin-inspired pile shaft geometries to assess the evolution of load transfer with depth. The results indicate that piles displaced in the cranial direction gradually shed load compared to piles displaced in the caudal direction due to the greater magnitudes of mobilized skin friction of the former. In addition, cranially displaced piles require more displacement to reach the maximum resistance compared to caudally displaced piles. When the piles were subjected to cyclic loading with a tensile bias, it was found that the cranially pulled piles failed in fewer cycles than the caudally pulled piles when normalized by the total shaft resistance but could resist greater

absolute loads. The results highlight the effect of both cranial and caudal directions on cyclic stability of pile shafts.

Cyclic interface shear tests were conducted using CNS conditions to better understand the mechanics governing the pile shaft behavior. The results indicate that under symmetric loading conditions, pile shaft elements fail in the caudal direction in a brittle manner. However, when a mean load bias is introduced in the cranial direction, the behavior changes and the interfaces fail by a progressive accumulation of displacements in the caudal direction. The results also provide insight to the effects of initial normal stress, loading amplitude, and boundary stiffness on the number of cycles to failure for both reference rough, smooth, and snakeskin-inspired surfaces.

These studies show the applicability of snakeskin-inspired geometries in piling applications. The agreement between laboratory and centrifuge pile tests indicate that trends observed in laboratory tests may inform field scale behavior. The use of the snakeskin-inspired surfaces readily exhibits directional-dependent load transfer behaviors which may be used to reduce or increase resistances in compression or pullout depending on the design requirements.

Acknowledgements

I would like to acknowledge and thank my supervisor, Prof. Alejandro Martinez, for his support, guidance, understanding, and overall contribution to my work over the course of this endeavor. His excitement for research, exploring new ideas, and solving problems has been a consistent inspiration.

I would also like the thank my dissertation committee, Prof. Ross Boulanger, and Prof. Jason DeJong for their guidance and insight to both lab and centrifuge testing and excellent suggestions for thinking about results from different perspectives. I would specifically like to thank Prof. DeJong for his guidance and advice in life, and general enthusiasm and willingness to look at data. Prof. Boulanger has been consistent in pushing me to think about soil mechanics starting from my first quarter up to this thesis. I would also like to thank Prof. Katerina Ziotopoulou, who has been the most exemplary teacher and mentor, and has believed in me at times I did not believe in myself.

Over the years I have been blessed with amazing teachers, without whom I would not be here. Thanks goes to Jo-Ann Panzardi, Kelli Horner, Groppi, Karl Ewald, Jim Hanson, Gregg Fiegel, Nephi Derbidge, Rob Moss, Mario Esola, and many others.

I would also like to thank the UC Davis Department of Civil and Environmental Engineering as well as the Center for Bio-mediated and Bio-inspired Geotechnics for funding of this work.

The greatest joy of graduate school was the friends we made along the way. My most sincere thanks, in no particular order, goes to Tyler Oathes, Maya El Kortbawi, Brian Sawyer, Tim Haynes, James Heins, Sam Follett, Sophia Palumbo, Danielle Charleston, and many others. I

Chapter 1. Introduction

MOTIVATION AND BACKGROUND

It has been asserted that understanding of the strength of materials may best be understood by physical experiments (Galilei, 1638). This approach was applied to soil – structure interfaces by Coulomb (1773), with various additions to the work occurring over the following centuries. In geotechnical engineering, the thin zone where a soil and a structural component interact is referred to as the soil-surface interface. Pile shafts are a classic example of a system where performance is governed by the shear resistance of a soil-structure interface under either monotonic or cyclic loading. Pile shaft resistance has been shown to be lower in pullout loading compared to compressive loading due to the Poisson effect or a rotation of principal stresses (McClelland 1974, DeNicola and Randolph 1993, Jardine et al. 2005). In many applications, it may be advantageous for piles to have a greater available shaft resistance in one direction of loading compared to the other. For example, a reaction pile with low shaft resistances during installation, and increased shaft resistance in pullout. Other potential loading scenarios may include piles or suction caissons of offshore jacket structures which can experience tensile bias cyclic loading during storm events (Merritt et al. 2012). To provide a potential solution to such loading conditions, a bio-inspired solution was employed.

The use of bioinspired strategies to address geotechnical challenges has gained popularity in recent years, with bio-inspired and bio-mediated processes collectively referred to as biogeotechnics (Martinez et al. 2021, DeJong et al. 2011). Use of biogeotechnics range from microbially induced calcite precipitation for liquefaction mitigation (DeJong et al. 2006, Montoya and DeJong 2015), bio-inspired penetration processes (Cortes and John 2018) analogous to cone

penetration testing investigated through both physical modelling (Naziri et al. 2022) and discrete element method (Chen et al. 2022), laboratory and centrifuge testing of tree root inspired anchorage systems (Burrall et al. 2020), to constitutive continuum modelling (El Kortbawi et al. 2022). Many biological systems have been observed to have directionally dependent frictional characteristics (Liu et al. 2015), including wool fibers (Lindberg and Gralén 1948), cat tongues (Noel and Hu 2018) and morphologic features for anti-herbivory (Hanley et al. 2007). In addition, many products benefit from directional-dependent resistance in the form of ratcheting, such as the freehub of a bicycle wheel or a ratchet wrench. Considering the utility of such ratcheting systems and the recent work in bio-inspired geotechnics, a suitable biological analogue for use in pile interface applications was considered.

Fundamental understanding of the factors governing the behavior at the soil – shaft interface is key in order to gain new insights into load transfer mechanisms. Seminal work in quantifying the role of surface roughness in the interactions at soil - structure was carried out by Uesugi and Kishida (1986), where a relationship between the roughness of the surface, the median particle size of the sand (D_{50}) and the interface friction angle was found. Based on this observation, they proposed the use of normalized roughness (R_n) to quantify the interactions, where the normalized roughness is the maximum roughness (R_{max}) of the surface measured over a distance equal to the D_{50}, divided by the D_{50} ($R_n = R_{max}/D_{50}$). This normalization results in a bilinear trend between the normalized roughness and interface friction angle at yield, where the interface friction angle increases until it reaches a value similar to the internal friction angle of the sand. The bilinear trend and normalized roughness parameter were based on tests with random surface roughness profiles from rusting and did not consider periodic geometric pattern of the surface profile.

Hryciw and Irsyam (1993) investigated the interface behavior of surfaces ribbed profiles, where the asperity height was tall compared to the spacing between ribs. For well-spaced asperities, it was found that a full passive zone formed over large surface displacements and the apparent interface friction angle exceeded the internal friction angle of the soil. For surfaces with closer inter-asperity spacing, a partial passive zone formed over a shorter displacement, and lower shear resistances were mobilized compared to the surfaces with well-spaced asperities. These results indicate that with correct surface geometry, apparent interface friction angles may exceed the internal friction angle of the soil due to the formation of passive zones. Work by Frost and DeJong (2005) and Martinez and Frost (2017) showed that measured interface friction angles for structured geometries can surpass the friction angle of the soil. Using partially structured surfaces where the asperity height was tall compared to the spacing, the effect of interface friction was isolated, showing that the effect of the passive resistances was contributing factor to resistances above the soil's friction angle. Furthermore, the authors reported that the relationship between the surface average roughness (R_a) and interface friction angle did not follow the same bilinear trend reported by Uesugi and Kishida (1986) but increased over a larger range of R_a to values greater than the internal friction angle.

With regard to interface systems, the ventral scales of snakes have been shown to mobilize directional-dependent friction when interacting with a substrate (Baum et al. 2014) and the geometric pattern of ventral scale profiles from different snake species has been shown to correlate to the particular habitat in which they evolved (Martinez et al. 2021). Tests between snake specimens and solid substrates have shown that forward movement, referred to as the caudal direction, results in lower frictional resistances compared to movement in the reverse direction, referred to as the cranial direction. In terms of a friction coefficient, ratios between the cranial and

caudal shearing direction range from 1.2 to 1.7 (Marvi and Hu 2012). Palumbo (2018) and Martinez et al. (2019) adapted the patterns from 3D scanned ventral scales from preserved snake specimens into rigid surfaces for use in soil – surface interface testing (Figure 1.1). The figure shows the decomposition of a model organism into component mechanisms or principles. For the purposes of this investigation, the profile geometry of the ventral scales was chosen. The ventral scales were scanned and idealized into a structure that could be manufactured on rigid surfaces for laboratory testing. Results from a series of interface shear testing revealed that the interface friction angle correlated with the ratio of asperity length (L) to asperity height (H). Shearing in the cranial direction resulted in larger interface friction angles compared to the caudal shearing direction, and surpassed the internal friction angle of the soil for small values of L/H. Additional studies have been conducted on a number of standard testing sands, and the results show broad agreement in that the L/H ratio captures the trend of decreasing interface friction angle with increasing L/H up to values of L/H ranging between 80 to 160 at which the interface friction angles become close to constant (Stutz and Martinez 2021, Lee and Chong 2022, Venu Latha et al. 2022). In addition, DEM studies simulating pile installation and pullout have shown similar surfaces to exhibit directional dependent shear resistance and stress rotation in the surrounding soil (Zhong, 2021). These results provided a basis for application of similar geometries that may be used on the surface of pile shafts with directionally dependent properties.

Pile shaft resistance in sand has been shown to depend on the radial effective stress and interface friction angle. These parameters may be affected by the method of installation, soil type, pile surface roughness, and direction of loading (i.e., compression or pullout). Various design methods account for these factors either through the combination of effects, such as the beta method (Meyerhof 1974) or by accounting for factors individually. For example, Lehane et al.

(2007) directly account for changes in radial effective stress during installation, interface friction angle, loss of radial effective stress due to frictional fatigue, and loading direction. Factors influencing the strength of soil – pile interfaces may be investigated through the use of both laboratory and centrifuge modelling. It has been shown that interface shear tests under constant normal stiffness conditions (CNS) capture the behavior of pile – shaft interfaces at the element level (Boulon and Foray 1986, Airey et al. 1992), and centrifuge modelling allows for assessing the global response of piles under both monotonic and cycling axial loading (White and Lehane 2004, Li et al. 2010, Zheng et al. 2019). The framework utilized to relate the global and element level behaviors is shown in Figure 1.2.

Laboratory and centrifuge methods are well suited to investigate the behavior of pile – shaft interfaces. In addition, recent development of novel bio-inspired surface geometries have been shown to have directionally-dependent frictional properties. Considering the potential application of pile shafts with directionally-dependent shear resistance, this thesis uses both testing methodologies towards to goal of assessing both the fundamental behavior of pile – shaft interfaces as well as the application of snakeskin-inspired geometries applied to pile shafts subjected to monotonic and cyclic axial loading.

SCOPE AND ORGANIZATION

Chapter 2 explores the monotonic and cyclic behavior of directionally-dependent surfaces under CNS boundary conditions and compares the trends with those from a parallel study centrifuge study on monotonically- and cyclically-loaded uninstrumented piles. The laboratory and centrifuge cyclic tests were displacement controlled, and the results were analyzed in terms of the maximum shear stress in one direction of loading compared to the other. The results indicate

agreement between the laboratory and centrifuge results and show that snakeskin-inspired surfaces have potential use in piling applications.

Chapter 3 presents the results from a series of centrifuge pile load tests conducted on instrumented smooth, rough, and snakeskin-inspired piles. An example of one pile with snakeskin-inspired shaft geometry is shown in Figure 1.3. The load distribution with depth at the end of installation and during pullout are compared. The load distributions are analyzed in terms of beta coefficients. The potential impacts of scaling are discussed, with a correction applied to account for the pile diameter to grain size ratio to provide reasonable values for field scale applications. The results show that the ratio of pullout to installation resistance can be modified either to be above or below the values expected from randomly structured pile shaft geometries by changing the installation direction and geometry of the snakeskin-inspired pile surfaces.

Chapter 4 investigates the axial cyclic stability of rough and snakeskin-inspired piles from centrifuge pile load tests within the framework of a cyclic interaction diagram. The tests were conducted under load-controlled conditions measured at the pile head with either symmetric or tensile bias loads. It was found that the cyclic stability in terms of number of cycles to failure depended on the geometry of the pile shaft and the magnitude of the loads applied. In addition, the stiffness response from the pile shaft shear resistance indicated the onset of a yield condition prior to failure which was unique for each pile type tested. The cycle number at which yield occurred compared to the cycle number at which failure occurred was used as a measure of the ductility or brittleness of the failure.

Chapter 5 aims to extend upon the results presented in Palumbo 2018 by defining the failure envelopes for two pairs of snakeskin-inspired surfaces with different asperity height and spacing, but the same *L/H* ratio. Particle Image Velocimetry results are presented to provide further insight

to the globally measured results. A method for systematically evaluating the shear band height from shear strain measurements is presented and used to assess potential differences observed in the failure envelopes of the snakeskin-inspired and reference rough and smooth surfaces.

Chapter 6 investigates the cyclic stability of soil-structure surfaces through laboratory interface shear testing. The testing series targeted the behavior of rough, smooth, and four snakeskin-inspired surfaces under various boundary stiffnesses, initial effective stresses and load bias conditions. The results highlight how factors such as the effective stress, boundary stiffness, surface roughness, and profile geometry influence the stability of a single pile shaft element.

Chapter 7 provides a summary of the findings presented herein and proposes potential future investigations.

Model Organism

Mechanisms/Principles

3D Scans of ventral scales

Profile geometry

Scale compliance

Angle of attack θ

Palumbo 2018

Ventral scales

Idealization

H. Nasicus profile
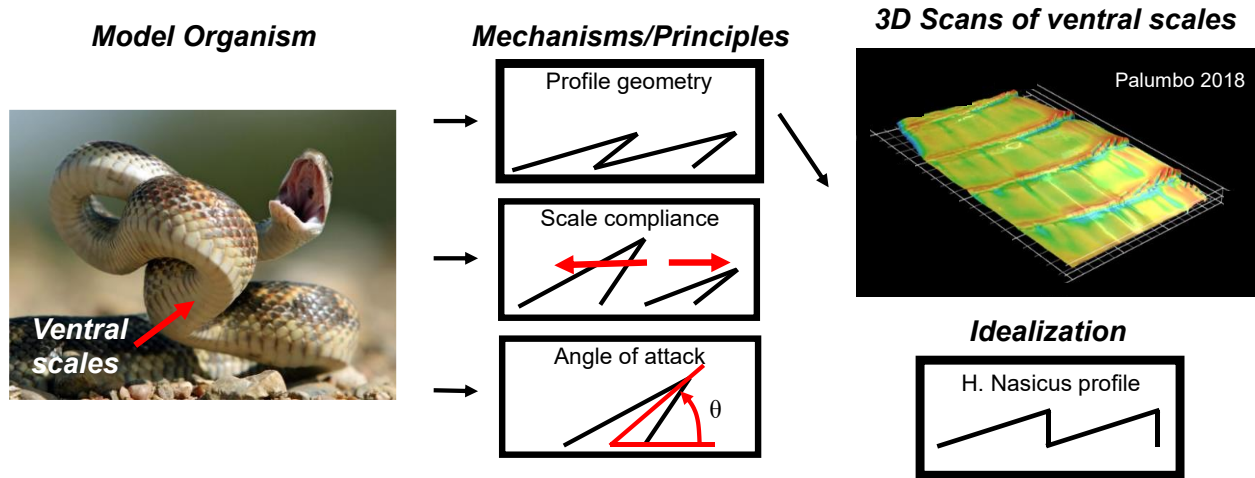
Figure 1.1. Methodology for translation of snake ventral scales into idealized profiles for soil-structure interface shear testing.

F_{cyclic} F_{avg}

τ_{cyclic}

k

σ'_{no}

τ_{avg}

σ'_n
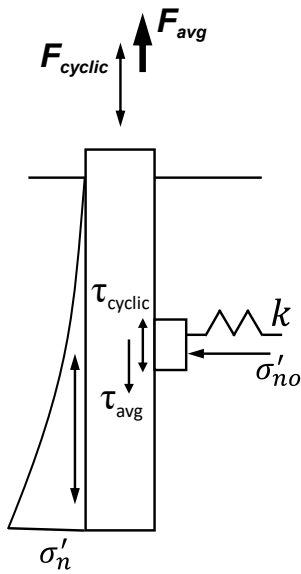
Figure 1.2. Schematic showing the response of global pile shaft (left) compared to an idealized element (right) modeled with a constant spring stiffness.

Figure 1.3. Internally instrumented pile with shaft geometry modelled after snake ventral scales.

REFERENCES.

Baum, M. J., A. E. Kovalev, J. Michels, and S. N. Gorb. 2014. "Anisotropic Friction of the Ventral Scales in the Snake Lampropeltis getula californiae." *Tribol Lett*, 54 (2): 139–150. https://doi.org/10.1007/s11249-014-0319-y.

Burrall, M., J. T. DeJong, A. Martinez, and D. W. Wilson. 2020. "Vertical pullout tests of orchard trees for bio-inspired engineering of anchorage and foundation systems." *Bioinspir. Biomim.*, 16 (1): 016009. https://doi.org/10.1088/1748-3190/abb414.

Chen, Y., A. Khosravi, A. Martinez, and J. DeJong. 2021. "Modeling the self-penetration process of a bio-inspired probe in granular soils." *Bioinspir. Biomim.*, 16 (4): 046012. https://doi.org/10.1088/1748-3190/abf46e.

Coulomb, C-A. 1773. Essai sur une application des règles de Maximis et Minimis à quelques problèmes de statique relatifs à l'architecture. Mémoire présenté à l'Académie royale dessciences, Paris.

De Nicola, A., and M. F. Randolph. 1993. "Tensile and Compressive Shaft Capacity of Piles in Sand." *J. Geotech. Engrg.*, 119 (12): 1952–1973. https://doi.org/10.1061/(ASCE)0733-9410(1993)119:12(1952).

DeJong, J. T., K. Soga, S. A. Banwart, W. R. Whalley, T. R. Ginn, D. C. Nelson, B. M. Mortensen, B. C. Martinez, and T. Barkouki. 2011. "Soil engineering *in vivo* : harnessing natural biogeochemical systems for sustainable, multi-functional engineering solutions." *J. R. Soc. Interface.*, 8 (54): 1–15. https://doi.org/10.1098/rsif.2010.0270.

DeJong, J. T., M. B. Fritzges, and K. Nüsslein. 2006. "Microbially Induced Cementation to Control Sand Response to Undrained Shear." *J. Geotech. Geoenviron. Eng.*, 132 (11): 1381–1392. https://doi.org/10.1061/(ASCE)1090-0241(2006)132:11(1381).

El Kortbawi, M., D. M. Moug, K. Ziotopoulou, J. T. DeJong, and R. W. Boulanger. 2022. "Axisymmetric Simulations of Cone Penetration in Biocemented Sands." *J. Geotech. Geoenviron. Eng.*, 148 (11): 04022098. https://doi.org/10.1061/(ASCE)GT.1943-5606.0002914.

Galilei, G., 1564-1642. 1638. *Discorsi e dimostrazioni matematiche : intorno à due nuoue scienze attenenti alla mecanica i movimenti locali*. Leida : Appresso gli Elsevirii, 1638.

Hanley, M. E., B. B. Lamont, M. M. Fairbanks, and C. M. Rafferty. 2007. "Plant structural traits and their role in anti-herbivore defence." *Perspectives in Plant Ecology, Evolution and Systematics*, 8 (4): 157–178. https://doi.org/10.1016/j.ppees.2007.01.001.

Jardine, R., F. Chow, R. Overy, and J. Standing. 2005. *ICP design methods for driven piles in sands and clays*.

Knodel, P., D. Airey, R. Al-Douri, and H. Poulos. 1992. "Estimation of Pile Friction Degradation from Shearbox Tests." *Geotech. Test. J.*, 15 (4): 388. https://doi.org/10.1520/GTJ10253J.

Lee, S.-H., and S.-H. Chong. 2022. "A Study on Friction Anisotropy between Sand and Surface Asperities of Plate Using Modified Direct Shear Test." *Journal of the Korean Geotechnical Society*, 38 (2): 29–38. https://doi.org/10.7843/KGS.2022.38.2.29.

Lehane, B. M., J. A. Schneider, and X. Xu. 2007. "Development of the UWA-05 Design Method for Open and Closed Ended Driven Piles in Siliceous Sand." *Contemporary Issues In Deep Foundations*, 1–10. Denver, Colorado, United States: American Society of Civil Engineers.

Li, Z., S. K. Haigh, and M. D. Bolton. 2010. "The Behavior of a Single Pile under Cyclic Axial Loads." *Deep Foundations and Geotechnical In Situ Testing*, 143–148. Shanghai, China: American Society of Civil Engineers.

Liu, Z., W. Yin, D. Tao, and Y. Tian. 2015. "A glimpse of superb tribological designs in nature." *Biotribology*, 1–2: 11–23. https://doi.org/10.1016/j.biotri.2015.02.002.

Martinez, A., D. Nguyen, M. S. Basson, J. Medina, D. J. Irschick, and S. Baeckens. 2021. "Quantifying surface topography of biological systems from 3D scans." *Methods Ecol Evol*, 12 (7): 1265–1276. https://doi.org/10.1111/2041-210X.13603.

Martinez, A., J. Dejong, I. Akin, A. Aleali, C. Arson, J. Atkinson, P. Bandini, T. Baser, R. Borela, R. Boulanger, M. Burrall, Y. Chen, C. Collins, D. Cortes, S. Dai, T. DeJong, E. Del Dottore, K. Dorgan, R. Fragaszy, J. D. Frost, R. Full, M. Ghayoomi, D. I. Goldman, N. Gravish, I. L. Guzman, J. Hambleton, E. Hawkes, M. Helms, D. Hu, L. Huang, S. Huang, C. Hunt, D. Irschick, H. T. Lin, B. Lingwall, A. Marr, B. Mazzolai, B. McInroe, T. Murthy, K. O'Hara, M. Porter, S. Sadek, M. Sanchez, C. Santamarina, L. Shao, J. Sharp, H. Stuart, H. H. Stutz, A. Summers, J. Tao, M. Tolley, L. Treers, K. Turnbull, R. Valdes, L. van Paassen, G. Viggiani, D. Wilson, W. Wu, X. Yu, and J. Zheng. 2022. "Bio-inspired geotechnical engineering: principles, current work, opportunities and challenges." *Géotechnique*, 72 (8): 687–705. https://doi.org/10.1680/jgeot.20.P.170.

Martinez, A., S. Palumbo, and B. D. Todd. 2019. "Bioinspiration for Anisotropic Load Transfer at Soil–Structure Interfaces." *J. Geotech. Geoenviron. Eng.*, 145 (10): 04019074. https://doi.org/10.1061/(ASCE)GT.1943-5606.0002138.

Marvi, H., and D. L. Hu. 2012. "Friction enhancement in concertina locomotion of snakes." *J. R. Soc. Interface.*, 9 (76): 3067–3080. https://doi.org/10.1098/rsif.2012.0132.

McClelland, B. 1974. "Design of Deep Penetration Piles for Ocean Structures." *J. Geotech. Engrg. Div.*, 100 (7): 709–747. https://doi.org/10.1061/AJGEB6.0000064.

Merritt, A. S., F. C. Schroeder, R. J. Jardine, B. Stuyts, D. Cathie, and W. Cleverly. 2012. "Development of Pile Design Methodology For an Offshore Wind Farm In the North Sea." SUT-OSIG-12-47.

Meyerhof, G. G. 1976. "Bearing Capacity and Settlement of Pile Foundations." *J. Geotech. Engrg. Div.*, 102 (3): 197–228. https://doi.org/10.1061/AJGEB6.0000243.

Montoya, B. M., and J. T. DeJong. 2015. "Stress-Strain Behavior of Sands Cemented by Microbially Induced Calcite Precipitation." *J. Geotech. Geoenviron. Eng.*, 141 (6): 04015019. https://doi.org/10.1061/(ASCE)GT.1943-5606.0001302.

Naziri, S., D. D. Cortes, C. Ridgeway, S. Ibarra, K. Provenghi, and J. A. Castelo. 2021. "Bioinspired Regolith Penetration Probe for Lunar Exploration." *ASCEND 2021*. Las Vegas, Nevada & Virtual: American Institute of Aeronautics and Astronautics.

Noel, A. C., and D. L. Hu. 2018. "The tongue as a gripper." *Journal of Experimental Biology*, 221 (7): jeb176289. https://doi.org/10.1242/jeb.176289.

Stutz, H. H., and A. Martinez. 2021. "Directionally dependent strength and dilatancy behavior of soil–structure interfaces." *Acta Geotech.*, 16 (9): 2805–2820. https://doi.org/10.1007/s11440-021-01199-5.

Vena Latha, G., P. Vangla, and R. Anilkumar. 2022. "Effect of snakeskin-inspired patterns on the shear response of soil - continuum interfaces." *International Journal of Geotechnical Engineering*, 16 (6): 759–775. https://doi.org/10.1080/19386362.2022.2066049.

Yoshimi, Y., and T. Kishida. 1981. "A Ring Torsion Apparatus for Evaluating Friction Between Soil and Metal Surfaces." *Geotech. Test. J.*, 4 (4): 145. https://doi.org/10.1520/GTJ10783J.

Zheng, B. L., B. L. Kutter, D. W. Wilson, J. Allmond, C. Hunt, and T. McNeilan. 2019. "Centrifuge Modeling of Cyclic Degradation of Axially Loaded Piles in Sand for Offshore

Wind Turbine Structures." *IJOPE*, 29 (2): 172–181. https://doi.org/10.17736/ijope.2019.tm86.

Chapter 2. Monotonic and Cyclic Frictional Resistance Directionality in Snakeskin-Inspired Surfaces and Piles

ABSTRACT

Interface friction is a governing parameter in the performance of piled foundations and other applications. Piles and other foundation elements typically mobilize a similar interface friction angle during loading in tension and compression. However, some applications may benefit from surfaces which mobilize higher shear resistances in one direction of loading relative to another. Such behavior can be achieved through inspiration from the underbelly scales of snakes, which produce frictional directionality or anisotropy. This paper presents the results of an experimental investigation on the monotonic and cyclic interface shear behavior of snakeskin-inspired surfaces and piles with sand. Laboratory test results provide evidence that snakeskin-inspired surfaces mobilize shear resistances, volumetric behavior, and strength degradation that depend on the shearing direction. Boundary conditions, sand relative density, and cyclic displacement amplitude are also shown to influence the interface shear response. Centrifuge pile load tests are used to evaluate the installation forces, pullout capacity, and cyclic loading response mobilized by snakeskin-inspired piles. These results suggest that snakeskin-inspired surfaces can readily mobilize skin friction that is dependent on the direction of displacement in piling applications.

15

INTRODUCTION

Piles and other foundation elements typically mobilize a similar interface friction angle during loading in both tension and compression. However, some applications like reaction piles for load tests, jacketed foundations for offshore structures, and deep foundations subjected to downdrag forces may benefit from surfaces that develop higher shear resistances in one direction relative to another. These surfaces may be used to improve desired performance, such as maximizing pullout capacity for a reaction pile, minimizing the accumulation of pullout deformations during cyclic loading of jacketed offshore foundations, and minimizing downdrag loads. A detailed investigation of the interface shear behavior of such surfaces is necessary to build the knowledge and experimental evidence required for implementing such surfaces in field applications.

Bioinspiration. Bioinspiration is the process of identifying and translating biological adaptations that efficiently cope with demands that are analogous to those controlling engineered systems. The process of evolution through natural selection has led organisms to develop unique adaptations for their survival. Over time, the organisms with adaptations that allow them to meet specific demands survive (Vogel 1998). These adaptations may be directed towards hunting, escaping predators, or conserving energy. Bioinspiration for frictional anisotropy can be obtained from adaptations present in the paws of certain mammals and birds, the leaves of some trees and grasses, and the scales of several reptiles. The ventral scales of many snake species, located along their underbelly skin, control the transfer of load with various substrates such as sandy and clayey soils, rock surfaces, tree bark, and the forest floor (Jayne 1985, 1986; Marvi et al. 2014; Lillywhite 2014). When a snake moves forward, its ventral scales shear in the caudal direction with respect to the

substrate, mobilizing low frictional resistances. Simultaneously, a snake anchors portions of its body to the substrate by moving them backwards, resulting in shearing in the cranial direction that mobilizes larger frictional resistances. This difference in frictional resistances has been referred to in the biological literature as frictional directionality, aeolotropy, or anisotropy.

Several authors have studied the frictional interactions between snake ventral scales and solid surfaces. Results of these investigations indicate that the ventral scales mobilize static friction coefficients that are greater in the cranial direction than in the caudal direction by 250% (Gray and Lissman 1950), 140% to 350% (Marvi et al. 2013), or 150% (Baum et al. 2014) depending on the snake species. Research has shown that scale shape, compliance, and the active control of the scales' angle of attack (i.e., angle of the scale relative to the horizontal) facilitate frictional anisotropy (Marvi 2013; Marvi et al. 2016). In addition, each scale contains nanoscale features called denticles that also contribute to frictional anisotropy. Similar to ventral scales, denticles have a highly asymmetric geometry, allowing them to preferentially interlock with surface features when moving in the cranial direction (e.g., Hazel et al. 1999).

Pile Skin Friction and Interface Shear Behavior. During the service life of a pile, the magnitude of normal effective stresses acting on the pile surface largely controls the magnitude of skin friction mobilized. The evolution of normal effective stresses is influenced by the loading applied to the pile and the boundary conditions imposed by the surrounding soil mass. Boulon and Foray (1986) derived a model from elastic cavity expansion theory that approximates the boundary conditions imposed by the surrounding soil mass on the pile with an elastic spring constant as follows:

$$k = \frac{4G}{D} \tag{1}$$

where k is the soil mass spring constant with units of stress per unit displacement, G is the operational shear modulus of the soil, and D is the pile diameter. In this framework, the evolution of normal effective stress σ'_n acting on the pile surface is determined by:

$$\sigma'_n = \sigma'_{no} - k\Delta \tag{2}$$

where σ'_{no} is the initial effective normal stress and Δ is the dilation or contraction of the soil in the shear band with dilation defined as negative. This framework has been implemented in the laboratory through Constant Normal Stiffness (CNS) boundary conditions, which have been shown to adequately model the skin friction behavior observed during pile load tests (e.g., Airey et al. 1992; Lehane et al. 1993; Fioravante 2002; Lehane and White 2005).

Other factors affecting the shear behavior of soil-structure interfaces in pile applications include the surface roughness of the structural material (e.g., Uesugi and Kishida 1986); loading conditions (e.g., Martinez and Frost 2018); soil properties and state such as particle shape and size, gradation, and relative density (D_R) (e.g., DeJong and Westgate 2009; Dietz and Lings 2006; Ho et al. 2011); and evolution of interface properties during installation and loading (e.g., Airey and Kelly 2010; Dietz and Lings 2010). The effect of the surface profile form on the transfer of load has also been studied. For instance, Wang et al. (2007a and 2007b) used the discrete-element method to show that the mobilized shear resistances correlate with the average contact normal orientation between the particles and the surface, which agreed well with laboratory results. Hryciw and Irsyam (1993) showed that well-spaced asperities can mobilize passive zones that may result in measured interface friction angles exceeding the internal soil friction angle. Frost and DeJong (2005) and Martinez and Frost (2017) showed that the asperity spacing and shape also influence the interface shear response.

Palumbo (2018) and Martinez et al. (2019) developed and tested 3D printed snakeskin-inspired surfaces. Three-dimensional scans of the ventral scales of preserved snake specimens were obtained and idealized to create 3D printed surfaces which were tested in a direct interface shear apparatus, as shown in Figure 2.1a. The surfaces were inspired by scans of the ventral scales of a ground dwelling snake (*H. nasicus*), an arboreal snake (*L. ahaetulla*), and a sidewinder snake (*C. cerastes*). Monotonic tests against the three types of surfaces indicated that shearing in the cranial direction mobilized greater peak and residual shear strength and dilation angle than shearing in the caudal direction. The anisotropy in shear strength was greatest for the surface inspired by the ground dwelling snake. In addition, Martinez et al. (2019) also performed Particle Image Velocimetry (PIV) analyses during their interface shear tests. The PIV analyses indicate that the difference in mobilized shear resistances is likely due to the formation of passive soil wedges ahead of the asperities during cranial shearing (Figure 2.2), which were not observed during caudal shearing. All tests presented in this paper were performed against surfaces inspired by the scales of the ground dwelling snake due to the directional dependent behavior of such surfaces. This study explores the response of interfaces with snakeskin-inspired surfaces subjected to monotonic and cyclic loading conditions under CNS and CNL boundary conditions. In addition, this work incorporates centrifuge pile load testing to explore similarities between element-scale and full-scale behavior.

MATERIALS AND METHODS

Interface Shear Tests. A series of direct interface shear tests were performed following ASTM D3080 standards on Ottawa F65 sand specimens and smooth, epoxied sand, and snakeskin-inspired surfaces. The tests were performed using a modified Geotac direct shear device

(Trautwein, Houston, TX) equipped with a bottom platen where the testing surfaces were mounted, as described in Martinez et al. (2019) and Martinez and Stutz (2019). This device measures normal and shear forces and horizontal and vertical displacements using load cells and linear potentiometers. The rectangular shear box had inner dimensions of 100 mm by 63.5 mm. The top cap was not restrained; this allowed for rotation to ensure that the normal stress on the specimen remained uniform, although it may lead to a non-uniform displacement field within the specimen. This configuration is equivalent to that employed by other studies (e.g., Boukpeti and White 2016; Martinez and Stutz 2019). In addition, Potts et al. (1987) showed by means of finite-element method analyses that the difference in mobilized strength is less than 5% between tests with fixed and non-fixed top caps. Monitoring of the shear box during testing confirmed that a gap between the box and the surface did not open throughout the tests. All tests were carried out at a shear rate of 1 mm/min and conducted using Constant Normal Stiffness (CNS) or Constant Normal Load (CNL) boundary conditions. During testing using CNS conditions, the vertical actuator used force-displacement feedback to apply a change in normal stress, $d\sigma'_n$, according to a specified stiffness given by $k = d\sigma'_n/dy$, where dy is the vertical displacement of the specimen.

Two reference surfaces and a bioinspired surface were used in this testing program. The reference surfaces consisted of machined, polished steel (with average surface roughness, R_a, of 1.5 μm) and epoxied Ottawa 20-30 sand (R_a of 144.1 μm and mean particle size, D_{50}, of 0.72 mm). The former, referred to as the reference smooth surface, was intended to model a sliding failure. The latter, referred to as the reference rough surface, was intended to induce failure within the soil mass. The bioinspired surface was manufactured of photosensitive resin using additive manufacturing with a Form2 3D printer (Formlabs, Cambridge, MA). The resin properties and manufacturing process are described in Martinez and Palumbo (2017) and Palumbo (2018). The

surfaces were modeled after 3D scans of the ventral scales of *H. nasicus*, as described in Martinez et al. (2019) and shown in Figure 2.1a. The profile geometry was defined by the asperity length and height. In this study, an asperity length of 12 mm and an asperity height of 0.30 mm were used, which were shown by Martinez et al. (2019) to mobilize frictional resistance anisotropy. Martinez and Palumbo (2017) showed that abrasion of the resin surfaces during testing was negligible for applied normal stresses smaller than 400 kPa. Table 2.1 presents surface roughness values and representative profiles of the testing surfaces. All profiles were measured using a Keyance VR-3100 white light noncontact digital microscope with a 0.1 μm resolution. The rough and bioinspired surfaces were textured over a central section with a length of 80 mm, leaving 10 mm untextured sections along the leading and trailing edges to reduce the potential effects of the shear box's rigid side boundaries, in accordance with previous studies (e.g., DeJong et al. 2003; Martinez and Stutz 2019; Martinez et al. 2019).

All the tests were performed with Ottawa F65, a poorly graded silica sand with D_{50} of 0.20 mm; coefficient of uniformity, C_u, of 1.71; coefficient of curvature, C_c, of 1.00; and a composition of 99.77% silica by mass. This sand has a maximum void ratio, e_{max}, of 0.83; minimum void ratio, e_{min}, of 0.52; specific gravity of solids, G_s, of 2.67; and a residual friction angle determined from direct shear tests, φ'_{res}, of 30° (e.g., Parra Bastidas 2016; Kutter et. al. 2018; Carey et. al. 2019; Palumbo 2018). All the tests were performed on air pluviated specimens with target D_R of either 85% or 50%.

The interface shear tests were conducted in two sequences to compare the effect of shearing direction. Cranial→caudal tests were conducted with an initial half-cycle in the cranial direction followed by a second half-cycle in the caudal direction. Conversely, caudal→cranial tests were conducted with an initial half-cycle in the caudal direction and a second half-cycle in the cranial

direction. When possible, tests were conducted to 50 cycles with displacement amplitudes of 1 or 2 mm. Under certain testing conditions, the contraction of the specimen due to cyclic loading caused either the normal stress to drop to a value near zero or the top cap to catch on the sides of the shear box. For these tests, the data presented corresponds to the portion of the test before these conditions occurred.

Centrifuge Modeling. A series of centrifuge pile load tests were performed to investigate the effects of the snakeskin-inspired texture on the shaft resistance of model piles. The pile load tests were conducted at the UC Davis Center for Geotechnical Modeling in the 9-m centrifuge at a gravitational field of 40 g. One smooth pile and four snakeskin-inspired piles were tested, all with diameters of 10 mm in model scale (400 mm in prototype scale) and conical tips with a 60° apex angle. The snakeskin-inspired piles were manufactured from smooth, brushed stainless steel and textured with profiles with an asperity height of 0.30 mm and length of 6 or 12 mm (Table 2.1). A distance equivalent to two pile diameters behind the pile tip was left untextured to minimize the potential interactions between the surface asperities and the tip. A load cell attached to the pile head recorded the force during all portions of the testing sequence. All piles were installed with a monotonic push to 290 mm followed by a 20 mm monotonic pullout test. Since the force was measured at the pile head, the monotonic pullout tests were used to determine the average mobilized skin friction. The average mobilized skin friction, τ_{avg}, was computed as the ratio of the total force measured at the pile head during a pullout test to the pile shaft's embedded surface area. The bioinspired piles were also subjected to displacement-controlled cyclic loading with a target amplitude of 0.50 mm. The amplitude of the cyclic loading applied to the piles is believed to be

small enough to avoid engagement of the tip, especially considering that the piles were retracted by 20 mm before initiation of the cyclic loading.

The pile load tests were conducted on deposits of dry Ottawa F65 sand. The specimen was prepared in a flexible beam container shown schematically in Figure 2.1b, with separate portions consisting of dense (D_R = 85%) and loose (D_R = 40%) sand. The dense and loose sections were prepared by air pluviation in 75 mm thick lifts to a depth of 490 mm (19.6 m in prototype scale). The piles were pushed at a minimum spacing equivalent to 10 pile diameters from other test locations and from the container boundaries, and to a depth equivalent to 20 pile diameters away from the bottom of the container. Under the 40 g field, the vertical effective stress at the pile tip at the maximum penetration depth was 198 kPa and 181 kPa in the dense and loose deposits, respectively.

RESULTS

Laboratory Monotonic Interface Shear Tests. Interface shear tests under CNL conditions were conducted on the snakeskin-inspired surface at normal effective stresses of 53, 80, and 156 kPa on dense specimens (D_R = 85%). The shear stress – horizontal displacement and vertical displacement – horizontal displacement curves are shown in Figures 2.3a to 2.3c. As the normal effective stress increased, the peak and residual strengths increased while the dilative volume changes in the first half-cycle decreased for both cranial→caudal and caudal→cranial tests. A difference in the mobilized shear stresses is evident, where cranial shearing (first direction in cranial→caudal tests and second direction in caudal→cranial tests) mobilized larger shear resistances than caudal shearing. The assumption of a linear failure envelope yields interface friction angles of 32.6° and

27.5° in the cranial and caudal directions, respectively. Dilation was also larger during cranial shearing in the first direction. These trends agree with results presented by Martinez et al. (2019).

Interface shear tests under CNS conditions were conducted on the bioinspired surface and dense specimens with initial normal stresses of 80 and 132 kPa, and with a boundary normal stiffness of 150 kPa/mm. Cranial shearing mobilized larger shear resistances than caudal shearing at both stress levels whether in the first or second half-cycles, as shown in Figures 2.4a and 2.4b. Shearing cranially first induced larger changes in normal stress, which is in agreement with the greater amount of soil dilation exhibited by cranial first shearing during CNL tests (Figures 2.3a and 2.3c). In the cranial second shearing direction (i.e., in caudal→cranial tests), the normal stresses tended to increase after an initial decrease. This increase in normal stresses during in the second direction was smaller during caudal second shearing (i.e., in cranial→caudal tests). The difference in mobilized shear strength between cranial and caudal shearing, whether in the first or second directions, is larger under CNS than under CNL conditions, highlighting how soil dilation contributes to the evolution of normal stresses.

Figure 2.5 presents results of CNS tests in both cranial→caudal and caudal→cranial sequences for the bioinspired surfaces and the reference smooth and rough surfaces (k = 150 kPa/mm, σ'_{no} = 80 kPa, target D_R = 85%). The stress ratio mobilized by the bioinspired surface displaced in the cranial first direction (solid black line) is similar to the ratio mobilized by the rough surface, whereas the stress ratio in the return caudal cycle is similar to the ratio mobilized by the smooth surface. This trend is similar but reversed for the caudal→cranial test (dashed black line): the stress ratio mobilized by shearing in the caudal first direction is slightly larger than the ratio mobilized by the smooth surface, whereas the stress ratio in the return cranial cycle is similar to the ratio mobilized by the rough surface. As shown by authors such as Uesugi and Kishida 1986

and Martinez and Frost 2017, the interface shear strength mobilized by surfaces composed of randomly-distributed asperities, such as the reference rough and smooth surfaces considered herein, can be characterized by a unique relationship with the surface roughness. In contrast, the snakeskin-inspired surface mobilizes interface shear strengths that are dependent on the shearing direction (i.e., cranial or caudal).

Laboratory Cyclic Interface Shear Tests. A series of cyclic interface shear tests were performed on each surface, summarized in Table 2.2. Tests 1 and 2 were conducted with reference smooth and rough surfaces to establish a baseline response. Subsequent tests were conducted with the bioinspired surface in the cranial first (i.e., cranial→caudal) and caudal first (i.e., caudal→cranial) directions with boundary stiffnesses that varied from 0 kPa/mm to 75, 150, 300, and 1000 kPa/mm in dense (Tests 3-14) and loose (Tests 15-22) sand specimens.

The reference rough surface (Test 1) mobilized larger shear stresses than the smooth surface (Test 2), as shown in Figure 2.6a. The shear strength mobilized by the reference surfaces degraded along failure envelopes that can be linearly approximated. These trends highlight typical cyclic interface behavior under constant normal stiffness conditions where rough surfaces have been shown to induce greater cumulative contraction and associated decreases in effective normal stresses due to the larger deformations induced within the shear band (e.g., Mortara et. al. 2007). The cyclic tests with snakeskin-inspired surfaces indicate that the maximum shear stresses mobilized in the cranial direction were greater than those mobilized in the caudal direction in both cranial→caudal and caudal→cranial tests (Tests 9 and 10, Figure 2.6c). In both tests, the maximum and minimum amplitude of shear strength mobilized per cycle degraded along envelopes which are asymmetric. These envelopes were fit with a Coulombic linear trend ($\tau = \sigma'_n \tan\delta_{mobilized}$) to

evaluate the mobilized interface friction angles, which generally implied larger friction angles mobilized during cranial shearing (Table 2.2). These envelopes do not necessarily correspond to failure but rather to the shear strength mobilized at the displacement amplitude used for the tests. Although the assumed linear envelopes may not capture the nonlinearity at low stresses, they provide a comparison of the difference in mobilized shear strengths.

Figures 2.7a to 2.7d show the stress paths of the first two cycles during the tests against the smooth, rough, and bioinspired surfaces. The stress path of the test with the rough surface exhibits a phase transformation line, where the tendencies changed from contractive to dilative, that lies below the envelope line in both shearing directions (Figure 2.7a). In contrast, the test with the smooth surface exhibited a phase transformation line that coincided with the envelope (Figure 2.7b). The tests with the snakeskin-inspired surfaces show an asymmetric response. Phase transformation occurs prior to reaching the envelope during shearing in the cranial direction, similar to the reference rough surface test (positive shear stress values in Figure 2.7c and negative shear stress values in Figure 2.7d). During shearing in the caudal direction, the phase transformation line closely coincides with the envelope line, similar to the reference smooth surface test (negative shear stress values in Figure 2.7c and positive shear stress values in Figure 2.7d).

All tests with bioinspired surfaces display a consistent shear stress – displacement response across all boundary stiffnesses, as shown by the evolution of shear and normal stresses for dense specimens (Tests 3 to 10, Figures 2.8a to 2.8d). As expected, the shear and normal stresses degrade at greater rates as the boundary stiffness increases. Degradation of normal stresses during the first few cycles generally occurred at a greater rate during the caudal→cranial tests; however, there is no apparent trend between the initial shearing direction and the normal stress magnitude at the end

of the 50th cycle. The stress paths for each test indicate that the degradation of stresses occurred along envelopes that were asymmetric regardless of the initial shearing direction.

Similar trends in the degradation of shear and normal stresses and stress paths were observed for the tests conducted on loose specimens (Tests 15 to 22) and tests conducted at larger displacement amplitudes (Tests 11 to 14). Figures 2.9a to 2.9c present these results in terms of the absolute maximum shear stress mobilized in each cycle for each loading direction. The shear stresses mobilized in the cranial→caudal tests become close to each other as the boundary normal stiffness increases. However, the shear stresses mobilized in the cranial direction are always greater during caudal→cranial tests. The results of these tests can be used to evaluate the difference in mobilized interface friction angles from Tests 3 to 22 (Figure 2.10). The parameter plotted in the figure, $(\delta_{cranial}/\delta_{caudal}) - 1$, takes a positive value when $\delta_{cranial}$ is greater, a negative value when δ_{caudal} is greater, and a value of zero when $\delta_{cranial}$ is equal to δ_{caudal}. These results indicate that as boundary stiffness increases, the difference between $\delta_{cranial}$ and δ_{caudal} decreases and that during all caudal→cranial tests, $\delta_{cranial}$ was significantly greater than δ_{caudal}. These results highlight that the testing sequence (i.e., cranial→caudal versus caudal→cranial) has an important effect on the difference in mobilized interface strength, quantified in terms of shear stresses or interface friction angles.

Centrifuge Monotonic Pile Load Tests. Centrifuge pile load tests were performed on four snakeskin-inspired piles and one smooth pile in dense and loose sand deposits (Table 2.1). A force – time series of a loading sequence on a snakeskin-inspired pile is shown in Figure 2.11 along with an indication of the different loading stages (caudally installed pile, $L = 12$ mm, $D_R = 85\%$). The bioinspired piles were first installed and subjected to a pullout test, after which the load on the pile

was immediately relaxed before initiating cyclic loading beginning in the same direction as the pullout test.

The snakeskin-inspired piles with surface texture with asperity length, L, of 6 and 12 mm installed in the cranial direction mobilized greater installation forces than the piles installed in the caudal direction in both dense and loose sand deposits, suggesting a greater compressive capacity (Figures 2.12a through 2.12c). In addition, the installation forces mobilized by the bioinspired piles were larger than those mobilized by the smooth pile. Figures 2.12d through 2.12f present the results in terms of the average shear stress normalized by initial vertical effective stress at the pile midpoint (τ_{avg} / $\sigma'_{vo,avg}$). For all cases, the caudally installed – cranially pulled piles mobilized greater normalized stresses than the cranially installed – caudally pulled piles. However, pulling in the caudal direction exhibited a stiffer initial response. The snakeskin-inspired piles mobilized pullout capacities that were up to 780% (cranial pullout) and 340% (caudal pullout) greater than those mobilized by the smooth pile. These differences are likely due to the larger radial effective stresses mobilized around the bioinspired piles during installation and pullout as well as the larger interface friction angle mobilized by the snakeskin-inspired surfaces. The instrumentation included in the piles does not provide the information required to quantify the relative contributions of each mechanism.

Centrifuge Cyclic Pile Load Test. Following monotonic pullout loading, the snakeskin-inspired piles were subjected to 40 cycles with a target displacement amplitude of 0.5 mm. Cyclic tests were conducted in the dense deposit for piles with asperity lengths of 6 and 12 mm. All test responses exhibit a similar asymmetric response as that previously described for the laboratory cyclic interface shear tests. For both tests conducted in the caudally installed – cranially pulled

piles (i.e., cranial→caudal cycling), shearing in the cranial direction initially mobilized significantly greater shear resistances than those mobilized in the caudal direction, but the capacity degraded at a greater rate (Figure 2.13a and 2.13c). For tests on the cranially installed – caudally pulled pile (i.e., caudal→cranial cycling), the caudal normalized stresses were greatest in the first two to three cycles (Figure 2.13b and 2.13d). However, the values in the caudal direction reduced with increasing cycle number, whereas those mobilized in the cranial second direction slightly increased by the end of cycling.

DISCUSSION

Monotonic Behavior in Element and Pile Load Tests. The shear and normal stress responses for the laboratory tests on the snakeskin-inspired surfaces under CNS conditions is consistent with observations of volumetric change behavior in the CNL tests, which exhibited larger dilative volumetric changes during cranial shearing. Cranial first shearing similarly induced larger increases in normal stress compared to caudal first shearing (Figures 2.4a and 2.4b). During the centrifuge pile load tests, greater installation forces were mobilized by the cranially installed pile, corresponding to greater compressive capacity. The pullout cranial shear response for the piles also indicates a significantly larger skin friction than the caudally-pulled piles, in agreement with the CNS laboratory tests (Figures 2.4a and 2.4b). This suggests a greater dilative response and an associated increase in radial effective stress during cranial shearing. These results suggest that the trends observed in the pile load tests are consistent with those from the laboratory tests even when installation effects are modeled.

Cyclic Behavior in Laboratory Tests. The cyclic behavior of the interfaces with snakeskin-inspired surfaces is affected by the initial loading direction, boundary stiffness, relative density, and displacement amplitude. In general, cyclic strength degradation increases as the boundary stiffness increases, relative density decreases, and cyclic displacement amplitude increases. The caudal→cranial tests show a consistent bias to mobilize larger shear resistances in the second (i.e., cranial) direction. The bias in cranial→caudal tests, however, depends on the boundary stiffness.

To quantify the relative difference between the shear resistances mobilized in cranial and caudal directions and capture relative rates of degradation, a Directional Frictional Resistance (DFR) parameter is defined as:

$$Directional\ Frictional\ Resistance, DFR = \frac{|\tau_{cranial}|}{|\tau_{caudal}|} - 1 \tag{3}$$

where $\tau_{cranial}$ and τ_{caudal} are the maximum amplitude of shear stress mobilized in any given cycle in the cranial and caudal shearing directions, respectively. A DFR value of 0.00 indicates that the same shear resistance is mobilized in cranial and caudal shearing directions, a positive value indicates that greater shear resistance is mobilized in the cranial direction, and a negative value indicates that greater shear resistance is mobilized in the caudal direction.

The DFR values shift from positive to negative in cranial→caudal tests as the boundary normal stiffness is increased, as shown in Figure 2.14a and 2.14b for tests on dense and loose specimens. During tests with boundary stiffnesses of 0 and 150 kPa/mm on dense specimens, DFR is negative during the first few cycles but reaches stable values of 0.30 and 0.05, respectively, with increasing cycle number. During the test with a boundary stiffness of 300 kPa/mm, DFR is also initially negative and increases to small positive values but then decreases again to negative values as cycle number increases. As the normal boundary stiffness is further increased to 1000 kPa/mm, the DFR values become negative after a few cycles. This trend indicates that increased boundary

stiffness results in a greater rate of degradation for cranial shear resistances relative to caudal shear resistances.

The caudal→cranial tests on dense and loose specimens show that the DFR values are always positive. This indicates that the shear resistances in the second, cranial direction are always greater and degrade at a smaller rate than those in the first, caudal direction. Figure 2.14c shows the results for cranial→caudal and caudal→cranial test pairs on dense specimens sheared with varying displacement amplitudes. For the same normal stiffness, the tests with a displacement amplitude of 2 mm show marginally smaller DFR values, but the results follow essentially the same trends as the tests with an amplitude of 1 mm.

Results from the laboratory tests were used to develop the DFR envelopes shown in Figure 2.15. For tests conducted in the cranial→caudal sequence, DFR values decrease as the boundary stiffness increases, the relative density decreases, and the cyclic displacement amplitude increases; all of these conditions lead to an increase in the rate of cyclic strength degradation. For tests conducted in the caudal→cranial sequence, DFR values increase with increasing boundary stiffness and cyclic displacement amplitude. Results throughout this investigation consistently highlight the important effect of testing sequence on the difference in mobilized interface strength. Although this difference is likely due to biases on the stress paths imposed during cranial or caudal shearing, the information obtained from the laboratory experiments should be complemented with local information of the evolution of state of stresses and fabric from numerical simulations or advanced experiments with tomography capabilities.

Cyclic Behavior in Pile Load Tests. The shear stresses mobilized during the cyclic centrifuge pile load tests were used to calculate DFR values with Eq. (3) and results are superimposed on the

envelopes obtained from the laboratory results (Figure 2.15). The DFR values obtained from the pile load tests are in general agreement with the envelopes determined from the laboratory tests, especially for larger cycle numbers. The caudally installed – cranially pulled piles (cranial→caudal cycling) mobilized particularly large positive DFR values during the initial 10 cycles, with values as large as 7.0 and 5.3 depending on the asperity spacing. DFR decreased with cycle number, reaching values between 0.35 and 0.10 for the pile with an asperity length of 6 mm and between -0.10 and -0.15 for the pile with an asperity length of 12 mm. The cranially installed – caudally pulled piles (caudal→cranial cycling) mobilized caudal shear resistances that were greater than the cranial ones during the initial three to four cycles, resulting in negative initial DFR values. However, the DFR rapidly increased, reaching values of about 2.30 by the end of the 40 cycles.

IMPLICATIONS IN PRACTICE

Results from the laboratory interface shear and centrifuge pile load tests are consistent. The load tests on cranially installed snakeskin-inspired piles highlight their ability to mobilize greater forces than the caudally-installed and smooth piles. While the greater mobilized forces may not be advantageous for installation, the greater compressive capacity does provide a benefit in terms of, for example, reducing the number or length of piles required to support a given axial compressive load. This may also be useful to decrease the consequences of downdrag loads during reconsolidation of liquefied sand. Conversely, the load tests on caudally installed piles show that the bioinspired piles can reduce installation forces and increase pullout capacity. The caudally installed – cranially pulled pile yields DFR values as large as 7.0 in the initial cycle, indicating a skin friction almost one order of magnitude greater in the cranial pullout direction, which may be useful for offshore structures with anchoring systems primarily loaded in tension.

The response to cyclic loading of the bioinspired surfaces and piles also suggests potential benefits. Caudal→cranial loading consistently mobilized greater shear resistances in the cranial direction, which may lead to reduction in the accumulation of pullout deformations in offshore piles due to environmental loads. The DFR results of the caudally installed – cranially pulled piles agree with the cranial→caudal laboratory tests, whereas the DFR values of the cranially installed – caudally pulled pile agree with those from the caudal→cranial laboratory tests. This suggests that the 20 mm pullout test, as opposed to the installation, establishes the bias in cyclic strength degradation and DFR value evolution with cycle number. While further research is required to evaluate the performance in field conditions, the results of this investigation provide preliminary evidence of the potential benefits of using snakeskin-inspired surfaces in the design of engineered foundation and anchorage systems.

CONCLUSIONS

The shear behavior of interfaces with snakeskin-inspired surfaces was investigated using laboratory interface shear tests and pile load tests performed in the centrifuge, with trends observed as follows.

- The snakeskin-inspired surfaces mobilized larger shear resistances in the cranial direction than in the caudal direction during monotonic loading. Cranial shearing resulted in greater dilative volumetric changes and increases in normal stresses than caudal shearing.

- The forces mobilized during monotonic pile cranial installation and pullout were significantly larger than those mobilized in the caudal direction.

- Cyclic displacement-controlled laboratory tests indicate that shear strength degradation is dependent on shearing direction (i.e., cranial versus caudal), boundary conditions, relative

density, and displacement amplitude. The stress paths of CNS tests indicate that the failure envelope and location of the phase transformation line also depend on shearing direction.

- The difference in mobilized shear resistances in the cranial and caudal directions was quantified using a Directional Frictional Resistance parameter. Cranial→caudal tests showed biases in both directions, depending on boundary stiffness, relative density, and displacement amplitude. The caudal→cranial tests mobilized shear resistances that were consistently larger in the second (i.e., cranial) direction.

- The cyclic load tests on piles of different asperity length also exhibited cyclic degradation. DFR values for caudally installed piles sharply decreased from initial values as large as 7.0 to negative values in later cycles. Greater cranial shear resistances were mobilized in the cranially installed piles, resulting in positive DFR values consistent with trends from the laboratory tests.

The results presented herein suggest that snakeskin-inspired surfaces can readily mobilize skin friction that is dependent on the direction of displacement and provide preliminary evidence of the potential benefits of using these surfaces in the design of engineered foundation and anchorage systems. While the influence of mean particle size to asperity height and length may play a role in the monotonic and cyclic behavior of bioinspired interfaces, and would be a relevant factor in design of such systems, study of the effect was outside the scope of this investigation. Further investigation into the behavior of these surfaces with different geometries under additional loading conditions may aid in the selection of piles with cranial or caudal installation directionality given site-specific soil conditions and expected loading.

DATA AVAILABILITY

Some or all data, models, or code generated or used during the study are available from the corresponding author by request.

ACKNOWLEDGEMENTS

REFERENCES

Airey, D. W., R. Al-Douri, and H. G. Poulos. 1992. "Estimation of pile friction degradation from shear box tests." *Geotech. Test. J.* 15 (4): 388–392. https://doi.org/10.1520/GTJ10253J.

Airey, D.W., and R. B. Kelly. 2010. "Interface behaviours from large diameter ring shear tests." *Proc. of the Res. Symp. Charact. Beh. Int.*, 1–6. Atlanta, GA: IOS Press, Fairfax, VA.

ASTM D 3080-11. 2011. "Standard test method for direct shear test of soils under consolidated drained conditions." *ASTM International*. West Conshohocken, PA.

Baum, M. J., A. E. Kovalev, J. Michels, and S. N. Gorb. 2014. "Anisotropic friction of the ventral scales in the snake Lampropeltis getula californiae." *Trib. Letters* 54 (2): 139–150. https://doi.org/10.1007/s11249-014-0319-y.

Boukpeti, N., and D. J. White. 2017. "Interface shear box tests for assessing axial pipe–soil resistance." *Géotechnique* 67 (1): 18–30. doi.org/10.1680/jgeot.15.P.112.

Boulon, M., and P. Foray. 1986. "Physical and numerical simulation of lateral shaft friction along offshore piles in sand." *Proc., 3rd Int. Conf. on Num. Methods in Offshore Piling*, Editions Techrig, 127–148. Paris, France.

Carey, T. J., N. Stone, B. L. Kutter. 2019. "Grain Size Analysis and Maximum and Minimum Dry Density Testing of Ottawa F-65 Sand for LEAP-UCD-2017." *Model Tests and Numerical Simulations of Liquefaction and Lateral Spreading*, LEAP-UCD-2017.

DeJong, J. T., M. F. Randolph, and D. J. White. 2003. "Interface load transfer degradation during cyclic load: a microscale investigation." *Soils Found.* 43 (4): 81–93. https://doi.org/10.3208/sandf.43.4_81.

DeJong, J. T., and Z. J. Westgate. 2009. "Role of initial state, material properties, and confinement condition on local and global soil-structure interface behavior," *J. Geotech. and Geoenviron. Eng.* 135 (11): 1646–1660. https://doi.org/10.1061/(ASCE)1090-0241(2009)135:11(1646).

Dietz, M., and M. Lings. 2006. "Postpeak strength of interfaces in a stress-dilatancy framework." *J. Geotech. and Geoenviron. Eng.* 132 (11): 1474–1484. https://doi.org/10.1061/(ASCE)1090-0241(2006)132:11(1474).

Dietz, M., and M. Lings. 2010. "Changes in surface roughness in multi-reverse sand-steel interface tests." *Proceedings of the Research Symposium on Characterization and Behavior of Interfaces*, 7–15. Atlanta, GA: IOS Press, Fairfax, VA.

Fakharian, K., and E. Evgin. 1996. "An automated apparatus for three dimensional monotonic and cyclic testing of interfaces." *Geotech. Testing J.* 19 (1): 22–31. https://doi.org/10.1520/GTJ11404J.

Fioravante, V. 2002. "On the shaft friction modelling of non-displacement piles in sand." *Soils Found*. 42 (2): 23–33. https://doi.org/10.3208/sandf .42.2_23.

Frost, J. D., and J. T. DeJong. 2005. "In situ assessment of role of surface roughness on interface response." *J. Geotech. Geoenviron. Eng.* 131 (4): 498–511. https://doi.org/10.1061/(ASCE)1090-0241(2005)131:4(498).

Gray, J., and H. W. Lissmann. 1950. "The kinetics of locomotion of the grass-snake." *J. Exp. Biol.* 26: 354–367.

Hazel, J., M. Stone, M. S. Grace, and V. V. Tsukruk. 1999. "Nanoscale design of snake skin for reptation locomotion via friction anisotropy." *J. Biomech.* 32 (5): 477–484. https://doi.org/10.1016/S0021-9290(99)00013-5.

Ho, T. Y. K., R. J. Jardine, and N. Anh-Minh. 2011. "Large-displacement interface shear between steel and granular media." *Géotechnique* 61 (3): 221–234. https://doi.org/10.1680/geot.8.P.086.

Hryciw, R. D., and M. Irsyam. 1993. "Behavior of sand particles around rigid ribbed inclusions during shear." *Soils Found*. 33 (3): 1–13. https:// doi.org/10.3208/sandf1972.33.3_1.

Jayne, B. C. 1985. "Swimming in constricting (Elaphe g. guttata) and nonconstricting (Nerodia fasciata pictiventris) colubrid snakes." *Copeia* 1985: 195–208. https://doi.org/10.2307/1444809.

Jayne, B. C. 1986. "Kinematics of terrestrial snake locomotion." *Copeia* 1986 (4): 915–927. https://doi.org/10.2307/1445288.

Kutter, B. L., T. J. Carey, T. Hashimoto, M. Zeghal, T. Abdoun, P. Kokkali, G. Madabhushi et al. 2018. "LEAP-GWU-2015 experiment specifications, results, and comparisons." *Soil Dyn. Eq. Eng.* 113 (2018): 616–628. https://doi.org/10.1016/j.soildyn.2017.05.018.

Lehane, B. M., R. J. Jardine, A. J. Bond, and R. Frank. 1993. "Mechanisms of shaft friction in sand from instrumented pile tests." *J. Geotech. Eng.* 119 (1): 19–35. https://doi.org/10.1061/(ASCE)0733-9410(1993)119:1(19).

Lehane, B. M., and D. J. White. 2005. "Lateral stress changes and shaft friction for model displacement piles in sand." *Can. Geotech. J.* 42 (4): 1039–1052. https://doi.org/10.1139/t05-023.

Lillywhite, H. B. 2014. *How snakes work: Structure, function and behavior of the world's snakes*. New York: Oxford University Press.

Martinez, A., and S. Palumbo. 2018. "Anisotropic Shear Behavior of Soil-Structure Interfaces: Bio-Inspiration from Snake Skin." *Proc. ASCE IFCEE 2018 Conf.*, *Orlando, FL.*

Martinez, A., and J. D. Frost. 2017. "The influence of surface roughness form on the strength of sand–structure interfaces." *Géotechnique Letters* 7 (2017): 104–111. https://doi.org/10.1680/jgele.16.00169.

Martinez, A., and J. D. Frost. 2018. "Undrained cyclic behavior of particulate-continuum interfaces subjected to torsional shear." *J. Geotech. Geoenviron. Eng.* 144 (9). https://doi.org/10.1061/(ASCE)GT.1943-5606.0001942.

Martinez, A., S. Palumbo, and B. D. Todd. 2019. "Bio-Inspiration for anisotropic load transfer at soil-structure interfaces." *J. Geotech. Geoenv. Eng.* 145 (10). https://doi.org/10.1061/(ASCE)GT.1943-5606.0002138.

Martinez, A., and H. Stutz. 2018. "Rate effects on the interface shear behaviour of normally and overconsolidated clay." *Geotechnique* 69 (9): 1–15. https://doi.org/10.1680/jgeot.17.P.311.

Marvi, H. 2013. "The role of functional surfaces in the locomotion of snakes." *Ph.D. dissertation*, Dept. of Mechanical Engineering, Georgia Institute of Technology.

Marvi, H., J. P. Cook, J. L. Streator, and D. L. Hu. 2016. "Snakes move their scales to increase friction." *Biotribology* 5 (3): 52–60. https://doi .org/10.1016/j.biotri.2015.11.001.

Marvi, H., and D. L. Hu. 2012. "Friction enhancement in concertina locomotion of snakes." *J. R. Soc.* 9 (76): 3067–3080. https://doi.org/10 .1098/rsif.2012.0132.

Marvi, H., J. Bridges, and D. L. Hu. 2013. "Snakes mimic earthworms: propulsion using rectilinear travelling waves." *J. R. Soc.* 10 (84). https://doi.org/10.1098/rsif.2013.0188.

Marvi, H., C. Gong, N. Gravish, H. Astley, M. Travers, R. L. Hatton, J. R. Mendelson III, H. Choset, D. L. Hu, and D. I. Goldman. 2014. "Sidewinding with minimal slip: Snake and robot ascent of sandy slopes." *Science* 346 (6206): 224–229. https://doi.org/10.1126/science.1255718.

Mortara, G., A. Mangiola, and V. N. Ghionna. 2007. "Cyclic shear stress degradation and post-cyclic behaviour from sand: Steel interface direct shear tests." *Can. Geotech. J*. 44 (7): 739–752. https://doi.org/10.1139 /t07-019.

Palumbo, S. 2018. "Anisotropic interface shear behavior of granular soil and surfaces biologically-inspired by snakeskin." *M.S. thesis*, Dept. of Civil and Environmental Engineering, Univ. of California, Davis.

Parra, A. 2016. "Ottawa F-65 Sand Characterization." *Ph.D. dissertation*, Dept. of Civil and Environmental Engineering, Univ. of California, Davis.

Uesugi, M., and H. Kishida. 1986. "Influential factors of friction between steel and dry sands." *Soils Found.* 26 (2): 33–46. https://doi.org/10.3208 /sandf1972.26.2_33.

Vogel, S. 1998. *Cat's Paws and Catapults: Mechanical Worlds of Nature and People*. W. W. Norton & Company, Inc., New York.

Wang, J., J. E. Dove, and M. S. Gutierrez. 2007. "Determining particulate–solid interphase strength using shear-induced anisotropy." *Granular Matter* 9: 231–240. https://doi.org/10.1007/s10035-006-0031-1.

Wang, J., J. E. Dove, and M. S. Gutierrez. 2007. "Anisotropy-based failure criterion for interphase systems." *J. Geotech. Geoenviron. Eng*. 133 (5): 599–608. https://doi.org/10.1061/(ASCE)1090-0241(2007)133:5(599).

Table 2.1. Summary of surfaces and piles used in laboratory and centrifuge testing program (note different y-axis scale on the smooth surface and smooth pile).
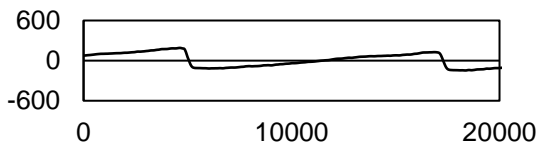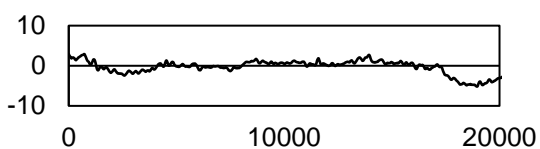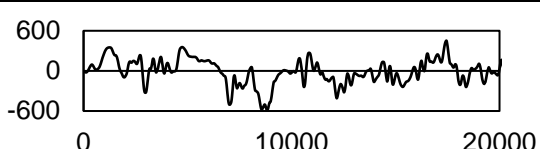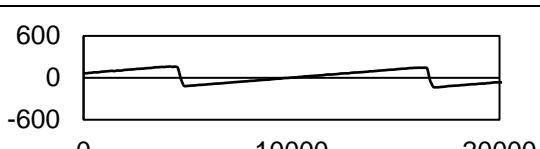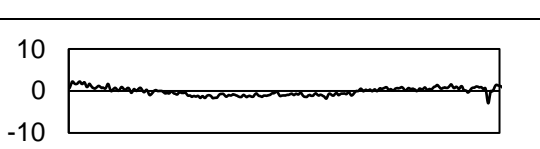
Surface	Profile (Axes in μm)	R_{max} (μm)	R_a (μm)	$R_{n,max}$ (R_{max}/D_{50})	$R_{n,a}$ (R_a/D_{50})
Bioinspired		333.3	92.9	1.666	0.464
Smooth		8.2	1.5	0.041	0.007
Rough		900.5	144.1	4.502	0.720
Bioinspired 12 mm Pile		333.3	96.5	1.667	0.482
Bioinspired 6 mm Pile		304.0	79.4	1.520	0.397
Smooth Pile		6.1	0.7	0.031	0.004

Table 2.2. Summary of cyclic constant normal stiffness tests.

Test No.	1st Cycle Shear Direction	σ'_{no} (kPa)	k (kPa/ mm)	Disp. Amplitude, δ_H (mm)	No. Cycles	D_R (%)	$\delta_{mobilized}$ (°) First Direction	$\delta_{mobilized}$ (°) Second Direction
1	Sandpaper	80	1000	1	10	85	30.5	30.5
2	Smooth	80	1000	1	10	84	10.1	15.9
3	Cranial	80	0	1	50	87	25.5	19.8
4	Caudal	80	0	1	50	88	17.6	30.9
5	Cranial	80	150	1	50	84	22.0	18.2
6	Caudal	80	150	1	50	89	13.5	29.0
7	Cranial	80	300	1	50	88	20.1	21.5
8	Caudal	80	300	1	50	80	15.9	24.0
9	Cranial	80	1000	1	50	88	17.4	18.2
10	Caudal	80	1000	1	50	88	14.4	22.9
11	Cranial	80	150	2	50	80	26.0	19.1
12	Caudal	80	150	2	50	93	12.4	19.3
13	Cranial	80	300	2	50	91	22.6	18.8
14	Caudal	80	300	2	50	78	10.0	16.6
15	Cranial	80	0	1	50	48	19.3	15.1
16	Caudal	80	0	1	50	54	12.6	24.0
17	Cranial	80	75	1	50	56	16.2	14.3
18	Caudal	80	75	1	50	57	10.1	22.0
19	Cranial	80	150	1	50	57	16.6	18.7
20	Caudal	80	150	1	50	49	13.1	19.0
21	Cranial	80	1000	1	50	52	16.0	22.8
22	Caudal	80	1000	1	50	56	11.0	18.8
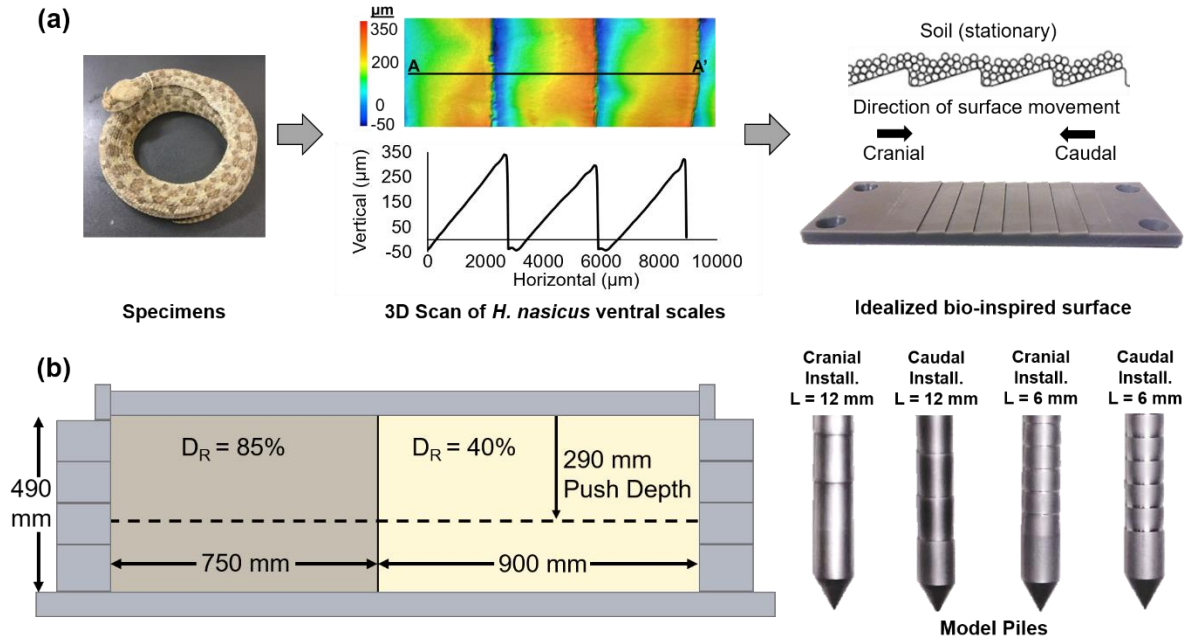
Figure 2.1. (a) Process for generation of snakeskin-inspired surfaces for laboratory tests and (b) centrifuge model container and model piles.
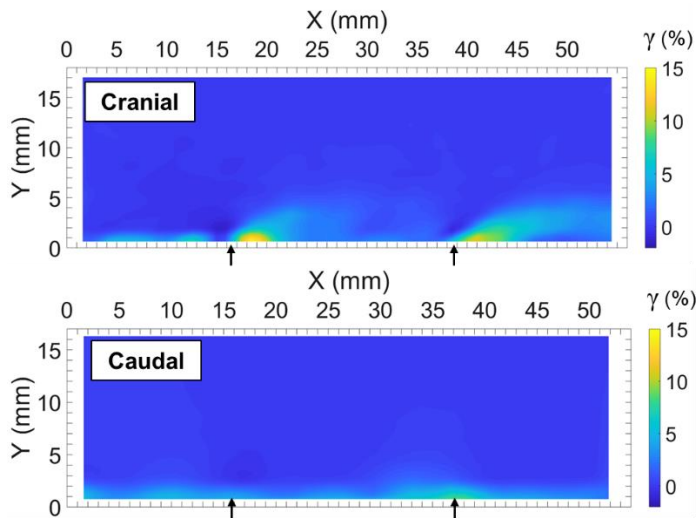
Figure 2.2. Strain field within a sand specimen from PIV analyses showing formation of passive soil wedges ahead of the asperities during cranial shearing but not during caudal shearing (black arrows indicate location of the asperities, data from Martinez et al. 2019).
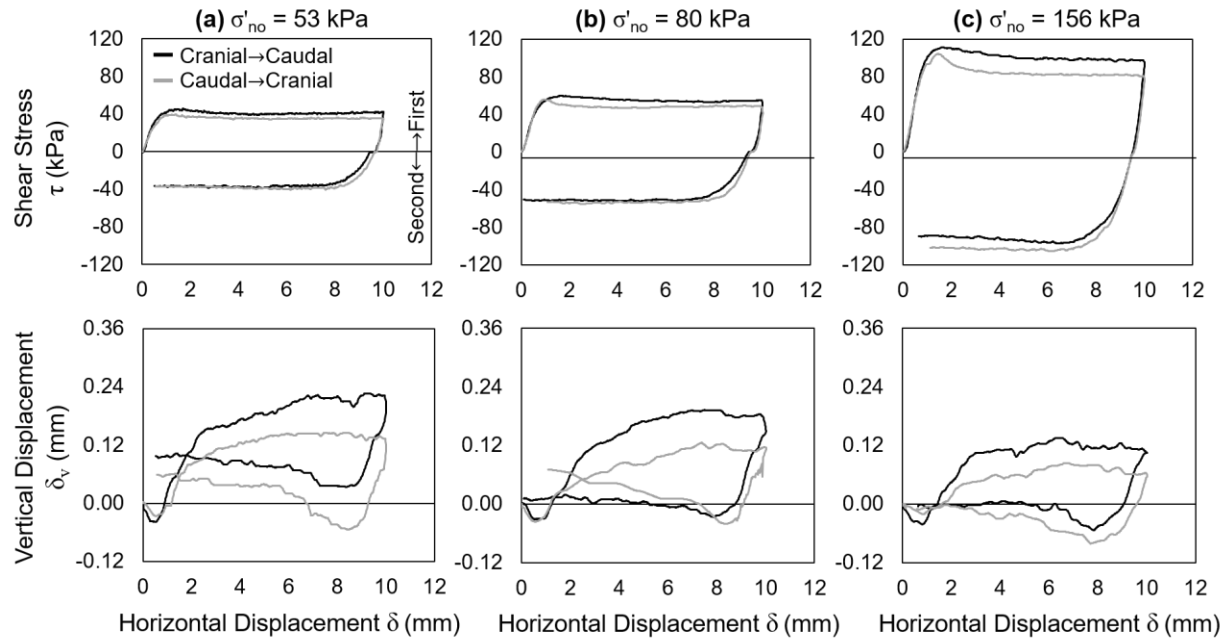
Figure 2.3. Single cycle tests on snakeskin-inspired surfaces conducted under CNL boundary conditions at (a) $\sigma'_n = 53$ kPa, (b) $\sigma'_n = 80$ kPa, and (c) $\sigma'_n = 156$ kPa (target $D_R = 85\%$).
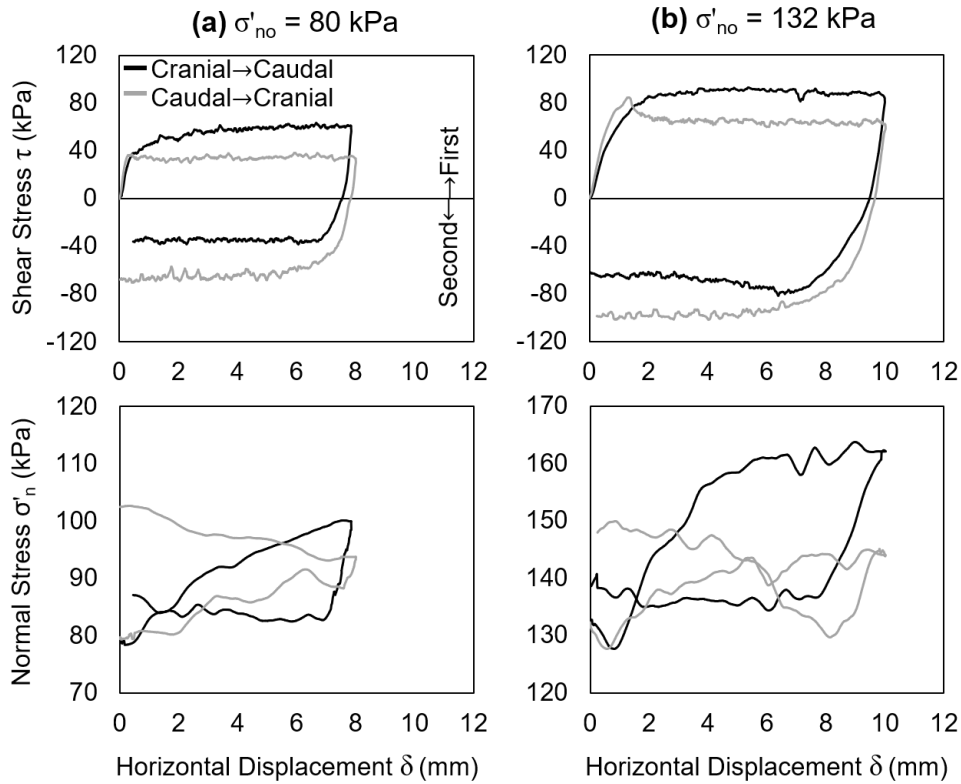
Figure 2.4. Single cycle tests on snakeskin-inspired surfaces conducted under CNS boundary conditions with a stiffness of 150 kPa/mm at initial stresses of (a) σ'_{no} = 80 kPa, (b) σ'_{no} = 132 kPa (target D_R = 85%).
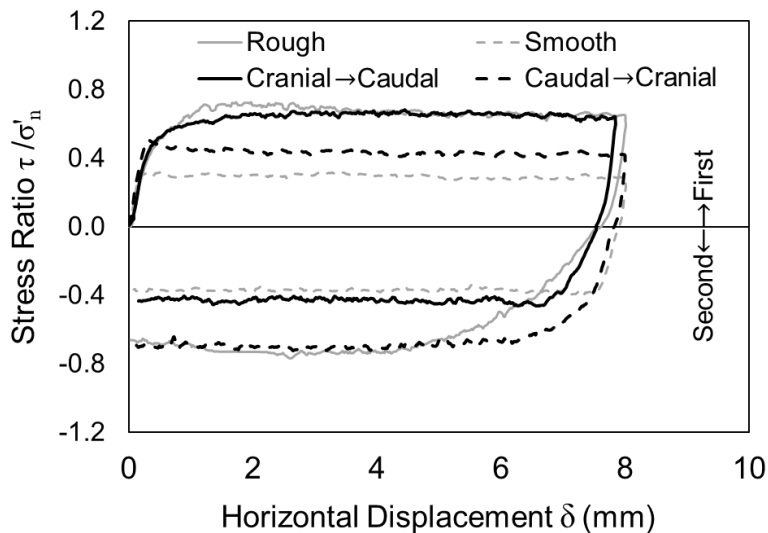
Figure 2.5. Normalized shear strength for tests against reference and snakeskin-inspired interfaces under CNS conditions (k = 150 kPa/mm, σ'_{no} = 80 kPa, target D_R = 85%).
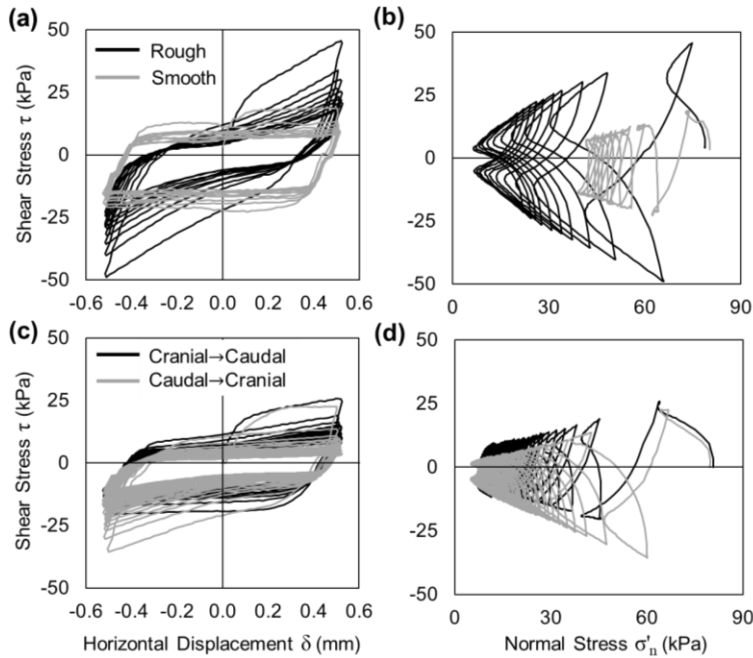
Figure 2.6. Cyclic interface shear test results: (a) shear stress – displacement curves and (b) stress paths against reference surfaces (Tests 1 and 2) and (c) shear stress – displacement curves and (d) stress paths against snakeskin-inspired surfaces (k = 1000 kPa/mm, σ'_{no} = 80 kPa, target D_R = 85%, δ_H = 1 mm).
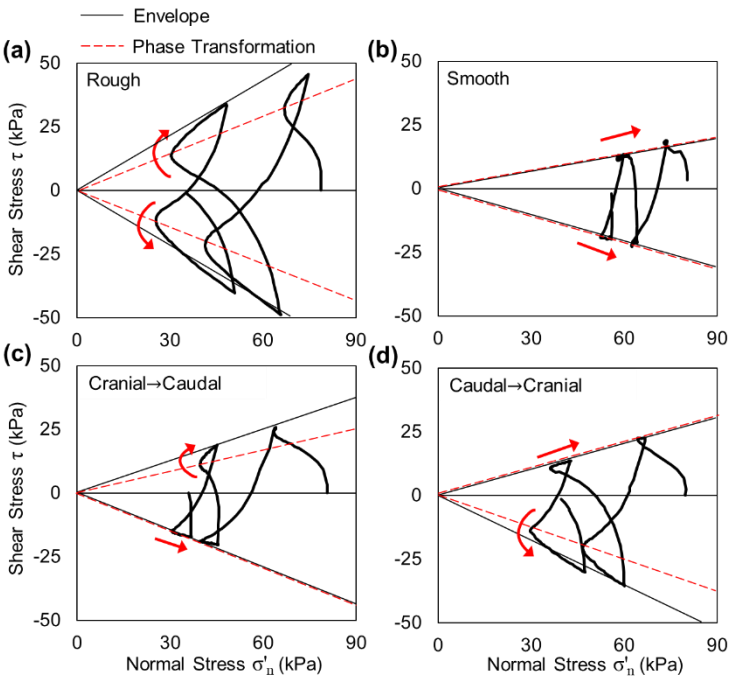
Figure 2.7. Comparison of failure envelopes and phase transformation lines of cyclic tests against (a) rough (Test 1), (b) smooth (Test 2), (c) bioinspired cranial→caudal (Test 9), and (d) bioinspired caudal→cranial (Test 10) surfaces (k = 1000 kPa/mm, σ'_{no} = 80 kPa, target D_R = 85%, δ_H = 1 mm).
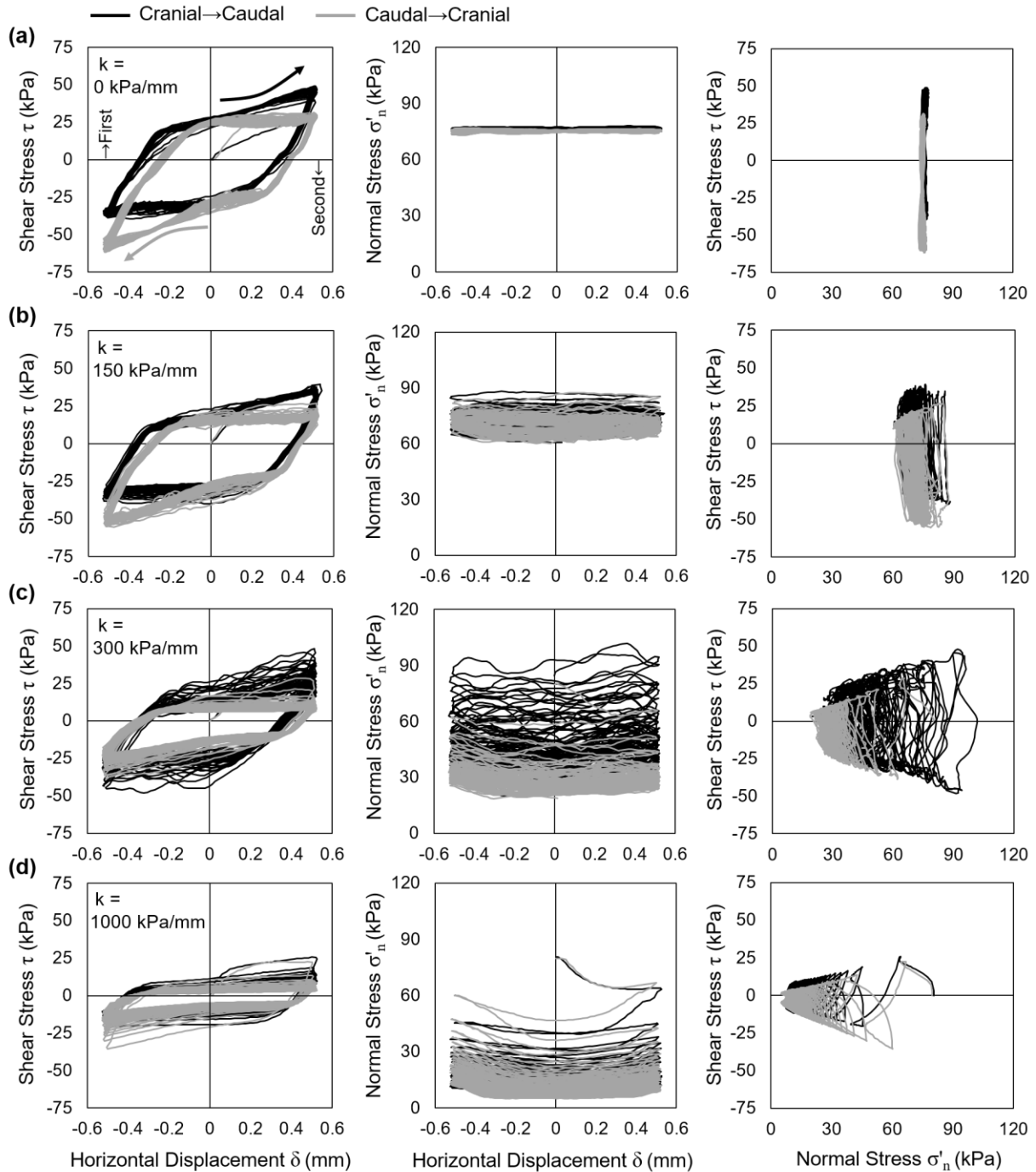
Figure 2.8. Shear stress – displacement, normal stress – displacement, and stress path curves for cyclic tests with boundary stiffness of (a) 0 kPa/mm (Tests 3 and 4), (b) 150 kPa/mm (Tests 5 and 6), (c) 300 kPa/mm (Tests 7 and 8), and (d) 1000 kPa/mm (Tests 9 and 10) (σ'_{no} = 80 kPa, target D_R = 85%, δ_H = 1 mm).
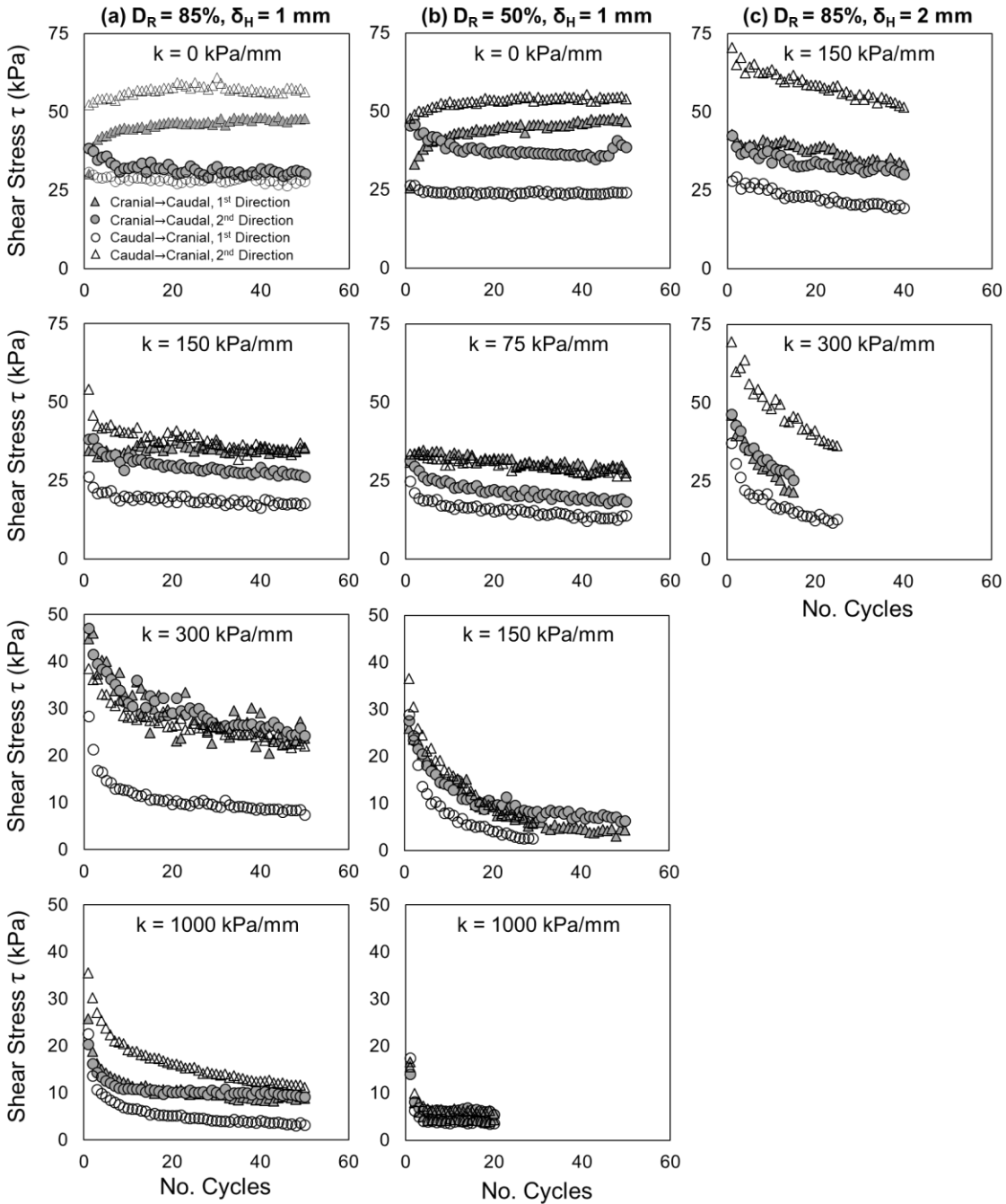
Figure 2.9. Absolute maximum shear stresses mobilized during cranial→caudal and caudal→cranial test pairs under varying boundary stiffness: (a) Target D_R = 85%, δ_H = 1 mm, σ'_{no} = 75 kPa, (b) target D_R = 50%, δ_H = 1 mm, σ'_{no} = 80 kPa, and (c) target D_R = 85%, δ_H = 2 mm, σ'_{no} = 80 kPa.
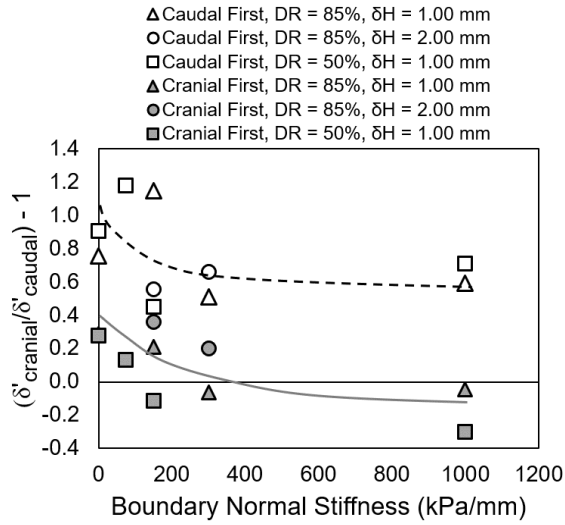
Figure 2.10. Ratio of mobilized interface friction angle as a function of boundary normal stiffness.
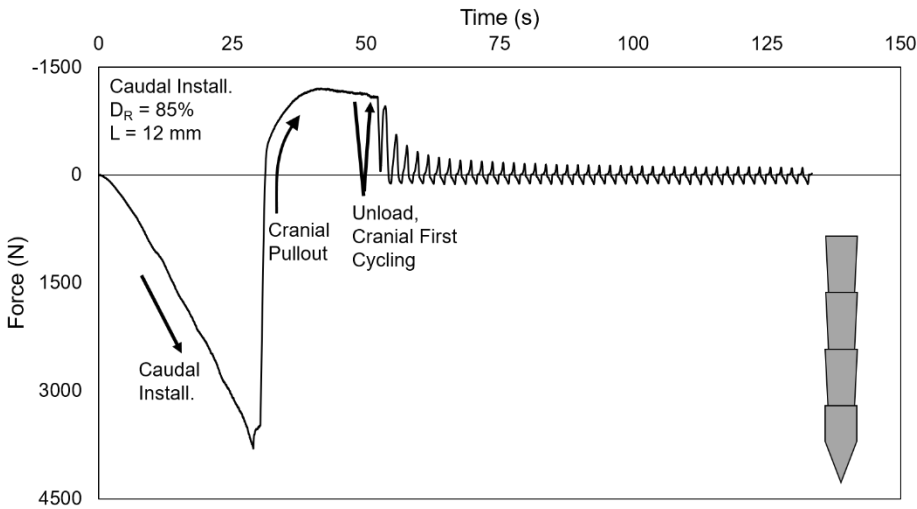
Figure 2.11. Typical time-load series of pile test sequence (caudally installed – cranially pulled, DR = 85%, L = 12 mm, δ_H = 1 mm).
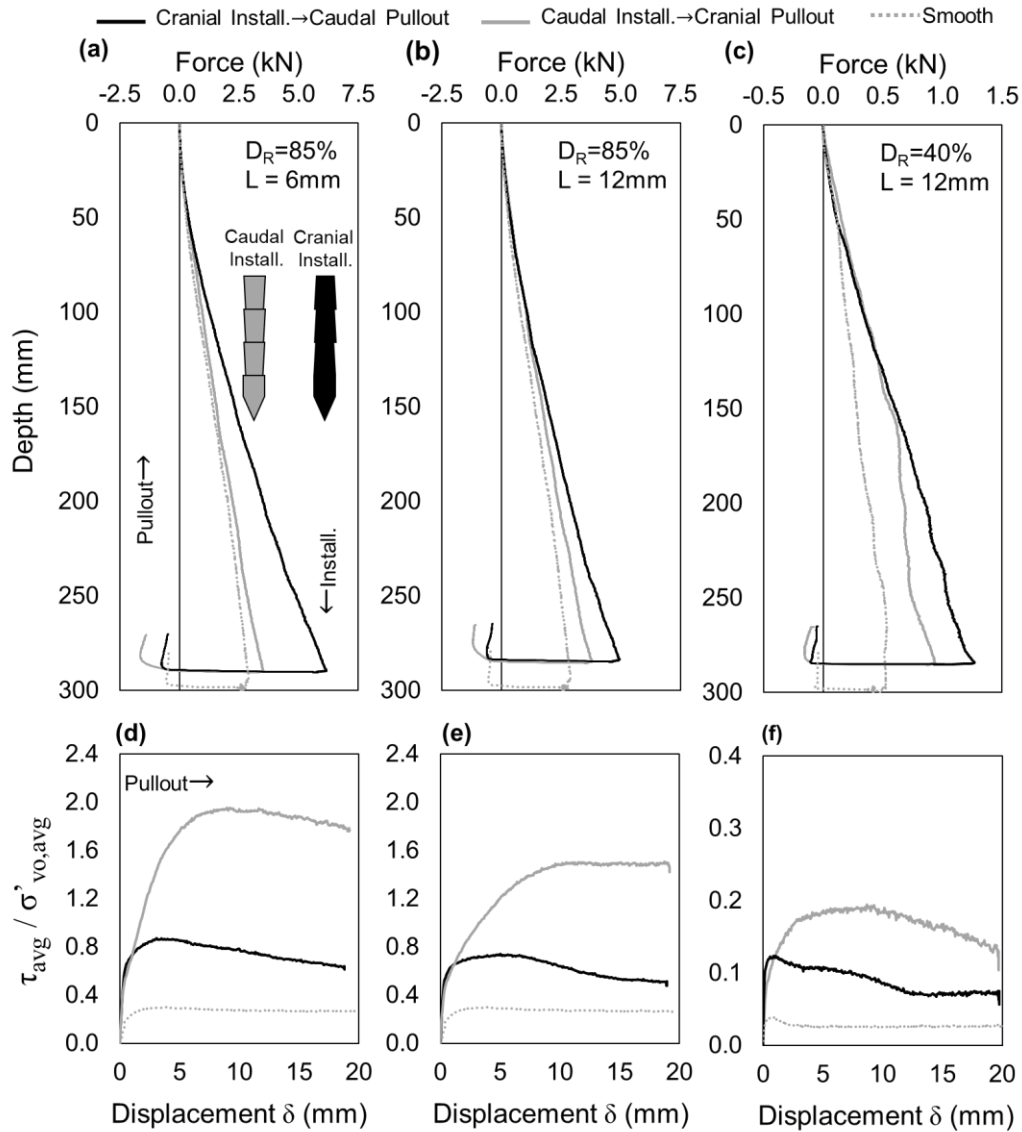
Figure 2.12. Measured force during monotonic installation and pullout for (a) and (d) pile with L of 6 mm in dense sand, (b) and (e) pile with L of 12 mm in dense sand, and (c) and (f) pile with L of 12 mm in loose sand (note different axes scales in (c) and (f)).
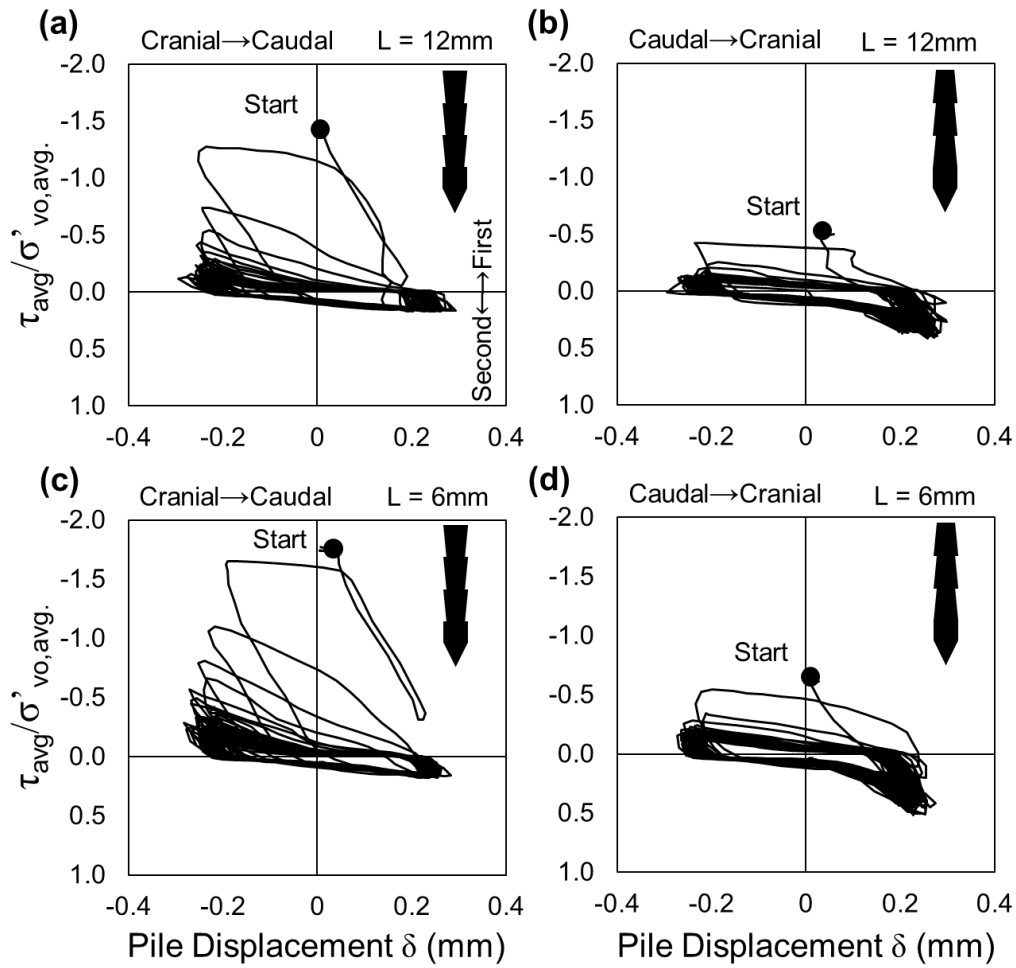
Figure 2.13. Cyclic pile load tests for (a) L = 12 mm cranial→caudal, (b) L = 12 mm caudal→cranial, (c) L = 6 mm cranial→caudal, and (d) L = 6 mm caudal→cranial tests (D_R = 85%. Note: negative values indicate tensile load and positive values indicate compressive load).
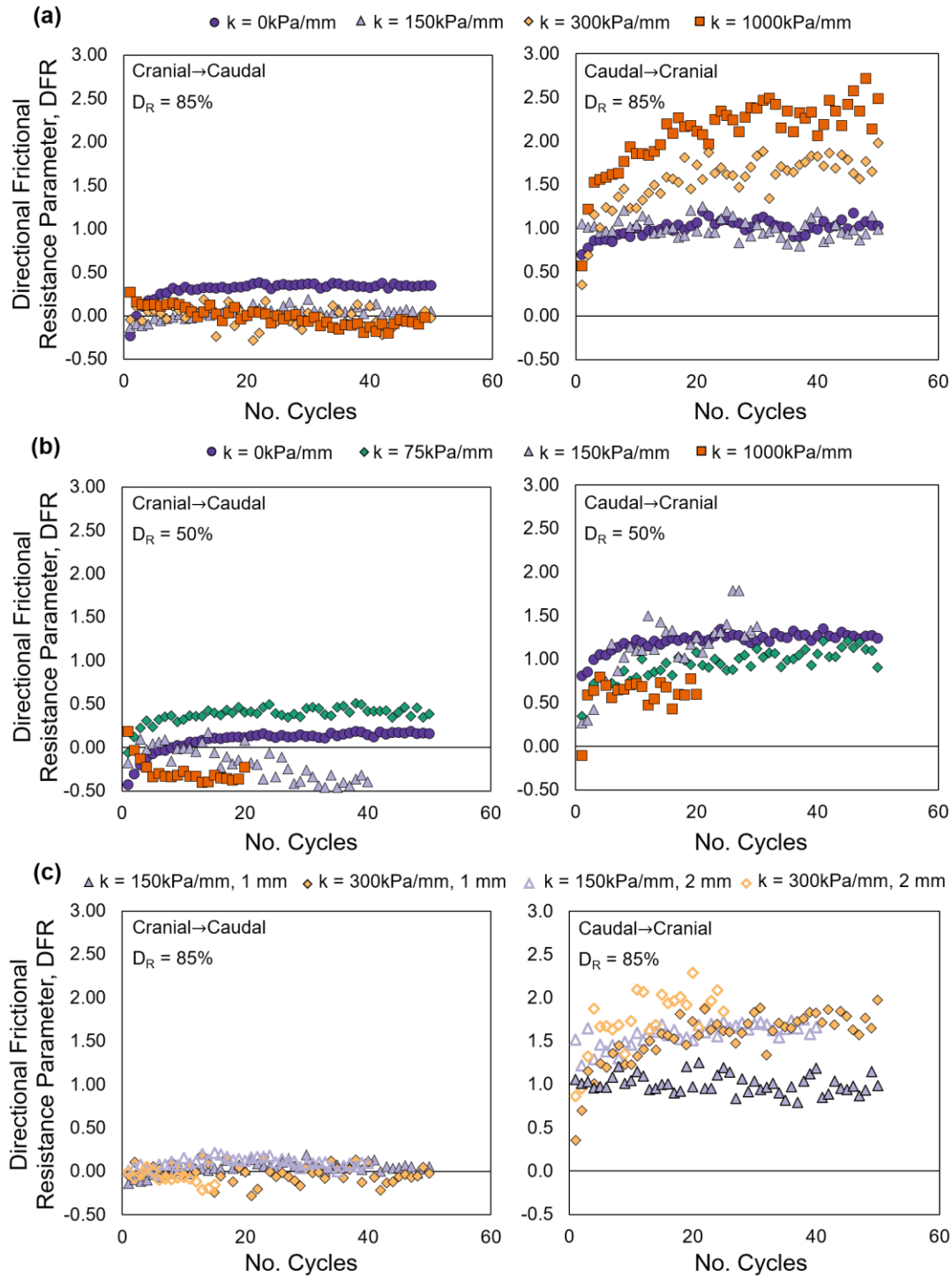
Figure 2.14. Comparison of Directional Frictional Resistance parameter (DFR) values for laboratory tests with varying boundary stiffness: (a) Target $D_R = 85\%$, $\delta_H = 1$ mm, $\sigma'_{no} = 80$ kPa (tests 3 to 10), (b) Target $D_R = 50\%$, $\delta_H = 1$ mm, $\sigma'_{no} = 80$ kPa (tests 15 to 22), and (c) Target $D_R = 85\%$, $\delta_H = 1$ mm and 2 mm, $\sigma'_{no} = 80$ kPa (tests 5 to 8 and 11 to 14).
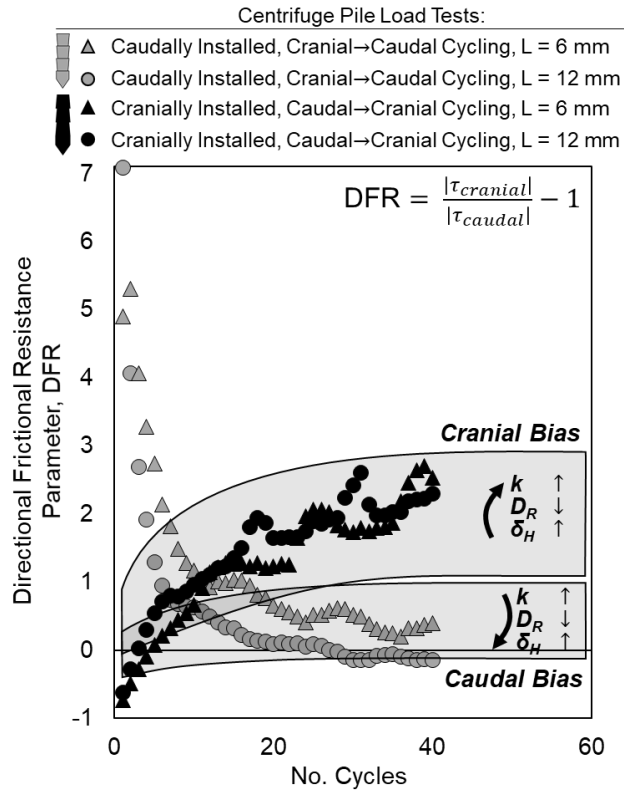
Figure 2.15. Comparison of Directional Frictional Resistance parameter (DFR) values from centrifuge cyclic load tests on dense sand with envelopes from laboratory cyclic interface shear tests.

Chapter 3. Load Transfer Directionality of Snakeskin-Inspired Piles During Installation and Pullout in Sands

This chapter was published in Journal of Geotechnical and Geoenvironmental Engineering (Editor's Choice) under the following citation and is presented here with minor edits.

ABSTRACT

Deep foundation applications, such as foundations for jacket structures and reaction piles, may benefit from larger shaft resistances during tensile than compressive loading. A suitable analog for designing surfaces whose load transfer depends on the direction of loading is the skin of snakes. Snake scales reduce friction when they move forward (i.e., caudal direction) and increase friction when they move backward (i.e., cranial direction). A series of centrifuge load tests were conducted on instrumented piles in medium-dense sand to investigate the load transfer behavior of piles with snakeskin-inspired surfaces. Load tests were performed on three bio-inspired piles, a reference rough pile, and a reference smooth piles at two embedment depths each. The results present distributions of axial load and shear stresses along the pile length and head load–displacement and local shear stress–displacement relationships. During both installation and pullout, the cranial shaft friction mobilized similar shear stress magnitudes and shear resistance distribution with depth to that of the rough pile, while similarities were observed between the caudal shaft friction and that of the smooth pile. The results show that the bio-inspired piles mobilize directionally-dependent

shaft capacities, where the ratio of capacities during cranial pullout to caudal installation was measured to be 1.6 to 2.1, as evidenced by the computed β coefficients. Variations in relative density in the centrifuge models were quantified by means of CPT soundings, and the pile test results were corrected for potential scaling effects to obtain β coefficients that are more representative of field conditions.

INTRODUCTION

The benefits and drawbacks of large frictional resistances have been investigated as early as Aristotle. For civil infrastructure projects, it may be advantageous to develop foundations based on interfaces that develop higher shaft resistances in one direction of loading than another. For foundations that mostly resist tensile loads, such as those for offshore jacket structures or piles used for reaction generation during load tests, surfaces that generate small resistances during installation compared to pullout may reduce costs if smaller equipment is required for their installation and if shorter or smaller diameter piles can achieve the desired capacity. Conversely, surfaces that increase the shaft resistance in compression may result in a reduction of the required pile dimensions to generate a given required load and may decrease the magnitude of downdrag-associated settlements due to consolidation of soft soils or reconsolidation of liquefied sand.

Pile skin friction. Pile shaft capacity primarily occurs as a function of the interaction between the soil and pile surface. The behavior is often simplified to compute a shaft resistance. For design, the unit shaft resistance in cohesionless soils, τ_s, can be computed by

$$\tau_s = (K \tan \delta')\sigma_v' = \beta \sigma_v' \qquad \text{Eq. 1}$$

53

where K is the lateral earth pressure coefficient, δ' is the interface friction angle, σ'_v is the vertical effective stress, and β is a coefficient that incorporates both K and δ'. Two approaches can be used to predict τ_s. In one approach, K and δ' can be accounted for individually. K has been shown to depend on installation method, soil state, and pile diameter and δ' is often taken as a function of mean particle diameter, D_{50}, and the surface roughness of the pile (Randolph 2003; Loukidis and Salgado 2008; Tovar-Valencia et al. 2017; Lehane et al. 2005; CUR 2001; Chen and Kulhawy 1994). In the other approach, the β-method can be used (API 2007; FHWA GEC 10) in which a factor is chosen that matches the installation method and expected loading conditions of the pile (Fellenius 2008; Rollins 2005; Lehane et al. 1993; White and Lehane 2004; Beringen 1979). In general, β factors have values between 0.6 and 1.0, with dense sands producing the larger values. Recommendations typically consist of reduction in axial shaft capacity during pullout to 70% to 85% of the compressive capacity (Fleming et al. 2008). The mechanisms leading to this difference in shaft capacity include the Poisson effect causing a decrease in mean confining stress during tensile loading and the rotation of principal effective stresses (De Nicola and Randolph 1993; Lehane et al. 1993).

The mobilization of pile shaft resistance is governed by the shear behavior of the interface between the pile and surrounding soil (Jardine et al. 1992; Everton 1992). Parameters that control the behavior of soil-structure interfaces include magnitude of surface roughness, typically quantified with the average roughness parameter, R_a, or the normalized roughness parameter, R_n (e.g., Uesugi and Kishida 1986; Dietz and Lings 2006; Tehrani et al. 2016), surface roughness form (e.g., Hryciw and Irsyam 1993; Martinez and Frost 2017), soil state and particle angularity (e.g., DeJong and Westgate 2009), and particle crushing and surface wear (e.g., Airey and Kelley 2010; Dietz and Lings 2010; Ho et al. 2011).

Friction directionality and bioinspiration. Different geometric solutions have been explored to develop surfaces that exhibit directionally-dependent resistance, such as the addition of ribs, spikes, and depressions (Jewell 1984; Dove and Frost 1996). However, due to the large possible number of geometries that can be considered, a complete parametric investigation is impractical. Martinez et al. (2021a) proposes that examining solutions in natural systems, which have been produced through natural selection, can help discover strategies and reduce parametric spaces. Examples of directionally-dependent surfaces include grass leaves, gecko feet, and shark and snake skin (Kulic et al. 2009; Marvi and Hu 2012; Tramsen et al. 2018).

The ventral scales along the underbody of snakes control the interactions with the substrate, which could be composed of soil, rock surfaces, tree bark, and debris. The ventral scales produce small frictional resistances when a snake moves forward and greater frictional resistances when it retracts. The lower friction direction is referred to as the caudal direction and the higher friction direction is referred to as the cranial direction (Gray and Lissmann 1950). It has been shown that the ratio of static friction coefficients between cranial and caudal directions in preserved snake specimens ranges from 1.2 to 3.5 (Marvi and Hu 2012; Marvi et al. 2013; Gray and Lissmann 1950).

Martinez et al. (2019) and Stutz and Martinez (2021) performed interface shear tests on snakeskin-inspired surfaces with asperities of varying geometry, and showed that shearing in the cranial direction mobilized a greater strength and dilatancy than shearing caudally for sands of different particle size and shape and relative density, and introduced the asperity length to height ratio, *L/H*. O'Hara and Martinez (2020) investigated the effects of boundary conditions, relative density, and cyclic loading, and reported greater capacities in the cranial direction for tests on sands. Huang and Martinez (2021) performed interface shear tests on specimens of normally

consolidated and overconsolidated clay, and concluded that shearing in the cranial direction generated greater drained and undrained interface strengths. Results of centrifuge load tests on uninstrumented piles by O'Hara and Martinez (2020) and Martinez and O'Hara (2021) indicate that the global shaft resistance is greater for cranial shearing during both installation and pullout testing. DEM simulations of snakeskin-inspired piles by Zhong et al. (2021) also show greater capacities in the cranial direction.

The objectives of the present investigation are to characterize the global and local load transfer behavior during installation and pullout loading and to quantify how these behaviors are influenced by the direction of loading in relation to the asperity orientation, asperity geometry, and embedment depth. This is done through a series of 14 monotonic centrifuge load tests in sand using piles instrumented with internal strain gauges. Analysis is presented in terms of distributions of shear forces and stresses with depth, shear stress–displacement relationships, and estimated K and β coefficients. Comparisons of the results with those from piles with reference rough and smooth surfaces are provided throughout the paper.

MATERIALS AND METHODS

Model piles. Five piles were used in this testing series. All the piles were constructed out of 2024 aluminum and have a total length of 420 mm, an outer diameter, B_{pile}, of 19.05 mm, and an average wall thickness of 3.05 mm. For the range of loads achieved in this study, the maximum pile compression was estimated to be 0.3 mm. Due to the small amount of compression, the pile behavior was approximated as rigid. Therefore, the pile head displacements are reported throughout this paper without accounting for the different compressive deformations along the pile shaft Three of the piles had snakeskin-inspired shaft surfaces and two piles had roughened and

polished shaft surfaces, which are referred to as the "rough" and "smooth" piles, respectively. All piles had an untextured portion with a length equivalent to $2B_{pile}$ behind the shoulder base to minimize the effects of the shaft texture on the base capacity. Fig. 3.1 shows the process for generating the bio-inspired piles. The asperities on each pile surface had a length, L, of 12 mm and a height, H, of either 0.30 or 0.72 mm. The specific asperity L and H values were chosen based on data from Martinez et al. (2019) and O'Hara and Martinez (2020), indicating that L/H ratios of 40 and 16.7, combined with the spacing $L = 12$ mm, exhibited pronounced directional differences in strength and dilation when sheared against Ottawa F65 sand. Table 3.1 presents surface roughness measurements from each pile shaft, where intra- and inter-asperity measurements are provided separately. The roughness surface values were calculated from profiles obtained using a Keyance (Osaka, Japan) VR-3100 white light noncontact digital microscope with a 0.1μm resolution. The pile naming convention is such that R refers to the cranial direction, D to the caudal direction, I is installation, P is pullout, and the number is the asperity height in mm. For example, pile RI-DP 0.30 corresponds to the cranially installed–caudally pulled pile with an asperity height of 0.30 mm. The critical state interface friction angle, δ'_{cs}, determined from laboratory testing on planar surfaces with the same texture as the piles and Ottawa F65 sand (Palumbo 2018), was found to be 30.3° and 19.0° for the rough and smooth surfaces in both shearing directions, 27.8° and 32.4° for the bio-inspired surfaces with an H of 0.3 mm in the caudal and cranial directions, respectively, and 32.6° and 36.9° for bio-inspired surfaces with an H of 0.72 mm in the caudal and cranial directions, respectively. Table 3.3 summarizes the interface friction angles.

Each pile was connected to an external load cell to measure the head load and internally instrumented with six S114L strain gauges, comprised of full bending compensated Wheatstone bridges. The strain gauges in the snakeskin-inspired piles were placed centrally between asperities

in order to reduce nonuniform strains from the varying pile wall thickness. Fig. 3.2(a) shows the strain gauge locations. The leading gauge was used to measure the pile base force, and the following gauges measured loads along the shaft. To calculate shear stresses along the pile length, a minimum difference in force between any two gauges was required to be larger than 2.5% of the maximum calibrated load to provide sufficient resolution. If two adjacent gauges did not achieve the limit, the next gauge was used in the calculation. If the terminal embedded strain gauge did not meet the criteria, the head load was used, and the distance between the gauge and ground surface was used to compute the area.

Centrifuge modeling. The pile load tests were conducted at the UC Davis Center for Geotechnical Modeling (CGM) on the 9-m radius centrifuge. Laws of similitude have been developed based on the equality of effective stress between the model and prototype, as summarized in Taylor (1995) and Garnier et al. (2007). Length scales with N ($N = g_{model}/g_{prototype}$), the stress is independent of N, and the force scales with N^2. Throughout this paper, the results are presented in prototype scale unless specified otherwise. All pile tests were conducted in dry deposits at a radial acceleration equivalent to 30 times Earth's average gravitational field ($N = 30$), with select cone penetration tests (CPT) conducted at 40g ($N = 40$). The CPT probe had a model diameter of 10 mm, D_{CPT}. All pile and CPT tests were conducted at a minimum spacing of 10 probe diameters away from boundaries and from adjacent test locations. At 30g, the prototype dimension of the pile diameter and length is 0.57 m and 12.6 m, respectively. A total of fourteen pile load tests and nine CPTs were performed in two soil deposits, referred to as KBO01 and KBO02. The locations of the load tests and CPT soundings are shown in Fig. 3.2(b) and listed in Table 3.2. The pile load test sequence consisted of in-flight installation by direct push to the desired shaft embedment depth

58

(10.5 m or 7.5 m), followed by a 0.76 m displacement pullout test consisting of 0.76 m of displacement (25.4 mm). The soil deposits were constructed with air pluviation to a uniform target relative density (D_R) equal to 65% using Ottawa F65 sand, following procedures established at the UC Davis CGM (Sturm 2019). Ottawa F65 is a poorly graded silica sand that has been characterized by numerous researchers, with typical properties for the batch used in these tests summarized in Carey et al. (2020) and Palumbo (2018). Sand properties include: $D_{50} = 0.20$ mm, coefficient of uniformity, $C_U = 1.71$, coefficient of curvature, $C_C = 1.00$, maximum void ratio, e_{max} = 0.78, minimum void ratio, $e_{min} = 0.51$, and critical state friction angle determined from direct shear tests, $\varphi_{CS,DS} = 29.6°$ (Martinez et al. 2019). The B_{pile} to D_{50} ratio was 95, which falls within typical recommendations to avoid grain size effects associated with centrifuge pile tests (Fioravante 2002; Garnier & König 1998; Bolton et al. 1999).

RESULTS

The results from CPT soundings and pile base resistances are first presented to assess spatial variability in the KBO01 and KBO02 soil deposits, which indicate reasonable uniformity within each deposit and between deposits. The shaft loads measured during the load tests are then presented to highlight the influence of the surface texture on the load transfer behavior during installation and pullout.

CPT soundings and pile installation base resistances. Five CPT soundings were performed at 40g in model KBO01 prior to the pile tests in order to estimate the D_R and expected installation force of the piles. Based on the estimated installation loads, all subsequent CPTs and pile tests in both deposits were conducted at 30g to avoid overloading the hydraulic actuation system. Figs. 3.3(a and c) present profiles of cone tip resistances (q_c) with depth (z) from each sounding, and

Figs. 3.3(b and d) present the corresponding normalized cone tip resistances (q_{cN}) as a function of normalized embedment ratio (z/B), where $q_{cN} = q_c/(q_c \cdot P_a)^{0.5}$, where P_a is the atmospheric pressure. As shown, the q_c profiles from the different portions are similar, with the exception of the profile from the SE portion (top right in Fig. 3.2(b)) of both deposits which have a lower resistance than the rest of the deposit. The normalized parameters q_{cN} and z/D_{CPT} allow comparison between deposits. Recommendations from Kim et al. (2016) were used to determine the critical depth ratio (z_{crit}/D_{CPT}) by estimating the z_{crit} at which q_{cN} values become nominally constant. The critical depth was estimated to be between 20 and 25 D_{CPT} equivalents for both deposits, which is consistent with results presented in Kim et al. (2016) for CPT soundings in soil deposits with similar D_R ranges.

The pile base resistance (q_b) profiles indicate similar trends as the CPT soundings (Figs. 3.4(a–c)). The piles were installed to depths of 10.5 m or 7.5 m by direct push at a model rate of 2 mm/s, leading to embedment ratios z/B of 18.3 and 13.1 (Table 3.2). Similar to the CPT profiles, the base measurements are similar in all sections of both deposits, with the exceptions of those corresponding to the SE portion (smooth pile for both embedment in KBO01 and DI-RP 0.72 pile in KBO02). O'Hara and Martinez (2022a) present a detailed discussion on the deposit variability, and show that the variation in q_b is associated with variability in D_R while the effect of the shaft texture on q_b is insignificant. The average final base resistance from the profiles in Figs. 3.4(a, b, and c) are 22.1, 14.9, and 23.3 MPa, respectively. The q_b profiles did not reach z_{crit} because the penetration depth was limited to z/B_{pile} less than 20.

Both q_c and q_b profiles show similar trends in resistance. To estimate D_R, average q_{cN} values at any given depth below z_{crit} were used in conjunction with the Jamiliokoski (2000) method, and both the q_b and q_c values at a depth of 3 m were used with the correlations provided in Carey et al.

(2020) for Ottawa F65 sand (Figs. 3.5(a and b)). The interpreted D_R profiles show the somewhat smaller magnitudes in the SE section of both deposits as well as the slight decrease in D_R at z/B_{pile} from 8 to 10, which could be due to deposit variability or differences between the predictions by the Jamiliokoski (2000) and Carey et al. (2020) correlations. Based on all q_c and q_b profiles, D_R for KBO01 ranged from 59 – 64% over the entire deposit and D_R for KBO02 ranged from 62 – 68% over the entire deposit, with the lower values concentrated in the SE zone of each deposit.

Using the interpreted D_R, the deposits were jointly assessed to evaluate the shear wave velocity, V_s, profile with depth. Fig. 3.5(d) presents the results, with the theoretical V_s profile calculated from the Hardin and Richart (1963) formulation. The formulation was modified with the lateral earth pressure, K, to account for the bender element orientation, which produced horizontally propagated and horizontally polarized shear waves. It was found that the theoretical profile enveloped the measured profile for values of K between 0.42 and 0.62, with a best fit of K = 0.51.

Installation and pullout axial load distribution. The characteristics of the load distributions with depth are shown to be dependent on the pile surface type. Figs. 3.6(a–e) present axial load distributions obtained at the end of installation and pullout. Fig. 3.6a shows that during the 10.5 m installation, the rough shaft mobilized the greatest head load, followed by the RI-DP 0.30, DI-RP 0.72, and DI-RP 0.30 piles, and the smooth pile mobilized the smallest resistance. The loads at different depths follow this trend, except for the DI-RP 0.30 pile which showed a load similar to that of the rough piles at depths greater than 6 m. These comparisons highlight the effect of the direction-dependence in load transfer, where the RI-DP 0.30 pile mobilized greater shaft forces than the DI-RP 0.72 and DI-RP 0.30 piles.

The trends in shaft loads change during the pullout stage, as shown in Fig. 3.6b. The DI-RP 0.72 pile mobilized the greatest shaft loads and the DI-RP 0.30 and rough piles mobilized similar loads at all depths. This comparison highlights the effect of the asperity height, where the taller asperities of the DI-RP 0.72 pile resulted in greater loads. The RI-DP 0.30 pile mobilized smaller loads than the DI-RP 0.30 pile, highlighting the change in trends compared to those observed during installation. The smallest shaft loads were mobilized by the smooth pile. While the smooth pile was pushed in nominally looser soil than the other piles ($\Delta D_R \sim 5\%$), the results from O'Hara and Martinez (2022a) show that this effect led to a maximum reduction in load of 15%. If this difference is accounted for, it can be concluded that the smooth pile mobilized a similar resistance to the piles installed or pulled in the caudal direction. Similar trends as those described for the installation and pullout stages are observed for the piles installed to a depth of 7.5 m in model KBO01 (Figs. 3.6(c and d)), and for the piles installed to a depth of 10.5 m in model KBO02 (Fig. 3.6(e)).

The axial load distributions with depth were fitted with an exponential rise equation:

$$Q(z) = Q_m - (Q_m - Q_0)e^{-k\frac{h}{B_{pile}}}$$

Eq. 2

where $Q(z)$ is the axial load at any given depth, Q_m is the load at the pile head, Q_0 is the load at the pile base, h is the distance measured from the pile base as shown in Fig. 3.6(a), and k is a fitting parameter that controls the rate of load shedding along the pile length. In the plotted exponential equations, the head and base loads were constrained by the experimentally measured values, while the parameter k was fitted by nonlinear regression.

Effect of shaft texture type on axial load distribution. In general, the load transfer behavior during cranial shearing is analogous to that of the rough pile in terms of magnitude and distribution

62

with depth while the load transfer behavior during caudal shearing is analogous to that of the smooth pile. The fitting parameter k is compared in Fig. 3.7(a and b) to evaluate the difference in load shedding behavior between pile types. The load transfer takes place gradually with depth when k is small, whereas large k values lead to sharper increases in load at depths closer to the pile base. Fig. 3.7(a) provides a comparison of the k parameter for the distributions at end of installation for piles embedded to 10.5 m and 7.5 m, and Fig. 3.7(b) provides a similar comparison at end of pullout. k is plotted as a function of the L/H ratio, which Martinez et al. (2019) and Stutz and Martinez (2021) showed to unify the trend in peak and residual interface friction and dilation angles and to capture the differences in the cranial and caudal directions. The rough pile is assigned an L/H of 1 and the smooth pile is assigned an L/H of 50 for visualization purposes. The parameter k is also plotted as a function of R_a, where the inter-asperity R_a is used when shearing in the cranial direction and the intra-asperity R_a is used when shearing in the caudal direction, to capture the direction-dependent load transfer behavior. Considering an R_a parameter that depends on the direction of loading enables showing results on a continuous scale, where each measurement indicates a specific interface behavior (i.e., caudal versus cranial shearing).

The results indicate that there is a sensitivity of the parameter k, which is a nominal measure of load transfer distribution, to both surface type and installation depth. The effect of the surface type is illustrated in Figs. 3.7(a and b) for the installation and pullout phases, respectively. There is a tendency for k to increase with increasing L/H or decrease with increasing R_a at the end of installation, and k is larger for the piles with shallower embedment for the rough, smooth, and DI-RP 0.30 piles. This effect is more pronounced in the pullout distributions, where the piles at 7.5 m have larger k values. However, it is noted that tests on piles with intermediate surface roughness magnitudes are required to better quantify the relationship between k and R_a. The effect of pile

embedment is also apparent when k is plotted as a function of the maximum head load, where k decreases more rapidly with Q_m for the piles embedded at 7.5 m and more gradually for the piles embedded at 10.5 m for both installation and pullout. The trends in the k parameter for the piles installed in model KBO02 are consistent with those presented in Fig. 3.7(a), which are not shown here for brevity.

DISCUSSION

Global and local shaft resistances during installation and pullout. The shaft resistance during installation and pullout exhibited directionally-dependent global and local behaviors, where shearing in the cranial direction mobilized greater skin friction than shearing in the caudal direction. Figs. 3.8(a–e) show global shaft load measurements at the end of installation and pullout loading from tests at an embedment depth of 10.5 m, where the embedment depth is measured from the ground surface to the pile tip. Consistent trends were obtained for the tests in KBO01 installed to 7.5 m and the tests in KBO02, which are not presented here for brevity. The global shaft load is determined as the difference between the head load and the load from the last strain gauge installed in the pile's textured portion (i.e., 80.0 mm from the pile tip, shown in Fig. 3.2(a)).

For the rough and smooth piles, the global shaft load was greater during installation compared to pullout (Figs. 3.8(a and e)), likely due to the decrease in effective stresses around the pile due to the rotation of principal effective stresses and associated soil contraction. As expected, the loads mobilized by the rough pile are considerably greater than those mobilized by the smooth pile. The RI-DP 0.30 pile exhibits a similar behavior, with significantly greater shaft loads during installation than pullout (Fig. 3.8(b)). Conversely, the DI-RP 0.30 and DI-RP 0.72 piles exhibited a greater shaft load during pullout compared to installation over the same displacement (Figs. 3.8(c and d)). In addition, these two piles exhibited a strain hardening response during pullout loading,

whereas the load during pullout for the other piles increased and then reach a constant value at smaller displacements. The ratio of loads at the end of pullout to end of installation for the rough, RI-DP 0.30, DI-RP 0.30, DI-RP 0.72, and smooth piles are 0.30, 0.20, 1.57, 1.70, and 0.41, respectively.

Similar trends in local resistance are observed with depth. Figs. 3.9(a–e) show the calculated local shear stress plotted at the midpoint of the pile section between two strain gauges during the installation and pullout phases. These results highlight the direction-dependence of the shear resistances, where greater shaft resistances are generated during pullout than during installation for the 0.30 DI-RP and 0.72 DI-RP piles (Figs. 3.9(c-d)). Ratios of shear stress at the end of pullout to end of installation ($\tau_{s,pullout}/\tau_{s,install.}$) are included in the figures, indicating values mostly greater than one for the DI-RP 0.30 and DI-RP 0.72 piles and smaller than one for the rough, RI-DP 0.30, and smooth piles.

Figs. 3.10(a–e) presents the local shear stress – head displacement measurements during the pullout tests of the piles at deep and shallow embedment in model KBO01. In general, the magnitude of shear resistances and initial stiffness is greater at larger depths for all piles. In agreement with Figs. 3.6, 3.8, and 3.9, the DI-RP 0.72 and rough piles mobilize the greater stresses, followed by the DI-RP 0.30, RI-DP 0.30, and smooth piles. The cranially-pulled and rough piles continue to mobilize shear resistances over greater head displacements (Figs. 3.10(a, c, and d)), whereas the rough and RI-DP 0.30 piles reach a nominally constant shear resistance early in the test. The shear stresses continue to increase over model head displacements of 6.7 to 13.3 mm (prototype displacement of 0.2 to 0.4 m) for the rough, DI-RP 0.72, and DI-RP 0.30 piles, while the shear stresses become close to constant at head displacements of 1.7 to 6.7 mm (prototype displacement of 0.05 to 0.2 m) for the RI-DP 0.30 pile. The shear resistance of the smooth pile

reaches a peak at 0.05 m (model displacement of 1.7 mm) followed by decrease then a subsequent hardening response, indicating initial sliding at the interface followed by strain hardening due to soil dilation.

The model pile displacements are in better agreement with the expected displacements to mobilize the peak interface shear strength, which are typically on the order of 1 to 10 mm (e.g., Uesugi and Kishida 1986; Jardine et al. 1992; Dietz and Lings 2006). While an exact formulation for the scaling of interface displacement required to mobilize the peak resistance in centrifuge pile tests has not been established, it has been found that interface dilation and shear band formation around model piles does not scale with the g level, as summarized in Garnier (2007). Similarly, shear strain does not scale with the g level. A simplified approach can be considered to explain the mobilization of shaft shear stress in a model pile, where the fully developed shear band is considered as the shear element and the shear strain of the element is the ratio of the shear displacement to shear band thickness. If the shear band thickness is assumed to be a function of model scale D_{50} (Stone and Wood 1992), then the displacement required to mobilize the maximum shear resistance must also be expressed in model scale to preserve the dimensionality in the shear strain (i.e., $\gamma = d_I/t_s$, where d_I is the interface displacement and t_s is the shear zone thickness). It is noted that scaling effects due to the relative size of the pile diameter to the shear band developed around the pile may also contribute to differences in peak shear stress (i.e., Lehane et al. 2003), and are addressed in the last section of this discussion.

Shear resistance distributions. The ultimate shear resistances mobilized at different depths along the pile shaft were used to compute distributions of β at the end of installation and pullout. Each set of data was analyzed assuming that β is a function of the vertical effective stress, similar to forms proposed by O'Neill and Reese (1999):

$$\frac{\tau}{\sigma'_v} = \beta = \beta_{max} - s(\sigma'_v)^m \qquad\qquad \text{Eq. 3}$$

where s and m are empirical fitting parameters. O'Neill and Reese (1999) suggest using an $m = 0.5$. In this study, an $m = 0.55$ was found to be the best-fit exponent based on a minimization of the mean square error and was used for all analyses. The β_{max} and s parameters were fit with linear regression independently for each data set. Figs. 3.11(a and b) show the shear stresses at the end of installation and pullout, while Figs. 3.12(a–e) present the corresponding $\beta_{install.}$ and $\beta_{pullout}$ values. Both figures present the results for the pile load tests in model KBO01, where the τ_s and β values are separated by installation depth by the symbol size. As shown, the embedment depth does not appear to affect the distribution of τ_s with depth. Therefore, the presented trendlines were determined based on the combined data for 10.5 and 7.5 m embedment depths.

At the end of installation, all piles exhibit the expected trend of increasing shear stress with depth (Fig. 3.11(a)). The local $\beta_{install.}$ coefficients for the rough and smooth piles decrease with depth (Fig. 3.12(a and e)), in agreement with published load test data (e.g., Fioravante et al. 1999). The $\beta_{install.}$ values increase with depth for the RI-DP 0.30 pile, while $\beta_{install.}$ has the least change with depth for the DI-RP 0.30 and DI-RP 0.72 piles (Figs. 3.12(c–d)), as evidenced by the low s values associated with the fitted equation. The rough pile has the largest $\beta_{install.}$ coefficients with values between 1.6 and 5.4, with the largest value at depths above 2 m. The $\beta_{install.}$ coefficients for the smooth pile have the smallest magnitudes, with values between 0.1 and 0.5, while the RI-DP 0.30 pile has $\beta_{install.}$ values between 1.1 and 2.8, and the DI-RP 0.30 and DI-RP 0.72 piles have values between 0.2 and 1.0 and 0.2 and 1.2, respectively.

At the end of the pullout phase, a similar trend of increasing shear stress with depth is apparent (Fig. 3.11(b)). The local $\beta_{pullout}$ values tend to increase with depth for all the piles, except for the DI-RP 0.30 pile which shows near-constant values with depth (Figs. 3.12(a–e)). The $\beta_{pullout}$

values are generally greatest for the DI-RP 0.72 and DI-RP 0.30 piles, with values between 0.9 and 1.6, followed by those for the rough pile, with values between 0.3 and 1.3. The $\beta_{pullout}$ values for the RI-DP 0.30 and smooth piles are similar, between 0.2 and 0.5. Figs. 3.12(a–e) also highlights the change in distribution of β with depth, where the trend for the rough and smooth piles changes from decreasing with depth at the end of installation to increasing with depth at the end of pullout. Comparison of the β values for installation and pullout for the snakeskin-inspired piles highlights the direction-dependence of the local stress. Namely, the β values are greater during installation for the RI-DP 0.30 pile, in a similar manner as the rough and smooth piles, while the β values are greater during pullout for the DI-RP 0.30 and DI-RP 0.72 piles.

Effect of pile surface type on β coefficients during installation and pullout. The changes in behavior for each pile between installation and pullout are further assessed by calculating the ratio of β_{avg} during pullout to β_{avg} during installation, $\beta_{pullout}/\beta_{install}$ (Table 3.3). The rough, RI-DP 0.30, DI-RP 0.72, DI-RP 0.30, and smooth piles have $\beta_{pullout}/\beta_{install}$ values of 0.36, 0.18, 2.07, 1.52, and 0.61. These values highlight the greater pullout skin friction mobilized by the DI-RP 0.72 and DI-RP 0.30 piles and the greater installation skin friction mobilized by the rough, RI-DP 0.30, and smooth piles. The ratios of tension to compression skin resistance for the rough and smooth piles are in general agreement with centrifuge results presented in De Nicola and Randolph (1993) and Blanc et al. (2015) who reported values from 0.50 to 0.72 for close-ended piles. These values further show that the ratios for the DI-RP and RI-DP piles fall outside the values typically measured for piles with rough or smooth surfaces.

Two additional ratios are considered to further evaluate possible installation and loading history effects due to the direction of the asperities during pile installation:

$$B_{DI-RP} = \left(\frac{\beta_{avg,cranial\ pullout}}{\beta_{avg,caudal\ install.}} \right) \qquad \text{Eq. 4}$$

$$B_{RI-DP} = \left(\frac{\beta_{avg,cranial\ install.}}{\beta_{avg,caudal\ pullout}} \right) \qquad \text{Eq. 5}$$

These parameters are defined for different pile types (i.e., Eq. 4 for DI-RP piles and Eq. 5 for RI-DP piles) such that values greater than one indicates greater shear resistance in the cranial direction. Therefore, differences between B_{DI-RP} and B_{RI-DP} values would suggest a dependency on the asperity orientation in the confining stress around the piles at the end of installation, changes in confining stress after pullout due to stress reversal, and directionally-dependent interface friction angles. The B_{DI-RP} ratios for the DI-RP 0.72 and DI-RP 0.30 piles are 1.6 and 2.1, respectively, while B_{RI-DP} for the RI-DP 0.30 pile is 5.5. Because the differences in interface friction angles between cranial and caudal shearing are between 4.3° and 7.5° (Table 3.3), they cannot solely account for this difference in response. Therefore, the significantly greater B_{RI-DP} ratio suggests a decrease in radial effective stresses around the pile due to the load reversal induced during caudal pullout loading. The results further suggest that piles installed in the caudal direction and subsequently loaded cranially can counteract the reduction in capacity typically observed for tensile loading of piles.

The effect of loss of confining stress from installation to pullout can be further explored by considering constant normal stiffness (CNS) interface shear tests, where the changes in normal effective stress around the soil–structure interface are coupled to soil contraction or dilation (Boulon and Foray 1986; Tabucanon et al. 1995). Figs. 3.13(a–d) show the results of single-cycle shear box interface tests between Ottawa F65 sand and planar surfaces with asperities with the same geometry as the pile shafts investigated herein ($L = 12$ mm, $H = 0.30$ and 0.72 mm, $L/H = 40$ and 16.7, $D_R = 85\%$, boundary stiffness $k = 150$ kPa/mm, and initial effective stress $\sigma'_n = 80$ kPa; O'Hara and Martinez (2020) provides a detailed description of the testing setup). The single-cycle test is an idealized analog to the end of installation and beginning of pullout in the pile tests.

The rough surface and the snakeskin-inspired surfaces mobilize greater shear stresses when they are displaced in the cranial direction (Figs. 3.13(a and b)). The loss of confinement ($\Delta\sigma'_n$) is considered by taking the difference between σ'_n at the end of shearing in the first direction and after 2 mm of displacement in the reverse direction (Figs. 3.13(c and d)). Fig. 3.13(e) shows $\Delta\sigma'_n$ as a function of L/H. As shown, the rough surface exhibits the largest $\Delta\sigma'_n$, followed by the RI-DP 0.30 and DI-RP 0.72 and surfaces, and the smooth and DI-RP 0.30 surfaces yield similar $\Delta\sigma'_n$ (note that the datapoint for the smooth surface is placed at an L/H of 50 for reference). Fig. 3.13(f) shows the ratio of shear stresses at the end of each cycle as a function of $\Delta\sigma'_n$, where the results are grouped by proposed mechanisms. The reference surfaces in Group 1 (rough and smooth) have ratios between 0.8 and 1.0, which result from slight soil contraction at the direction reversal, followed by minimal dilation-induced increases in shear stress. The RI-DP 0.30 surface in Group 2 has a ratio of 0.6, which results from dilation-induced increases in effective stresses in the first, cranial direction, followed by contraction at the beginning of the second, caudal direction. The DI-RP 0.30 and DI-RP 0.72 surfaces in Group 3 have ratios of 2.0 and 1.7, which are produced by the minimal dilation in the first, caudal direction, and the strong dilation induced in the second, cranial direction that causes a concomitant increase in effective stresses. The trends observed in the laboratory tests are in general agreement with the differences in β coefficients for the rough and RI-DP 0.30 piles, resulting in greater $\beta_{install.}$ than $\beta_{pullout}$. It is noted that while D_R for the laboratory tests is higher than the pile load tests, the reported trends are also expected to be valid for sand at a D_R of 60% to 70%.

Scaling effects. Various researchers have noted that scaling effects may prevent direct comparison between tests on small model piles and field-scale tests due to the size of the shear band t_s, compared to B_{pile}. Loukidis and Salgado (2008) present a numerical investigation relating the

70

effects of t_s/B_{pile} on the earth pressure coefficient (K) around piles. Scale effects were found to be negligible for t_s/B_{pile} ratios smaller than 0.01, whereas K could increase by a factor of 2 from t_s/B_{pile} = 0.01 to 0.1. Tovar-Valencia et al. (2018) applied this t_s/B_{pile} correction to model displacement piles tested in a calibration chamber and found satisfactory agreement with measurements from full-scale tests.

To account for the scaling effects, the installation β_{avg} from the distributions presented in Figs. 3.8(a–e) were used in conjunction with the interface friction angles corresponding to each surface (Table 3.4) to back calculate an initial average lateral earth pressure, K_{avg} ($K_{avg} = \beta_{avg}/tan(\delta'))$. To apply the Loukidis and Salgado (2008) correction, the thickness of the shear band for each surface type was obtained from Particle Image Velocimetry measurements from Palumbo (2018) and Martinez et al. (2019), who performed tests on planar surfaces with the same asperity geometry as those of piles tested in this study. The t_s values agree well with published relationships indicating $t_s \approx 10D_{50}$ for rough surfaces and $t_s \approx 0$ for smooth surfaces where sliding occurs between the soil and surface. Then, the K_{avg} values were corrected using a field-scale t_s/B_{pile} value of 0.001. Based on the corrected values ($K_{corr.}$), corrected β_{avg} values ($\beta_{avg\ corr.}$) were calculated using the corresponding interface friction angles, as shown in Table 3.4 for installation.

This analysis yields installation $K_{avg.}$ values for the rough and RI-DP 0.30 piles that are greater than the Rankine passive lateral earth pressure coefficient (K_p) of 3.0, which suggests an effect of circumferential stresses around the piles on the centrifuge results, as previously discussed for tests on small piles (Lehane et al. 2005). However, the K_{corr} values are all smaller than 3.0. The $\beta_{avg\ corr.}$ values for the rough pile are reduced by a factor of 2.10. Similarly, $\beta_{avg\ corr.}$ values for RI-DP 0.30 reduce by a factor of 1.97, and reduce by a factor of 1.28 for DI-RP 0.72. The β_{avg} values for the smooth and DI-RP 0.30 piles do not change due to their negligible shear band thickness.

As shown, the corrected β_{avg} values in Table 3.4 are in general agreement with recommended β values for displacement piles in medium dense sand (i.e., CFEM 1992). It is noted that it was not possible to apply this correction to the pullout β_{avg} values due to the lack of shear band thickness developed during a reverse load cycle.

CONCLUSIONS

A series of centrifuge pile load tests were conducted on three snakeskin-inspired piles, a rough pile, and a smooth pile in two medium-dense sand deposits. The load tests were performed on internally-instrumented piles, and the test sequence consisted of in-flight installation to prototype embedment depths of 10.5 or 7.5 m followed by pullout tests. CPT tip resistances and pile base resistances were used to assess the deposit variability, and it was found that both deposits had comparable relative densities.

The load transfer behavior was evaluated in terms of distributions of axial load along the pile length. The axial loads were greatest for piles displaced in the cranial direction and the rough pile during both installation ($Q_m = 8.43 - 9.58$MN) and pullout ($Q_m = 0.95 - 1.23$MN), while the axial loads were smallest for the piles displaced in the caudal direction and the smooth pile during both installation ($Q_m = 5.37 - 6.47$MN) and pullout ($Q_m = 0.49 - 0.67$). Because a given bio-inspired pile is installed and pulled in different directions (i.e., cranial installation and caudal pullout or vice versa), these results highlight the dependence of the load transfer of a single pile on the direction of loading relative to the asperity orientation. The axial load was found to decrease gradually over the pile length for the cranially-displaced and rough piles, indicating significant load shedding. The shedding of load in the caudally-displaced and smooth piles was significantly smaller, resulting in sudden changes in axial load near the pile base.

72

For each pile, the shaft resistances increased with increasing embedment. The differences in shaft resistances between installation and pullout were quantified through β coefficients. The cranially-displaced and rough piles mobilized the largest average and local β values during both installation and pullout than the caudally-displaced and smooth piles. For example, the RI-DP 0.3 pile mobilized $\beta_{install.}$ of 2.13 and $\beta_{pullout}$ of 0.39, while the DI-RP 0.30 pile mobilized $\beta_{install.}$ of 0.53 and $\beta_{pullout}$ of 1.11. Comparison of the $\beta_{install.}$ and $\beta_{pullout}$ values highlights the effects of stress reversal on the decrease in normal stresses around the piles, which appear to be largest for the rough pile followed by the DI-RP piles (i.e., caudally-installed, cranially-pulled), based on results from CNS interface shear tests. The ratio of average $\beta_{pullout}$ to $\beta_{install.}$ coefficients for the DI-RP 0.30 and DI-RP 0.72 piles was calculated between 1.52 and 2.07, indicating significantly greater pullout capacities despite the aforementioned decrease in radial stresses. Scaling effects due to a large shear band to pile diameter ratio were accounted for semi-empirically to estimate β_{avg} values more representative of field conditions. The corrected values are in general agreement with those expected from field pile load tests, indicating promise for further work on field-scale experiments. In parallel with field scale validation, efforts should be made to evaluate economical methods of manufacturing piles with bioinspired pile shafts that can be used at a production scale using custom machining tooling for steel piles, textured framework for pre-cast concrete piles, or extrusion and molding processes for polymer-based piles, as discussed by O'Hara and Martinez (2022a).

Data Availability Statement

Some or all data, models, or code generated or used during the study are available in a repository or online in accordance with funder data retention policies at DesignSafe-CI under PRJ-3320 at https://doi.org/10.17603/ds2-3148-wp47.

ACKNOWLEDGEMENTS

REFERENCES

Beringen, F. L., D. Wind, and W. R. Van Hooydonk. 1979. "Results of loading tests on driven piles in sand." *Recent developments in the design and construction of piles*. 213–225. London, UK: Institution of Civil Engineers

Blanc, M., Thorel, L., Isorna, R., Dano, C., Kotronis, P., and M. Philippe. "Centrifuge investigation of the axial cyclic behaviour of a single pile used for the foundation of a jacket type offshore wind turbine." *Frontiers in offshore geotechnics*, *ISFOG*, Jun 2015, Oslo, Norway. 521-526.

Bolton, M. D., M. W. Gui, J. Garnier, J. F. Corte, G. Bagge, J. Laue, and R. Renzi. 1999. "Centrifuge cone penetration tests in sand." *Géotechnique* 49 (4): 543–552.

Boulon, M., and P. Foray. 1986. "Physical and numerical simulation of lateral shaft friction along offshore piles in sand." *Proc., 3rd Int. Conf. on Num. Methods in Offshore Piling*, Editions Techrig, Paris, France, 127–148.

Canadian Geotechnical Society, Foundations Committee. 1992. *Canadian foundation engineering manual*. Canadian Geotechnical Society.

Carey, T. J., A. Gavras, and B. L. Kutter. 2020. "Comparison of LEAP-UCD-2017 CPT Results." *Model Tests and Numerical Simulations of Liquefaction and Lateral Spreading.* 117–129. Springer, Cham.

Carey, T. J., N. Stone, and B. L. Kutter. 2020. "Grain size analysis and maximum and minimum dry density testing of Ottawa F-65 sand for LEAP-UCD-2017." *Model tests and numerical simulations of liquefaction and lateral spreading*. 31–44. Springer, Cham.

CUR. 2001. "Bearing capacity of steel pipe piles." *Report 2001-8.* Gouda, The Netherlands: Centre for Civil Engineering Research and Codes.

DeJong, J. T. 2001. *Investigation of particulate-continuum interface mechanisms and their assessment through a multi-friction sleeve penetrometer attachment*. Georgia Institute of Technology.

DeJong, J. T., and Z. J. Westgate. 2009. "Role of initial state, material properties, and confinement condition on local and global soil-structure interface behavior." *J. Geotech. Geoenviron. Eng.* 135 (11): 1646–1660.

De Nicola, A., and Randolph, M. F. 1993. "Tensile and compressive shaft capacity of piles in sands." *J. Geotech. Geoenviron. Eng.* 119 (12): 1952–1973.

Dietz, M., and M. Lings. 2010. "Changes in surface roughness in multi-reverse sand-steel interface tests." *Proc., Research Symp. on Characterization and Behavior of Interfaces*., 7–15.

Dietz, M., and M. Lings. 2006. "Postpeak strength of interfaces in a stress dilatancy framework." *J. Geotech. Geoenviron. Eng.* 132 (11): 1474–1484.

Dove, J. E., and J. D. Frost. 1996. "A method for measuring geomembrane surface roughness." *Geosynthetics International* 3 (3): 369–392.

Everton, S. J. 1991. *Experimental study of frictional shearing resistance between non-cohesive soils and construction materials.* MSc. Dissertation.

Fellenius, B. H. 2008. "Effective stress analysis and set-up for shaft capacity of piles in clay." *From research to practice in geotechnical engineering,* 384–406.

Fioravante, V. 2002. "On the shaft friction modelling of non-displacement piles in sand." *Soils Found*. 42 (2): 23–33.

Fioravante, V., V. N. Ghionna, M. Jamiolkowski, and H. Sarri. 1999. Shaft friction modeling of non-displacement piles in sand. *Proc. Analysis, design, construction, and testing of deep foundations.*

Fleming, K., A. Weltman, M. Randolph, and K. Elson. 2008. *Piling engineering*. CRC press.

Garnier, J., and D. Konig. 1998. "Scale effects in piles and nail loading tests in sand." *Proc. Int. Conf. Centrifuge 98*, Tokyo, Balkema, Rotterdam, 1: 205–210.

Garnier, J., C. Gaudin, S. M. Springman, P. J. Culligan, D. Goodings, D. Konig, B. Kutter, R. Phillips, M. F. Randolph, and L. Thorel. 2007. "Catalogue of scaling laws and similitude questions in geotechnical centrifuge modelling." *Int. J. Phys. Model. Geotech. 7* (3): 01–23.

Gray, J., and H. W. Lissmann. 1950. "The kinetics of locomotion of the grass-snake." *J. Exp. Biol.* 26: 354–367.

Hardin, B.O., and E. Richart, 1963. "Elastic wave velocities in granular soils." *J. Soil Mech. Found. Div*. 89 (1): 33–65.

Ho, T. Y. K., R. J. Jardine, and N. Anh-Minh. 2011. "Large-displacement interface shear between steel and granular media." *Géotechnique* 61 (3): 221–234.

Huang, L. and A. Martinez 2021. "Load transfer anisotropy at snakeskin-inspired clay-structure interfaces." Int. Found. Conf. Equip. Expo, Dallas, TX.

Hryciw, R. D., and M. Irsyam. 1993. "Behavior of sand particles around rigid ribbed inclusions during shear." *Soils Found.* 33 (3): 1–13.

Jardine, R. J., S. J. Everton, and B. M. Lehane. 1992. Friction Coefficients For Piles In Cohesionless Materials, Dordrecht, *SUT Int. Conf,* Kluwer, 661–680.

Jardine, R. J., F. C. Chow, R. Overy, and J. Standing. 2005. "ICP design methods for driven piles in sands and clays." Thomas Telford, London.

Jewell, R. A., G. W. E. Milligan, and D. Dubois. 1984. "Interaction between soil and geogrids." *Polymer grid reinforcement*. Thomas Telford Publishing, 18–30.

Kim, J.H., Y. W. Choo, D.J. Kim, and D. Kim. 2016. "Miniature cone tip resistance on sand in a centrifuge." *J. Geotech. Geoenviron. Eng.* 142 (3).

Kulic, I. M., M. Mani, H. Mohrbach, R. Thaokar, and L. Mahadevan. 2009. "Botanical ratchets." *Proc. R. Soc. B.* 27 (6): 2243–2247.

Lauder, G. V. 1996. *The argument from design*, 55–91. Adaptation.

Lehane, B. M., R. J. Jardine, A. J. Bond, and R. Frank. 1993. "Mechanisms of shaft friction in sand from instrumented pile tests." *J. Geotech. Eng.* 119 (1): 19–35.

Lehane, B. M., J. A. Schneider, and X. Xu. 2005. "The UWA-05 method for prediction of axial capacity of driven piles in sand." *Frontiers in offshore geotechnics*, *ISFOG,* 683–689.

Loukidis, D., and R. Salgado. 2008. "Analysis of the shaft resistance of non-displacement piles in sand." *Géotechnique 58* (4): 283–296.

Martinez, A., and J. D. Frost. 2017. "The influence of surface roughness form on the strength of sand–structure interfaces." *Géotechnique Lett.* 7 (1): 104–111.

Martinez, A., and K. B. O'Hara. 2021. "Skin friction directionality in monotonically- and cyclically-loaded bio-inspired piles in sand." *Deep Found. Inst. J.* 15 (1).

Martinez, A., J. DeJong, I. Akin, A. Aleali, C. Arson, J. Atkinson, P. Bandini, T. Baser, R. Borela, R. Boulanger, M. Burrall, Y. Chen, C. Collins, D. Cortes, S. Dai, T. DeJong, E. Del Dottore, K. Dorgan, R. Fragaszy, D. Frost, R. Full, M. Ghayoomi, D. Goldman, N. Gravish, I. L. Guzman, J. Hambleton, E. Hawkes, M. Helms, D. L. Hu, L. Huang, S. Huang, C. Hunt, D. Irschick, H. Lin, B. Lingwall, W. A. Marr, B. Mazzolai, B. McInroe, T. Murthy, K. O'Hara, M. Porter, S. Sadek, M. Sanchez, C. Santamarina, L. Shao, J. Sharp, H. Stuart, H. H. Stutz, A. P. Summers, J. Tao, M. Tolley, L. Treers, K. Turnbull, R. Valdes, L. van Paassen, G. Viggiani, D. Wilson, W. Wu, X. Yu, and J. Zheng. 2021a. "Bio-inspired geotechnical engineering: principles, current work, opportunities and challenges." Published online in *Géotechnique*.

Martinez, A., D. Nguyen, D. J. Irschick, M. S. Basson, and S. Baeckens. 2021b. "Quantifying surface topography of biological systems from 3D scans." *Methods Ecol. Evol*. 12: 1265–1276. doi: https://doi.org/10.1111/2041-210X.13603

Martinez, A., S. Palumbo, and B. D. Todd. 2019. "Bio-Inspiration for anisotropic load transfer at soil-structure interfaces." *J. Geotech. Geoenviron. Eng.* 145 (10).

Marvi, H., and D. L. Hu. 2012. "Friction enhancement in concertina locomotion of snakes." *J. Roy. Soc. Int.* 9 (76): 3067–3080.

Marvi, H., J. Bridges, and D. L. Hu. 2013. "Snakes mimic earthworms: propulsion using rectilinear travelling waves." *J. Roy. Soc. Int.* 10 (84).

O'Hara, K. B., and A. Martinez. 2020. "Monotonic and cyclic frictional resistance directionality in snakeskin-inspired surfaces and piles." *J. Geotech. Geoenviron. Eng.* 146 (11).

O'Hara, K.B., and Martinez, A. (2022a). "Shaft and base capacity of snakeskin-inspired piles from centrifuge pile load tests." In press for *GeoCongress* 2022.

O'Hara, K. and Martinez, A. (2022b) "Centrifuge monotonic pullout and displacement controller cyclic tests on bioinspired and reference piles.", in Multiscale investigation of load transfer directionality of bioinspired surfaces under monotonic and cyclic loading. *DesignSafe-CI.* https://doi.org/10.17603/ds2-3148-wp47.

O'Neill, M. W., and C. R. Lymon. 1999. "Drilled shafts: Construction procedures and design procedures and design methods." ADSC.

Palumbo, S. 2018. *Anisotropic interface shear behavior of granular soil and surfaces biologically-inspired by snakeskin*. MSc. Dissertation. University of California, Davis.

Stone, K. J. L., and D. Muir Wood. 1992. "Effects at dilatancy and particle size observed in model tests on sand." *Soils Found.* 32 (4): 43–47.

Sturm, A. P. 2019. *On the liquefaction potential of gravelly soils: Characterization, triggering and performance*. Diss. University of California, Davis.

Stutz, H. H., and A. Martinez. 2021. "Directionally-dependent strength and dilatancy behavior of soil-structure interfaces." Published online in *Acta Geotechnica*.

Tabucanon, J. T., D. W. Airey, and H. G. Poulos. 1995. "Pile skin friction in sands from constant normal stiffness tests." *J. Geotech. Test.* 18 (3): 350–364.

Tehrani, F. S., F. Han, R. Salgado, M. Prezzi, R. D. Tovar, and A. G. Castro. 2016. "Effect of surface roughness on the shaft resistance of non-displacement piles embedded in sand." *Géotechnique* 66 (5): 386–400.

Tovar-Valencia, R. D., A. Galvis-Castro, R. Salgado, and M. Prezzi. 2018. "Effect of surface roughness on the shaft resistance of displacement model piles in sand." *J. Geotech. Geoenviron. Eng.* 144 (3). 04017120.

Tramsen, H. T., S. N. Gorb, H. Zhang, P. Manoonpong, Z. Dai, and L. Heepe. 2018. "Inversion of friction anisotropy in a bio-inspired asymmetrically structured surface." *J. R. Soc.* 15 (138).

Uesugi, M., and H. Kishida. 1986. "Influential factors of friction between steel and dry sands." *Soils Found.* 26 (2): 33–46.

Zhong, W., Liu, H., Wang, Qi., Zhang, W., Li, Y., Ding, X., and Chen, L. 2021. "Investigation of the penetration characteristics of snake skin-inspired pile using DEM. *Acta Geotech*, 16: 1849-1865.

Table 3.1. Roughness parameters for pile shaft sections.

Roughness parameters		Rough pile	RI-DP 0.30	DI-RP 0.30	DI-RP 0.72	Smooth pile
Intra-asperity	R_a (μm)	40.06	0.53	0.58	0.51	0.45
	R_z (μm)	338.51	3.03	3.27	2.79	2.60
Inter-asperity	R_a (μm)	-	84.64	88.26	193.91	-
	R_z (μm)	-	306.37	318.20	720.45	-
	L/H	~1	40	40	16.7	>100

Table 3.2. Test parameters for CPT soundings and pile load tests.

Model	Test location	Test designation	Model diameter, B (mm)	Push depth, z/B
KBO01	CPT1	SE Push	10	40
KBO01	CPT2	Central Push	10	40
KBO01	CPT3	SW Push	10	40
KBO01	CPT4	NW Push	10	40
KBO01	CPT5	NE Push	10	40
KBO01	P1	Smooth	19.05	18.3
KBO01	P2	Smooth	19.05	13.1
KBO01	P3	Rough	19.05	13.1
KBO01	P4	Rough	19.05	18.3
KBO01	P5	DI-RP 0.72	19.05	18.3
KBO01	P6	DI-RP 0.72	19.05	13.1
KBO01	P7	RI-DP 0.30	19.05	13.1
KBO01	P8	DI-RP 0.30	19.05	13.1
KBO01	P9	RI-DP 0.30	19.05	18.3
KBO01	P10	DI-RP 0.30	19.05	18.3
KBO02	CPT1	SE Push	10	40
KBO02	CPT3	SW Push	10	40
KBO02	CPT4	NW Push	10	40
KBO02	CPT5	NE Push	10	40
KBO02	P3	Rough	19.05	18.3
KBO02	P2	DI-RP 0.72	19.05	18.3
KBO02	P5	DI-RP 0.30	19.05	18.3
KBO02	P11	RI-DP 0.30	19.05	18.3

Table 3.3. Global β values during installation and pullout for 10.5 m embedment tests.

Shaft type	$\beta_{install.}$	$\beta_{pullout}$	$\beta_{pullout}$ / $\beta_{install.}$
Rough pile	2.79	1.00	0.36
RI-DP 0.30	2.13	0.39	0.18
DI-RP 0.30	0.53	1.11	2.07
DI-RP 0.72	0.87	1.32	1.52
Smooth pile	0.34	0.21	0.61

Table 3.4. Measured and corrected β_{avg} values during installation for 10.5 m embedment tests.

Shaft type	β_{avg}	δ'_{cs}*	t_s (mm)[1]	t_s/B	K_{avg}	$K/(K_{t_s/B=0.001})$[2]	$K_{corr.}$	$\beta_{avg\ corr.}$
Rough pile	2.79	30.3	2.0	0.10	4.77	2.08	2.30	1.34
RI-DP 0.30	2.13	32.4	1.8	0.09	3.36	1.97	1.71	1.08
DI-RP 0.30	0.53	27.8	0.0	0.00	1.01	--	--	0.53
DI-RP 0.72	0.87	32.6	0.5	0.03	1.36	1.28	1.06	0.68
Smooth pile	0.34	19.0	0.0	0.00	0.87	--	--	0.34

[1]Data from Palumbo (2018) and Martinez et al. (2019), [2]Adapted from Loukidis and Salgado 2008

(a) Preserved snake specimens

(b) 3D Scans of ventral scales

(c) 0.72mm Caudal Install. · 0.30mm Cranial Install. · 0.30mm Caudal Install. · Rough · Smooth

Bio-inspired and reference piles (to scale)
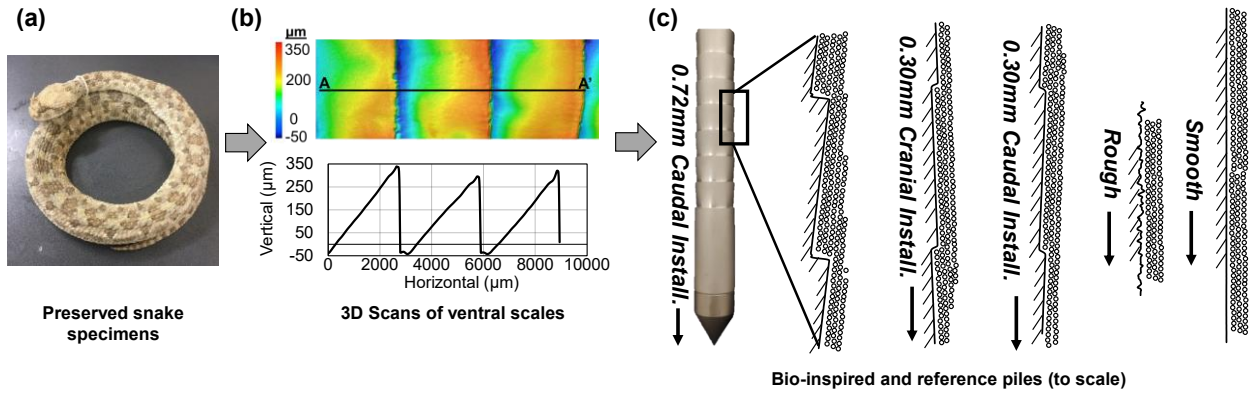
Figure 3.1. Bio-inspired translation from (a) preserved snake specimens to (b) idealized geometries from snake ventral scale scans to (c) piles with shaft textures based on ventral scale geometry.

(a)

298.2 mm
226.1 mm
154.2 mm
142.2 mm
80.0 mm
51.3 mm

B_{pile} = 19.05 mm
L_{pile} = 420 mm
t_w = 3.2 mm

Strain Gage

East

(b)

KBO01/02

01CPT5, 02CPT5

$10B_{CPT}$, typ.

01CPT1, 02CPT2

$10B_{pile}$, typ.

01P10   01P4   01P3. 02P3   01P2, 02P2   01P1

North

01 benders

01CPT2

02P11

South

01/02 benders

01P9   01P8   01P7   01P6   01P5, 02P5

01CPT4, 02CPT4

KBO01, D_R = 59 – 64%
KBO02, D_R = 62 – 68%

01CPT3, 02CPT3

West
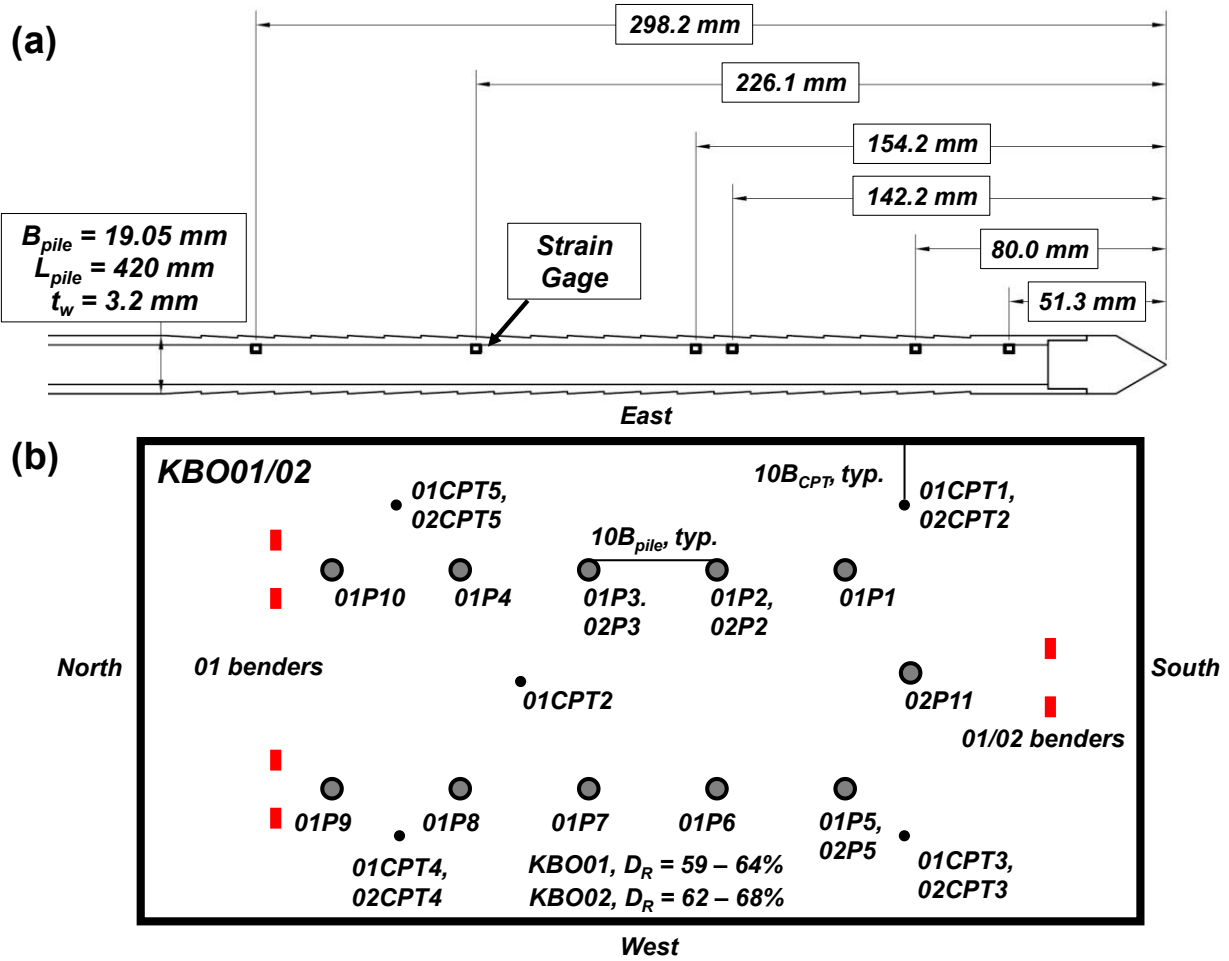
Figure 3.2. (a) Pile gage configuration for all piles, and (b) plan view and test locations for models KBO01 and KBO02 (abbreviated as 01 and 02 in the location labels).

84
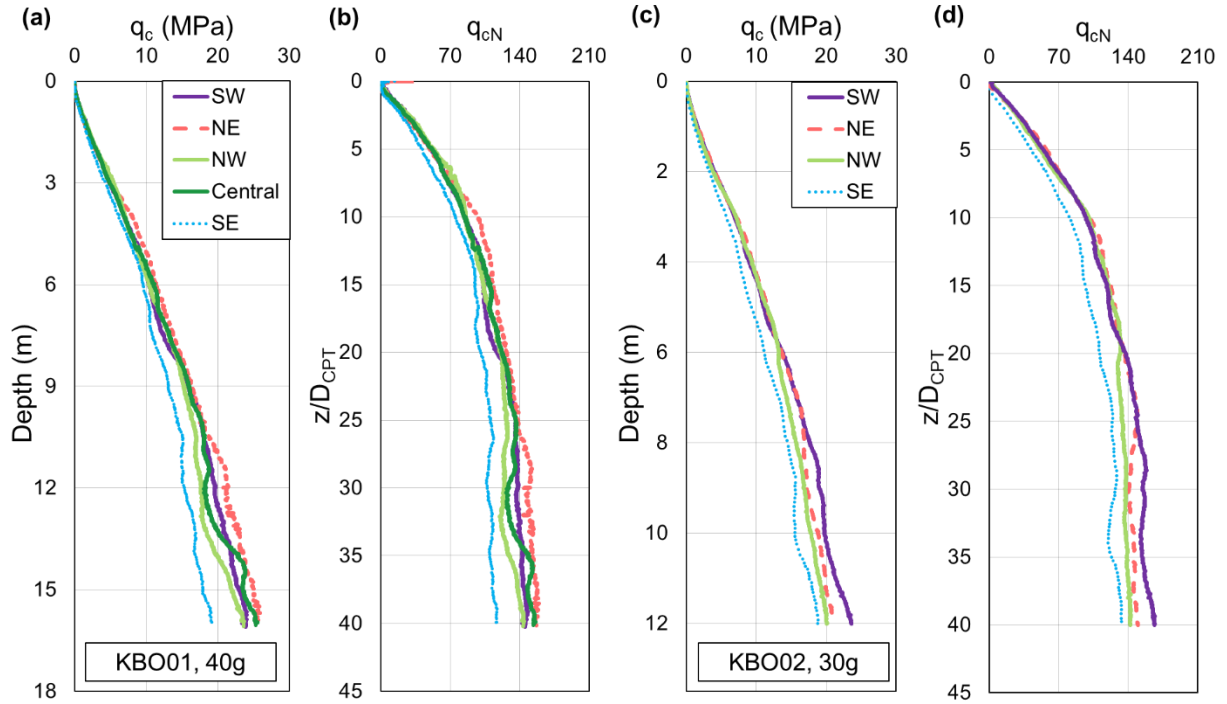
Figure 3.3. (a) q_c and (b) q_{cN} profiles from all soundings conducted in KBO01, and (c) q_c and (d) q_{cN} profiles from all soundings conducted in KBO02.
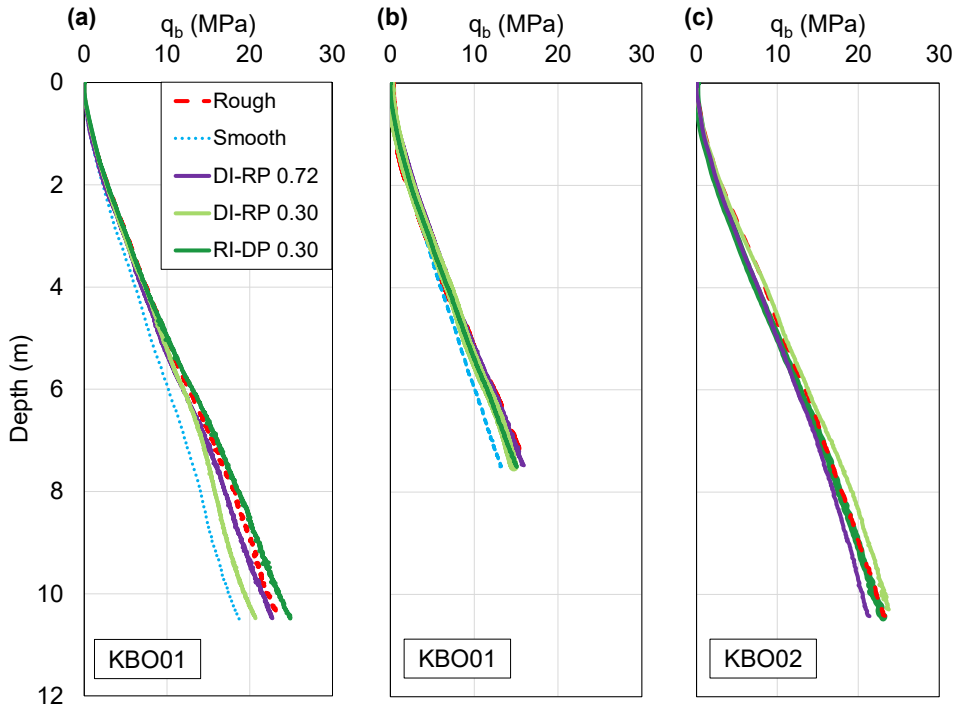
Figure 3.4. Profiles of q_b for (a) piles installed to 10.5 m in KBO01 (Tests P1, P4, P5, P9, and P10), (b) piles installed to 7.5 m in KBO01 (Tests P2, P3, P6, P7, and P8), and (c) piles installed to 10.5 m in KBO02 (Tests P2, P3, P5, and P11).
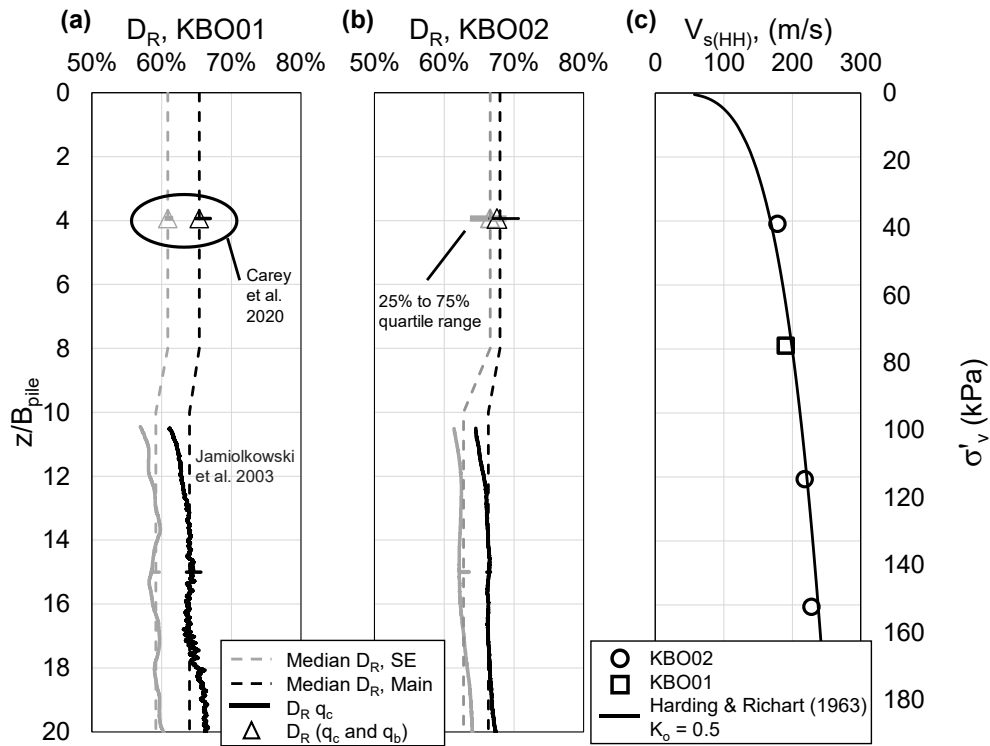
Figure 3.5. D_R and V_s profiles from KBO01 and KBO02: (a) D_R measurements and interpreted profiles in KBO01, (b) D_R measurements and interpreted profiles in KBO02, and (c) best fit K_0 for V_s measurements.
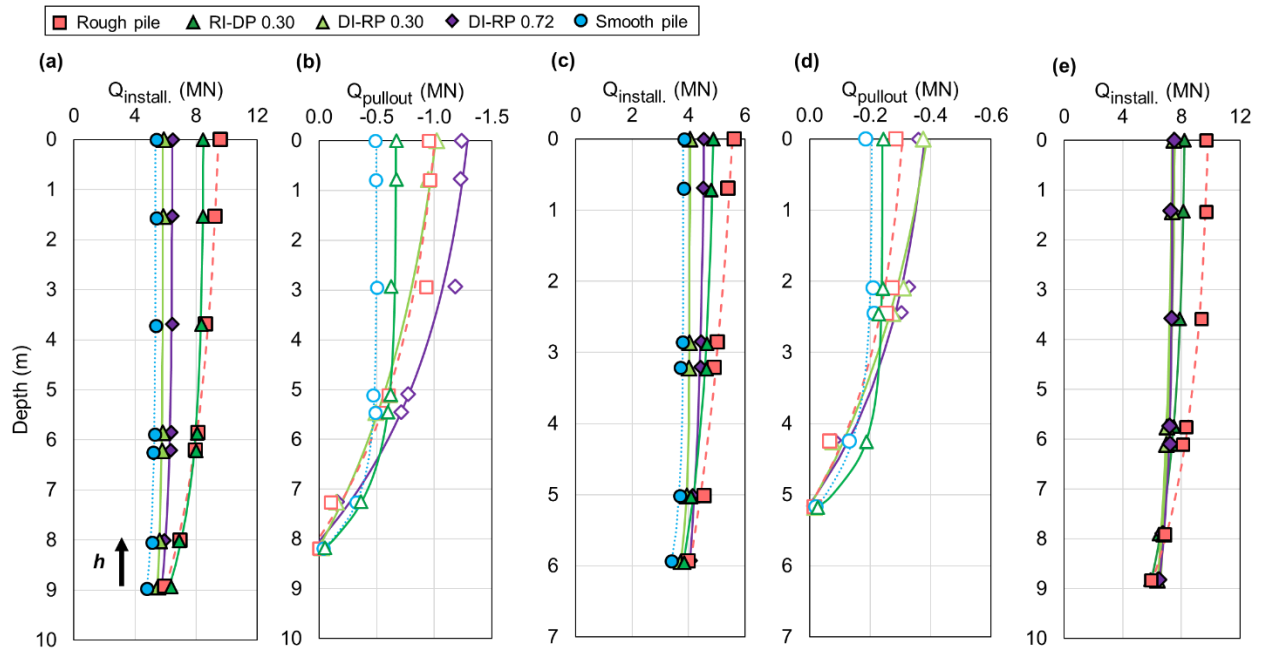
Figure 3.6. Axial load distributions for piles during (a) deep embedment installation and (b) pullout in KBO01 (Tests P1, P4, P5, P9, and P10), (c) shallow embedment installation and (d) pullout in KBO01 (Tests P2, P3, P6, P7, and P8), and (e) deep embedment installation in KBO02 (Tests P2, P3, P5, and P11) (note: relationships plotted correspond to Eq. 2).
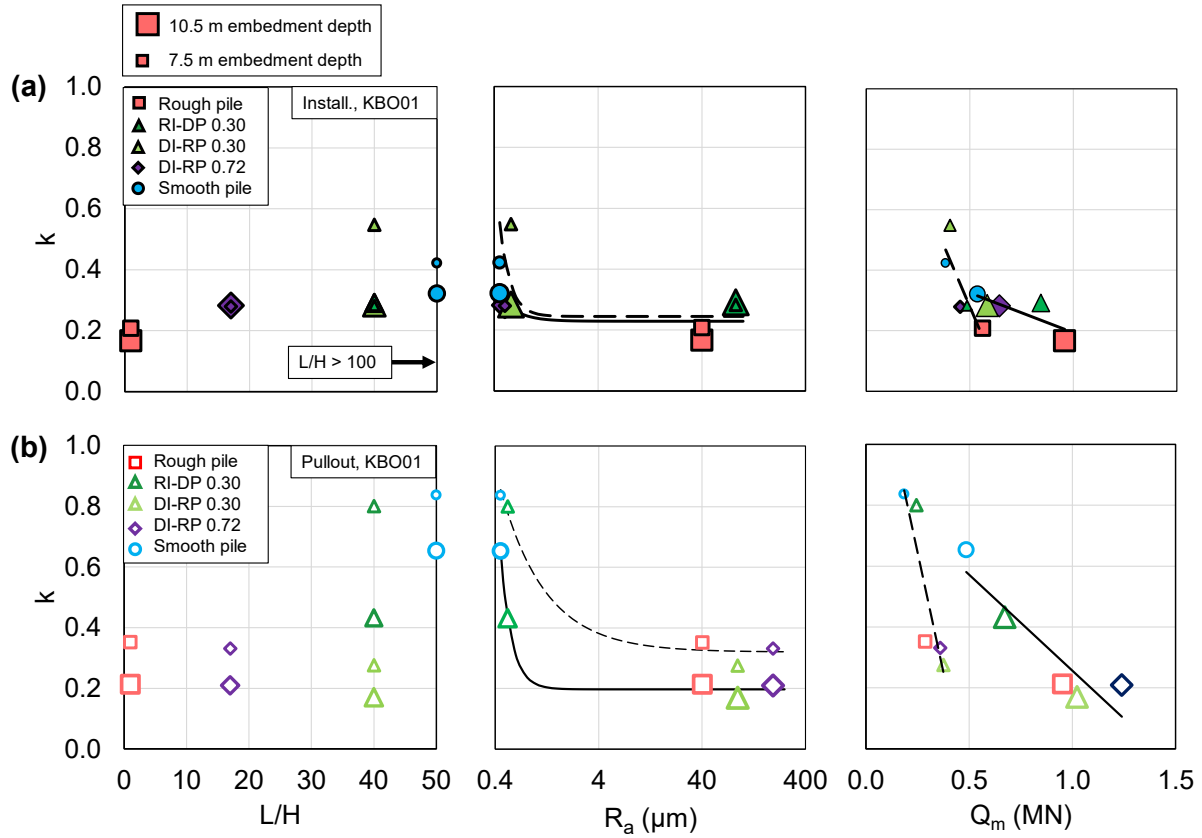
Figure 3.7. (a) *k* parameter from installation phase and (b) *k* parameter from pullout phase as a function of *L/H*, R_a, and Q_m (note: all results are from model KBO01; *L/H* values for the rough and smooth piles are assumed to be 1 and 50, respectively, for visualization purposes).
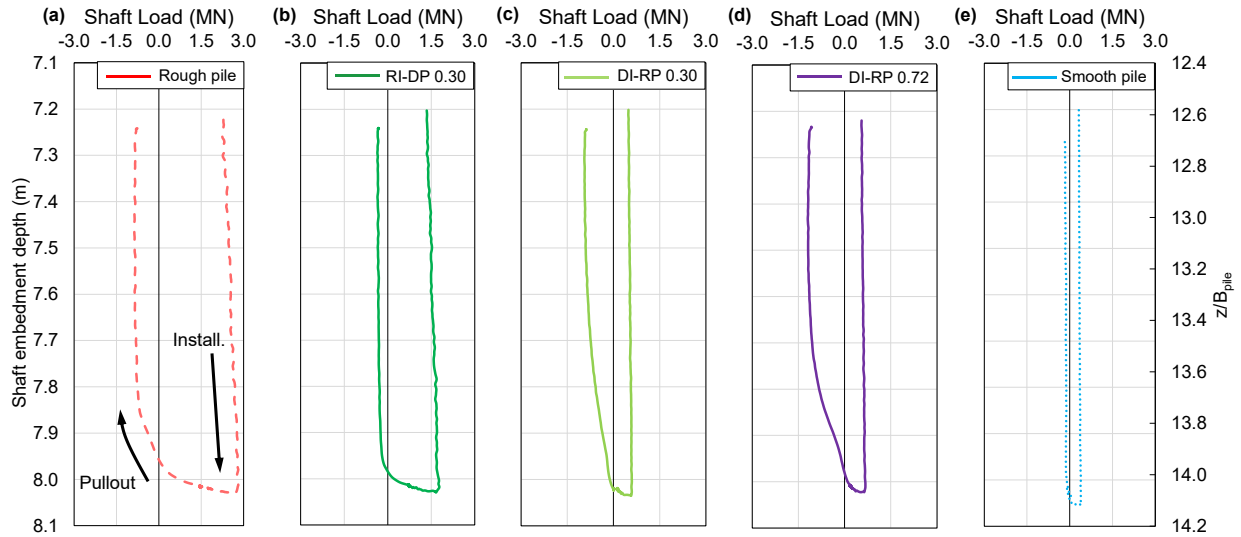
Figure 3.8. Global shear stresses for end of installation and beginning of pullout of (a) rough pile (Test P4), (b) RI-DP 0.30 pile (Test P9), (c) DI-RP 0.30 pile (Test P10), (d) DI-RP 0.72 pile (Test P5), and (e) smooth pile (Test P1) in model KBO01.
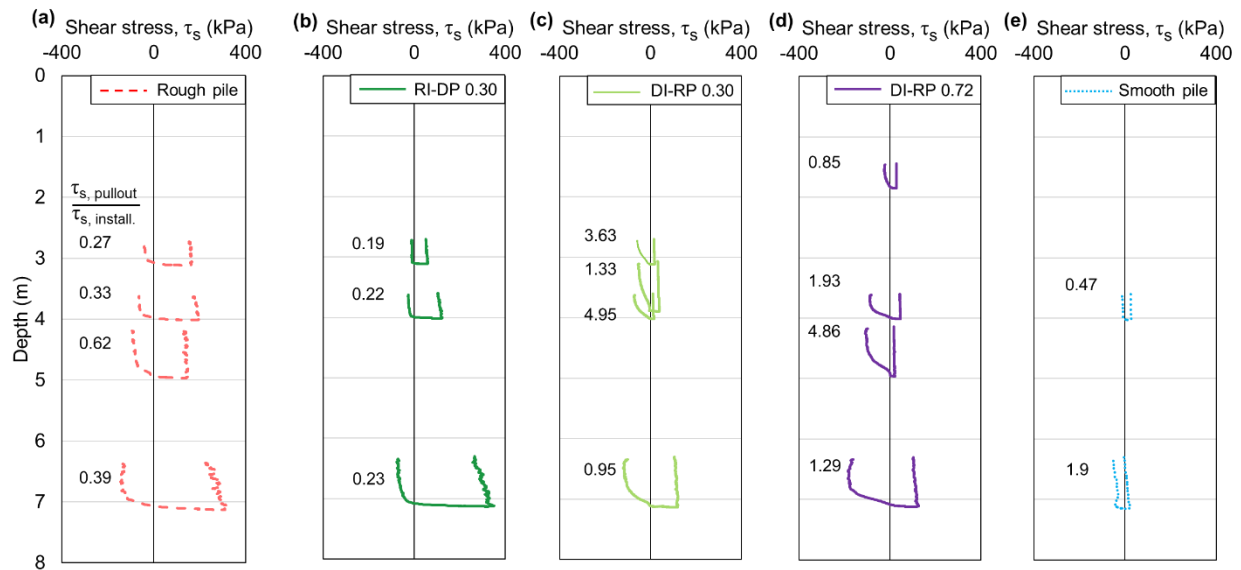
Figure 3.9. Local shear stress at depth for end of installation and beginning of pullout of (a) rough pile (Test P4), (b) RI-DP 0.30 pile (Test P9), (c) DI-RP 0.30 pile (Test P10), (d) DI-RP 0.72 pile (Test P5), and (e) smooth pile (Test P1) in model KBO01 (note: numbers in figures are the ratios of end of pullout shear stress to end of installation shear stress, $\tau_{s,pullout}/\tau_{s,install.}$).
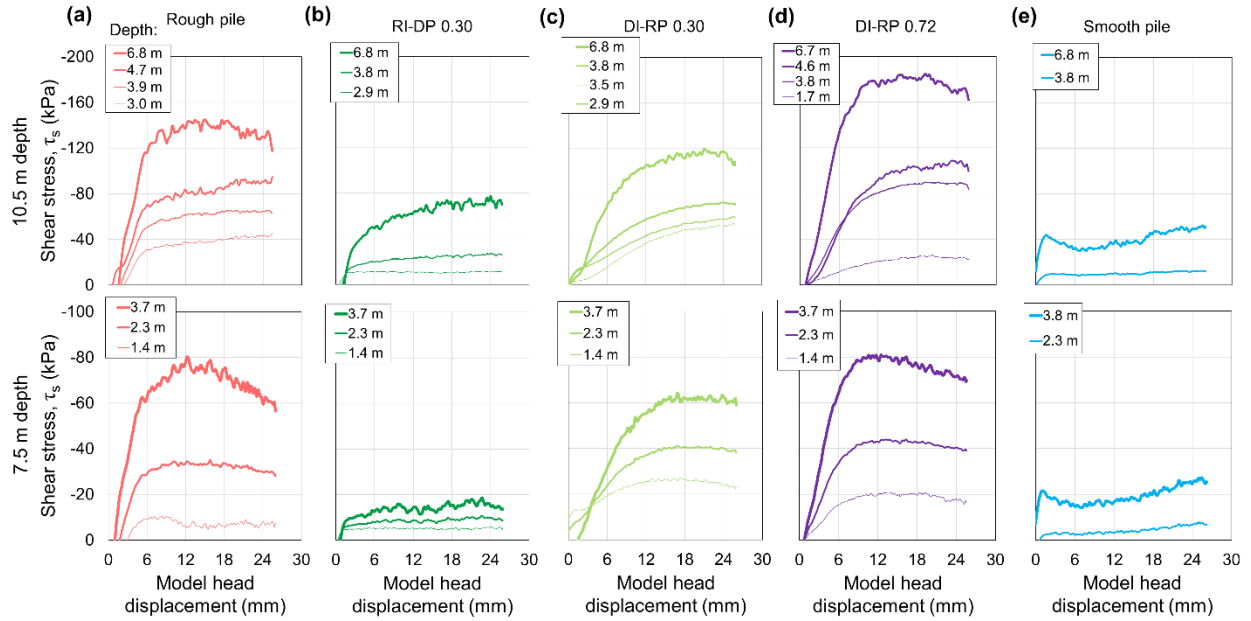
Figure 3.10. Local shear stress with pile head displacement for pullout loading of (a) rough pile (Tests P3 and P4), (b) RI-DP 0.30 pile (Tests P7 and P9), (c) DI-RP 0.30 pile (Tests P8 and P10), (d) DI-RP 0.72 pile (Tests P5 and P6), and (e) smooth pile (Tests P1 and P2) in model KBO01. Top and bottom rows correspond to 10.5 m and 7.5 m installation depths, respectively.
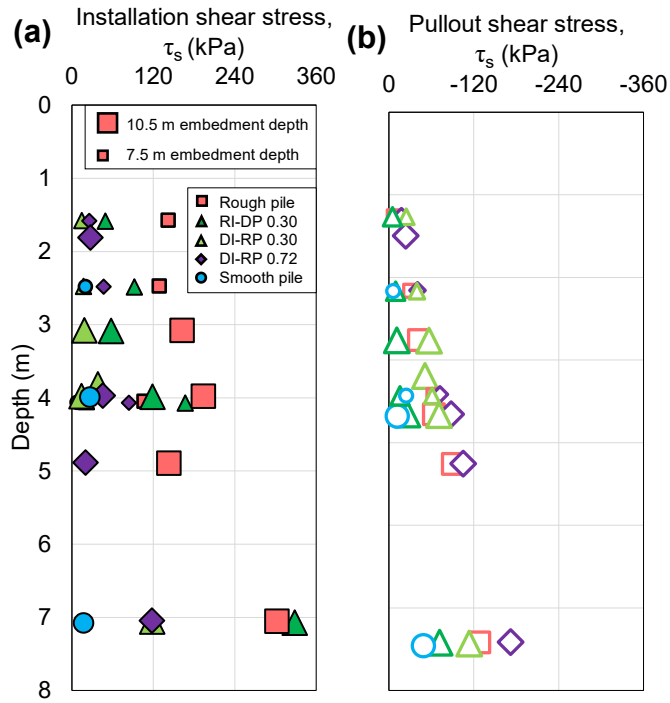
Figure 3.11. Local shear resistances for all piles in model KBO01 (Tests P1 to P10) at (a) end of installation and (b) end of pullout .
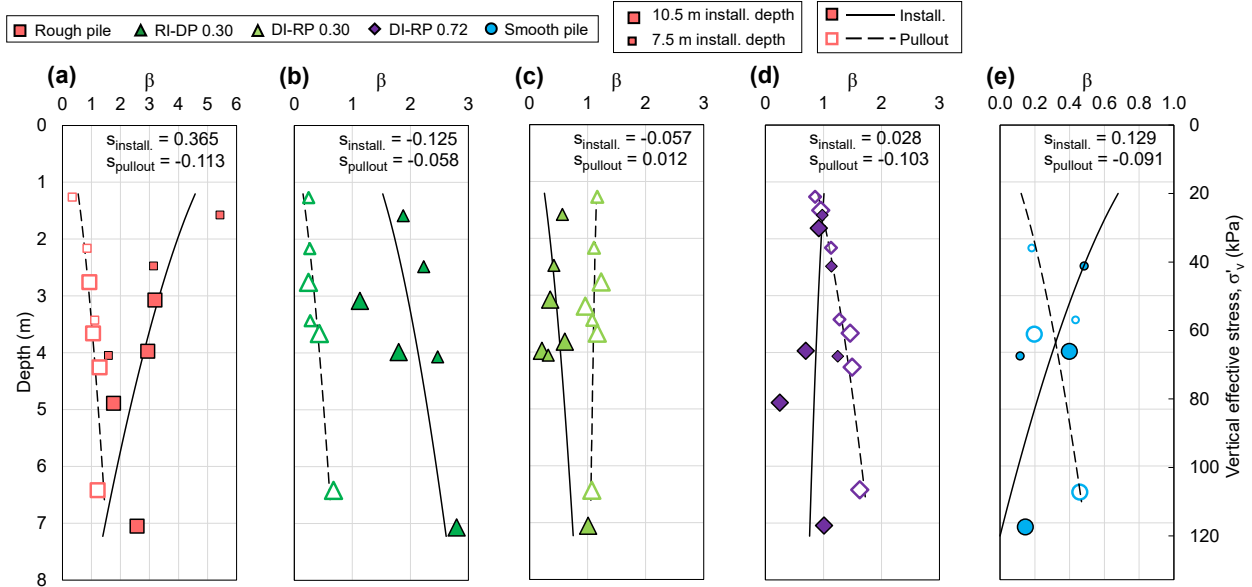
Figure 3.12. Local β coefficients at end of pullout for all piles in model KBO01: (a) rough (Tests P3 and P4), (b) RI-DP 0.30 (Tests P7 and P9), (c) DI-RP 0.30 (Tests P8 and P10), (d) DI-RP 0.72 (Tests P5 and P6), and (e) smooth (Tests P1 and P2) piles (note: relationships plotted correspond to Eq. 3; x-axis in (e) is reduced).
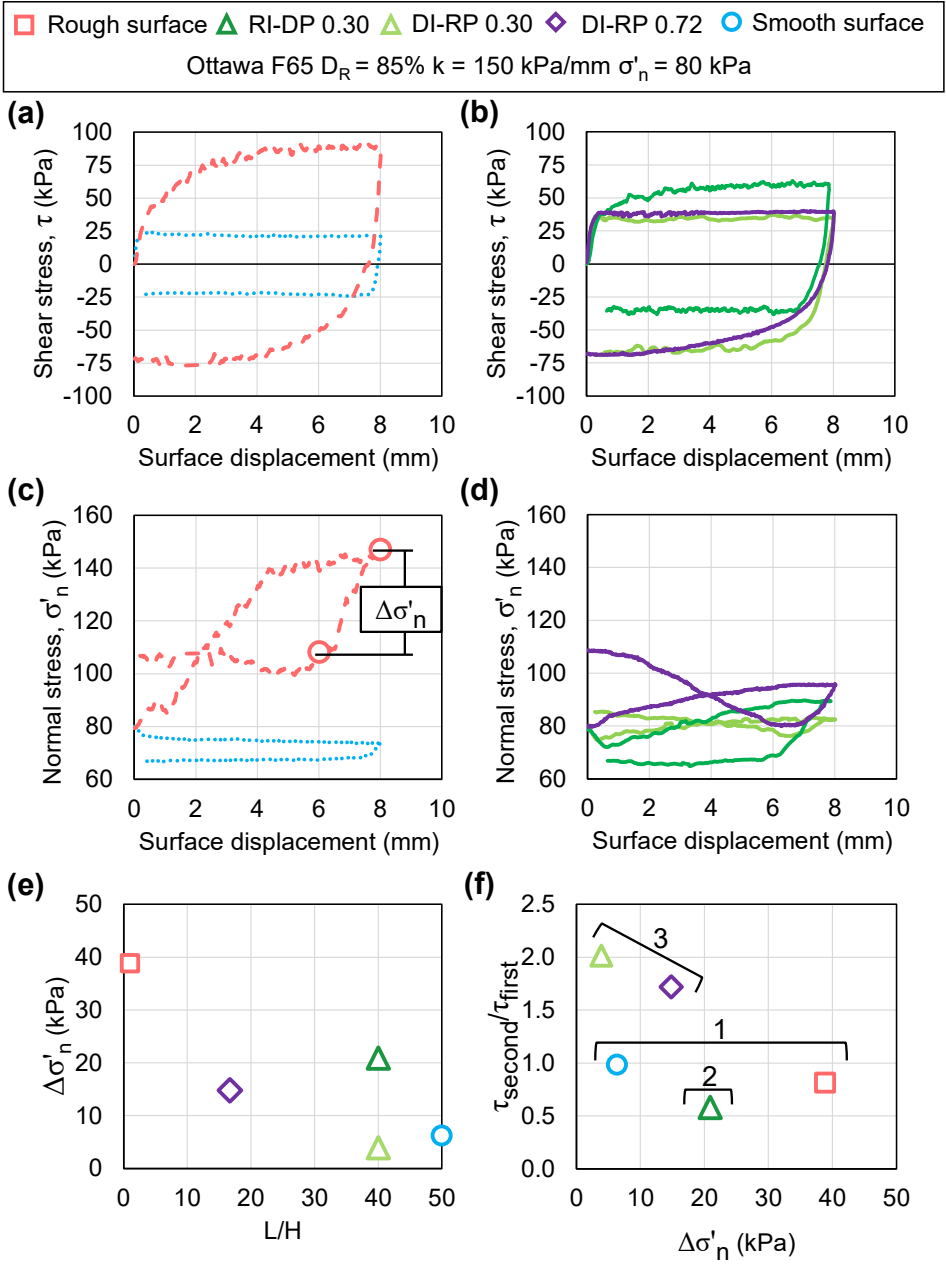
Figure 3.13. CNS interface shear test results for (a) and (b) shear stress – displacement response and (c) and (d) normal stress – displacement response. (e) Decrease in normal stress following a change in direction as a function of *L/H* and (f) ratio of shear resistance in second shearing direction to first shearing direction as a function of change in normal stress, grouped by proposed mechanism.

Chapter 4. Cyclic axial response and stability of snakeskin-inspired piles in sand

At the time of writing the dissertation, this chapter is under review by Acta Geotechnica and is presented herein with minor edits under the following citation.

O'Hara, K.B., Martinez A (2022). Cyclic axial response and stability of snakeskin-inspired piles in sand. Submitted to Acta Geotechnica.

ABSTRACT

Piles subjected to cyclic axial loading can experience loss of serviceability due to accumulation of excessive deformations, which is a common failure mode for offshore foundations. This investigation examines the cyclic behavior of piles with snakeskin-inspired surface textures that produce direction-dependent shearing and volume change. Centrifuge pile load test were performed on three piles with snakeskin-inspired surfaces, one which was cranially-installed and caudally-pulled and two with asperities of varying height which were caudally-installed and cranially-pulled. Tests were also performed on a reference rough pile and a reference smooth pile. The experiments, performed at an acceleration equivalent to 30g, investigated the effect of the surface texture on the capacity, load transfer, and cyclic behavior of the piles. The load-controlled cyclic experiments performed with various combinations of mean and cyclic loads show that the cranially-pulled piles failed in a smaller number of cycles due to the accumulation of deformations in the compressive, caudal stage of the cycles. However, failure of the caudally-pulled pile was more brittle, with fewer cycles between yielding and failure in comparison to the cranially-pulled piles. Cycling led to greater degradation of the local shaft capacity of the cranially-pulled piles,

resulting in a greater proportion of the total head load being carried by the pile base in compression. The evolution of global pile stiffness was not influenced by the surface texture; it was found to depend on the ratio of the mean to cyclic load, with larger ratios leading to increases in stiffness. Analysis using stability diagrams shows that in terms of absolute loads, the cranially-pulled piles are stable over a larger range of mean and cyclic loads. However, the caudally-pulled piles have larger regions of stability in terms of the mean and cyclic loads normalized by the pile capacity. The results provide evidence of the effect that bio-inspired surface textures can have on the stability of piles and show the tradeoffs that emerge due to the direction-dependent shaft resistance mobilization.

INTRODUCTION

Piles for offshore structures are subjected to significant cyclic environmental and operational loads. Extensive investigation on the stability of offshore piles subjected to cyclic axial loading has led to the understanding that the combination of the applied mean and cyclic loads are governing parameters in the accumulation of displacements, degradation of stiffness and loss of shaft capacity (Poulos 1988). Research has also shown that the capacity of pile shafts may benefit from bioinspired surfaces derived from the ventral scales of snakes (Martinez et al. 2019; Martinez et al. 2022). These surfaces create a directionally-dependent response in terms of interface strength and dilation due to their asymmetric geometry, where loading in the cranial direction leads to greater interface friction angles and soil dilation than loading in the caudal direction. These surfaces may be beneficial for deep foundations whose loading has a bias towards a given direction (i.e., piles in offshore jacket structures).

This paper presents the results of a series of load-controlled cyclic axial centrifuge tests of snakeskin-inspired piles in sand installed in flight with a direct push. The piles were internally instrumented to measure axial loads along the pile length. The results and discussion aim to evaluate the failure mode exhibited by the different pile types, quantify the accumulation of axial displacements and degradation of pile stiffness, compare the pile behavior at yield and failure, and assess the pile stability.

Pile interface behavior. It is well established that the interface friction angle between a soil and structural material (δ') and the effective normal stress acting on the pile shaft (σ'_n) are the governing parameters affecting the shear resistance of a pile shaft (τ), given by:

$$\tau = \sigma'_n tan\delta'$$

Laboratory interface shear testing has found that the evolution of the normal effective stress at a soil-structure interface depends on the soil state (DeJong and Westgate 2009), boundary conditions (Afzali-Nejad et al. 2021), stress reversal (O'Hara and Martinez 2022a), mineralogy and particle crushing (Zhou et al. 2020, Rui et al. 2021), temperature (Di Donna et al. 2016), and displacement magnitude (Ho et al. 2011). The σ'_n evolution acting on a pile surface has been shown to depend on similar parameters as observed in laboratory testing. Specifically, installation may result in particle crushing (Yang et al. 2010), the pile diameter influences the boundary condition (Bolon and Foray 1986), and stress reversals may lead to effects such as friction fatigue during installation (White and Lehane 2004) or reduced tensile capacity (De Nicola and Randolph 1993).

The interface friction angle of sands is traditionally related to the normalized surface roughness (Uesugi and Kishida 1986) or average surface roughness (Chow 1997) of the pile shaft. The value of δ' has been found to be limited by the internal friction angle of the soil, φ', for

randomly structured surfaces such as rusted steel or rough concrete. In contrast, apparent $\delta' > \varphi'$ conditions can be observed when surfaces are periodically structured (Hryciw and Irysam 1993, Martinez and Frost 2017). To find efficient surface textures that can be applied to soil-structure interfaces, a bioinspired process in geotechnical engineering applications has been proposed (Martinez et al. 2022). Specifically, surfaces and pile shafts with snakeskin-inspired geometries exhibit differences in interface shear resistance and volumetric changes based on the direction of relative displacement between the surface asperities and the soil, with shearing in the cranial direction mobilizing greater interface strength and soil dilation than the caudal direction (Palumbo 2018, Martinez et. al. 2019, O'Hara and Martinez 2020). Martinez and O'Hara (2021) and O'Hara and Martinez (2022a) showed that the load transfer in snakeskin-inspired piles loaded monotonically is influenced by the direction of loading in relation to the asperity geometry (i.e., cranial versus caudal) due to differences in dilation-induced changes in σ'_n, magnitudes of δ', and stress reversal effects.

Cyclic stability criteria and interaction diagrams. The stability of piles subjected to cyclic axial loads has been defined in terms of the applied loads at the pile head and the number of cycles needed to reach a specific failure criterion. Poulos (1988) proposed an interaction diagram to quantify the number of cycles to failure of piles loaded in tension and compression as a function of the mean load (Q_m) and cyclic load (Q_{cy}) normalized by the pile's ultimate capacity (Q_{tot}). Three zones of stability were proposed, designated as Stable (*S*), Metastable (*MS*), and Unstable (*U*) based on the magnitude and rate of displacement accumulation. This framework has been applied extensively to assess the stability of offshore piles that are subjected to cyclic axial loads from

97

storm, wave, and operational events (Jardine and Chow 1996, Atkins 2000, Merritt et al. 2012, Jardine 2020).

The cyclic stability of piles has been investigated using field and centrifuge tests (Jardine and Standing 2000, Jardine et al. 2012, Blanc et al. 2015). The results indicate that the *S* zone encompasses a wide range of mean loads below a threshold cyclic load, and the *U* and *MS* zones dominate in the two-way loading regime where stress reversals occur. Calibration chamber load tests on instrumented piles have provided further insight regarding the loss of radial effective stress around the piles during cyclic loading, providing experimental evidence of the mechanism leading to reduction of shaft resistance (Tsuha et al. 2012, Jardine et al. 2013a). Additional factors affecting the performance of pile shafts subjected to cyclic axial loading, such as aging effects (Rimoy et al. 2015), cyclic load sequence (Blanc and Thorel 2016, O'Hara and Martinez 2020), and cycle number and load amplitude (Zheng et al. 2019), have been investigated. Broadly, the results of these investigations indicate that interaction diagrams are suitable for describing the expected accumulated axial displacement behavior of piles subjected to cyclic axial loads, although tracking Q_{tot} at different test stages presents a challenge in the interpretation of results.

MATERIALS AND METHODS

Model Piles. Three instrumented piles with asymmetric periodic surfaces inspired by snake ventral scales were manufactured. The piles were constructed out of 2024 aluminum pipe, with a total length of 420 mm, outer diameter of 19.05 mm, and wall thickness of 3.05 mm. Martinez et al. (2019) and O'Hara and Martinez (2020) provide a description of the process for designing the bioinspired surfaces. Two reference piles were also manufactured with rough or smooth surfaces with average roughness (R_a) and maximum roughness (R_z) values such that interface failure occurs

within the soil mass (i.e., $\delta' = \varphi'$ conditions) or by sliding at the interface (i.e., $\delta' < \varphi'$ conditions), respectively. The bioinspired piles were machined to have asperities with a length (L) of 12 mm and a height (H) of either 0.30 or 0.72 mm, as shown in Figure 4.1a. The reference piles are referred to as rough or smooth, while the bioinspired piles are designated such that R refers to the cranial direction (soil against asperities), D to the caudal direction (soil with asperities), I to installation, P to pullout, and the number is the asperity height in mm. For example, the DI-RP 0.72 pile is installed in the caudal direction, pulled in the cranial direction, and has an asperity height of 0.72 mm. Figure 4.1a shows schematics of cranial and caudal installation. The R_a and R_z values of all five piles are reported in Table 4.1, along with the L/H values. Intra-asperity roughness values are measured between adjacent asperities and describe the sliding between the particles and the pile surface that takes place in the caudal shearing direction. In contrast, inter-asperity roughness values are measured across asperities which are related to the interlocking between particles and asperities during cranial shearing.

Each pile was internally instrumented with six Vishay S114L full bending-compensated Wheatstone bridges strain gauges to measure axial load (Figure 4.1b). The strain gauges were installed centrally between asperities to reduce nonuniform strains from the varying pile wall thickness. The piles had strain gages located near their tip to estimate the base resistance and along their shaft to measure the axial load along the pile length. The global shaft load was calculated as the difference between the head load and the load measured at the base strain gage. Local shaft loads were calculated as the load differences between adjacent strain gauges.

Centrifuge Modeling. Centrifuge modeling can be used to assess the system-level response of geostructures subjected to a variety of loading conditions by applying a gravitational field to a

scale model such that the model is subjected to a target effective stress representative of the prototype field scale system. By matching the effective stress between the model and prototype, other physical parameters may be scaled according to laws of similitude, summarized in Garnier (2007). Relevant physical parameters for this study are the length, stress, and force, which scale with N^* ($N^* = g_{model}/g_{prototype}$), are independent of N^*, and scale with N^{*2}, respectively. Additionally, the frequency of loading was kept in a pseudo static range, and scales with N^*. Throughout this paper, prototype-scaled quantities are reported except where noted otherwise.

All pile load tests were performed in uniform deposits of sand at a centrifugal acceleration of 30 times Earth's gravity ($N^* = 30$). All pile tests were conducted at a minimum spacing of $10B_{pile}$ away from boundaries and adjacent test locations, as shown in the schematic of the sand deposit presented in Figure 4.1c. The pile diameter (B_{pile}) to median particle size (D_{50}) ratio was 95, in accordance with minimum ratios between 50 and 100 recommended in Garnier (2007).

Two dry soil deposits, KBO01 and KBO02, were constructed using air-pluviated Ottawa F65 sand to a target relative density (D_R) equal to 65%. This sand is poorly graded, has a D_{50} of 0.20 mm, maximum void ratio (e_{max}) of 0.78, minimum void ratio (e_{min}) of 0.51, and critical state friction angle of 30.1° determined from direct shear tests ($\varphi'_{CS,DS}$) (Martinez et al. 2019). Figures 4.2a and 4.2b presents a summary of the tip resistance (q_c) measurements obtained from in-flight Cone Penetration Tests (CPTs) in the KBO01 and KBO02 deposits, showing reasonable agreement within each model. The CPT performed in the SE corner of the model yielded smaller q_c values, particularly at depths greater than 6 m. As outlined in detailed in O'Hara and Martinez (2022a) and O'Hara and Martinez (2022b), this is due to a smaller D_R in the SE portion of the model. Figures 4.2c and d show the analyzed D_R profiles from q_c and the pile base resistance, q_b based on the Jamiolkowski et al. (2003) and Carey et al. (2020) correlations and indicate that both models

fall within a D_R range from 59 to 68%, with the interpreted depth profiles showing a slight D_R decrease at depth (Z) normalized by pile diameter (Z/B_{pile}) between 8 and 10. The pile base resistance was used for analysis only for the Carey et al. (2020) correlation as it did not reach a sufficient Z/B_{pile} to use the Jamiolkowski et al. (2003) correlation. Push data with q_b from all piles in KBO02 are available through the DesignSafe repository. In-flight installation records for the load tests are not included here for brevity, but can be found in the DesignSafe online repository (O'Hara and Martinez 2022c).

The loading sequence for each test was defined using RMCTools (Delta Computer Systems, Washington) and applied with a hydraulic actuator. The monotonic pullout tests on all five piles were conducted in KBO01, while the cyclic tests were conducted on the three snakeskin-inspired piles and the rough pile in KBO02 (Table 4.2). All piles were installed to a depth of 10.5 m (350 mm in model scale) with a direct push at a rate of 1 cm/s. The monotonic pullout tests were performed by pulling the piles in tension for a distance of 0.76 m (25.4 mm in model scale); these results were used to evaluate Q_{tot} for the five different pile types. All actuation for the cyclic tests was commanded through displacement feedback with load limits. After the cyclic piles were installed to the target depth, they were unloaded to the target tensile Q_m for the particular test. Afterwards, the cyclic loading between the tensile unloading limit ($Q_m - Q_{cyc}$) and the compressive loading limit ($Q_m + Q_{cyc}$) was applied. The cyclic loading period (T) for all tests was between 0.17 s and 1.7 s in model scale and between 10 and 2000 cycles were conducted during any given test.

RESULTS

The results from the monotonic pullout tests are first presented to determine the shaft capacity and load mobilization response of each pile. The results of cyclic tests that exhibited U and MS stability

are then evaluated, with focus on the accumulation of displacements over a range of load combinations. The cyclic tests are also used to establish boundaries between the *S*, *MS*, and *U* zones in an interaction diagram for the different piles, with a particular focus on the effect of the shaft texture and directionality (i.e., cranially- versus caudally-installed) on the cyclic failure. The pile response parameters used to describe the cyclic tests along with the achieved cyclic loads mapped on an interaction diagram are provided graphically in Figures 4.3a-c. The cycles to failure for each test are indicated in Figure 4.3c. In addition, all Q_m/Q_{tot} combinations reflect either a symmetric loading condition or a tensile load bias. The stability of each pile, as included in Table 4.1, was specified following the criteria defined by Rimoy et al. (2013) in this investigation, defined as:

- Stable: low and stabilizing accumulated axial displacements that remain below 1% of the pile diameter (B_{pile}) and show small rates of displacement accumulation (< 1 mm/1000 cycles) up to 1000 cycles (*N*) without causing loss of operational static shaft capacity.

- Metastable: accumulated axial displacements between 1% and 10% of B_{pile} or rates of displacement accumulation between 1 mm/1000 cycles and 1 mm/10 cycles, with failure requiring more than 100 cycles.

- Unstable: cyclic failure within 100 cycles, involving either accumulated axial displacements greater than 10% of B_{pile} or rates of displacement accumulation greater than 1 mm/10 cycles.

For the *U* and *MS* regimes, the number of cycles of failure (N_f) is defined by the stated criteria, while *S* tests are designated as $N_f > 1000$.

Pile shaft capacity and stiffness. The shaft capacity was influenced by the shaft texture, as shown by the tests performed in the KBO01 deposit. Figure 4.4a presents the head load with model displacement (Δz), showing that the DI-RP 0.72 pile had the highest capacity, followed by the rough, DI-RP 0.30, RI-DP 0.30, and the smooth piles, respectively. The piles pulled in the cranial direction (i.e., DI-RP 0.72 and DI-RP 0.30) mobilized greater pullout loads than the pile pulled in the caudal direction (i.e., RI-DP 0.30). Figure 4.4b shows the pullout curve for each pile normalized by its maximum load (Q/Q_{tot}) against the displacement normalized by the pile diameter ($\Delta z/B_{pile}$). These results highlight the displacement required to the peak capacity for each pile type, where the DI-RP 0.30 pile requires the greatest displacement, followed by the DI-RP 0.72, and rough piles, respectively, while the RI-DP 0.30 and smooth piles require the smallest displacement to reach their Q_{tot}. These differences reflect the interactions at the soil-pile interface, where the cranially-pulled piles transfer load through passive resistances that require more displacement to mobilize, while the caudally-pulled and smooth piles transfer load through sliding which requires little displacement to fully mobilize (Martinez and Frost 2017; Martinez et al. 2019).

The initial stiffness and rate of load mobilization were also influenced by the shaft type. Figures 4.4c and 4.4d present the Q and Q/Q_{tot} values at a displacement (Δz) equivalent to 0.5% of B_{pile}; the values are plotted as a function of R_a, where the intra-asperity R_a values are used for the piles displaced in the caudal direction and the inter-asperity R_a values are used for the cranially-displaced piles. This is done to describe the behavior over a continuous range of R_a values and has been shown to capture the load transfer behavior of snakeskin-inspired piles and surfaces (O'Hara and Martinez 2022a). The RI-DP 0.30, smooth, and rough piles have similar high stiffnesses at displacements equal to 0.5% B_{pile}, while the DI-RP 0.30 and 0.72 piles have the lowest stiffnesses (Figure 4.4c). In terms of the normalized loads, the smooth and RI-DP 0.30 piles achieve the

greatest loads, followed by the rough, DI-RP 0.30 and DI-RP 0.72 piles, respectively, showing that

the normalized pile stiffness decreases as R_a is increased and that the normalized stiffness is greater

in the caudal shearing direction despite the smaller absolute pile capacity.

Cyclic shaft capacity response. Cyclic loading with tension and compression load limits were

applied on the piles. All normalized load combinations are referred to throughout the text by their

coordinates on an interaction diagram, defined as (Q_m/Q_{tot}, Q_{cyc}/Q_{tot}). Two typical examples of a

load – cycle number response are presented in Figures 4.5a and b for the RI-DP 0.30 and DI-RP

0.30 piles. The piles are cycled at a target normalized load combination of (0.16, 0.63), with the

specific achieved load combination noted in Figures 4.5a and b. As shown, the DI-RP 0.30 pile

was subjected to a higher absolute load magnitude than the RI-DP 0.30 pile due to the former's

greater Q_{tot}, but both piles were subjected to similar normalized load combinations. For this

particular example, the DI-RP 0.30 pile failed in 13 cycles and the RI-DP 0.30 pile failed in 6

cycles.

All piles showed a decrease of local shaft capacity with depth, indicating a progressive

failure from the deeply embedded shaft sections upwards to the ground surface. To assess the

changes in shaft load from the initial cycle to N_f for each pile type, the final load measured by each

strain gauge (P_f) was normalized by the load measured after the first cycle (P_0). Figures 4.6a-d

shows the proportional shaft load (P_f/P_0) along the pile length for the tests conducted at the load

combinations noted. Because the head load is specified to be constant throughout cycling, P_f/P_0 is

near 1 at the pile head by definition, while changes at depth reflect the redistribution of loads along

the pile length. Figure 4.6a shows the normalized loads for the RI-DP 0.30 and DI-RP 0.30 piles

for Q_m/Q_{tot} = -0.02 to -0.01 and Q_{cyc}/Q_{tot} = 0.65 to 0.69. The RI-DP 0.30 pile has a greater P_f/P_0 at

all depths compared to the DI-RP 0.30 pile. The results in Figure 4.6b show that the rough pile exhibits the greatest proportional reduction in load for $Q_m/Q_{tot} = 0.13$ to 0.23 and $Q_{cyc}/Q_{tot} = 0.57$ to 0.68, followed by the DI-RP 0.30 and DI-RP 0.72 piles, and the RI-DP 0.30 pile experiences the least loss load reduction. Figures 4.6c and d show similar trends, where the cranially pulled piles have a lower proportional shaft load at failure compared to the caudally pulled pile. These results indicate that the progressive failure is most pronounced for the rough pile, followed by the cranially-pulled pile, and least pronounced in the caudally-pulled pile.

Cyclic failure behavior. The U and MS tests conducted with symmetric loads and tension bias show the effect of the load combination, and shaft directionality and asperity height of the bioinspired piles. Figure 4.7 shows the accumulated displacements from each cyclic test, with N_f indicated for each test. Comparing the RI-DP 0.30 and DI-RP 0.30 piles, the DI-RP 0.30 pile fails by the displacement rate criterion in 3 of the 4 tests, while the RI-DP 0.30 pile fails by the 10% displacement criterion in 3 of the 4 tests. In all 4 tests, the DI-RP 0.30 pile has a smaller N_f compared to the RI-DP 0.30 pile. The DI-RP 0.72 pile tends to fail in the fewest number of cycles, whereas the rough pile shows the greatest N_f compared to the other pile types as seen in Figure 4.7b. For all piles, N_f tends to decrease as either the mean load or cyclic load is increased.

These results suggest that the pile surface texture affects the base – shaft interaction, resulting in different failure responses. To assess the differences in N_f between pile types, the proportion of the head load carried by pile base (Q_b/Q_{head}) and the single amplitude displacement in the compressive direction are presented as a function of cycle number (Figures 4.8a-c). The results show that Q_b/Q_{head} is consistently lower for the RI-DP 0.30 pile than for the DI-RP 0.30 pile, indicating that the cranially-installed piles rely the least on the base capacity to reach the

specified compressive load due to the greater interface friction angle and dilation-induced increases in radial effective stress in the cranial direction (O'Hara and Martinez, 2020). In contrast, the caudally-installed piles mobilize a greater base capacity magnitude in compression for all load combinations. For the tests with Q_m/Q_{tot} = 0.13 to 0.23 and Q_{cyc}/Q_{tot} = 0.57 to 0.68, the rough pile exhibits the largest Q_b/Q_{head} values after the first cycle.

The accumulation of single amplitude displacement in compression for each pile appears to have inverse trends as compared to those for Q_b/Q_{head}, as shown in Figures 4.8d-f . Specifically, piles with greater Q_b/Q_{head} require greater single amplitude displacements to meet the compression load limit defined at the pile head. These trends clarify the mechanism leading to differences in N_f based on the shaft texture orientation, where the caudally-installed, cranially-pulled piles at any given load combination fail in fewer cycles due to the larger displacements during the compressive portion of each cycle, likely causing greater degradation of stiffness in the soil surrounding the piles. This may be explained by the base resistance in the DI-RP piles requiring larger displacements to mobilize the ultimate capacity compared to its shaft resistance. In contrast, since the RI-DP pile has a larger shaft capacity during installation than the DI-RP piles, it requires a smaller base load to be mobilized, leading to smaller single amplitude displacements.

The apparent relationship between larger compressive displacements leading to fewer N_f in pullout can be further explained by comparing individual stress – displacement loops for each pile. Figures 4.9a and b present the head load – displacement curves for all tests conducted at an average load combination of (0.16, 0.63) at N = 2 and N = 16. The RI-DP 0.30 pile requires the smallest single amplitude displacement to reach the compressive load criteria, followed by the rough pile, then the DI-RP 0.30 and DI-RP 0.72 piles, respectively. The larger compressive displacements lead to elongation of the stress loops on the unloading portion of the response,

causing more work being done in each cycle and greater accumulation of plastic deformations. Further discussion of differences in N_f between pile types is provided in the discussion section.

Unloading stiffness response. Each pile exhibited changes in the cyclic global unloading stiffness (k_u) dependent on the load combination while the effects of the shaft geometry are not readily apparent. The k_u is calculated as the ratio of the cyclic load measured at the pile head to the double amplitude (*DA*) displacement on the unloading loop, where the start of each loop is defined at the start of tensile unloading (Figure 4.3a). Figures 4.10a-d show k_u for tests conducted on each pile type, with different load combinations indicated by the marker type and N_f for each test indicated with the highlighted marker. For *S* tests, N_f was taken to be 1000 cycles since the stability criteria used are not defined past $N = 1000$. Figures 4.10e-h shows the normalized k_u values for each test ($k_u/k_{u,ref}$), where k_u at $N = 2$ is used as $k_{u,ref}$ since it was the first cycle to include both full unload and reload portions. The evolution of both k_u and $k_u/k_{u,ref}$ shows that for all tests there is an initial increase in the stiffness, followed by a decrease or plateau until N_f. For tests conducted at low cyclic load amplitudes, specifically DI-RP 0.30 (0.21, 0.29), RI-DP 0.30 (0.18, 0.31) and (-0.02, 0.47), DI-RP 0.72 (0.07, 0.27), and rough pile (0.07, 0.06), there is a trend of an initial increase in k_u, followed by a decrease to a nominally constant value until failure. In contrast, the tests at the higher cyclic load amplitudes show an initial increase in k_u, followed by a rapid decrease in stiffness until failure.

The $k_u/k_{u,ref}$ values indicate that the final unloading stiffness of the pile is dependent on the load combination. Here, the load combination is characterized using the Q_m/Q_{cyc} ratio, where $Q_m/Q_{cyc} = 0$ indicates symmetric loading and $Q_m/Q_{cyc} = 1.0$ is the onset of one-way loading. The stiffness ratio $k_u/k_{u,ref}$ is plotted as a function of Q_m/Q_{cyc} and N_f in Figures 4.11a and 11b. The

$k_u/k_{u,ref}$ values tend to increase as Q_m/Q_{cyc} is increased, with a crosover to $k_u/k_{u,ref}$ greater than 1.0 at approximately $Q_m/Q_{cyc} = 0.5$ regardless of the pile type. Conversely, Figure 4.11b shows that there is no apparent trend between $k_u/k_{u,ref}$ and N_f, indicating that the number of cycles to failure does not significantly affect the final stiffness of the pile – soil system. These results are in general agreement with results presented in Rimoy et al. (2013), where the unloading stiffness ratios tend to increase compared to the initial stiffness for one-way loading tests or tests with a small tensile bias. The authors attribute the effect to the plastic deformations accumulating primarily on the compressive loop of each cycle.

DISCUSSION

Global pile stiffness response. The cyclic global unloading stiffness k_u is related to both Q_{cyc}/Q_{tot} and the *DA* displacement. Figures 4.12a and b shows an example of individial matched data points for *DA* displacement, Q_{cyc}/Q_{tot}, and k_u calculated at each cycle from all tests on the DI-RP 0.30 pile. It is noted that small changes in Q_{cyc}/Q_{tot} over the course of a test are due to variations in actuation leading to greater achieved load than command load, particularly at the initial cycles as shown in Figures 4.5a and 5b. The maximum standard deviation in Q_{cyc}/Q_{tot} within a test was 0.045 across this investigation. Figure 4.12b shows the *DA* displacement – k_u relationship to be nominally log-linear, with offsets that depend on the applied Q_{cyc}/Q_{tot}. The offsets are due to the smaller *DA* displacement values and larger k_u values for the tests with smaller Q_{cyc}/Q_{tot}. By definition, the data points for cycles from each pile type should fall on a surface defined by:

$$k_u = A^* \left(\frac{Q_{cyc}/Q_{tot}}{DA} \right)$$

where A^* is a fitting parameter with units of MN obtained through nonlinear regression. A surface for each pile was fit over the range of all cyclic data available, as shown in Figure 4.12c for the

RI-DP 0.30 pile. The A^* parameter decreased from 3,322 MN for DI-RP 0.72, to 2787 MN for the rough pile, 2495 MN for the DI-RP 0.30 pile, and 2,119 MN for the RI-DP 0.30 pile. The fitted surfaces for all four piles and are shown in Figure 4.13a, with slices of k_u at given Q_{cyc}/Q_{tot} values presented in Figures 4.13b-d. The surfaces for all piles indicate a decrease in k_u with increasing Q_{cyc}/Q_{tot} and *DA* displacement. The slices at $Q_{cyc}/Q_{tot} = 0.3$, 0.5, and 0.7 indicate that for a given stiffness and Q_{cyc}/Q_{tot}, the *DA* displacement is lowest for the RI-DP 0.30 pile, followed by the DI-RP 0.30, rough, and DI-RP 0.72 piles, respectively. These figures highlight that the relationship between Q_{cyc}/Q_{tot}, *DA* displacement and k_u is influenced by the shaft texture, regardless of the evolution of k_u with N (i.e., Figure 4.10).

Shaft secant stiffness degradation. The shaft unloading secant stiffness ($G_{sec,u}$), determined as using the shear resistance measured along the textured portion of the pile (i.e., between gauge 2 and the pile head), tends to fall into one of two regimes when analyzed in terms of the double amplitude displacement. $G_{sec,u}$ as a function of *DA* displacement are presented for DI-RP 0.30 and RI-DP 0.30 piles in Figures 4.14a-d and 15a-d, respectively. Initially, the $G_{sec,u}$ – *DA* displacement response is nominally linear in log-log space. Prior to N_f, marked with the triangle symbol, the response shifts to a new operational log linear relationship. The cycle number at which deviation from the initial stiffness line to the secondary stiffness line occurs is defined herein as the cycles to yield (N_y) and is marked with a circle symbol in the figures. This value was chosen by maximizing the correlation coefficient between the fitted log-log linear relationships for each regime (initial and secondary) in the $G_{sec,u}$ – *DA* displacement response, as shown in Figures 4.14 a-d and 4.15 a-d.

Based on the $G_{sec,u} - DA$ diplacement curves, the RI-DP 0.30 pile exhibits yielding at a cycle number close to the number of cycles to failure. However, it is noted that the transition from the initial $G_{sec,u} - DA$ displacement line to the line after yielding is not necessarily a well-defined point. Namely, for some piles there is a transition between the $G_{sec,u} - DA$ displacement lines. This is apparent in the test conducted at a load combination of (-0.01, 0.67) and (-0.01, 0.47), where the transition occurs over three to 40 cycles (Figure 4.14a and 4.14c).

The $G_{sec,u} - DA$ displacement lines for the DI-RP 0.30 pile indicate a significant number of cycles between N_y and N_f (Figures 4.15a-d). This deviation is hypothesized to be the region where plastic strains at the interface begin to dominate the displacement behavior, which aligns with the results in Figures 4.7a-d showing the significant accumulation of displacements between N_y and N_f. Figures 4.7a-d show that in every test conducted on the snakeskin-inspired piles, N_y occurs at lowest accumulated displacements for the the DI-RP 0.72 pile, followed by the DI-RP 0.30 pile, and the highest displacements for the RI-DP 0.30 pile.

The brittleness of the pile failure can be characterized by the ratio between N_f and N_y. Figure 4.16 presents the N_y/N_f ratio as a function of Q_m/Q_{cyc} for the snakeskin-inspired piles. There is no clear effect of Q_m/Q_{cyc} on N_y/N_f, as shown by the values oscillating around the averages for each pile. However, the DI-RP piles show significantly smaller N_y/N_f values than the RI-DP 0.30 pile. Greater N_y/N_f values indicate a more brittle failure response as seen for the RI-DP 0.30 pile in Figures 4.7a-7d, with an average N_y/N_f of 0.91. On the other hand, the DI-RP 0.30 and DI0RP 0.72 piles exhibit a more ductile response, with N_y/N_f of 0.53 and 0.50, respectively. These results highlight how the change in the G_{sec} from an initial to secondary regimes (Figure 4.15a-15d) aligns with the onset of rapid displacement accumulation (Figure 4.7a-7d) for the DI-RP 0.30 and DI-RP 0.72 piles, characterized by low N_y/N_f ratios. In contrast, the change in G_{sec} for the RI-DP 0.30

pile (Figure 4.14a-4.14d) occurs well into the region of rapid accumulation of displacements (Figure 4.7a-4.7d), characterized by a high N_y/N_f ratio.

Cyclic stability diagrams and implications on pile stability. The cyclic stability of the different pile types was affected by the orientation (i.e., DI-RP versus RI-DP) and height of the asperities. The cyclic stability of each pile can be defined in cyclic stability diagrams in terms of the applied absolute (i.e., Q_{cyc} and Q_m) or normalized (i.e., Q_{cyc}/Q_{tot} and Q_m/Q_{tot}) loads. Figures 4.17a and b presents stability diagrams for the RI-DP 0.30, DI-RP 0.30, and DI-RP 0.72 piles inferred from the N_f values and stability designations presented in Table 4.2 and Figure 4.3c. The contours for the rough piles were taken from Jardine and Standing (2012) due to the lack of sufficient data points in this study to define them. The U and MS boundary lines were anchored at $Q_m/Q_{tot} = 0.90$ and $Q_{cyc}/Q_{tot} = 0.10$, which assumes that no cyclic failure occurs below 10% cyclic loading (Jardine et al. 2005b) regardless of the shaft type. In terms of absolute loads, the ultimate capacity for each pile type is shown as a downward Q_{tot} diagonal line, (Figure 4.17a). The results show that the DI-RP piles and the rough pile have a wider range of load combinations in *MS* conditions in comparison with the RI-DP piles. The rough pile requires the highest Q_{cyc} magnitudes to transition to *U* conditions at Q_m smaller than about 0.75 MN. The MS zone of the DI-RP 0.72 pile is longer in the horizontal direction, indicating that it requires greater Q_{cyc} for Q_m values greater than about 0.75 to reach *U* conditions. Interestingly, the RI-DP 0.30 pile requires the greatest Q_{cyc} magnitudes to transition from *S* to *MS* conditions at Q_m values smaller than 0.5 MN reflecting this pile's greater N_f values. The zone between the *MS* and *U* conditions for the RI-DP 0.30 is the smallest among the piles, reflecting its brittle failure behavior (i.e., Figure 4.16). The boundaries between stability

zones for the DI-RP 0.30 pile are largely located between the correcponsing boundaries for the DI-RP 0.72 and RI-DP 0.30 pils.

The interaction diagrams in terms of the normalized loads show that the combination of loads to reach *MS* conditions for the DI-RP and rough piles shifts downward in relation to the RI-DP pile. The load combinations for *MS* conditions also shift downward for the DI-RP piles as the surface roughness increases. Consequently, the transition from *S* to *MS* conditions occurs at the largest normalized load combinations for the RI-DP 0.30 pile, followed by rough, DI-RP 0.30, and DI-RP 0.72 piles, respectively. To quantify the stability zones in the normalized interaction diagram, a simplified prediction for N_f contours provided in Jardine et al. (2005b) was fitted to the contours in Figure 4.17b. The procedure assumes the change in static capacity due to *N* cycles at a given cyclic load follows this functional form:

$$\frac{\Delta Q_{m\ static}}{Q_{tot}} = A(B + \frac{Q_{cyc.}}{Q_{tot.}})N^C$$

where $\Delta Q_{m\ static}$ is the reduction in mean load from the ultimate capacity line at a given Q_{cyc}/Q_{tot} value, *A* defines the slope of the contour lines, *B* controls the value of Q_{cyc}/Q_{tot} at which the contour lines intersect the Q_{tot} line, and *C* controls the relative spacing between contours. For the fitting procedure conducted, it was assumed that *B* = -0.10 for all pile types, as previously described. The *A* and *C* parameters for the rough pile were taken from Jardine and Standing (2012). For the snakeskin-inspired piles, the *A* and *C* parameters were calculated by minimizing the residuals between both the slopes and intercepts between the experimentally derived and predicted contours at *N* = 100 and *N* = 1000. Figures 4.18a-d shows the *A* and *C* values for each fitted relationship as a function of R_a in the direction of pullout. The *A* parameter increases with R_a and appears to saturate at high values. The *C* parameter increases linearly with R_a; however, given that *C* acts exponentially in Equation 1 it is likely that it also saturates at larger R_a values where further

increases in R_a should lead to no further changes in the spacing of the contours. While these results should be supplemented with further data for surfaces with a broader range of R_a values, the results presented in Figures 4.18a and 18b show that the slope of the contours in normalized load space decreases and the distance between the contour increases as the R_a of the pile surface is increased.

The results presented have shown that the orientation of the snakeskin-inspired asperities has an important effect on the pile stability. Implications of the stability diagrams in terms of absolute loads can be discussed in terms of efficiency per unit length or in terms of stability at a given demand load. Figure 4.17a provides a comparison of material efficiency, where each pile was installed to the same depth. The DI-RP 0.30 and 0.72 piles provide a higher absolute limit between the *MS* and *U* zones compared to the RI-DP 0.30 pile, showing that for a given pile length, the cranially pulled piles provides a higher upper limit of cyclic stability. In contrast, the stability diagrams in terms of normalized loads provide a comparison of stability if the piles were designed to a specific Q_m and Q_{cyc} load combination in relation to their respective Q_{tot} values (Figure 4.17b). In this case, the RI-DP 0.30 provides the highest upper limit on the *MS* zone but would require a greater embedment depth to have the same Q_{tot} as the DI-RP 0.30 or 0.72 piles. In both scenarios, the RI-DP 0.30 piles suffers from the drawback of having brittle failure response, resulting in a narrow *MS* zone.

CONCLUSIONS

A series of centrifuge pile load tests were conducted to assess the effect of the snakeskin-inspired texture on the load transfer, accumulation of deformations, evolution of global and shaft stiffness, and cyclic stability of piles subjected to cyclic and monotonic load. Experiments were performed on a cranially-installed, caudally pulled pile (i.e., RI-DP 0.30), two caudally-installed, cranially

113

pulled piles with different asperity height (i.e., DI-RP 0.30 and DI-RP 0.72), a reference rough pile, and a reference smooth pile. The cyclic load-controlled tests were performed to evaluate the behavior of the piles in the two-way loading where stress reversal take place.

The cranially-pulled pile with the largest asperities mobilized the highest resistance during monotonic pullout loading, followed by the rough pile and DI-RP 0.30 pile. The caudally-pulled and smooth piles exhibited the lowest resistance, but exhibited a stiffer response compared to the cranially-pulled and rough piles. This trend reflects the local load transfer mechanisms, where smoother surfaces result in more slippage at the soil-structure interface which is characterized by smaller interface friction angles and dilation but greater initial stiffness.

For any combination of normalized loads (i.e., Q_m/Q_{tot} and Q_{cyc}/Q_{tot}), the cranially-pulled piles failed in a smaller number of cycles in comparison with the caudally-pulled piles. The cranially-pulled piles exhibited a greater cyclic degradation of local and global shaft resistances, indicating a progressive failure propagating from greater depths towards the pile head. This led to a greater proportion of the total load being carried by the base of the cranially-pulled piles during the compression part of any given cycle, which resulted in greater displacements in compression that are evident in the head load – displacement loops.

The evolution of the global unloading pile stiffness did not correlate with the type of pile texture. However, the evolution of global pile stiffness shows a dependency on the combination of applied loads, characterized by the ratio of the mean to cyclic load (i.e., Q_m/Q_{cyc}), where the unloading stiffness tends to increase with number of cycles as the tensile load bias on the pile decreases. The caudally-pulled pile was shown to have a more brittle failure than the cranially-pulled piles. This was quantified by means of the ratio of the yield cycle to failure cycle ratio (N_y/N_f) which takes an average value of 0.93 for the RI-DP 0.30 pile, in contrast with the average

for the DI-RP 0.30 and DI-RP 0.72 piles which are smaller than or equal to 0.53. The yield cycle was defined as the cycle at which the shaft unloading stiffness – cyclic double amplitude displacement deviated from a log-linear relationship.

The cyclic stability of the snakeskin-inspired piles was evaluated based on the interaction diagrams used in the design of offshore piles. In terms of absolute magnitudes, the cranially-pulled piles had a wider zone of *metastable* conditions in terms of both cyclic and mean load, while the caudally-pulled pile exhibited *stable* conditions at a greater range of cyclic loads when the mean load was lower than a threshold of about 0.55 MN. These differences reflect the slower accumulation of deformations but more brittle failure behavior of the caudally-pulled pile. In terms of loads normalized by each pile's corresponding ultimate tensile capacity, the caudally-pulled pile has the greatest limit between *stable* and *metastable* and between *metastable* and *unstable* responses.

REFERENCES

Afzali-Nejad, A., Lashkari, A., and Martinez, A. (2021). Stress-Displacement Response of Sand–Geosynthetic Interfaces under Different Volume Change Boundary Conditions. *Journal of Geotechnical and Geoenvironmental Engineering*, *147*(8), 04021062. https://doi.org/10.1061/(ASCE)GT.1943-5606.0002544

Aghakouchak, A., Sim, W. W., and Jardine, R. J. (2015). Stress-path laboratory tests to characterise the cyclic behaviour of piles driven in sands. *Soils and Foundations*, *55*(5), 917–928. https://doi.org/10.1016/j.sandf.2015.08.001

Atkins Consultants Ltd., (2000). Cyclic degradation of offshore piles. HSE Offshore Technology Report OTO 2000 013. Health and Safety. Executive, London.

Blanc, M., and Thorel, L. (2016). Effects of cyclic axial loading sequences on piles in sand. *Géotechnique Letters*, *6*(2), 163–167. https://doi.org/10.1680/jgele.15.00155

Blanc, M., Thorel, L., Isorna, R., Dano, C., Kotronis, P., and Philippe, M. (2015). Centrifuge investigation of the axial cyclic behaviour of a single pile used for the foundation of a jacket type offshore wind turbine. In V. Meyer (Ed.), *Frontiers in Offshore Geotechnics III* (pp. 521–526). CRC Press. https://doi.org/10.1201/b18442-65

Boulon, M., and Foray, P. (1986). "Physical and numerical simulation of lateral shaft friction along offshore piles in sand." *Proc., 3rd Int. Conf. on Num. Methods in Offshore Piling*, Editions Techrig, Paris, France, 127-148.

Carey, T. J., Stone, N., and Kutter, B. L. (2020). Grain Size Analysis and Maximum and Minimum Dry Density Testing of Ottawa F-65 Sand for LEAP-UCD-2017. In B. L. Kutter, M. T. Manzari, and M. Zeghal (Eds.), *Model Tests and Numerical Simulations of Liquefaction*

and Lateral Spreading (pp. 31–44). Springer International Publishing. https://doi.org/10.1007/978-3-030-22818-7_2

De Nicola, A., and Randolph, M. F. (1993). Tensile and Compressive Shaft Capacity of Piles in Sand. *Journal of Geotechnical Engineering*, *119*(12), 1952–1973. https://doi.org/10.1061/(ASCE)0733-9410(1993)119:12(1952)

DeJong, J. T., and Westgate, Z. J. (2009). Role of Initial State, Material Properties, and Confinement Condition on Local and Global Soil-Structure Interface Behavior. *Journal of Geotechnical and Geoenvironmental Engineering*, *135*(11), 1646–1660. https://doi.org/10.1061/(ASCE)1090-0241(2009)135:11(1646)

Di Donna, A., Ferrari, A., and Laloui, L. (2016). Experimental investigations of the soil–concrete interface: Physical mechanisms, cyclic mobilization, and behaviour at different temperatures. *Canadian Geotechnical Journal*, *53*(4), 659–672. https://doi.org/10.1139/cgj-2015-0294

Dietz, M., and Lings, M. (2010). "Changes in surface roughness in multi-reverse sand-steel interface tests." *Proc., Research Symp. on Characterization and Behavior of Interfaces*., 7–15.

Dove, J. E., and Frost, J. D. (1996). A Method for Measuring Geomembrane Surface Roughness. *Geosynthetics International*, *3*(3), 369–392. https://doi.org/10.1680/gein.3.0067

Fioravante V., Ghionna V.N., Pedroni S., and Porcino D. (1999). A constant normal stiffness direct shear box for soil-solid interface tests. *Rivista Italiana di Geotecnica*, 33(3): 7–22.

Fioravante, V. (2002). On the Shaft Friction Modelling of Non-Displacement Piles in Sand. *Soils and Foundations*, *42*(2), 23–33. https://doi.org/10.3208/sandf.42.2_23

Garnier, J., Gaudin, C., Springman, S. M., Culligan, P. J., Goodings, D., Konig, D., Kutter, B., Phillips, R., Randolph, M. F., and Thorel, L. (2007). Catalogue of scaling laws and similitude questions in geotechnical centrifuge modelling. *International Journal of Physical Modelling in Geotechnics*, *7*(3), 01–23. https://doi.org/10.1680/ijpmg.2007.070301

Gray, J. and Lissmann H. W. (1950). "The kinetics of locomotion of the grass-snake." *Journal of Experimental Biology* 26.4: 354-367.

Ho, T. Y. K., Jardine, R. J., and Anh-Minh, N. (2011). Large-displacement interface shear between steel and granular media. *Géotechnique*, *61*(3), 221–234. https://doi.org/10.1680/geot.8.P.086

Hryciw, R. D., and Irsyam, M. (1993). Behavior of Sand Particles Around Rigid Ribbed Inclusions During Shear. *Soils and Foundations*, *33*(3), 1–13. https://doi.org/10.3208/sandf1972.33.3_1

Jardine R. J. and Chow F.C., "New Design Methods for Offshore Piles", Marine Technology Directorate, 1996. London.

Jardine R. J., Everton S.J., Lehane B.M.. (1992). Friction Coefficients For Piles In Cohesionless Materials, Dordrecht, SUT Int. Conf, Publisher: Kluwer, Pages: 661-680

Jardine, R. J. (2020). Geotechnics, energy and climate change: The 56th Rankine Lecture. *Géotechnique*, *70*(1), 3–59. https://doi.org/10.1680/jgeot.18.RL.001

Jardine, R. J., and Standing J. R. (2000). "Pile load testing performed for HSE cyclic loading study at Dunkirk, France. V. 1."

Jardine, R. J., Zhu, B. T., Foray, P., and Yang, Z. X. (2013). Measurement of stresses around closed-ended displacement piles in sand. *Géotechnique*, *63*(1), 1–17. https://doi.org/10.1680/geot.9.P.137

Jardine, R. J.,, Chow, F.C. , Overy, R., and Standing, J. (2005). *ICP design methods for driven piles in sands and clays* (Vol. 112). London: Thomas Telford.

Jardine, R., Puech, A., and Andersen, K. H. (2012). *Keynote Address: Cyclic Loading of Offshore Piles: Potential Effects And Practical Design*. SUT-OSIG-12-06.

Kulić, I. M., Mani, M., Mohrbach, H., Thaokar, R., and Mahadevan, L. (2009). Botanical ratchets. *Proceedings of the Royal Society B: Biological Sciences*, *276*(1665), 2243–2247. https://doi.org/10.1098/rspb.2008.1685

Lehane, B. M., Jardine, R. J., Bond, A. J., and Frank, R. (1993). Mechanisms of Shaft Friction in Sand from Instrumented Pile Tests. *Journal of Geotechnical Engineering*, *119*(1), 19–35. https://doi.org/10.1061/(ASCE)0733-9410(1993)119:1(19)

Martinez, A., and Frost, J. D. (2017). The influence of surface roughness form on the strength of sand–structure interfaces. *Géotechnique Letters*, *7*(1), 104–111. https://doi.org/10.1680/jgele.16.00169

Martinez, A., and O'Hara, K. B. (2021). "Skin friction directionality in monotonically- and cyclically-loaded bio-inspired piles in sand." *Deep Found. Inst. J.,* 15(1).

Martinez, A., DeJong, J., Akin, I., Aleali, A., Arson, C., Atkinson, J., Bandini, P., Baser, T., Borela, R., Boulanger, R., Burrall, M., Chen, Y., Collins, C., Cortes, D., Dai, S., DeJong, T., Del Dottore, E., Dorgan, K., Fragaszy, R., Frost, D., Full, R., Ghayoomi, M., Goldman, D., Gravish, N., Guzman, I.L., Hambleton, J., Hawkes, E., Helms, M., Hu, D.L., Huang, L., Huang, S., Hunt, C., Irschick, D., Lin, H., Lingwall, B., Marr, W.A., Mazzolai, B.,

McInroe, B., Murthy, T., O'Hara, K., Porter, M., Sadek, S., Sanchez, M., Santamarina, C., Shao, L., Sharp, J., Stuart, H., Stutz, H.H., Summers, A.P., Tao, J., Tolley, M., Treers, L., Turnbull, K., Valdes, R., van Paassen, L., Viggiani, G., Wilson, D., Wu, W., Yu, X. and Zheng, J. (2022). "Bio-inspired geotechnical engineering: principles, current work, opportunities and challenges". Geotechnique., Vol. 72, No. 8. https://doi.org/10.1680/jgeot.20.P.170

Martinez, A., Palumbo, S., and Todd, B.D. (2019). "Bio-Inspiration for anisotropic load transfer at soil-structure interfaces." *J. Geotech. and Geoenviron.*, 145(10).

Marvi, H., and Hu, D. L. (2012). Friction enhancement in concertina locomotion of snakes. *Journal of The Royal Society Interface*, *9*(76), 3067–3080. https://doi.org/10.1098/rsif.2012.0132

Merritt, A. S., Schroeder, F. C., Jardine, R. J., Stuyts, B., Cathie, D., and Cleverly, W. (2012). *Development of Pile Design Methodology For an Offshore Wind Farm In the North Sea*. SUT-OSIG-12-47.

O'Hara, K. B., and Martinez, A. (2020). Monotonic and Cyclic Frictional Resistance Directionality in Snakeskin-Inspired Surfaces and Piles. *Journal of Geotechnical and Geoenvironmental Engineering*, *146*(11), 04020116. https://doi.org/10.1061/(ASCE)GT.1943-5606.0002368

O'Hara, K. B., and Martinez, A. (2022). Load Transfer Directionality of Snakeskin-Inspired Piles during Installation and Pullout in Sands. *Journal of Geotechnical and Geoenvironmental Engineering*, *148*(12), 04022110. https://doi.org/10.1061/(ASCE)GT.1943-5606.0002929

Palmeria, E. M., and Milligan, G. W. E. (1989). Scale and other factors affecting the results of pull-out tests of grids buried in sand. *Géotechnique*, *39*(3), 511–542. https://doi.org/10.1680/geot.1989.39.3.511

Palumbo, S. (2018). *Anisotropic interface shear behavior of granular soil and surfaces biologically-inspired by snakeskin*. University of California, Davis.

Pincus, H., Tabucanon, J., Airey, D., and Poulos, H. (1995). Pile Skin Friction in Sands from Constant Normal Stiffness Tests. *Geotechnical Testing Journal*, *18*(3), 350. https://doi.org/10.1520/GTJ11004J

Poulos, H. G. (1988). Cyclic Stability Diagram for Axially Loaded Piles. *Journal of Geotechnical Engineering*, *114*(8), 877–895. https://doi.org/10.1061/(ASCE)0733-9410(1988)114:8(877)

Rimoy, S. P., Jardine, R. J., and Standing, J. R. (2013). Displacement response to axial cycling of piles driven in sand. *Proceedings of the Institution of Civil Engineers - Geotechnical Engineering*, *166*(2), 131–146. https://doi.org/10.1680/geng.12.00052

Rimoy, S., Silva, M., Jardine, R., Yang, Z. X., Zhu, B. T., and Tsuha, C. H. C. (2015). Field and model investigations into the influence of age on axial capacity of displacement piles in silica sands. *Géotechnique*, *65*(7), 576–589. https://doi.org/10.1680/geot.14.P.112

Rui, S., Wang, L., Guo, Z., Cheng, X., and Wu, B. (2021). Monotonic behavior of interface shear between carbonate sands and steel. *Acta Geotechnica*, *16*(1), 167–187. https://doi.org/10.1007/s11440-020-00987-9

Samanta, M., Punetha, P., and Sharma, M. (2018). Influence of surface texture on sand–steel interface strength response. *Géotechnique Letters*, *8*(1), 40–48. https://doi.org/10.1680/jgele.17.00135

Schlosser, F., and Guilloux, A. (1981). Le frottement dans le renforcement des sols. *Revue Française de Géotechnique*, *16*, 65–77. https://doi.org/10.1051/geotech/1981016065

Schmoldt, A., Benthe, H. F., and Haberland, G. (1975). Digitoxin metabolism by rat liver microsomes. *Biochemical Pharmacology*, *24*(17), 1639–1641.

Sturm, A.P. (2019). *On the liquefaction potential of gravelly soils: Characterization, triggering and performance*. University of California, Davis.

Stutz, H. H., and Martinez, A. (2021). Directionally dependent strength and dilatancy behavior of soil–structure interfaces. *Acta Geotechnica*, *16*(9), 2805–2820. https://doi.org/10.1007/s11440-021-01199-5

Tramsen, H. T., Gorb, S. N., Zhang, H., Manoonpong, P., Dai, Z., and Heepe, L. (2018). Inversion of friction anisotropy in a bio-inspired asymmetrically structured surface. *Journal of The Royal Society Interface*, *15*(138), 20170629. https://doi.org/10.1098/rsif.2017.0629

Tsuha, C. H. C., Foray, P. Y., Jardine, R. J., Yang, Z. X., Silva, M., and Rimoy, S. (2012). Behaviour of displacement piles in sand under cyclic axial loading. *Soils and Foundations*, *52*(3), 393–410. https://doi.org/10.1016/j.sandf.2012.05.002

Uesugi, M., and Kishida, H. (1986). Influential Factors of Friction Between Steel and Dry Sands. *Soils and Foundations*, *26*(2), 33–46. https://doi.org/10.3208/sandf1972.26.2_33

White, D. J., and Lehane, B. M. (2004). Friction fatigue on displacement piles in sand. *Géotechnique*, *54*(10), 645–658. https://doi.org/10.1680/geot.2004.54.10.645

Yang, Z. X., Jardine, R. J., Zhu, B. T., Foray, P., and Tsuha, C. H. C. (2010). Sand grain crushing and interface shearing during displacement pile installation in sand. *Géotechnique*, *60*(6), 469–482. https://doi.org/10.1680/geot.2010.60.6.469

Zheng, B. L., Kutter, B. L., Wilson, D. W., Allmond, J., Hunt, C., and McNeilan, T. (2019). Centrifuge Modeling of Cyclic Degradation of Axially Loaded Piles in Sand for Offshore

Wind Turbine Structures. *International Journal of Offshore and Polar Engineering*, *29*(2), 172–181. https://doi.org/10.17736/ijope.2019.tm86

Zhou, W., Guo, Z., Wang, L., Li, J., and Rui, S. (2020). Sand-steel interface behaviour under large-displacement and cyclic shear. *Soil Dynamics and Earthquake Engineering*, *138*, 106352. https://doi.org/10.1016/j.soildyn.2020.106352

Table 4.1. Roughness parameters for pile shaft sections

Pile Name / Roughness parameters		Rough pile	RI-DP 0.30	DI-RP 0.30	DI-RP 0.72	Smooth pile
Intra-asperity	R_a (µm)	40.057	0.531	0.582	0.508	0.452
	R_z (µm)	338.510	3.033	3.268	2.788	2.604
Inter-asperity	R_a (µm)	-	84.640	88.261	193.906	-
	R_z (µm)	-	306.370	318.201	720.447	-
	L/H	1	40	40	17	>100

Table 4.2. Summary of cyclic tests conducted in models KBO01 and KBO02, with test location and designation corresponding to Figure 4.1c.

Model	Test location	Test type	Pile type	Q_{tot} (MN)	Q_m/Q_{tot}*	Q_{cyc}/Q_{tot}	N_f	Stability
KBO01	P3	Monotonic	Smooth	0.74	-	-	-	-
KBO01	P4	Monotonic	Rough	1.27	-	-	-	-
KBO01	P1	Monotonic	DI-RP 0.72	1.50	-	-	-	-
KBO01	P2	Monotonic	RI-DP 0.30	0.95	-	-	-	-
KBO01	P16	Monotonic	DI-RP 0.30	1.12	-	-	-	-
KBO02	P3	Cyclic	Rough	**	0.14	0.57	26	U
KBO02	P4	Cyclic	Rough	**	0.07	0.06	>1000	S
KBO02	P1	Cyclic	DI-RP 0.72	**	-0.02	0.43	76	U
KBO02	P2	Cyclic	DI-RP 0.72	**	0.20	0.60	2	U
KBO02	P16	Cyclic	DI-RP 0.72	**	0.07	0.24	879	MS
KBO02	P5	Cyclic	DI-RP 0.30	**	0.00	0.69	10	U
KBO02	P6	Cyclic	DI-RP 0.30	**	0.21	0.68	6	U
KBO02	P7	Cyclic	DI-RP 0.30	**	-0.01	0.50	214	MS
KBO02	P8	Cyclic	DI-RP 0.30	**	0.22	0.49	47	U
KBO02	P9	Cyclic	DI-RP 0.30	**	0.43	0.49	19	U
KBO02	P10	Cyclic	DI-RP 0.30	**	0.21	0.29	>1000	S
KBO02	P11	Cyclic	RI-DP 0.30	**	-0.02	0.47	1109	S
KBO02	P12	Cyclic	RI-DP 0.30	**	-0.02	0.65	73	U
KBO02	P13	Cyclic	RI-DP 0.30	**	0.18	0.31	>1000	S
KBO02	P14	Cyclic	RI-DP 0.30	**	0.17	0.62	13	U
KBO02	P15	Cyclic	RI-DP 0.30	**	0.37	0.46	29	U

*Positive values indicate tension. **Assumed equal to the measured Q_{tot} value on the same pile type in model KBO01.
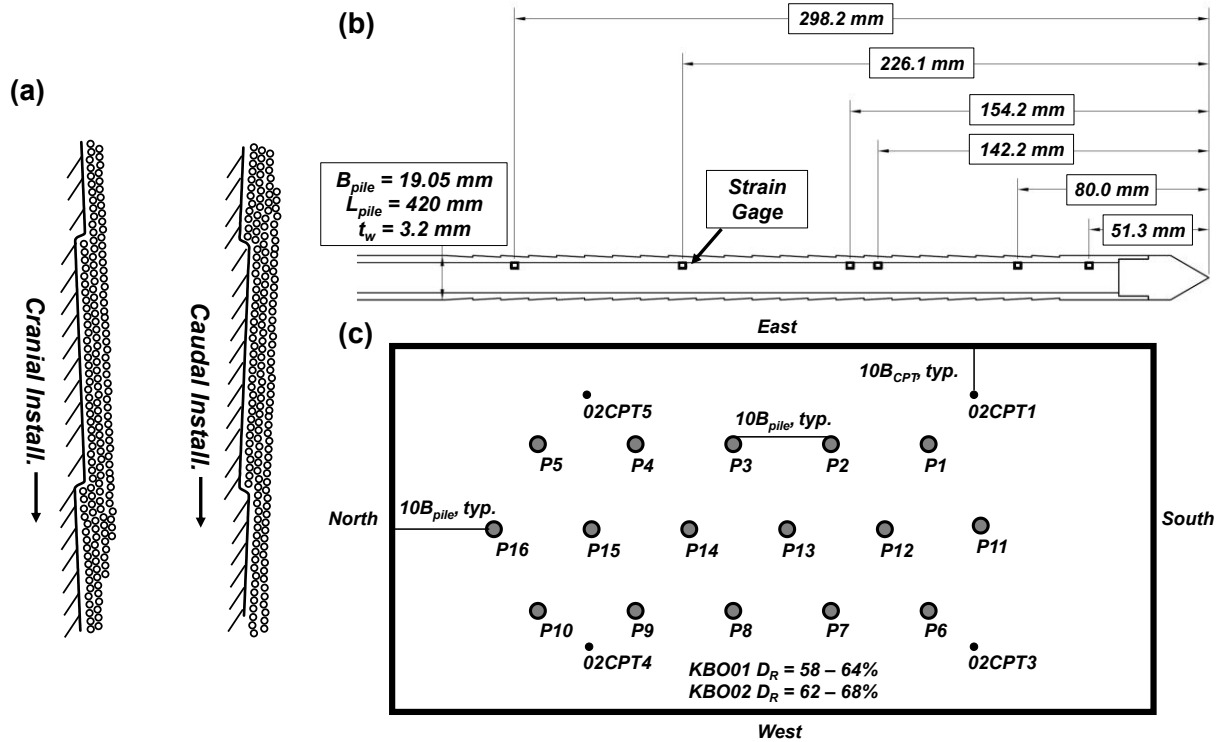
Figure 4.1. (a) schematic of cranial and caudal installation directionality (b) Pile gauge configuration for all shaft types, (c) Model plan view and test locations for KBO01 and 02,
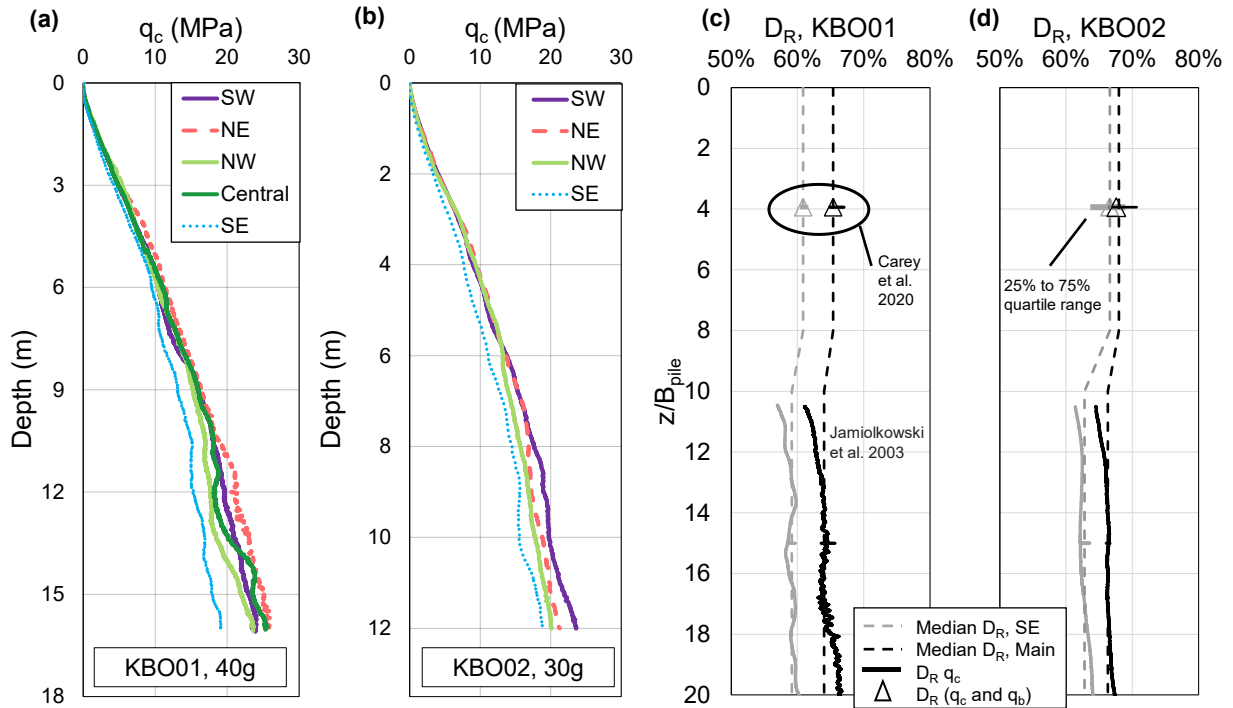
Figure 4.2. q_c values from CPT soundings in (a) KBO01 and (b) KBO02, with analyzed D_R profiles for (c) KBO01 and (d) KBO02
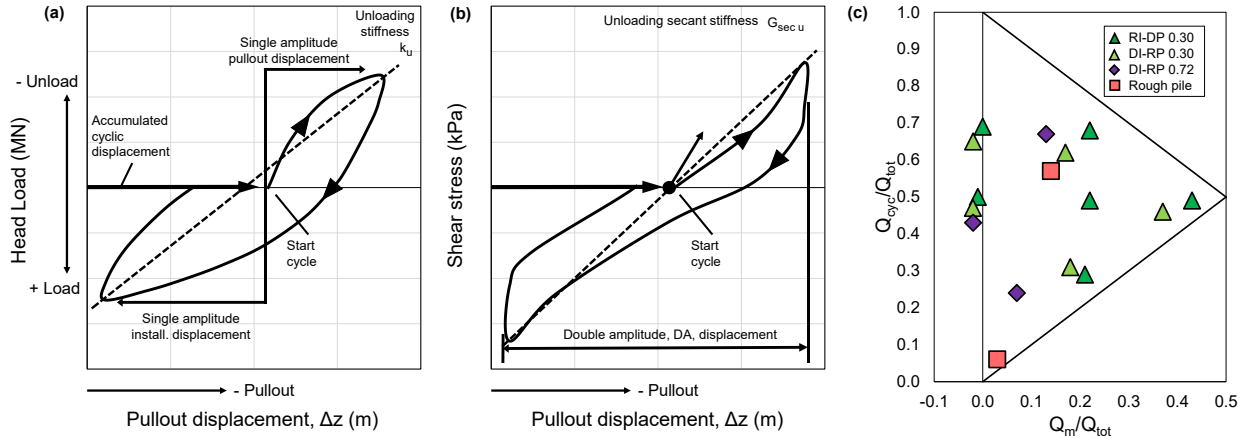
Figure 4.3. (a) and (b) Definitions of parameters used to describe cyclic test results and (c) load combinations applied during cyclic tests.
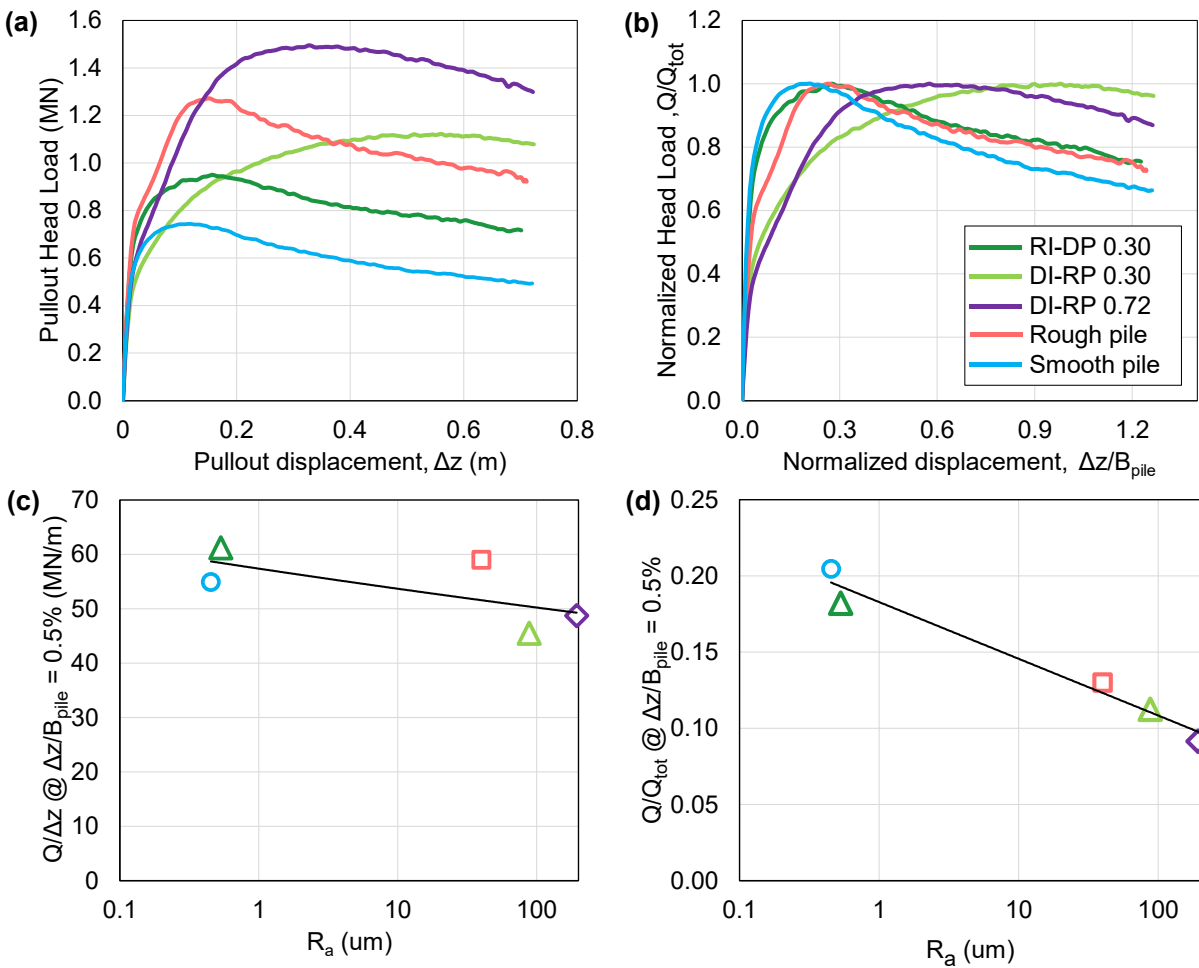
Figure 4.4. Results of monotonic pullout tests: (a) head load with displacement, (b) normalized head load with normalized displacement, and (c) secant stiffness and (d) at Q/Q_{tot} at a displacement equivalent to 0.5% of the pile diameter.
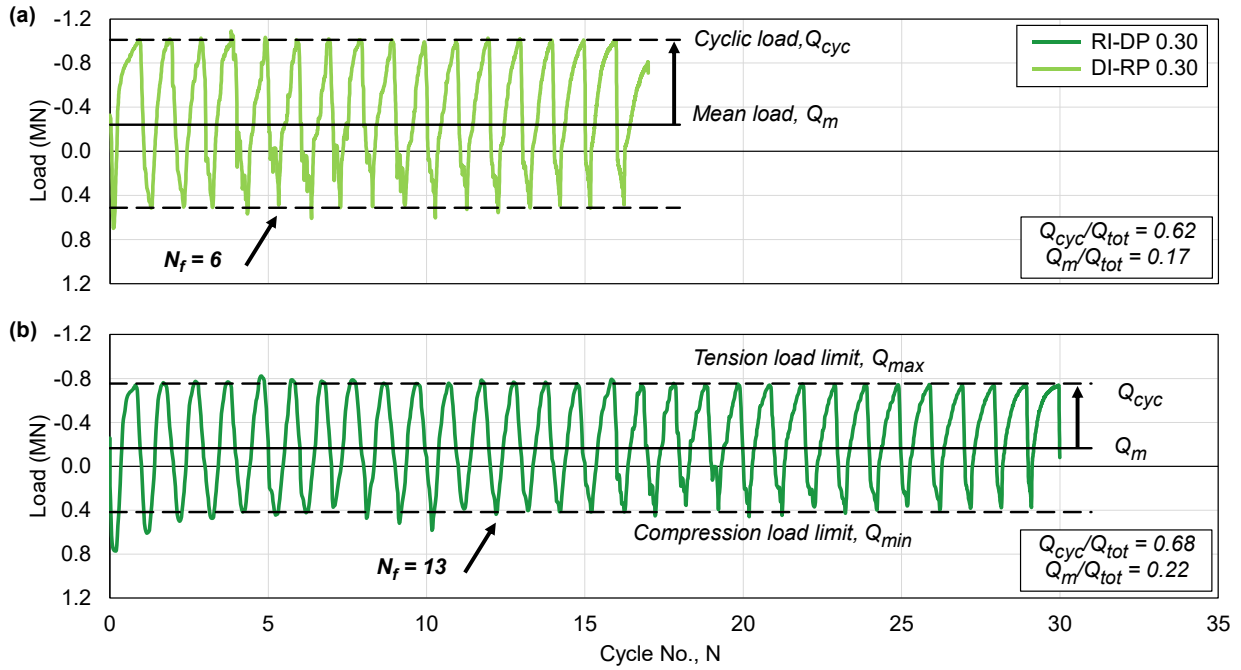
Figure 4.5. Load – cycle number history for (a) DI-RP 0.30 pile and (b) RI-DP 0.30 pile.
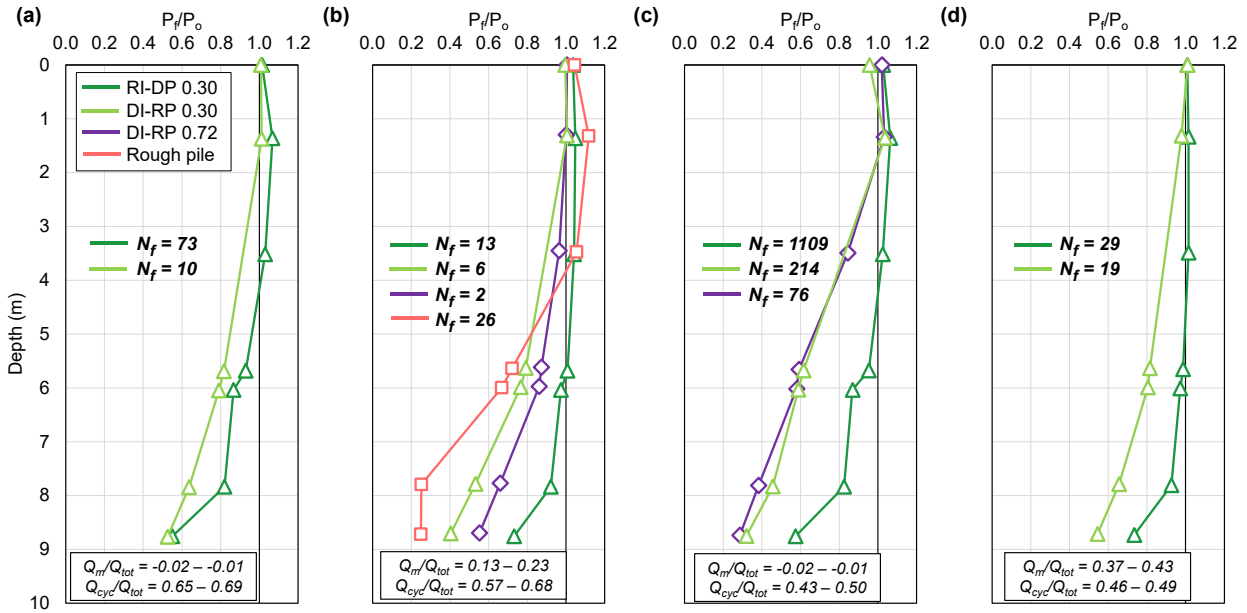
Figure 4.6. Proportional axial load carried by shaft sections with depth where P_o corresponds to loads at $N = 1$, and P_f corresponds to loads at N_f, noted in each figure for (a) $Q_m/Q_{tot} = -0.02$ to -0.01 and $Q_{cyc}/Q_{tot} = 0.65$ to 0.69, (b) $Q_m/Q_{tot} = 0.13$ to 0.23 and $Q_{cyc}/Q_{tot} = 0.57$ to 0.68 (c) $Q_m/Q_{tot} = -0.02$ to -0.01 and $Q_{cyc}/Q_{tot} = 0.43$ to 0.50 and (d) $Q_m/Q_{tot} = 0.37$ to 0.43 and $Q_{cyc}/Q_{tot} = 0.46$ to 0.49.
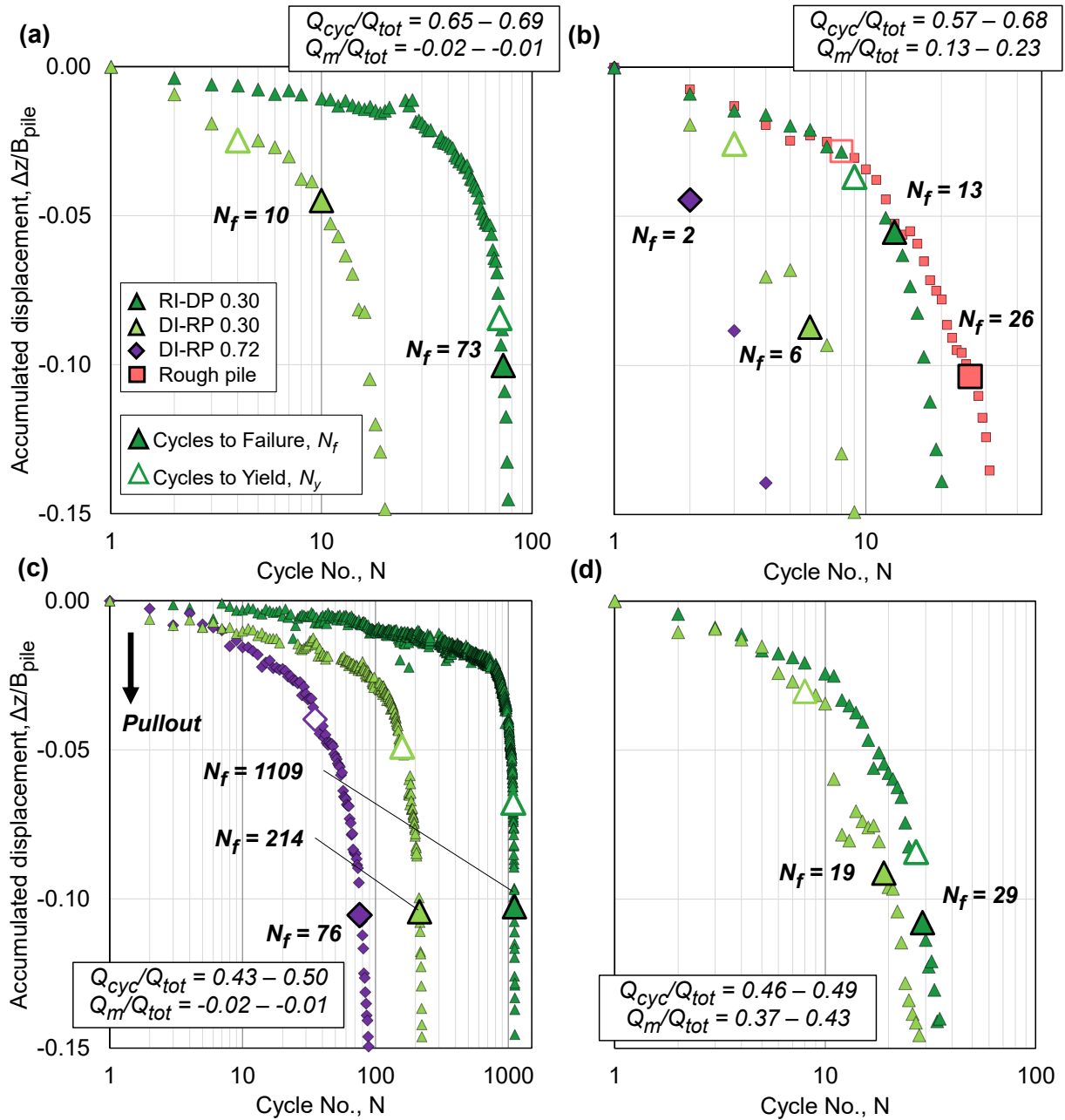
Figure 4.7. Accumulated axial displacement response for all U and MS tests with (a) Q_m/Q_{tot} = -0.02 to -0.01 and Q_{cyc}/Q_{tot} = 0.65 to 0.69, (b) Q_m/Q_{tot} = 0.13 to 0.23 and Q_{cyc}/Q_{tot} = 0.57 to 0.68 (c) Q_m/Q_{tot} = -0.02 to -0.01 and Q_{cyc}/Q_{tot} = 0.43 to 0.50 and (d) Q_m/Q_{tot} = 0.37 to 0.43 and Q_{cyc}/Q_{tot} = 0.46 to 0.49. The large open symbols denote number of cycles to yield while the large closed symbols denote number of cycles to failure
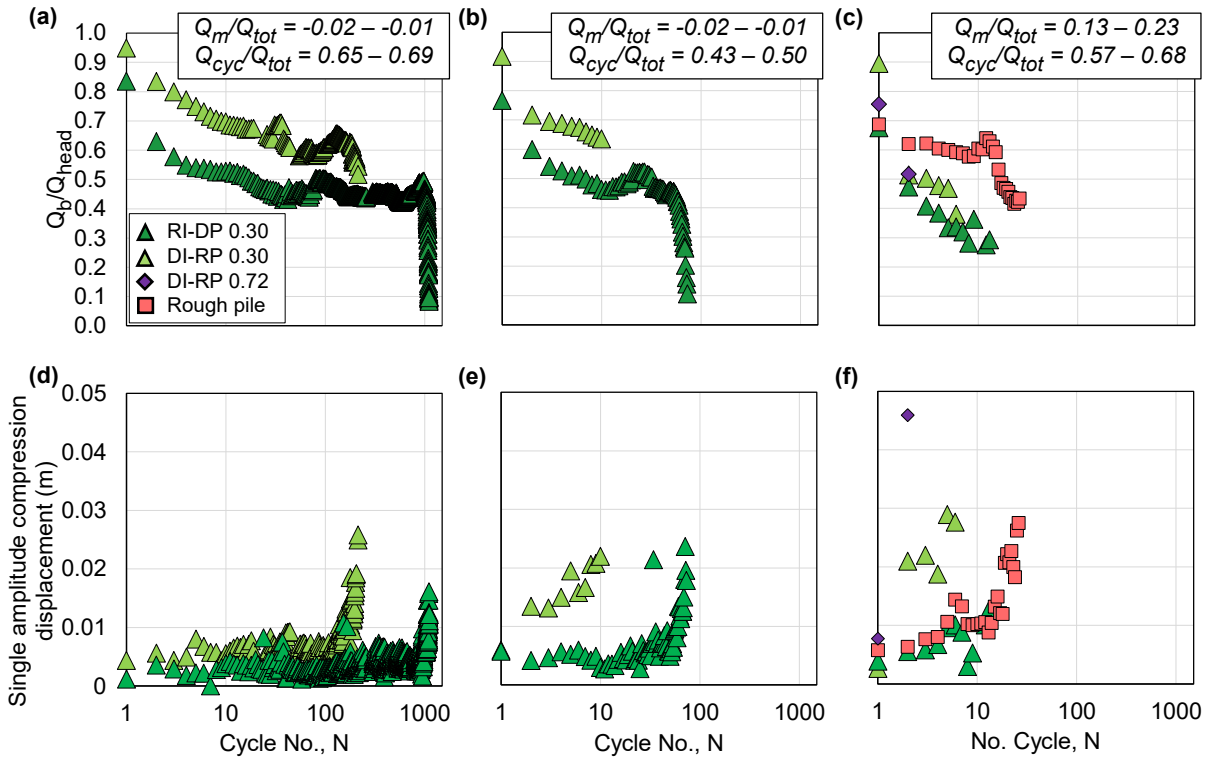
Figure 4.8. Cycle number response for (a) – (c) base load ratio for specified loading combinations, (d) – (f) single amplitude displacement in compressive loading direction
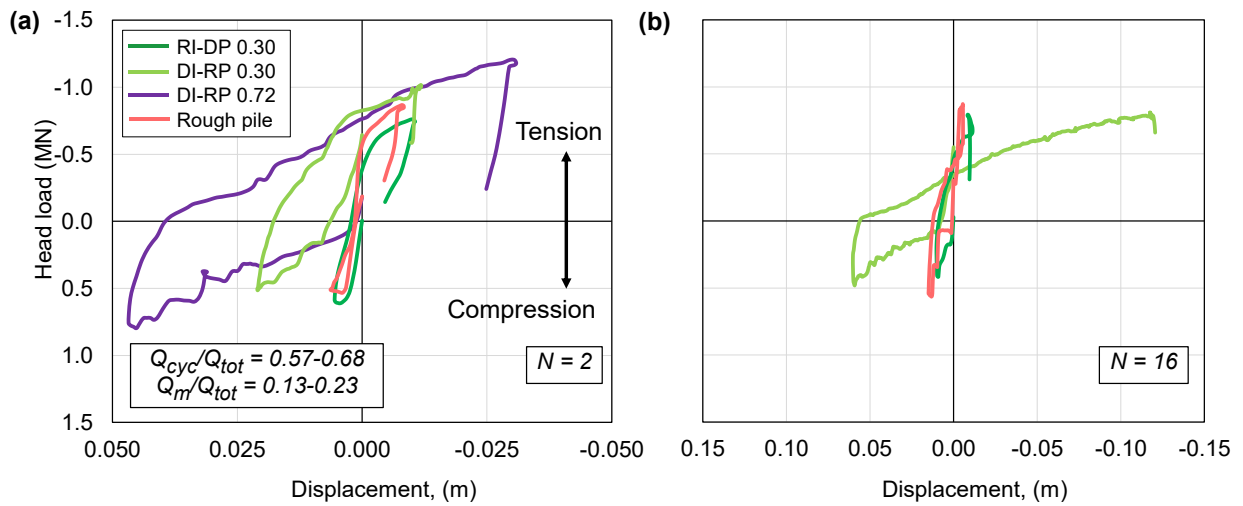
Figure 4.9. (a) Load – displacement response at N = 2, (b) Load – displacement response at N = 16 for a load combination of $Q_{cyc}/Q_{tot} = 0.57 – 0.68$ and $Q_m/Q_{tot} = 0.13 – 0.23$.
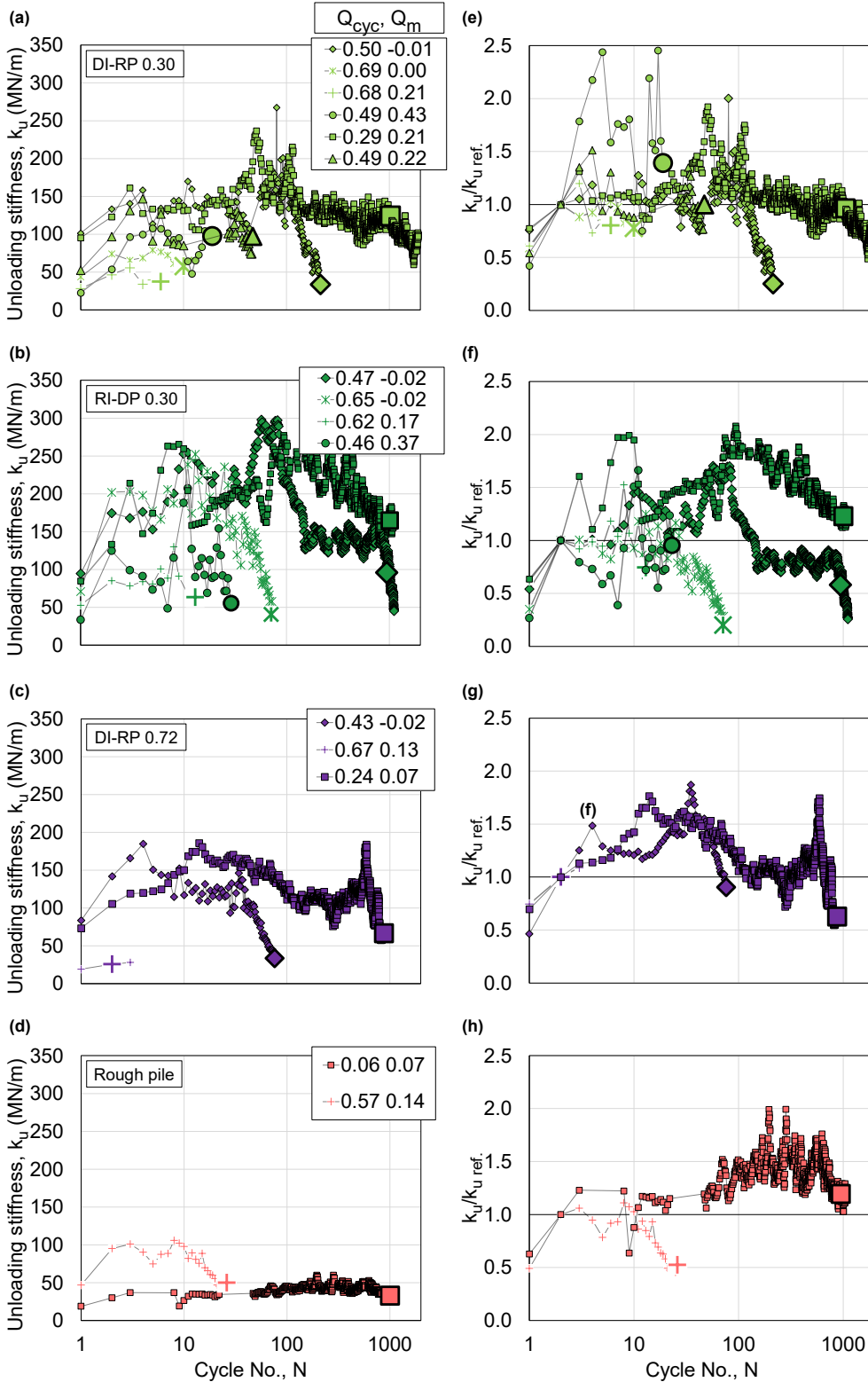
Figure 4.10. Unloading stiffness evolution for (a) DI-RP 0.30 (b) RI-DP 0.30 (c) DI-RP 0.72 (d) rough piles, and normalized unloading stiffness response for (e) DI-RP 0.30 (f) RI-DP 0.30 (g) DI-RP 0.72 (h) rough piles. Note: highlighted symbols mark N_f for U and MS conditions, and N_f taken as 1000 for S conditions
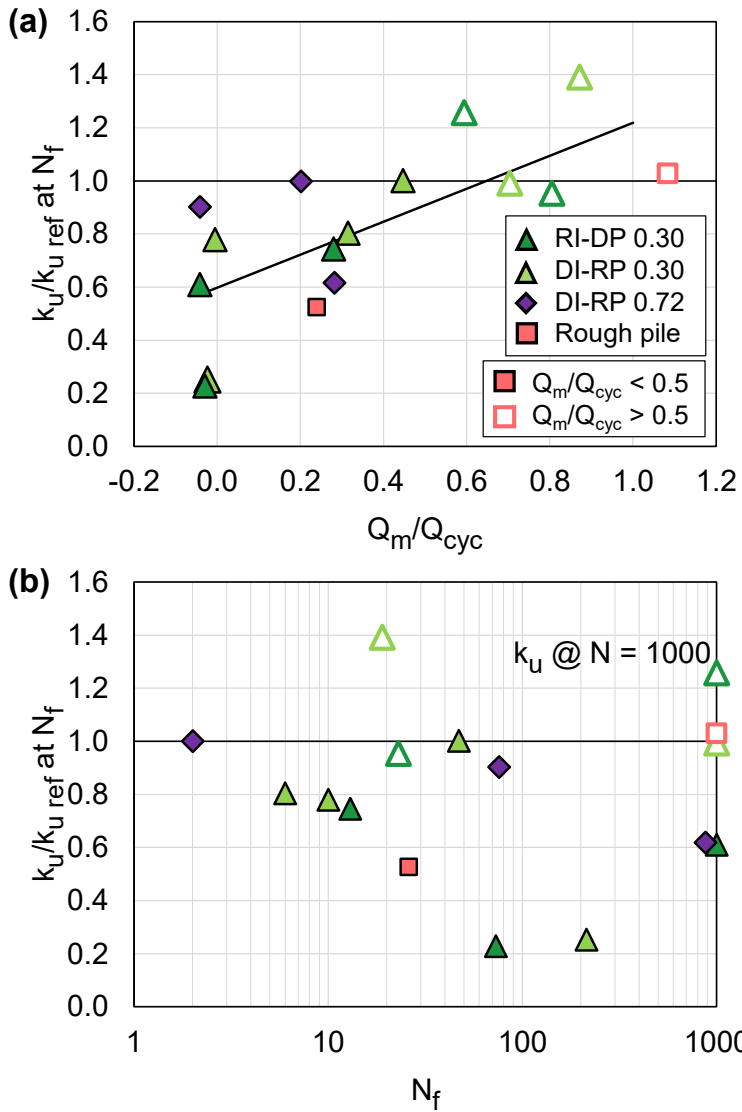
Figure 4.11. Stiffness ratio at the failure cycle as a function of (a) Q_m/Q_{cyc} and (b) cycles to failure.
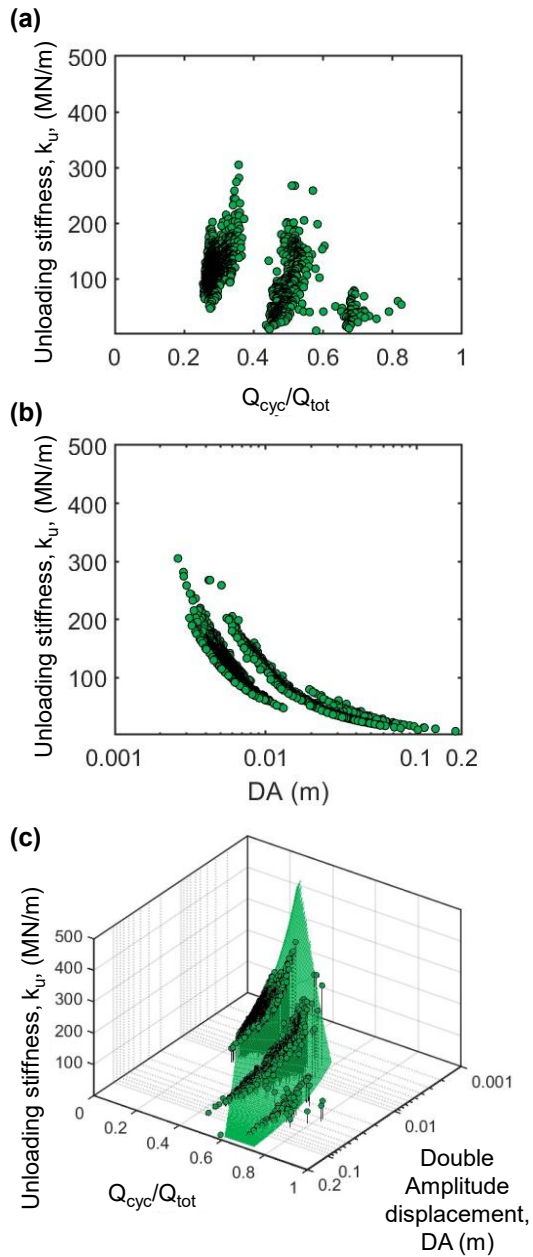
Figure 4.12. Unloading stiffness as function of (a) achieved Q_{cyc}/Q_{tot} (b) *DA* displacement (c) fitted surface for all cycles for the RI-DP 0.30 pile.
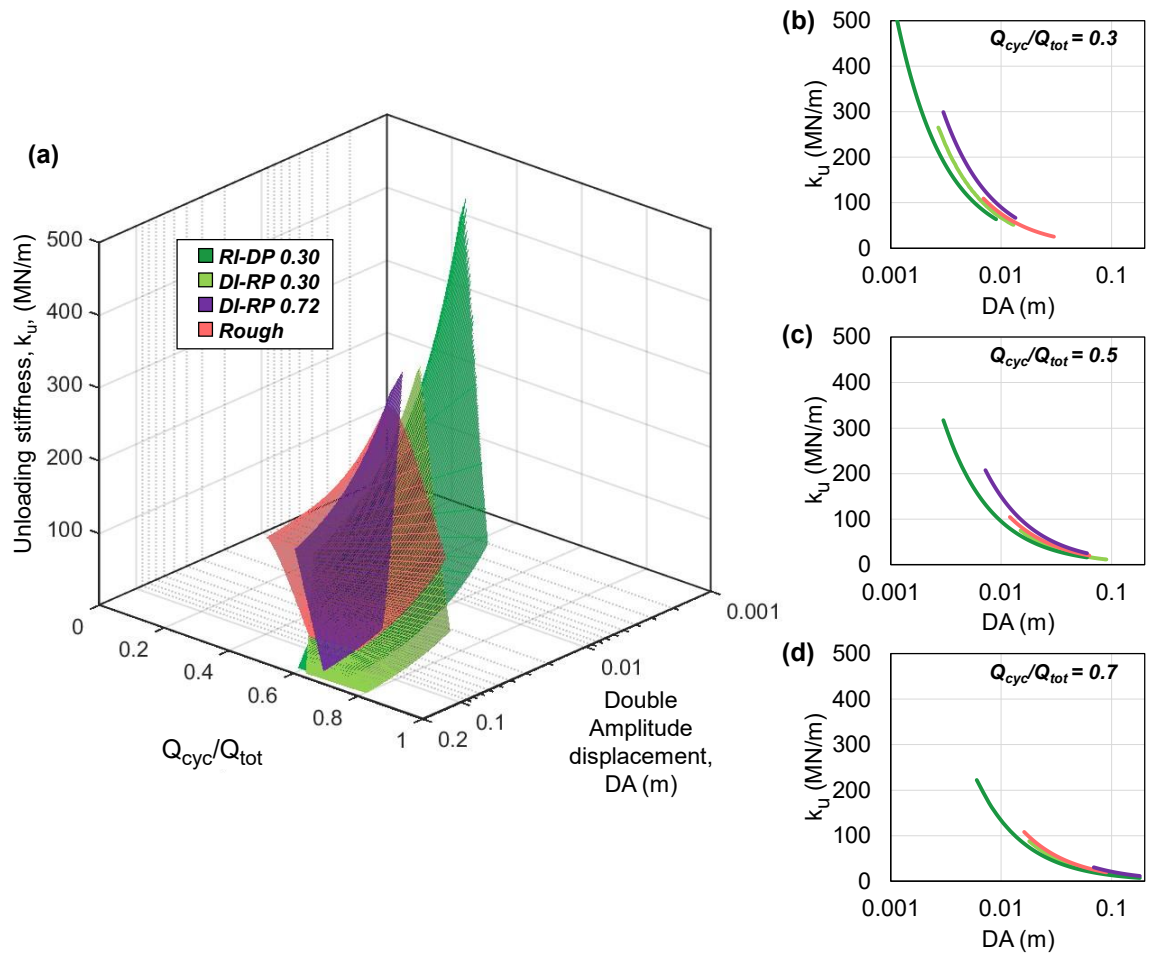
Figure 4.13. (a) Fitted k_u, Q_{cyc}/Q_{tot}, and DA displacement surfaces for all pile types tested in cyclic loading, with slices taken at Q_{cyc}/Q_{tot} of (b) 0.3 (c) 0.5 (d) 0.7.
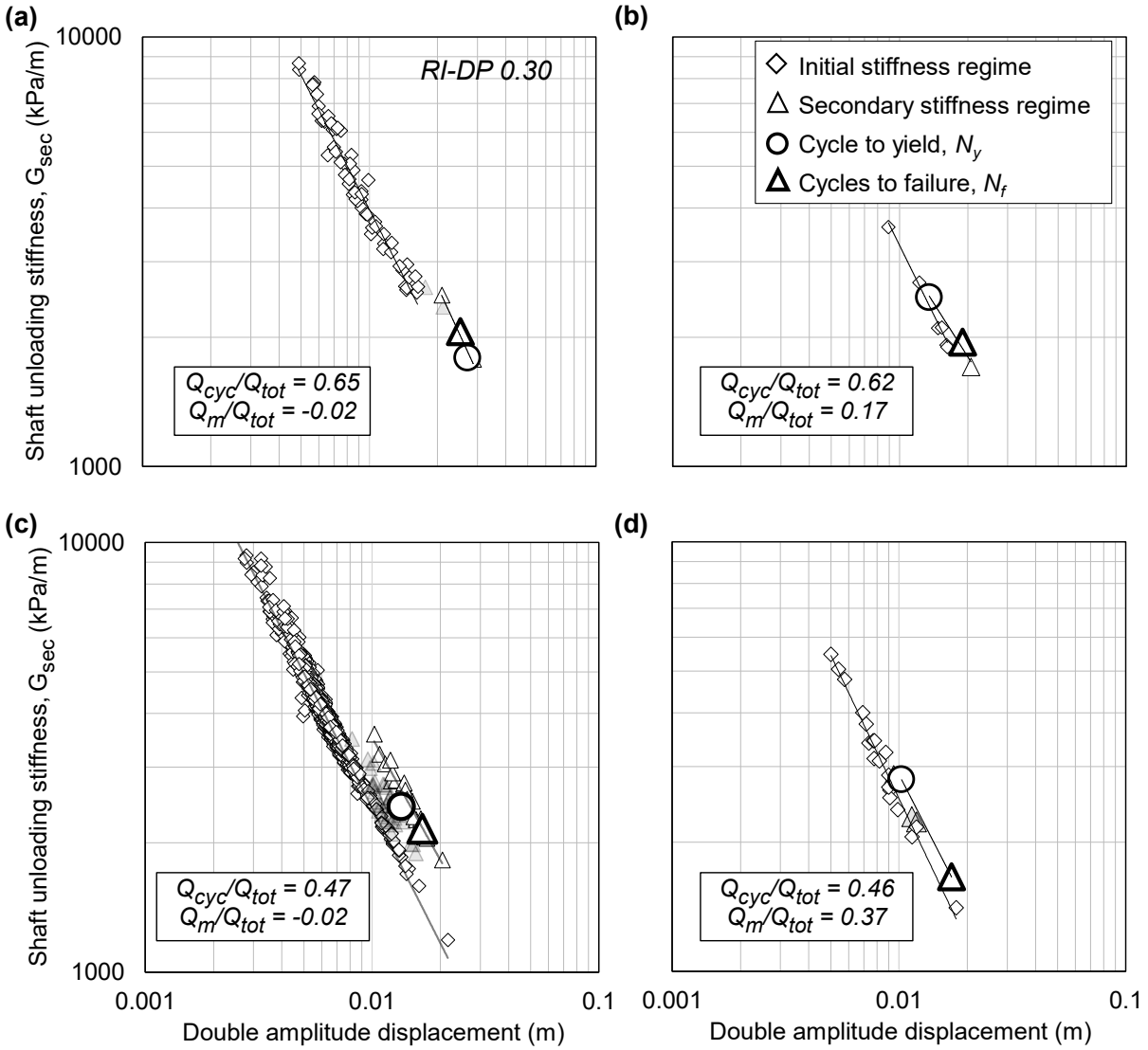
Figure 4.14. (a) – (d) Secant stiffness response from tests conducted on RI-DP 0.30 piles at specified load combinations. Note: transparent triangles correspond to range of cycles where N_y was not uniquely defined by fitting procedure.

134
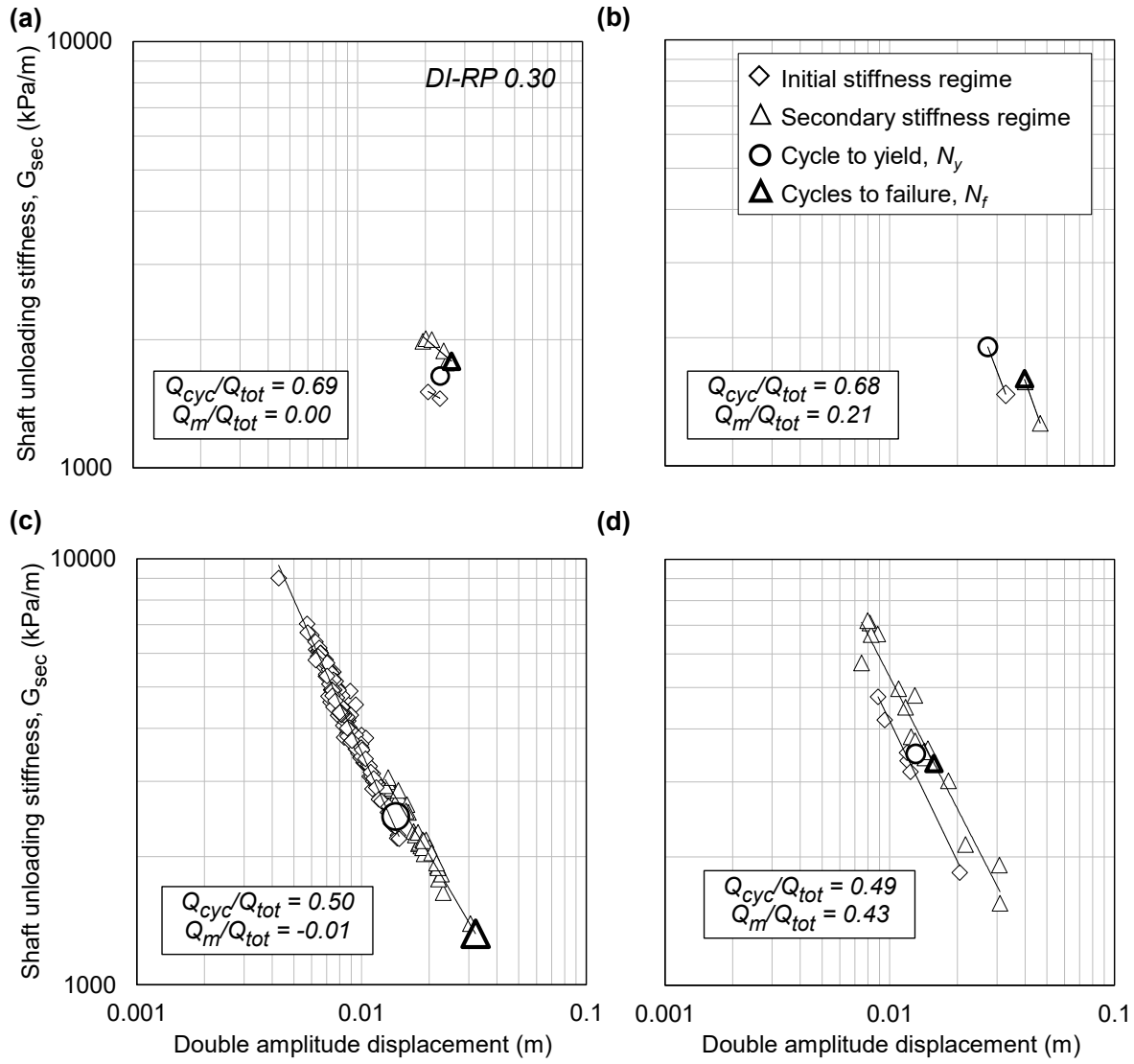
Figure 4.15. (a) – (d) Secant stiffness response from tests conducted on DI-RP 0.30 piles at different load combinations.
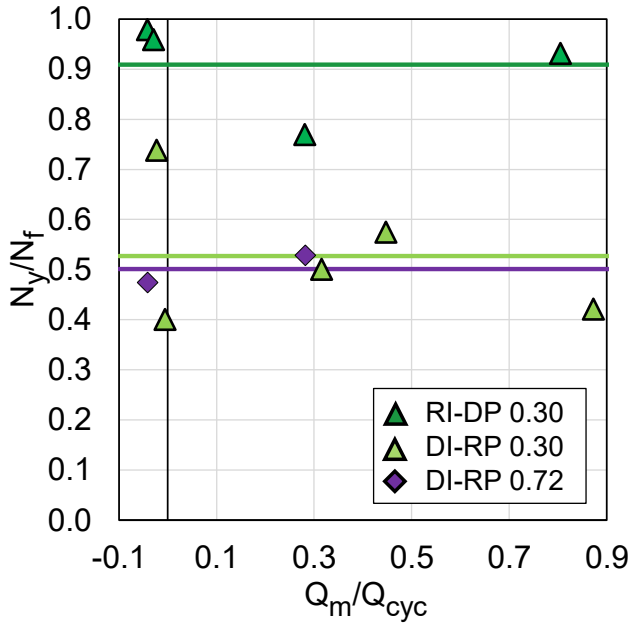
Figure 4.16. Ratio of N_y to N_f for RI-DP 0.30, DI-RP 0.30, and DI-RP 0.72 piles, with average values indicated with horizontal lines
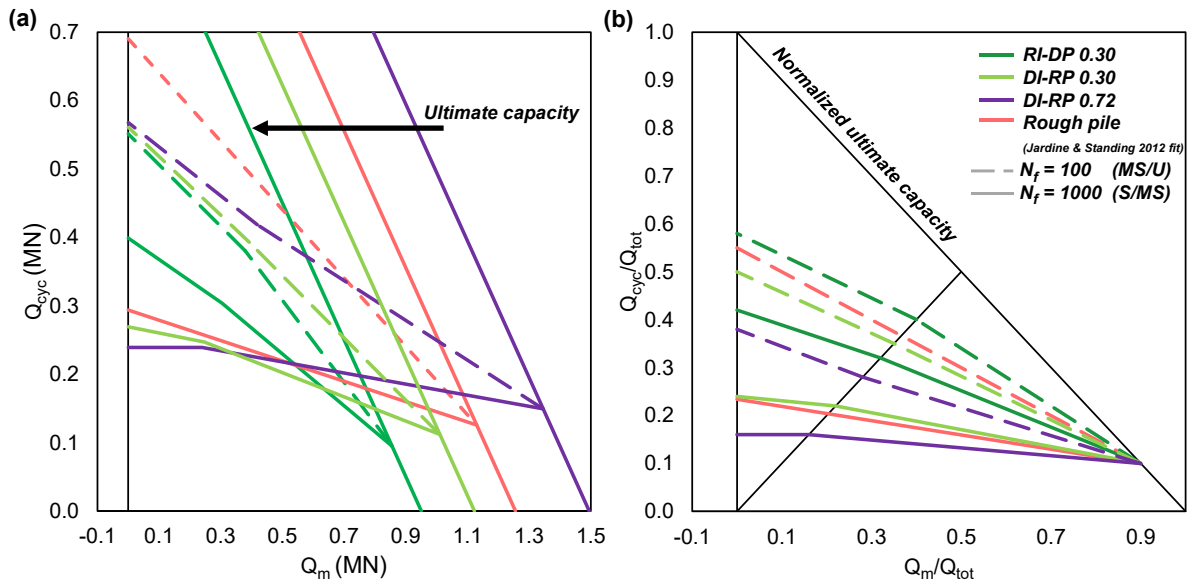
Figure 4.17. Cyclic stability zones between one-way and two-way loading for RI-DP 0.30, DI-RP 0.30, and DI-RP 0.72 piles for (a) absolute capacities and cyclic loads and (b) normalized capacities and cyclic loads
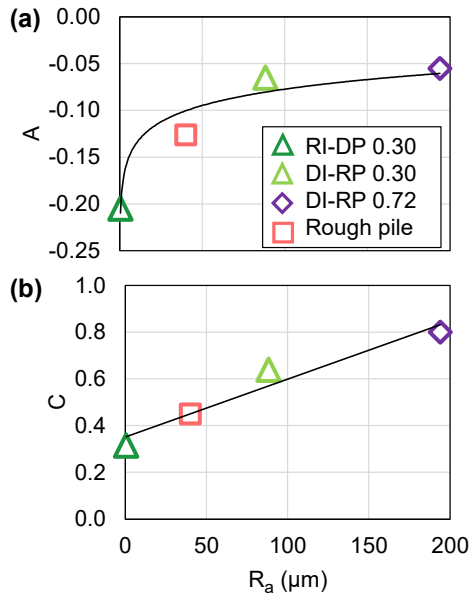
Figure 4.18. A and C parameters for N_f contour lines of an interaction diagram as a function of average roughness R_a

Chapter 5. Direction-dependent failure envelopes and meso-scale load transfer mechanisms for snakeskin-inspired surfaces

ABSTRACT

The interface friction angle between sand and snakeskin-inspired surfaces has been found to correlate to the ratio of the asperity length (L) to the asperity height (H), but the mechanisms leading to this effect have not yet been fully described. This study aims to provide a robust dataset regarding the interface friction angles associated with four snakeskin-inspired surfaces with similar L/H ratios but different values of L and H to assess the uniqueness of the aforementioned relationship. The results indicate that the failure envelopes associated with the snakeskin-inspired surfaces are better described with nonlinear functions over the range of stresses tested, while the failure envelopes of reference rough and reference smooth surfaces are well-fitted with linear functions. The interface friction angles obtained from the experiments with snakeskin-inspired surfaces show that the L/H ratio does not capture the trend of decreasing interface friction angle with increasing L/H ratio for the combinations of L and H investigated. Particle Image Velocimetry (PIV) analyses were conducted to assess whether the globally measured stress ratio values correlated to the magnitude and distribution of shear strains induced by the snakeskin-inspired surfaces. The results from the PIV analysis provide insight regarding the potential mechanisms leading to nonlinearity in the failure envelopes associated with the snakeskin-inspired surfaces.

INTRODUCTION

Study of the load transfer mechanisms occurring between granular materials and structural surfaces has increased as infrastructure applications have expanded to areas such as landfill liners, soil nails, and deep foundations. In general, it has been found that the strength of a soil – structure

interface is governed by the strength of the soil and the surface roughness of the structure, and the frictional properties have been largely assumed to be similar in one direction compared the opposite. The emerging field of bio-inspired geotechnics has led to development of novel geometric patterns that may be applied to the surface of structural elements and provide frictional resistances that vary depending on the direction of loading. Various researchers have found that the strength of such surfaces correlates to the ratio of asperity L to H, but the literature has not clearly assessed the underlying mechanisms leading to the changes in strength.

This paper aims to provide a systematic assessment of the failure envelope characteristics of such surfaces, supplemented with meso-scale analysis to better understand the observations. Failure envelopes were interpreted for rough and smooth reference surfaces and four snakeskin inspired surfaces with tests conducted at a minimum of three initial normal effective stress values. The failure envelopes associated with the snakeskin-inspired surfaces showed a nonlinear trend over the range of normal effective stress studied. Particle Image Velocimetry was conducted on each surface at a low and high initial normal effective stress to assess potential mechanisms underlying the nonlinear trend.

Interface shear behavior. The maximum shear resistance (τ) between a cohesionless soil and structural surface may be described with a normal effective stress (σ'_n) dependent failure condition:

$$\tau = \sigma'_n tan\delta' \qquad \text{Eq. 1}$$

where δ' is the interface friction angle of the soil-structure interface. When the structural surface has randomly structured asperities (i.e., rough concrete), the steady state interface friction angle, δ'_{ss} saturates at $\delta'_{ss} = \varphi'_{ss,\ DS}$ conditions, where $\varphi'_{ss,\ DS}$ is the steady state interface friction angle determined from a direct shear tests, and decreases in a bilinear relationship as the surface

roughness decreases (i.e., polished steel). Apparent $\delta'_{ss} > \varphi'_{ss,\,DS}$ conditions have been observed when the surface profile is periodically structured (Hryciw and Irysam 1993, Martinez and Frost 2017), although a unique relationship with surface roughness parameters has not been reported (Martinez et. al. 2019). Bio-inspired periodic surfaces have been derived based on the profiles of the ventral scales of snakes, resulting in surfaces with asymmetric profiles that mobilize greater interface friction angles and dilation in one shearing direction compared to the other (Martinez et al. 2019). For these surfaces, the cranial direction refers to movement of the asperities against the soil, resulting in a large interface friction angle and volumetric change behavior. The opposite shearing direction is referred to as the caudal direction, where the surface asperities move with the soil resulting in a comparatively smaller interface friction angle and less pronounced volumetric change behavior.

Review of the interface shear behavior of snakeskin-inspired surfaces. A number of laboratory studies have been conducted on snakeskin-inspired surfaces. Most of these studies use terminology introduced by Palumbo (2018) and Martinez et al. (2019) to reference the directionality of the surface movement relative to the soil (i.e., cranial versus caudal shearing). Similarities and differences with regards to the effect of the geometry of the snakeskin-inspired asperities, quantified in terms of H and L, can be identified in the published data. To compare δ'_{ss} values between the different studies, the values are normalized by the direct shear internal friction angle of each soil used ($\delta'_{ss}/\varphi'_{ss,\,DS}$). If the study did not report the direct shear internal friction angle at steady state, a typical value from literature was used. The $\delta'_{ss}/\varphi'_{ss,\,DS}$ values for both cranial and caudal shearing directions are presented in Figures 5.1a-5.1b. A description of each investigation is first provided in the proceeding paragraphs, followed by a comparison of the reported trends.

Martinez et al. (2019) conducted tests on 11 unique surfaces with ratios of L to H ranging from 16.7 to 240 with Ottawa 20-30 and Ottawa F65 sands at high relative densities. Friction angles were calculated from individual tests conducted at σ'_n of 75 kPa. The study found that δ'_{ss} decreased as L was increased and H was decreased. Furthermore, the results show that the L/H ratio can be used to correlate the surface geometry and shearing direction (i.e., cranial versus caudal) to the interface friction angle, where surfaces displaced in the cranial direction mobilize higher interface friction angles for any given L/H. The cranial and caudal δ'_{ss} values decreased with increasing L/H, with values reaching a constant value between L/H values of 80 and 160. The study also reported Particle Image Velocimetry (PIV) results showing that shearing in the cranial direction led to greater shear and volumetric strains within the sand mass.

Stutz and Martinez (2021) further investigated the effect of L/H on the interface friction angle of interfaces of snakeskin-inspired surfaces and Ottawa F65 and Hostun sands of different relative densities. The study utilized six surfaces with matched L/H ratios of 43, 83, and 120 but varying H and L values. Interface friction angles were calculated from single tests performed at σ'_n of 75 kPa. The results from the tests conducted on the Ottawa F65 sand indicate no difference in the interface friction angle over the range of L/H values tested, whereas the tests conducted on the Hostun sand show a decrease in the interface friction angle with increased L/H, in general agreement with observations from Martinez et al. (2019). Lee and Chong (2022) conducted tests between Joomunjin standard sand and snakeskin-inspired surfaces with L/H ratios between 16.7 and 120. The interface friction angle was calculated based on a linear fit failure envelope evaluated from tests conducted at σ'_n of 100, 200, and 300 kPa. The results show a consistent decrease in the interface friction angle as L/H increases, although for surfaces with similar L/H values of 16.7 and 20, there is a noticeable difference in the friction angle. Venu Latha et al. (2022) conducted tests

141

on two surfaces with *L/H* values of 50 and 150 on both glass beads and quarry sand. Interface friction angles were determined from linear failure envelopes obtained from tests conducted at σ'_n of 10, 25, and 50kPa. For both soil types, there was no observed variation in the interface friction angle from *L/H* of 50 to 150, similar to observations by Stutz and Martinez (2021) on Ottawa F65 sand.

The results from Martinez et al. (2019), Lee and Chong (2022), and Stutz and Martinez (2021) on Hostun sand show a decrease in $\delta'_{ss}/\varphi'_{ss,\,DS}$ as the *L/H* is increased accompanied by small changes in $\delta'_{ss}/\varphi'_{ss,\,DS}$ at *L/H* values greater than about 100. In contrast, the results from Venu Latha et al. (2022) and Stutz and Martinez (2021) on Ottawa F-65 sand indicate little change in $\delta'_{ss}/\varphi'_{ss,\,DS}$ across a *L/H* values between 40 and 100, regardless of grain size. Results from Martinez et al. (2019) on Ottawa 20-30 sand and from Lee and Chong (2022) indicate that while $\delta'_{ss}/\varphi'_{ss,\,DS}$ values at matched *L/H* are similar, the $\delta'_{ss}/\varphi'_{ss,\,DS}$ values at *L/H* between 16.7 and 20.0 have differences as large as 0.2. These trends suggest that the *L/H* parameter satisfactorily unifies the data at large *L/H* values, while it is unclear whether this is the appropriate parameter at low *L/H* values due to scatter in the datasets.

Given the variation in $\delta'_{ss}/\varphi'_{ss,\,DS}$ at a given *L/H*, this paper aims to provide a detailed analysis of the failure envelopes and interface friction angles associated with surfaces with the same *L/H* ratio but different *L* and *H* values. In addition, PIV is used to assess the potential mechanisms leading to the global observations associated with surfaces of different geometry during shearing in the cranial direction, including differences in the zones of large deformations and thickness of the induced shear bands.

MATERIALS AND METHODS

Interface shear testing. A series of direct interface shear tests were conducted with a modified Geotac Direct Shear device (Trautwein, Houston, TX). The device accommodates a bottom platen where the testing surface is mounted. The shear box is rectangular in cross-section with inner dimensions of 100.0 mm in length, 63.5 mm in width, and 25.4 mm in height. One side of the shear box is fitted with a clear Perspex window to allow image capture. Normal and shear forces were measures with vertically and horizontally mounted load cells, and the vertical and horizontal displacements were measured with linear potentiometers. The device is described in detail in Martinez et al. (2019) and Martinez and Stutz (2019). The interface shear tests were conducted at a shearing rate of 0.5 mm/min using constant normal stiffness (CNS) boundary conditions with a normal stiffness (k) of 300 kPa/mm. The use of a CNS boundary condition is used to capture the change in normal effective stress around interfaces due to volumetric changes, typically used in studies related to piles and soil nails (Tabucanon et al. 1995, Porcino et al. 2003).

A total of six surfaces were used in this investigation. A reference rough and a reference smooth surface were used to capture failure behavior dominated by particle interlocking and shearing within the soil mass or by interfacial sliding between the soil and surface, respectively. Four snakeskin-inspired surfaces with L/H values of 20 or 40 were also tested. The surfaces with $L/H = 20$ had $L = 12$ mm and $H = 0.60$ mm (i.e., L12H0.6) and $L = 6$ mm and $H = 0.30$ mm (i.e., L6H0.3), while the surfaces with $L/H = 40$ had $L = 12$ mm and $H = 0.30$ mm (i.e., L12H0.3) and $L = 24$ mm and $H = 0.60$ mm (i.e., L24H0.6). The surfaces were created using 3D printing using a FormLabs Form2 SLA printer and FormLabs Grey PLA resin. The material properties of the finished surfaces are available through the manufacturer, and further assessed in Palumbo (2018). The average surface roughness values associated with each surface are presented in Table 5.1, with values either measured between asperities, associated with the caudal shearing direction, or across

asperities, associated with the cranial shearing direction. Throughout this paper, the cranial direction is referred to as "CR" and the caudal direction is referred to as "CD". Ottawa 20-30 sand was used in all experiments, which is a poorly graded subangular sand with a minimum void ratio (e_{min}) of 0.49, maximum void ratio (e_{max}) of 0.71, and median particle size (D_{50}) of 0.72 mm. The values of e_{max} and e_{min} were verified through the simplified procedure outlined in Carey et al. (2020). Samples were air pluviated to a target relative density of 85%, with tests conducted herein ranging from 80 – 90%. To account for box friction, at the end of each test the normal load was removed, and the surface was displaced 0.5 mm forward and backwards. The load measured in each direction was assumed to be the magnitude of box friction. Each test was corrected by the measured friction by subtracting this magnitude from the measured loads.

Particle Image Velocimetry. PIV is a digital image correlation technique that can be used to track movement of patches in an image by correlating pixels between sequential frames. GeoPIV-RG (Stainer et al. 2016) was used in this study. GeoPIV has been used extensively in laboratory testing of interfaces (DeJong et al. 2006; Martinez et al. 2019; Martinez and Stutz 2019). Images used in the PIV analysis were taken using a Dino-Lite Digital Microscope, capturing a 1580 pixel by 650-pixel portion of the shear box. Each image spanned the central portion of the interface, where the height was taken from the top the asperity in each frame. Image to object space calibration factors were calculated based on known spacing markers on the surfaces. A patch size of 30 px by 30 px was used in each analysis, which nominally corresponds to the sand's D_{50}. Figure 5.2 shows a typical example of the area and patch size used for the PIV analysis. Note the dyed sand particles which were added to provide contrast for the analysis. The analysis was run in Eulerian mode, with a minimum tolerable full field correlation coefficient of 0.75. Each analysis

was then filtered, with any patch with a correlation coefficient less than 0.80 removed. The geoSTRAIN function was then used to calculate the shear and volumetric strains from the start to end of the forward cycle of each test, defined at shear displacements of 0 mm to 8mm, respectively.

RESULTS

The results from interface shear tests on the six surfaces are first presented in terms of the shear stress – displacement and normal effective stress – displacement responses. A summary of the tests is presented in Table 5.2. Then, the meso-scale PIV results are presented to quantify the disturbance zones for two bio-inspired surfaces. For analysis of the results, steady state failure conditions are considered when additional shear displacements result in no changes in shear and normal effective stress.

Interface shear response. The reference rough and smooth surfaces exhibited typical interface shear behaviors under CNS boundary conditions, where the rough surface mobilizes greater shear stresses and increases in normal effective stress than the smooth surface. Figures 5.3a-5.3b shows the stress ratio (τ/σ'_n) – horizontal displacement and normal effective stress ratio – horizontal displacement responses for the rough surface, with the initial normal effective stresses indicated in the legend. The peak τ/σ'_n is greater for the test conducted at $\sigma'_{no} = 26$ kPa and deceases as σ'_{no} is increased. In addition, while significant strain softening can be observed in the test at $\sigma'_{no} = 26$ kPa, no degradation is observed for the test at $\sigma'_{no} = 213$kPa. The normal effective stress response reflects the dilation-induced changes in normal effective stress due to the CNS boundary condition, where the test conducted at $\sigma'_{no} = 26$ kPa exhibits a σ'_n at the end of the test equivalent to 3.7 σ'_{no}, whereas the test conducted at $\sigma'_{no} = 213$ kPa exhibits a σ'_n at the end of the test equivalent to 1.3

σ'_{no}. The stress paths presented in Figure 5.3c also show the variations in $\underline{\tau}$ and σ'_n. These results reflect the high degree of interlocking in this interface leading to a behavior that is governed by shearing within the soil mass. The tests conducted on the smooth surface indicate a behavior associated with interfacial sliding at the interface. The τ/σ'_n – horizontal displacement response shown in Figure 5.3d shows that there is a distinct peak in stress ratio that is followed by a gradual decrease to a near-constant steady state value at the end of the test for the tests performed at different σ'_{no}. For all tests, there is small dilation-induced changes in σ'_n, as shown in Figures 5.3e-5.3f.

The snakeskin-inspired surfaces exhibit an interface shear behavior similar to the rough surface in the cranial direction and similar to the smooth surface in the caudal direction. For tests conducted in the CR-CD sequence on the L12H0.3 ($L/H = 40$) surface, the peak τ/σ'_n decreases as σ'_{n0} is increased, and the evolution of τ/σ'_n in the forward cranial direction transitions from strain softening to strain hardening (Figure 5.4a). After about 2 mm of displacement in the reverse caudal direction, τ/σ'_n reaches values that are smaller than in the initial cranial direction which decrease as σ'_{n0} is increased. The σ'_n/σ'_{n0} values by the end of the forward cranial cycle decreases as σ'_{n0} is increased, highlighting the suppression of dilation (Figure 5.4b). These changes in shear and effective stress during the initial and reverse direction are also shown by the stress paths (Figure 5.4c). The peak and steady state τ/σ'_n values during the initial, caudal direction of CD-CR tests also decrease as σ'_{n0} is increased; however, the shear response is characterized by an initial peak followed by stain softening (Figure 5.4d). The tests show dilation-induced increases in normal effective stress which decrease in magnitude as σ'_{n0} is increased (Figure 5.4e-5.4f).

The stress ratio response for the tests conducted on the other three snakeskin-inspired surfaces show similar trends as those reported for the L12H0.3 surface. Results are provided in

146

Figures 5.5a-5.5f for the L12H0.6 ($L/H = 20$) surface for both CR-CD and CD-CR test sequences. For CR-CD tests, there is a decrease in the peak and steady state τ/σ'_n values as σ'_{n0} is increased, which are accompanied by smaller increases in σ'_n/σ'_{n0}. Also, the mobilized τ/σ'_n values are greater in the cranial direction irrespective of test sequence, while the CR-CD tests generate greater increases in σ'_n/σ'_{n0} during the first direction. The results for the tests on the L24H0.6 and L06H0.3 surfaces are included in Figures S5.1 and S5.2 in the supplementary material.

Normal effective stress ratio. The normal effective stress ratio – displacement responses of the CNS interface shear tests indicates that for all the snakeskin-inspired surfaces, the σ'_n/σ'_{no} ratio at steady state decreases as σ'_{no} increases. Figures 5.6a-5.6b show steady state σ'_n/σ'_{no} values at the end of the forward cycle for tests in initial cranial and caudal directions. The figures also include the steady state σ'_n/σ'_{no} values for the rough and smooth surfaces. The rough surface tends to induce the greatest dilation-induced changes in σ'_n for a given σ'_{no}, followed by the surfaces displaced in the cranial and caudal directions, respectively, and the smooth surfaces induce minimal σ'_{no} changes. For tests conducted at $\sigma'_{no} = 26$ kPa in the cranial direction, the L12H0.6 ($L/H = 20$) surface results in the greatest σ'_n/σ'_{no} values, followed by the L6H0.3 ($L/H = 20$) surface, and the L12H0.3 and L24H0.6 ($L/H = 40$) surfaces result in a smaller σ'_n/σ'_{no} values with similar magnitudes. As σ'_{no} increases to 212 kPa, the σ'_n/σ'_{no} values for all snakeskin-inspired surfaces decrease to closer magnitudes between 1.01 and 1.16 due to the suppression of dilation.

For tests in the caudal direction, the L12H0.6 ($L/H = 20$) surface results in the greatest σ'_n/σ'_{no} values, followed by the L6H0.3 ($L/H = 20$) surface, and the L12H0.3 and L24H0.6 ($L/H = 40$) surfaces resulting in the smallest σ'_n/σ'_{no} values which have similar magnitudes. The reduction of σ'_n/σ'_{no} with increasing σ'_{no} is more pronounced for the caudal test. At σ'_{no} of 106 kPa, the σ'_n/σ'_{no}

values collapse to similar magnitudes between 1.04 and 1.13. The more pronounced decrease in σ'_n/σ'_{no} for the caudal tests indicate the smaller interface dilation with respect to the cranial tests. It is noted that the decrease in σ'_n/σ'_{no} with increasing σ'_{no} depends on the boundary stiffness, with greater k values likely leading to more pronounced decreases in σ'_n/σ'_{no} with σ'_{no} for dense specimens due to suppressed dilation.

Stress ratios and failure envelopes. At steady state, the shear stress (τ_{ss}), normal effective stress ($\sigma'_{n,ss}$), and stress ratio ($\tau_{ss}/\sigma'_{n,ss}$) values were found to vary based on the surface type (i.e., rough, smooth, snakeskin-inspired), shearing direction (i.e., CR or CD), and the magnitude of effective stresses. The results are presented in terms of $\tau_{ss}/\sigma'_{n,ss}$ as a function of $\sigma'_{n,ss}$ (Figures 5.7a-5.7b and 5.8a-5.8d) and of τ_{ss} as a function of $\sigma'_{n,ss}$ (Figures 5.7c-5.7d and 5.8e-5.8h). The $\tau_{ss}/\sigma'_{n,ss}$ - $\sigma'_{n,ss}$ relationship is fitted with a logarithmic decrease equation as follows:

$$\frac{\tau_{ss}}{\sigma'_{n,ss}} = r - s \log \sigma'_{n,ss} \qquad\qquad \text{Eq. 1}$$

where r represents the $\tau_{ss}/\sigma'_{n,ss}$ magnitude at $\sigma'_{n,ss}$ of 1 kPa, and s represents the rate of change in $\tau_{ss}/\sigma'_{n,ss}$ with $\sigma'_{n,ss}$. The τ_{ss} - $\sigma'_{n,ss}$ data points were fitted with a linear failure envelope as follows:

$$\tau_{ss} = \sigma'_{n,ss} \tan \delta'_{ss}{}' \qquad\qquad \text{Eq. 2}$$

where δ'_{ss} is the interface friction angle at steady state. To capture possible non-linearity in the failure envelope, the following a power-law fit was also considered:

$$\tau_{ss} = a\sigma'_{n,ss}{}^{b} \qquad\qquad \text{Eq. 3}$$

where a and b are fitting parameters. For the special case when $b = 1$, Eq. 3 equation becomes Eq. 2, with a representing $\tan\delta'_{ss}$. For the rough, smooth, and snakeskin-inspired surfaces, Eqs. 1 - 3 were fitted from $\sigma'_{n,ss} = 0$ to 300kPa by least squares linear regression. A summary of the r, s, δ'_{ss}, a, and b values are presented in Table 5.1.

The stress ratio and failure envelope fits for the reference rough, smooth, and snakeskin-inspired surfaces show unique differences at the steady state condition. Over the range of σ'_n evaluated, the $\tau_{ss}/\sigma'_{n,ss}$ values are near constant for both rough and smooth surfaces, with fitted s values of 0.0132 and 0.0015, respectively (Figures 5.7a-5.7b). In terms of the linear or curved failure envelopes, shown with solid and dashed lines, respectively, in Figures 5.7c-5.7d, the rough surface has a greater interface friction angle than the smooth surface. These values are in good agreement with published values for the steady state or residual friction angle of Ottawa 20-30 (i.e., Martinez and Frost, $\varphi'_{SS, DS} = 29.3^o$) and expected interface friction angle ratios, $\delta'_{ss}/\varphi'_{ss, DS}$. Specifically, the rough surface has $\delta'_{ss}/\varphi'_{ss, DS}$ of 1.01 for a normalized roughness ($R_n = R_a/D_{50}$) of 1.25 compared to an expected value of $\delta'_{ss}/\varphi'_{ss, DS} = 1$ (Uesugi and Kishida 1986), while the smooth surface has $\delta'_{ss}/\varphi'_{ss, DS}$ of 0.46 for $R_n = 0.004$ compared to an expected value of $\delta'_{ss}/\varphi'_{ss, DS}$ of about 0.40 to 0.48 (Uesegi and Kishida 1986; Han et al. 2018). These results show less than a 5% error in accuracy from average accepted values, giving confidence in the measured interface friction values obtained. The nonlinearity of the power fit failure envelope can be elucidated from the b parameter, where $b = 1$ would result in a linear failure envelope. The power function fit to the tests on the rough and smooth surfaces result in b of 0.977 and 0.996, respectively. These results indicate that relationships can be considered nominally linear, with the rough surface showing a slight deviation from linearity. A linear failure envelope from Mohr-Coulomb theory assumes a brittle shear failure between two frictional materials. For a smooth surface, a brittle failure is most likely to occur, with no additional energy expenditure required (Mohr 1878) by mechanisms which may cause a non-linear failure response, such as particle-surface interlocking (Lee and Seed 1967).

The stress ratios and failure envelopes measured during the forward cycles of tests with the snakeskin-inspired surfaces show a nonlinear behavior. Figures 5.8a-5.8h shows the results from

all tests conducted on each snakeskin-inspired surface in both the CR and CD directions. For all surface types, the $\tau_{ss}/\sigma'_{n,ss}$ values decreases with increasing $\sigma'_{n,ss}$ more rapidly in the CR direction than in the CD direction. The results show greater s parameter values in the CR direction, with values between 0.033 and 0.075, than in the caudal direction, with values between 0.025 and 0.051 in the caudal direction (Table 5.1). The failure envelopes associated with the CR and CD directions are better fitted with the non-linear relationship (Eq. 3), also showing greater non-linearity in the cranial direction. The a parameters are always larger in the cranial direction than in the caudal direction, in agreement with the interface friction angles obtained from the linear fit (Eq. 2).

To compare the friction angles calculated based on the linear and non-linear failure envelopes, an interface friction angle calculated at 100 kPa using Eq. 3 and the parameters in Table 5.1 (δ'_{100}), along with δ' from Eq. 2, are presented as a function of L/H and R_a for each surface in Figures 5.9a-5.9b. The δ'_{100} values calculated from Eq. 3 are greater compared to δ'; the difference between the friction angles is greater for the snakeskin-inspired surfaces than the reference rough or smooth surfaces, reflecting the near-linearity of the failure envelopes of the reference surfaces shown in Figure 5.7. The empirical evidence highlights that the $\tau_{ss}/\sigma'_{n,ss}$ and δ'_{ss} values for the snakeskin-inspired surfaces depend on the magnitude of $\sigma'_{n,ss}$. The results indicate that the snakeskin-inspired surfaces have a nonlinear failure envelope; thus, snakeskin-inspired surfaces may exhibit $\delta'_{ss}/\varphi'_{ss,\,DS}$ greater than one at lower normal effective stresses if $\delta'_{ss}/\varphi'_{ss,\,DS}$ is determined based on tests with a rough surface from direct shear tests. These findings suggest that a constant interface friction angle is not a full descriptor of the failure envelope for snakeskin-inspired surfaces across the range of stresses investigated in both this study and from the studies summarized in Figure 5.1.

Particle Image Velocimetry. PIV analyses were conducted on the first direction of tests with the rough, smooth and snakeskin-inspired surfaces in the CR direction to examine the potential mechanisms leading to the observed decrease in stress ratio with increasing effective stress to explore whether the *L/H* parameter captures the underlying mechanisms. The analyses were conducted at σ'_{no} of 26 and 211kPa to capture changes over an order of magnitude. The validity of the displacement fields generated from the PIV analyses was evaluated by comparing the average vertical displacement from the topmost row of patches against the measurements from the vertical LVDT in the shear box. Figure 5.10a compares the vertical displacements as a function of horizontal displacements from tests with the rough surface at $\sigma'_{n0} = 26$ and 213kPa from the PIV analysis with those from the vertical LVDT. The results indicate that there is a reasonable agreement in the evolution and final value of vertical displacements. However, the PIV results appear to overpredict the interface dilation at the beginning of the test compared to the globally measured results. In order to assess the data, the interface dilation angle was interpreted from each measurement at the point corresponding to the observed peak shear stress ratio, noted in Figure 5.10a, and compared to the difference between the peak and steady state interface friction angles. The analysis indicates that the PIV results provide better agreement with Bolton's relationship, presented in Figure 5.10b.

Shear (γ) and volumetric (ε_v) strain heat maps for the rough and smooth surface are presented in Figure 5.11a-d for $\sigma'_{n0} = 26$ tests. Each figure presents cumulative shear strains at the end of the forward cycle of each test (0 to 8 mm horizontal displacement). In the shear strain maps, cool colors are associated with low shear strains, while warm colors are associated with larger strains. In the volumetric strain maps, cool colors are associated with dilation, and warm colors contraction. Dilation is reported as negative volumetric strains and contraction as positive. In the

151

shear strain map for the rough surface (Figure 5.11a), it can be seen that shear strains are concentrated near the surface. In the shear strain map for the smooth surface there are negligible shear strains both at the surface and throughout the assessed area (Figure 5.11b). In the volumetric strain map for the rough surface, there are zones of dilation and contraction near the surface, with the magnitude of dilation being larger than contraction. This is important to note that while from a global perpective there is dilation, there are also zones of contraction within the interface zone where shear banding occurs. On the other hand, there are negligible volumetric strains throughout the soil mass when sheared against the smooth surface (Figure 5.11d).

The shear and volumetric strain profiles at given elevations obtained from the tests conducted on the snakeskin-inspired surfaces show different patterns based on the surface geometry. Shear and volumetric strain profiles for tests conducted on the L12H0.3 surface at initial normal effective stresses of 26 and 216 kPa are presented. The initial and final location of the asperities is noted in each figure with an arrow. Two full asperity lengths (center and right) and a partial one (left) are included in the field of view. The γ profiles from the test at σ'_{n0} of 26 kPa exhibit distinct high values in the zones immediately ahead of each asperity at elevations smaller than $10D_{50}$ (Figure 5.12a). At an elevation of $10D_{50}$, the γ magnitudes are negligible. Similar trends are observed for the test conducted at $\sigma'_{no} = 213$ kPa (Figure 5.12b). The ε_v profiles at elevations smaller than $10D_{50}$ indicate zones of dilation near the location of the asperities, and either smaller dilative strains or contraction at locations behind the asperities (Figures 5.12c-12d). At an elevation of $10D_{50}$, the ε_v magnitudes are near-zero regardless of the initial normal effective stress.

The γ and ε_v profiles from the tests on the L24H0.6 surface have similar features as those from the L12H0.3 surface, where both surfaces have an L/H value of 40. The figures show a single full sperity (right) and a partial one (left). The γ profiles from the test on the L24H0.3 surface

exhibit distinct peaks in the zones immediately ahead of each asperity at elevations smaller than $10D_{50}$, while at an elevation of $10D_{50}$ the γ magnitudes are near-zero for tests performed at σ'_{no} of 26 kPa and 213 kPa (Figure 5.13a-5.13b). The ε_v profiles at elevations of 1.9 D_{50} show zones of dilation ahead of the final asperity location and contraction behind the asperities (Figure 5.13c-5.13d) for both σ'_{no} values, while at an elevation of $10D_{50}$ the volumetric strains are negligible. While the trends in γ and ε_v profiles are similar between the L12H0.3 and L24H0.6 surfaces, the magnitudes and spatial distribution of shear and volumetric strains vary for each surface type despite the fact that both surfaces have the same L/H. The profiles for the L12H0.3 and L24H0.6 surfaces are also presented alternatively as heat maps in the supplementary materials as Figure S5.3.

Shear band assessment. The shear strain profiles along the height of the specimens and the interpreted shear bands were found to be affected by the surface type and magnitude and evolution of the effective stress during the interface shear tests. The γ at different constant elevations were binned to obtain average, maximum, and minimum shear strain profiles. The average shear strain – height profiles from the snakeskin-inspired surfaces at the end of the forward cranial cycle are presented in Figures 5.14a-5.14d. Each shear strain profile exhibits a typical pattern where strains increase at a rapid rate at locations close to the surface. Regardless of the surface geometry, there are negligible γ at a distance approximately equivalent to $10D_{50}$ (7.2 mm) from the surface. For all surfaces, the γ magnitudes in the interface zone decrease as σ'_{no} increases. It is noted that the surfaces with $L/H = 20$ led to larger shear strains than the surfaces with $L/H = 40$.

To systematically find the average and maximum shear band height, a power function was fit to the γ – height profiles and the point of maximum curvature was calculated explicity. The

shear band height was taken to be the elevation of the center of the osculating circle that defines the point of maximum curvature, as shown in Figure 5.15. This method was not applicable to the minimum shear band height since the minimum γ profiles did not consistently show a sharp increase in shear strains near the surface. Table 5.3 presents the shear band height determined from each analysis. The rough surface generated the tallest shear band, followed by the snakeskin-inspired surfaces with an L/H of 20 and 40, respectively, and the smooth surface produced minimal shear banding. The shear band height either decreases or remains nominally constant as σ'_{no} is increased, accompanied by the aforementioned decrease in average γ with increasing σ'_{no}, in general agreement with published results (i.e., DeJong and Westgate 2009). This can be explained by an increase in interfacial sliding at the soil-structure interface as σ'_{no} is increased due to the a reduction in the interlocking between the surface aspeirties and the sand particles.

Figure 5.16a shows the average shear strain within the shear band from each analyis and the globally measured τ_{ss}/σ'_{nss} from each associated test. The magnitude of shear strain are greatest for the L12H0.6 surface at σ'_{no} of 26 kPa, followed by the rough surface. The rough surface shows only a small reduction in γ as σ'_{no} is increased from 26 to 213 kPa, while the surfaces with L/H of 20 have more significant changes in γ with σ'_{no}. Namely, for the L12H0.6 surface, the γ decreases from 1.06 to 0.63, while for the L6H03, the γ decreases from 0.84 to 0.69. In contrast, both surfaces with L/H of 40 surfaces have average and maximum γ of about 0.47 and 0.38. The smooth surface induces the least γ at both stress levels due to the large slippage at the soil-structure interface. Figure 5.16b shows the change in shear strain ($\Delta\gamma$) in the interface as a function of the change in stress ratio ($\Delta\tau_{ss}/\sigma'_{nss}$) as σ'_{no} increases from 26 kPa to 213 kPa. The $\Delta\tau_{ss}/\sigma'_{nss}$ tends to increase as the $\Delta\gamma$ increases. This provides supporting evidence that with increasing σ'_n, the γ within the shear

bands decrease causing a more pronounced nonlinearity in the failure envelope as shown in Figures 5.7 and 5.8 and Table 5.2.

Differences in the asperity-particle interactions between the reference surfaces (i.e., rough and smooth) and the snakeskin-inspired surfaces can be inferred from variations in the shear band height along the surfaces' length. To investigate this, the maximum shear band height is plotted against the average shear band height for the tests on the rough, smooth, and snakeskin-inspired surfaces at σ'_{n0} of 26 and 213 kPa (Figure 5.17). The 1:1 line in the figure indicates no variation in the shear band height. There is no systematic variation of shear band height with changes in σ'_{n0}; however, the results indicate that the snakeskin-inspired surfaces all have a larger variation in shear band height compared to the rough or smooth surfaces. Namely, the variation between the average and maximum shear band height is equivalent to about $0.67D_{50}$ for all snakeskin-inspired surfaces, while this variation is of about $0.18D_{50}$ for the rough and smooth surfaces. These differences are related to the shear strain profiles at different elevations shown in Figures 5.12 and 5.13, where the rough and smooth surfaces induce shear bands that can be characterized as planar, in agreement with previous published results (DeJong and Westgate 2009; DeJong et al. 2003). In contrast, the snakeskin-inspired surfaces likely induce undulating shear bands that as a result have a greater total area for the same unit length of soil-structure interface.

The results in Figures 5.16a-5.16b and 17 may provide insight into the trends between the interface friction and the L/H ratio, as previously reported by Martinez et al. (2019) and Stutz and Martinez (2021). Figure 5.16a shows that surfaces with the same L/H ratio led to similar average shear strains, although for the $L/H = 20$ surfaces at σ'_{n0} of 26 there is some discrepency which may be due to variations in initial relative density. The average shear strains show better agreement for the $L/H = 40$ surfaces at both σ'_{n0} conditions. The results suggest that the surface geometry may

fundamentally correlate to the shear strains within the shear band, but that *L/H* is not sufficient to capture this trend. Another trend observed is the tendency for surfaces with *L/H* ratios less than approximately 40 to mobilize $\delta'_{ss}/\varphi'_{ss,\,DS}$ ratios greater than one, as shown in Figure 5.1. Figure 5.17 shows how the variation in shear band height is large compared to that of a rough surface. Larger shear band variations may correlate to shearing planes with greater areas, which would result in larger apparent interface friction angles if these are calculated assuming planar shear planes. In addition, it would be advantageous to conduct a reanalysis of all available data to consider the shear resistance as function of not just an interface friction angle, but also due to a component from passive resistance in the zones ahead of asperities, taking into account the normal effective stress level and the number and spacing of asperities. These results are preliminary and should be supplemented with tests conducted at higher stress levels in order to elucidate the potential mechanisms postulated herein.

CONCLUSIONS

This paper presents the results of a series of monotonic interface shear tests with constant normal stiffness boundary conditions on both reference rough and smooth surfaces and snakeskin-inspired surfaces at different initial normal effective stresses to assess the failure envelopes and friction angle associated with each surface. Particle image velocimetry was conducted to assess potential mechanisms leading to the *L/H* relationship and the failure envelope characteristics.

It was found that the rough and smooth surfaces resulted in nominally linear failure envelopes across the range of stresses tested, with values of interface friction angle agreeing well with published relationships. In contrast, the snakeskin-inspired surfaces resulted in failure envelopes that were better described by a nonlinear functions in both the CR and CD direction.

The decrease in the steady state stress ratio with increasing initial normal effective stress was greater in the CR direction compared to the CD direction. If an equivalent linear interface friction angle is calculated from the nonlinear failure envelope, it may result in an interface friction angle greater than the internal friction angle of the soil, in agreement with previously published work that shows similar behavior.

The PIV results show that the snakeskin-inspired surfaces result in profiles of shear strain with large variations near the asperities, while the reference surfaces have less variation across their profile. The results suggest that the snakeskin inspired surfaces have larger changes in shear strains in the interface zone as the initial normal effective stress increases compared to the reference rough and smooth surfaces. These results correlate well to the globally measured stress ratios, where smaller changes in shear strain with increasing effective stress correspond to smaller changes in stress ratio. In addition, a method for systematically calculating the shear band height from the shear strains was presented. This method was applied to find the average and maximum shear band height for each surface, and it was found that the snakeskin-inspired surfaces had a larger variation in shear band height compared to the reference smooth and rough surfaces. The results presented herein provide supporting evidence to the existing knowledge of periodically structured surfaces modelled after the ventral scales of snakes may result in interface friction angles larger than the internal friction angle of the soil depending on the test conditions. It is shown that L/H does not uniquely describe the interface friction angle for every combination of L and H, but that it may capture the trend of decreasing interface friction angle across large changes in L/H.

Data. Data is available under DesignSafe under PRJ-3320 or upon request.

REFERENCES

Carey, T. J., N. Stone, and B. L. Kutter. 2020. "Grain Size Analysis and Maximum and Minimum Dry Density Testing of Ottawa F-65 Sand for LEAP-UCD-2017." *Model Tests and Numerical Simulations of Liquefaction and Lateral Spreading*, B. L. Kutter, M. T. Manzari, and M. Zeghal, eds., 31–44. Cham: Springer International Publishing.

DeJong, J. T., and Z. J. Westgate. 2009. "Role of Initial State, Material Properties, and Confinement Condition on Local and Global Soil-Structure Interface Behavior." *J. Geotech. Geoenviron. Eng.*, 135 (11): 1646–1660. https://doi.org/10.1061/(ASCE)1090-0241(2009)135:11(1646).

DeJong, J. T., M. F. Randolph, and D. J. White. 2003. "Interface Load Transfer Degradation During Cyclic Loading: A Microscale Investigation." *Soils and Foundations*, 43 (4): 81–93. https://doi.org/10.3208/sandf.43.4_81.

Han, F., E. Ganju, R. Salgado, and M. Prezzi. 2018. "Effects of Interface Roughness, Particle Geometry, and Gradation on the Sand–Steel Interface Friction Angle." *J. Geotech. Geoenviron. Eng.*, 144 (12): 04018096. https://doi.org/10.1061/(ASCE)GT.1943-5606.0001990.

Hryciw, R. D., and M. Irsyam. 1993. "Behavior of Sand Particles Around Rigid Ribbed

 Inclusions During Shear." *Soils and Foundations*, 33 (3): 1–13.

 https://doi.org/10.3208/sandf1972.33.3_1.

Lee, K. L., and H. B. Seed. 1967. "Drained Strength Characteristics of Sands." *J. Soil Mech. and*

 Found. Div., 93 (6): 117–141. https://doi.org/10.1061/JSFEAQ.0001048.

Lee, S.-H., and S.-H. Chong. 2022. "A Study on Friction Anisotropy between Sand and Surface

 Asperities of Plate Using Modified Direct Shear Test." *Journal of the Korean*

 Geotechnical Society, 38 (2): 29–38. https://doi.org/10.7843/KGS.2022.38.2.29.

Martinez, A., and J. D. Frost. 2017. "The influence of surface roughness form on the strength of

 sand–structure interfaces." *Géotechnique Letters*, 7 (1): 104–111.

 https://doi.org/10.1680/jgele.16.00169.

Martinez, A., and O'Hara, K.B. (2021). "Skin friction directionality in monotonically- and

 cyclically-loaded bio-inspired piles in sand." *Deep Found. Inst. J.,* 15(1).

Martinez, A., S. Palumbo, and B. D. Todd. 2019. "Bioinspiration for Anisotropic Load Transfer

 at Soil–Structure Interfaces." *J. Geotech. Geoenviron. Eng.*, 145 (10): 04019074.

 https://doi.org/10.1061/(ASCE)GT.1943-5606.0002138.

Mohr, O. (1878). *Technische mechanik*. K. Wittwer.

O'Hara, K. B., and A. Martinez. 2022. "Load Transfer Directionality of Snakeskin-Inspired Piles

 during Installation and Pullout in Sands." *J. Geotech. Geoenviron. Eng.*, 148 (12):

 04022110. https://doi.org/10.1061/(ASCE)GT.1943-5606.0002929.

Palumbo, S. (2018). *Anisotropic interface shear behavior of granular soil and surfaces*

 biologically-inspired by snakeskin. University of California, Davis.

Pincus, H., J. Tabucanon, D. Airey, and H. Poulos. 1995. "Pile Skin Friction in Sands from

  Constant Normal Stiffness Tests." *Geotech. Test. J.*, 18 (3): 350.

  https://doi.org/10.1520/GTJ11004J.

Porcino, D., V. Fioravante, V. Ghionna, and S. Pedroni. 2003. "Interface Behavior of Sands from

  Constant Normal Stiffness Direct Shear Tests." *Geotech. Test. J.*, 26 (3): 19513.

  https://doi.org/10.1520/GTJ11308J.

Stanier, S. A., J. Blaber, W. A. Take, and D. J. White. 2016. "Improved image-based

  deformation measurement for geotechnical applications." *Can. Geotech. J.*, 53 (5): 727–

  739. https://doi.org/10.1139/cgj-2015-0253.

Stutz, H. H., and A. Martinez. 2021. "Directionally dependent strength and dilatancy behavior of

  soil–structure interfaces." *Acta Geotech.*, 16 (9): 2805–2820.

  https://doi.org/10.1007/s11440-021-01199-5.

Tabucanon, J., D. Airey, and H. Poulos. 1995. "Pile Skin Friction in Sands from Constant

  Normal Stiffness Tests." *Geotech. Test. J.*, 18 (3): 350.

  https://doi.org/10.1520/GTJ11004J.

Uesugi, M., and H. Kishida. 1986. "Influential Factors of Friction Between Steel and Dry

  Sands." *Soils and Foundations*, 26 (2): 33–46.

  https://doi.org/10.3208/sandf1972.26.2_33.

Vena Latha, G., P. Vangla, and R. Anilkumar. 2022. "Effect of snakeskin-inspired patterns on

  the shear response of soil - continuum interfaces." *International Journal of Geotechnical

  Engineering*, 16 (6): 759–775. https://doi.org/10.1080/19386362.2022.2066049.

Table 5.1. Summary of stress ratio and failure envelope parameters.

Surface	L/H	R_a	s	r	δ'	a	b	δ'_{100}
Rough	-	135.30	0.0132	0.643	29.5	0.645	0.977	30.2
Smooth	-	0.45	0.0015	0.250	13.5	0.247	0.996	13.6
L12H0.3-R	40	100.03	0.0593	0.716	22.4	0.832	0.864	24.0
L12H0.3-D	40	0.43	0.0250	0.372	13.6	0.401	0.903	14.4
L12H0.6-R	20	181.22	0.0698	0.926	29.3	1.029	0.884	31.1
L12H0.6-D	20	0.42	0.0511	0.515	14.3	0.605	0.831	15.5
L24H0.6-R	40	150.58	0.0329	0.614	23.4	0.643	0.927	24.7
L24H0.6-D	40	0.42	0.0277	0.351	11.9	0.374	0.886	12.5
L6H0.3-R	20	86.67	0.0748	0.834	23.9	0.991	0.846	25.9
L6H0.3-D	20	0.41	0.0351	0.442	14.7	0.428	0.898	15.0

Table 5.2. Summary of all interface shear tests conducted.

Surface	Cycle	σ'_{no}	σ'_{nss}	τ_{ss}	τ_{ss}/σ'_{nss}	Surface	Cycle	σ'_{no}	σ'_{nss}	τ_{ss}	τ_{ss}/σ'_{nss}
Smooth	Forward	213	212	53	0.25	L24H0.6, CD	Return	27	23	5	0.23
Smooth	Forward	105	103	24	0.23	L24H0.6, CD	Return	213	184	37	0.2
Smooth	Forward	27	27	7	0.26	L24H0.6, CD	Forward	27	28	8	0.3
Smooth*	Forward	26	27	7	0.27	L24H0.6, CD	Forward	107	105	24	0.22
Smooth*	Forward	212	210	46	0.22	L24H0.6, CD	Forward	213	209	45	0.21
Smooth	Return	213	202	50	0.24	L6H0.3, CR	Forward	106	130	59	0.45
Smooth	Return	105	97	26	0.27	L6H0.3, CR	Forward	26	51	27	0.54
Smooth	Return	27	19	4	0.21	L6H0.3, CR	Forward	210	215	88	0.41
Rough*	Forward	27	97	61	0.63	L6H0.3, CR*	Forward	26	53	29	0.54
Rough*	Forward	213	281	160	0.57	L6H0.3, CR*	Forward	210	237	109	0.46
Rough	Return	213	202	110	0.54	L6H0.3, CR	Return	100	125	51	0.41
Rough	Return	27	43	24	0.57	L6H0.3, CR	Return	26	35	17	0.47
L12H0.6, CR	Forward	106	154	87	0.57	L6H0.3, CR	Return	210	192	77	0.4
L12H0.6, CR	Forward	25	64	39	0.62	L6H0.3, CD	Return	106	96	24	0.25
L12H0.6, CR	Forward	53	95	52	0.55	L6H0.3, CD	Return	26	22	6	0.28
L12H0.6, CR	Forward	213	239	133	0.56	L6H0.3, CD	Return	210	178	38	0.21
L12H0.6, CR*	Forward	25	63	43	0.68	L6H0.3, CD	Return	26	26	9	0.36
L12H0.6, CR*	Forward	213	256	140	0.55	L6H0.3, CD	Return	210	188	58	0.31
L12H0.6, CR	Return	25	57	37	0.65	L6H0.3, CD	Forward	106	120	32	0.27
L12H0.6, CR	Return	53	74	47	0.63	L6H0.3, CD	Forward	26	32	12	0.37
L12H0.6, CR	Return	106	98	60	0.61	L6H0.3, CD	Forward	210	210	56	0.27
L12H0.6, CR	Return	213	222	122	0.55	L12H0.3, CR	Forward	27	48	24	0.51
L12H0.6, CD	Return	106	99	26	0.26	L12H0.3, CR	Forward	53	71	33	0.47
L12H0.6, CD	Return	25	14	5	0.37	L12H0.3, CR	Forward	107	125	57	0.46
L12H0.6, CD	Return	53	47	17	0.36	L12H0.3, CR*	Forward	27	48	25	0.52
L12H0.6, CD	Return	213	187	47	0.25	L12H0.3, CR*	Forward	213	215	92	0.43
L12H0.6, CD	Return	25	22	8	0.35	L12H0.3, CR	Return	27	37	17	0.47
L12H0.6, CD	Forward	25	52	16	0.31	L12H0.3, CR	Return	53	56	25	0.45
L12H0.6, CD	Forward	53	71	22	0.31	L12H0.3, CR	Return	107	115	48	0.42
L12H0.6, CD	Forward	106	112	28	0.25	L12H0.3, CR	Return	213	207	73	0.35
L12H0.6, CD	Forward	213	229	56	0.25	L12H0.3, CD	Forward	27	36	11	0.29
L24H0.6, CR	Forward	107	115	60	0.52	L12H0.3, CD	Forward	53	61	16	0.27
L24H0.6, CR*	Forward	27	47	24	0.52	L12H0.3, CD	Forward	107	117	33	0.28
L24H0.6, CR*	Forward	213	215	91	0.42	L12H0.3, CD	Forward	213	226	51	0.23
L24H0.6, CR	Return	27	21	10	0.48	L12H0.3, CD	Return	27	25	7	0.29
L24H0.6, CR	Return	107	98	44	0.45	L12H0.3, CD	Return	53	43	12	0.27
L24H0.6, CR	Return	213	188	76	0.41	L12H0.3, CD	Return	107	89	22	0.25
L24H0.6, CD	Return	107	84	18	0.21						

Table 5.3. Interpreted shear band height from shear strain profiles.

Surface	Shear band height (D_{50})	
	$\sigma'_{no} = 26$ kPa	$\sigma'_{no} = 213$ kPa
Rough	6.7	5.7
Smooth	0.8	0.5
L12H0.6 (*L/H* = 20)	3.9	3.4
L6H0.3 (*L/H* = 20)	3.8	3.8
L24H0.6 (*L/H* = 40)	2.4	2.6
L12H0.3 (*L/H* = 40)	3.1	3.1
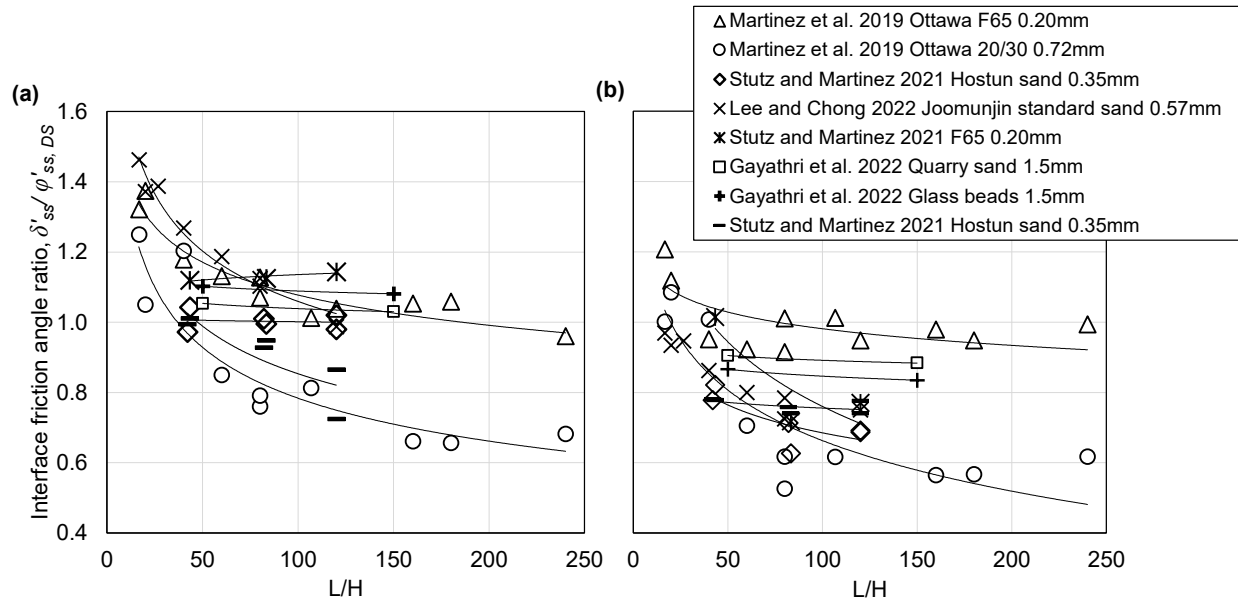
Figure 5.1. Summary of steady state interface friction angle ratios from studies reviewed herein for (a) cranial direction and (b) caudal direction.
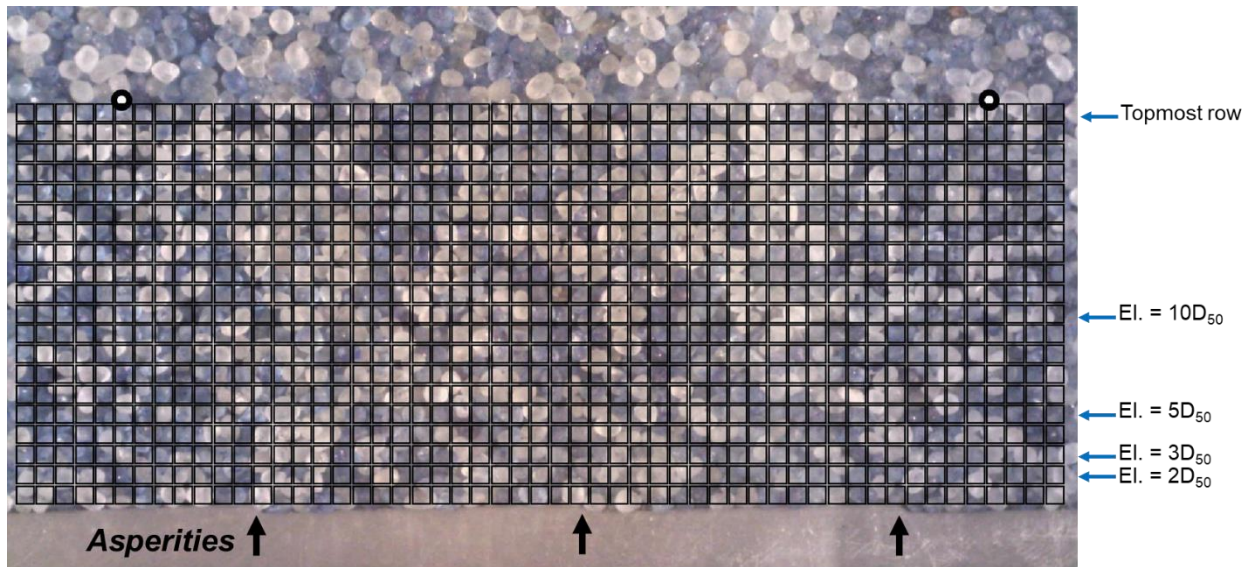
Figure 5.2. Image analysis region from PIV analysis. L12H0.3 surface shown. Control points visible on either side of image.
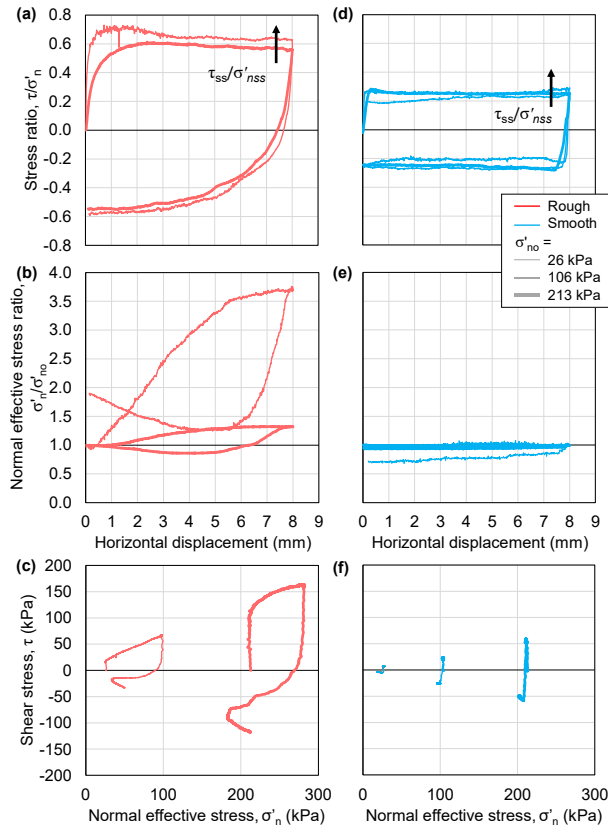
Figure 5.3 Stress ratio – displacement, effective stress ratio – displacement, and stress path response for tests on rough (a-c) and smooth (d-f) surfaces. Steady state condition noted in Stress ratio – displacement in forward cycle of each test.
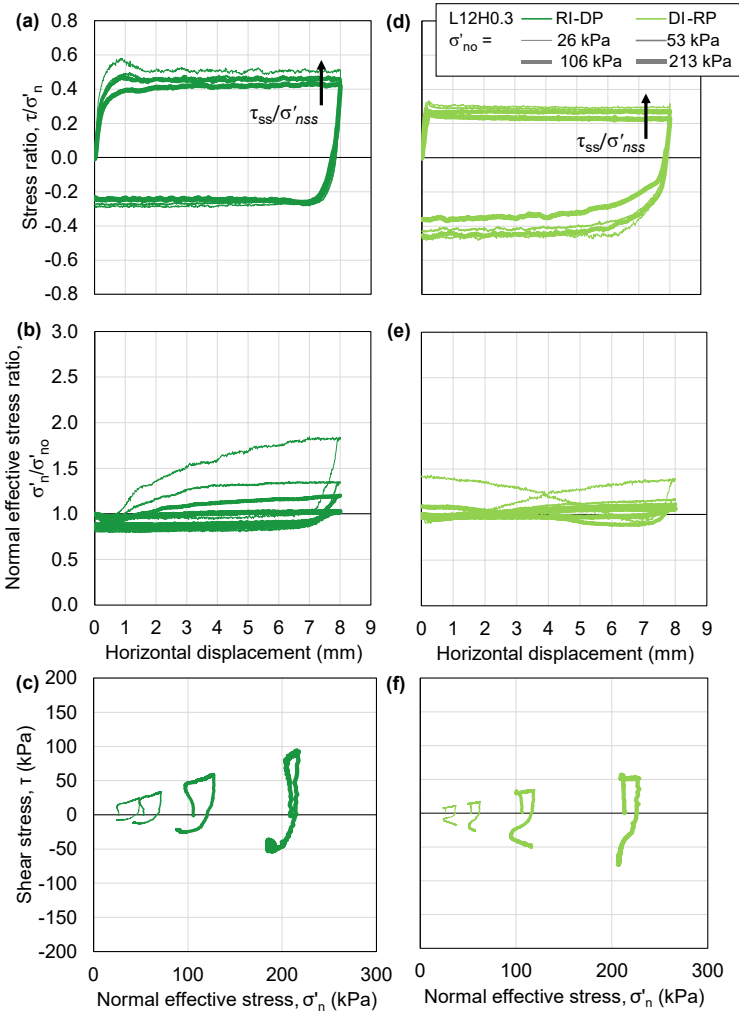
Figure 5.4. Stress ratio – displacement, effective stress ratio – displacement, and stress path response for tests on the L12H0.3 surface in CR-CD (a-c) and CD-CR (d-f) directions. Steady state condition noted in Stress ratio – displacement in forward cycle of each test.
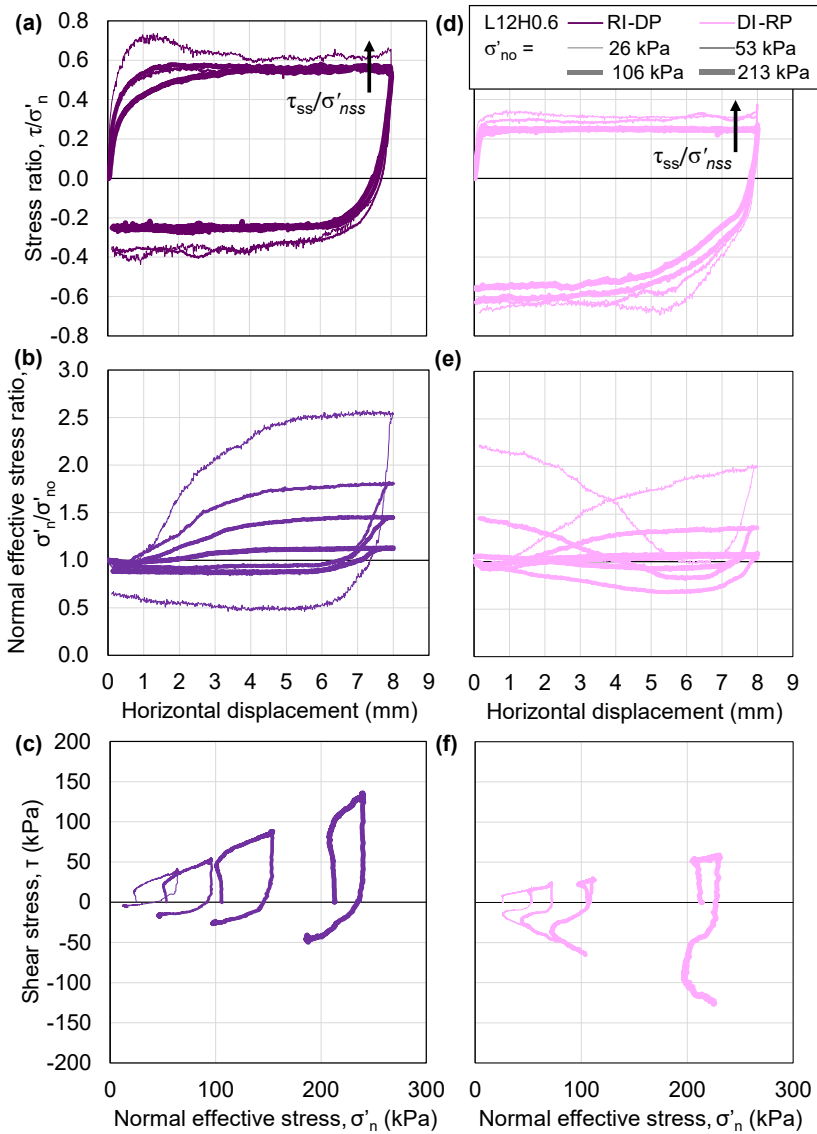
Figure 5.5. Stress ratio – displacement, effective stress ratio – displacement, and stress path response for tests on the L12H0.6 surface in CR-CD (a-c) and CD-CR (d-f) directions. Steady state condition noted in Stress ratio – displacement in forward cycle of each test.
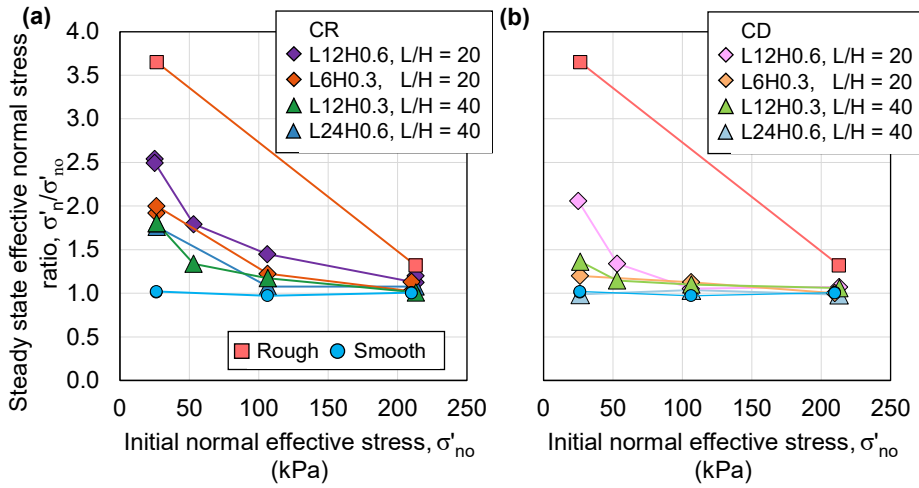
Figure 5.6. Normal effective stress ratios as a function of initial normal effective stress for the (a) CR and (b) CD forward directions, with values from tests on the rough and smooth surfaces for reference. All samples prepared to $D_R = 80 - 90\%$.
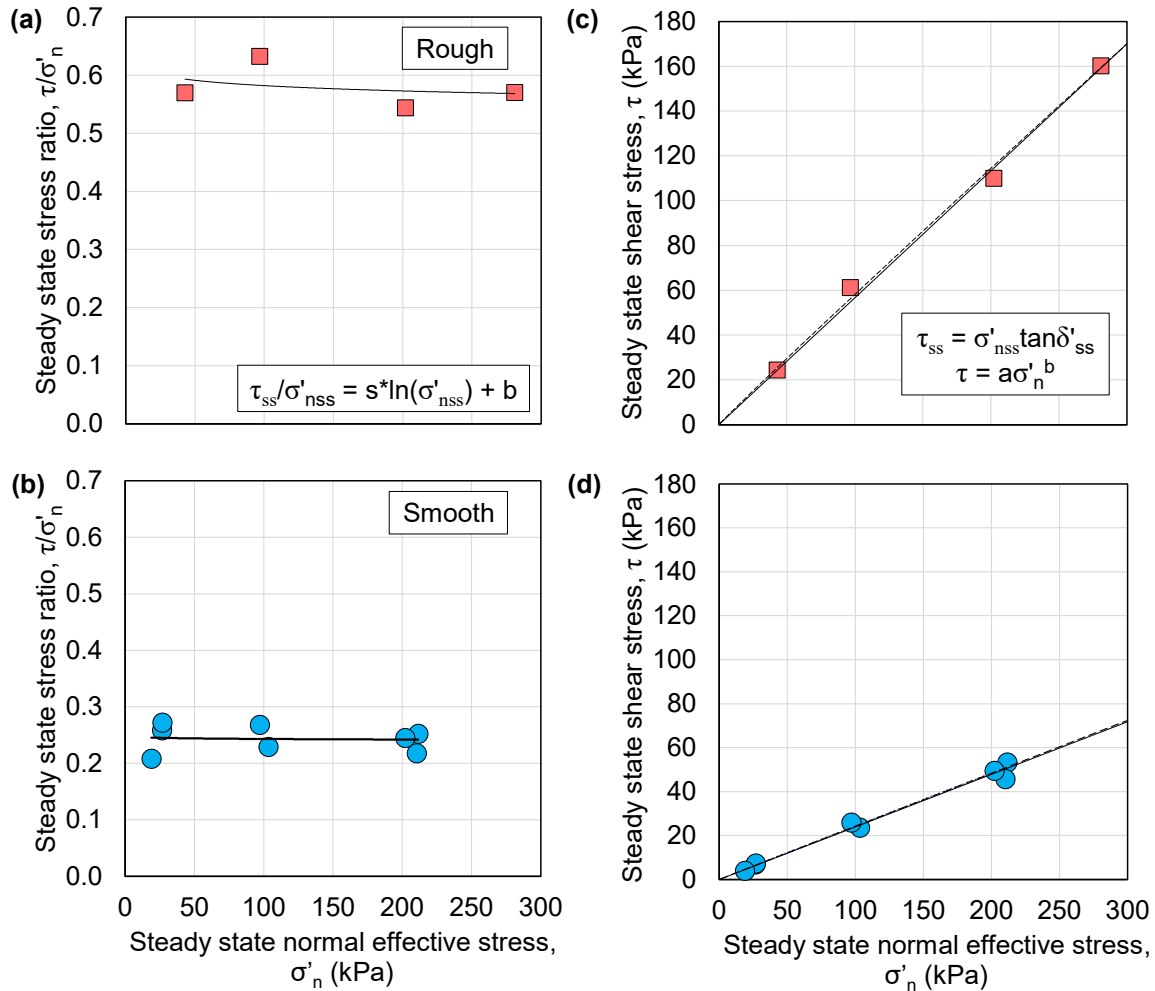
Figure 5.7. Steady state stress ratio as a function of steady state normal effective stress for tests on the (a) rough and (b) smooth surfaces. Failure envelopes fitted to the shear stress - normal effective stress results at steady state for the (a) rough (b) smooth surfaces.
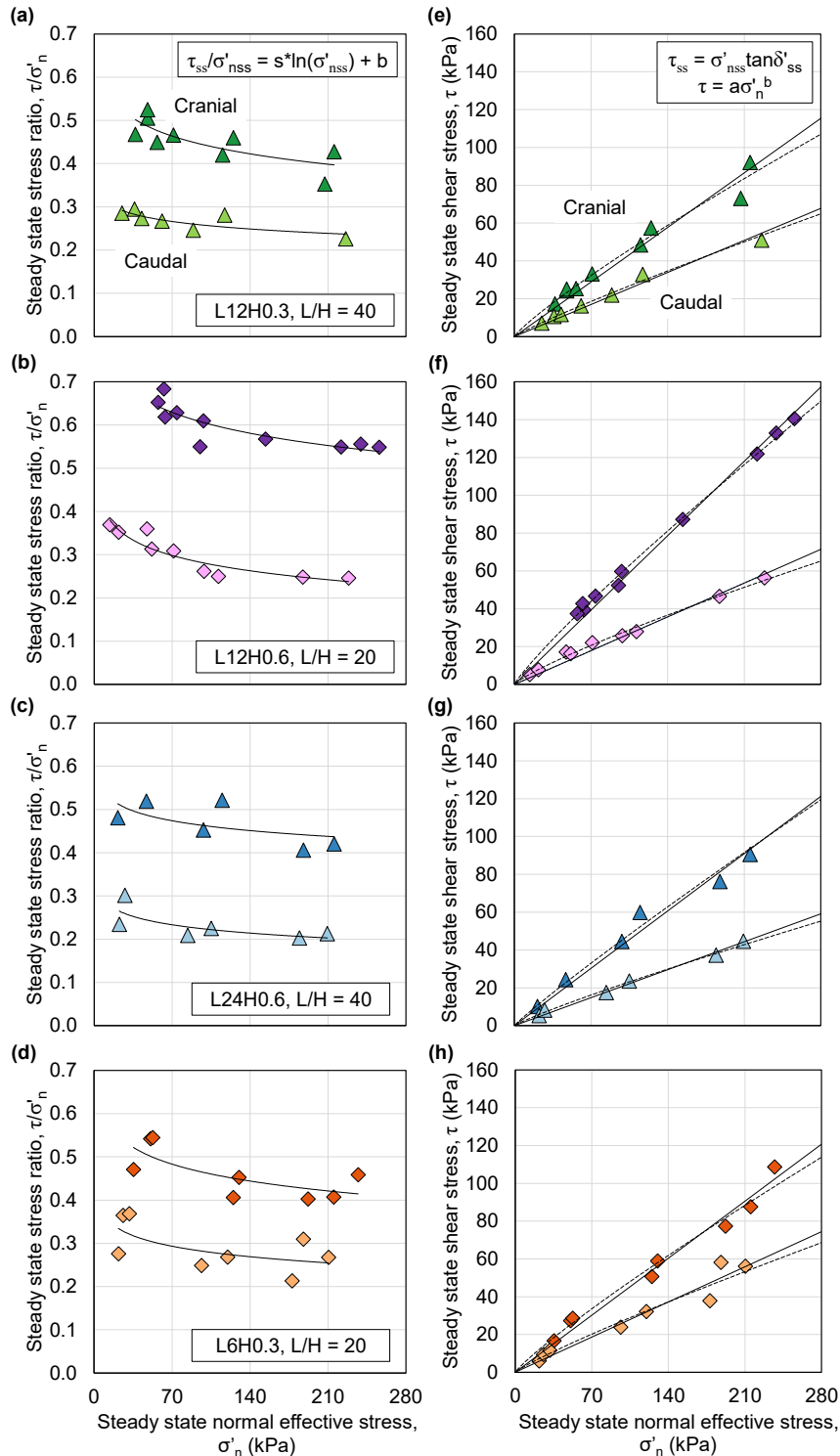
Figure 5.8. Steady state stress ratio as a function of steady state effective stress for the (a) L24H0.6 (b) L12H0.6 (c) L12H0.3 and (d) L6H0.3 surfaces. Failure envelopes fitted to the shear stress - effective stress results at steady state for the for the (a) L24H0.6 (b) L12H0.6 (c) L12H0.3 and (d) L6H0.3 surfaces.
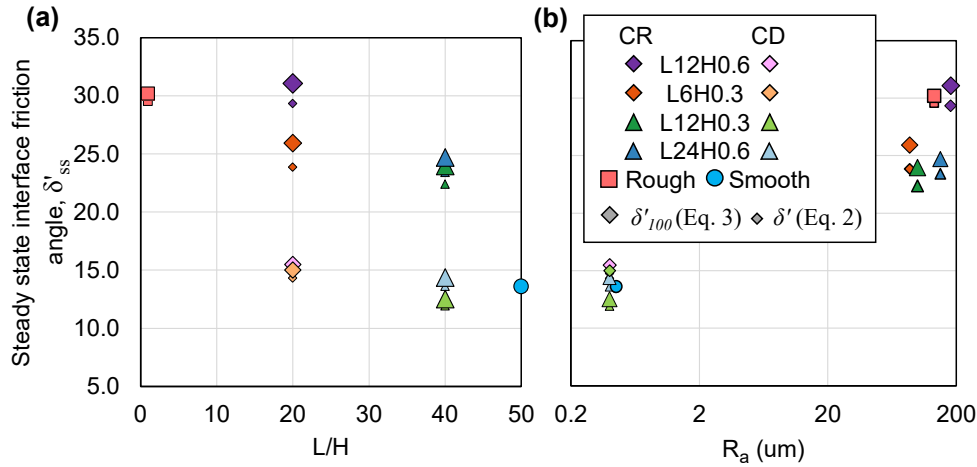
Figure 5.9. Steady state interface friction angles determined from Eqs. 2 and 3 as a function of (a) *L/H* and (b) R_a. Note: equivalent δ' from power fit calculated at $\sigma'_n = 100$ kPa.
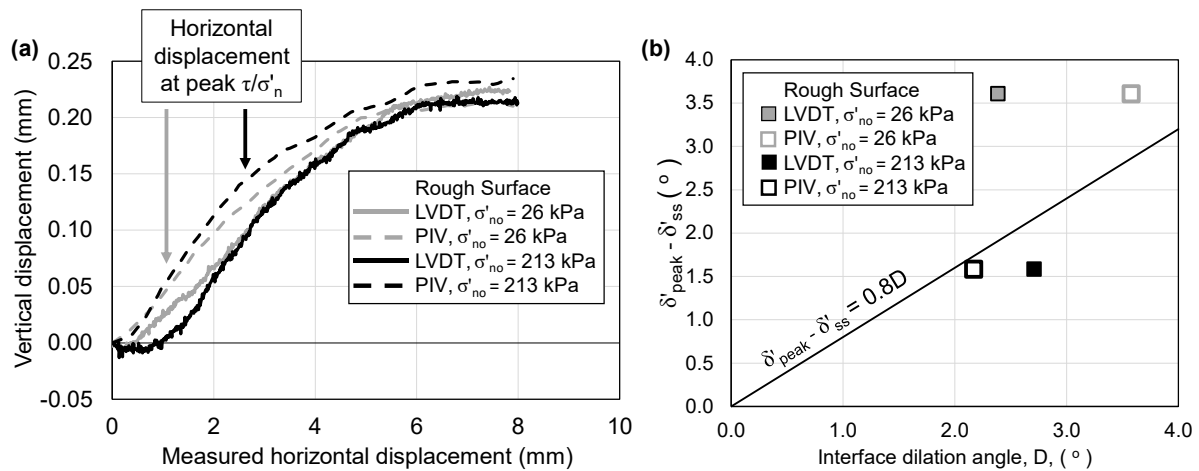
Figure 5.10. (a) Comparison of vertical displacement from instrument measurement and PIV analysis. (b) Interpreted interface dilation angle taken at the horizontal displacement corresponding to the peak stress ratio for noted tests. Results presented alongside Bolton's relationship.
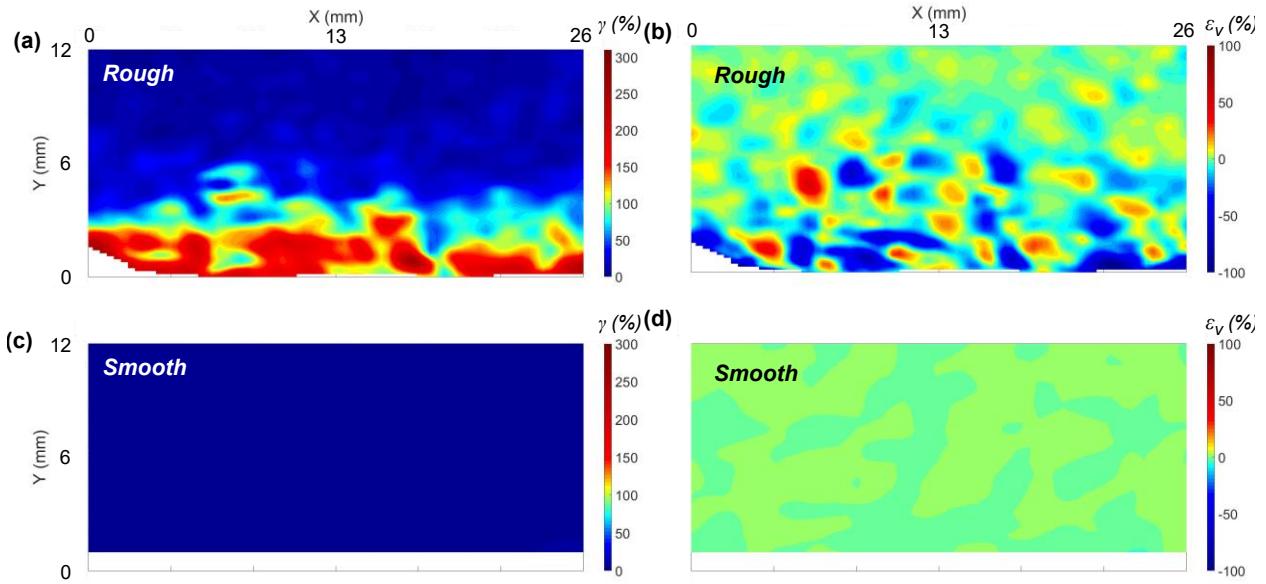
Figure 5.11. Shear and volumetric strain maps for rough (a,b) and smooth (c,d) surfaces for $\sigma'_{no} = 26$ kPa
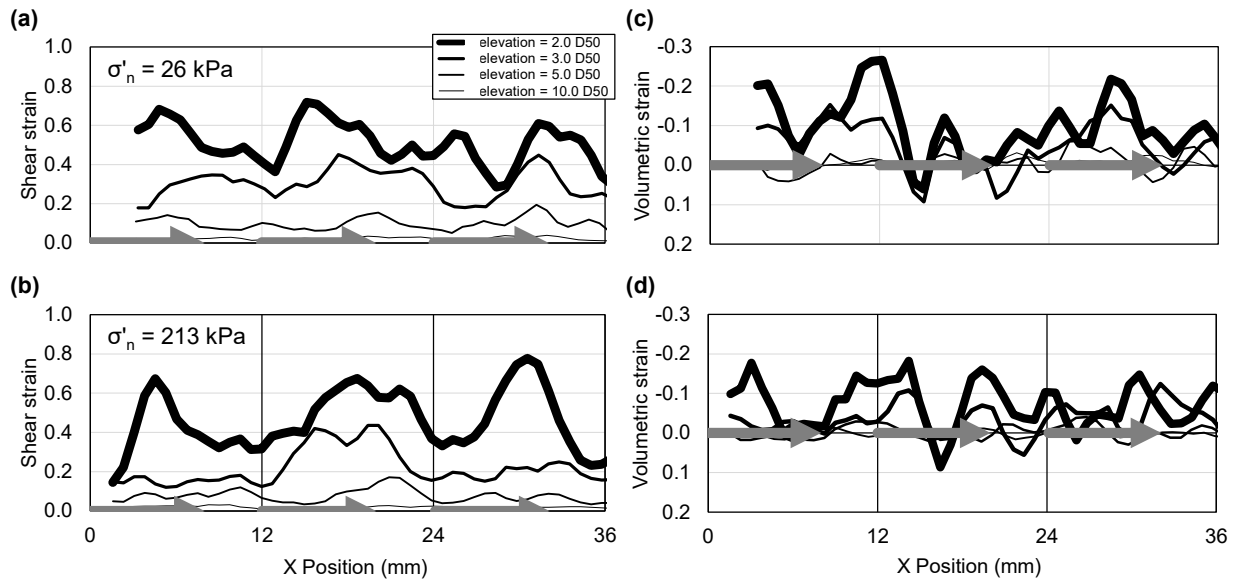
Figure 5.12. Shear strain and volumetric strain profiles at constant elevations for tests on the L12H0.3 surface at $\sigma'_{no} = 26$ (a,c) and 213 kPa (b,d), with arrows indicating asperity displacement

171
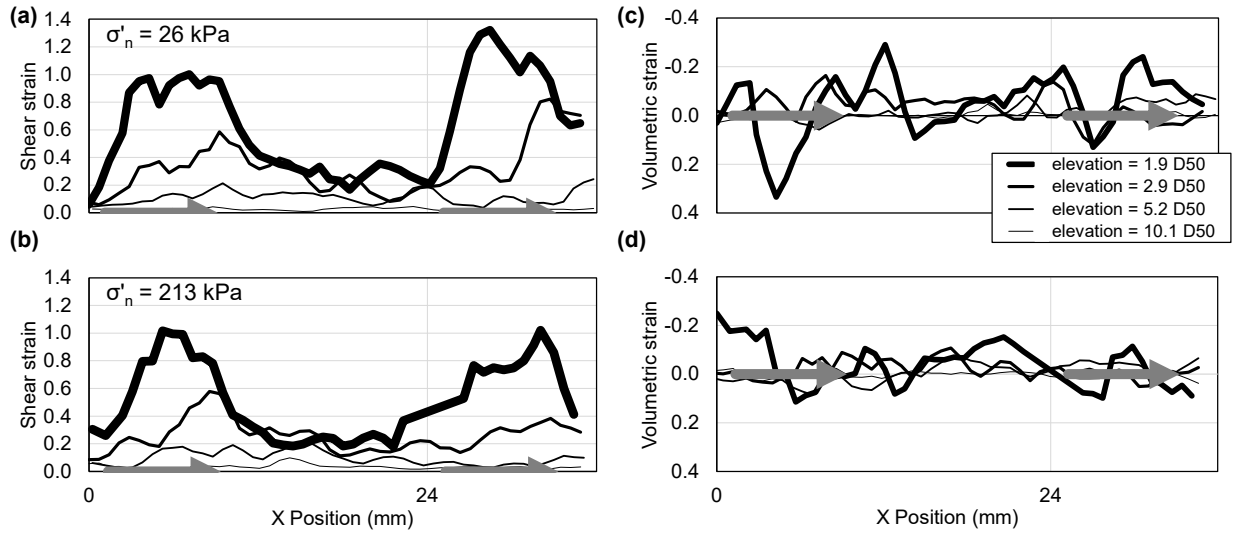
Figure 5.13. Shear strain and volumetric strain profiles at constant elevations for tests on the L24H0.6 surface at σ'_{no} = 26 (a,c) and 213 kPa (b,d), with arrows indicating asperity displacement
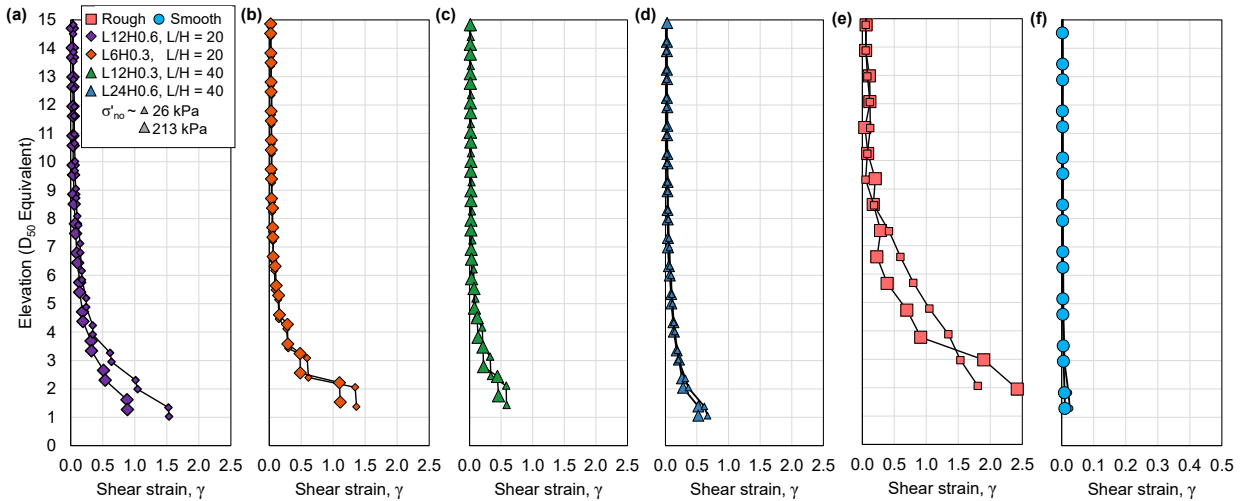
Figure 5.14. Average shear strain profiles at σ'_{no} = 26 and 213 kPa for tests on the (a) L24H0.6 (b) L12H0.6 (c) L12H0.3, (d) L6H0.3, (e) rough, and (f) smooth surfaces at 8mm displacement. Note different X axis scale on (f)
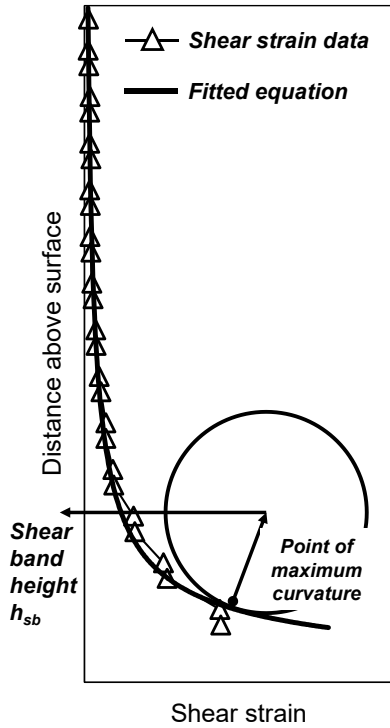
Figure 5.15. Methodology for evaluating the shear band height from shear strain profiles. Schematic shows fitted function with location of calculated highest curvature and associated osculating circle.
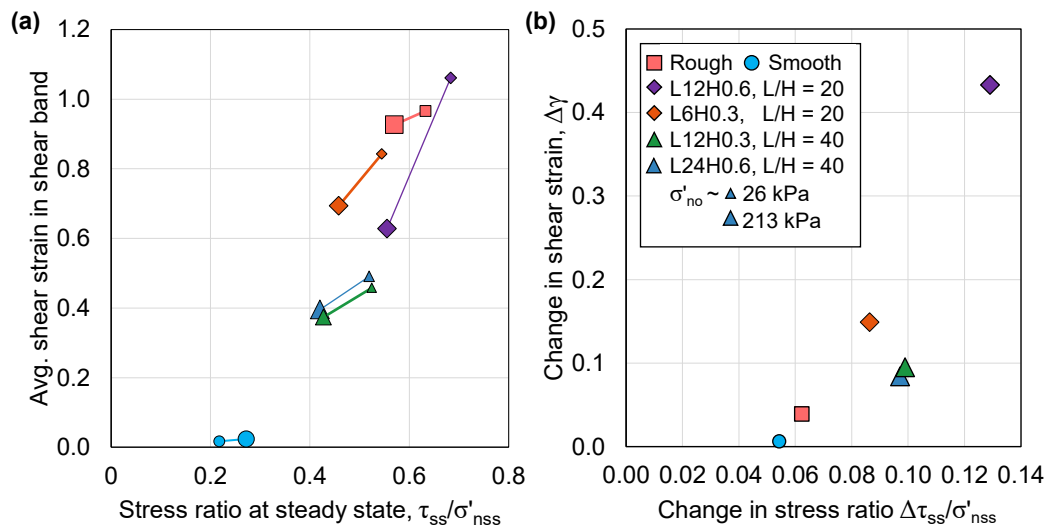
Figure 5.16. (a) Average shear strain in the shear band zone as a function of steady state stress ratio and (b) change in shear strain as a function of change in stress ratio.
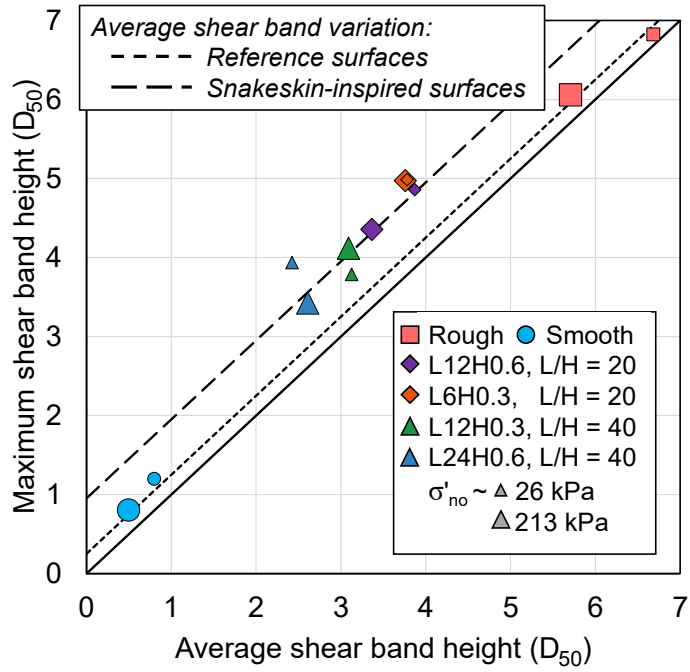
Figure 5.17. Average and maximum shear band heights for tests on the snakeskin-inspired and reference surfaces.

SUPPLEMENTARY FIGURES
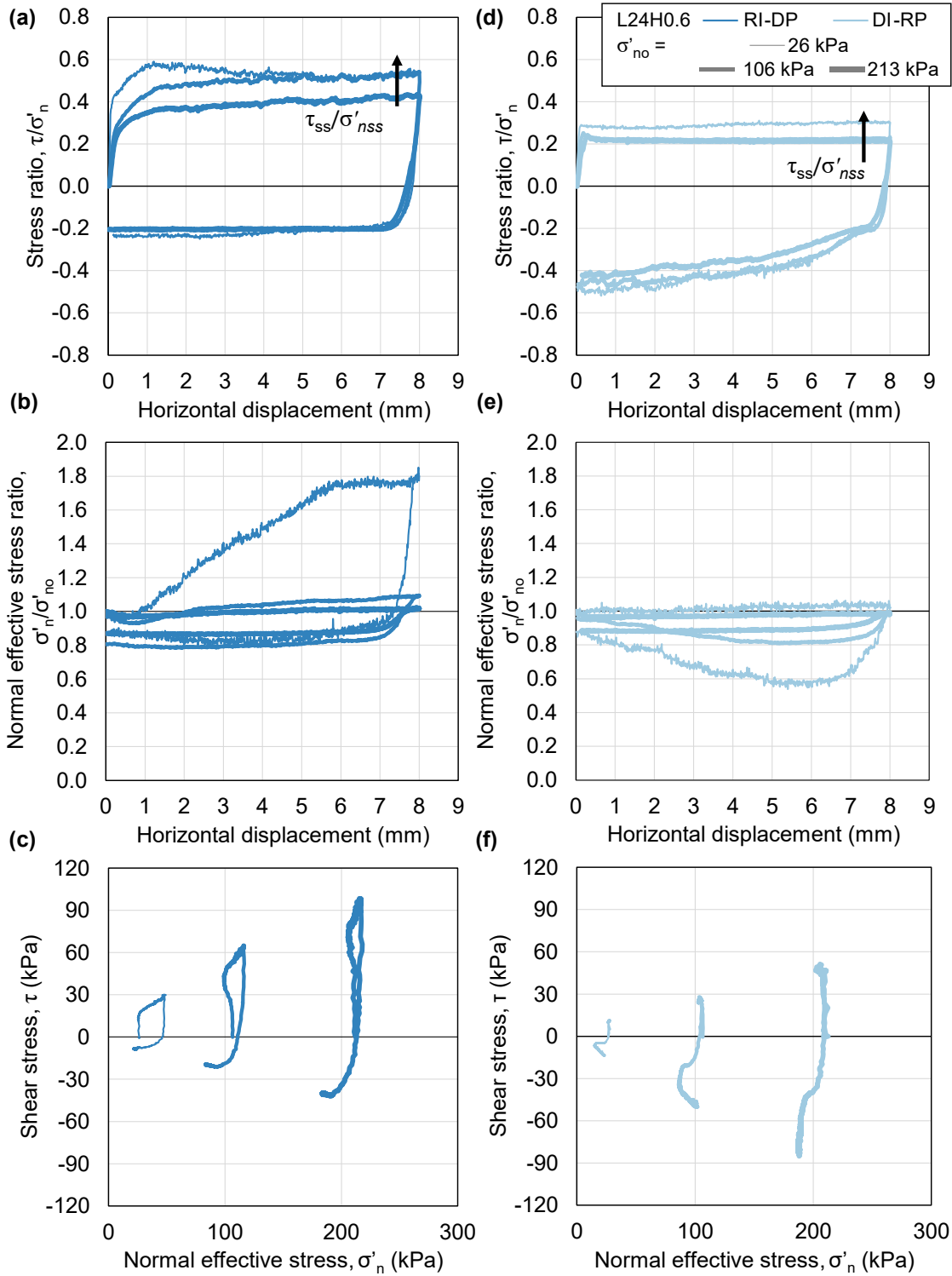
Figure S5.1. Stress ratio – displacement, effective stress ratio – displacement, and stress path response for tests on the L24H0.6 surface in CR-CD (a-c) and CD-CR (d-f) directions.
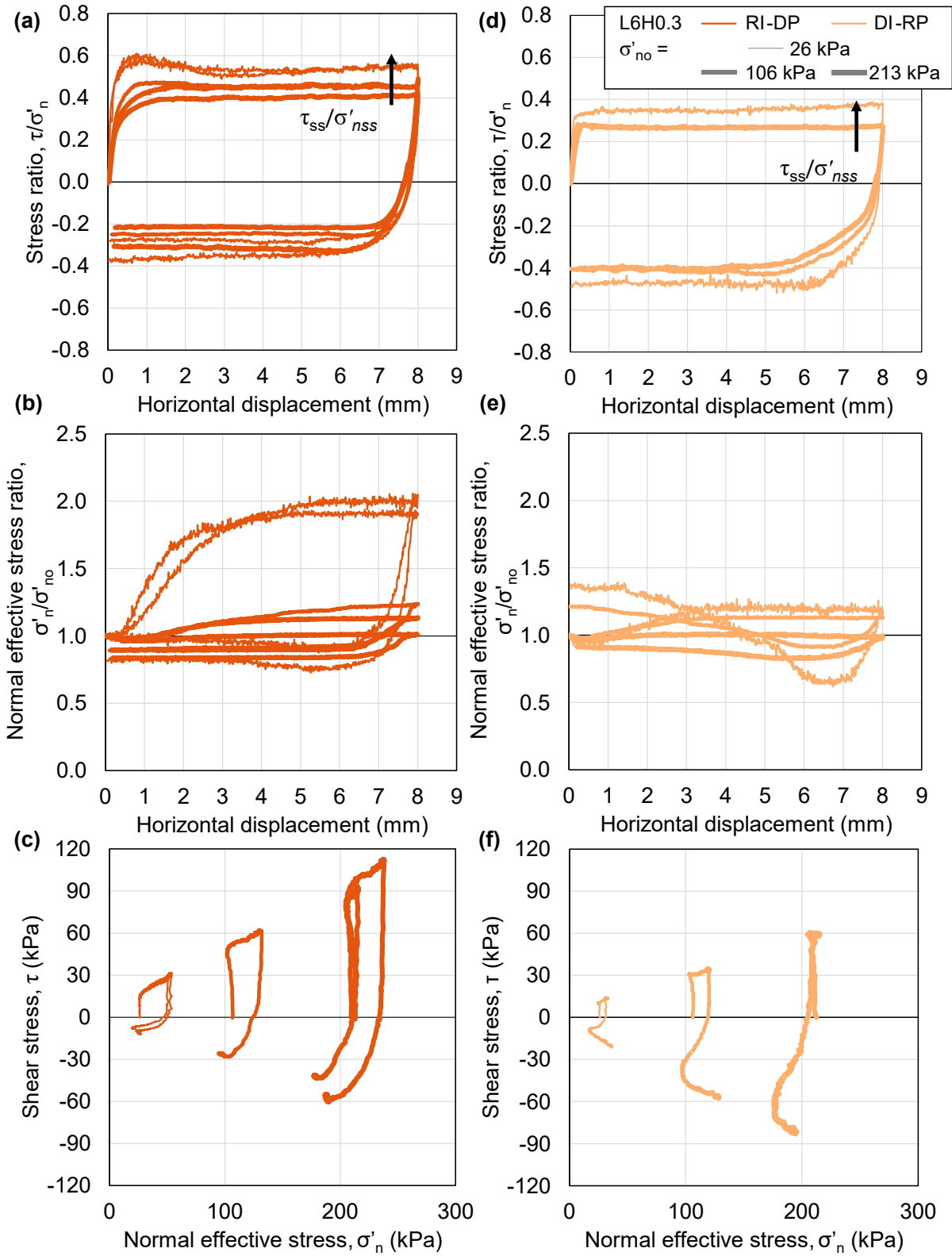
Figure S5.2. Stress ratio – displacement, effective stress ratio – displacement, and stress path response for tests on the L6H0.3 surface in CR-CD (a-c) and CD-CR (d-f) directions.
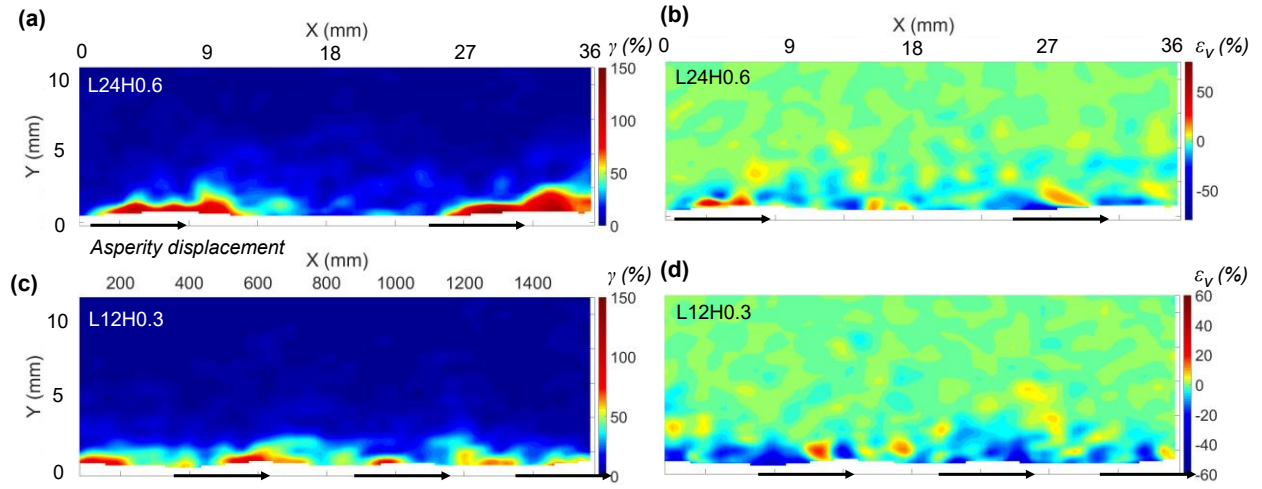
Figure S5.3. Shear and volumetric strain maps for L24H0.6 (a,b) and L12H0.3 (c,d) surfaces for $\sigma'_{no} = 26$ kPa

Chapter 6. Cyclic failure of sand-structure interfaces considering the effects of surface roughness and profile asymmetry

ABSTRACT

Pile load tests in the field provide insight into the failure of pile shafts under cyclic axial loading. However, these tests can be time consuming, costly, and may not be able to provide accurate measurements of local shear and normal effective stresses. Laboratory interface shear testing under Constant Normal Stiffness (CNS) boundary conditions have been shown to reasonably model the load transfer response of the unit shaft resistance. These tests are efficient and economical compared to pile load tests and can be conducted in a variety of soil and stress conditions. To assess the cyclic stability of pile shafts, a laboratory investigation was conducted on reference rough and smooth surfaces and on four snakeskin-inspired surfaces. The tests examined the effects of surface roughness, profile asymmetry, boundary stiffness, mean shear stress bias and initial normal effective stress level. Results indicate that the boundary stiffness, which is linked to the pile diameter and sand stiffness, plays a crucial role in the stability of pile shaft elements, where higher boundary stiffness leads to fewer cycles to failure. Under symmetric loading, the interfaces with snakeskin-inspired surfaces always failed in the caudal direction, associated with low frictional resistances. However, when a large enough static shear stress bias was introduced, the interface failed in the cranial side, associated with higher frictional resistances. The stress paths of tests on the reference and snakeskin-inspired surfaces led to a failure and phase transformation conditions that may be experienced by a pile shaft. The findings indicate that the cyclic stability of a pile shaft element may be better understood by considering the shaft profile geometry and soil state compared to global behavior measured at a pile head.

INTRODUCTION

Pile load tests from field and centrifuge testing provide predictions of stability as a function of the mean and cyclic load measured at the pile head. The stability of a pile subjected to a cyclic axial load is determined by the number of cycles required to reach a displacement criterion, either in terms of accumulated displacement or rate of displacement (Chan and Hanna 1980). Pile load testing is limited in its ability to assess the influence of individual parameters, such as the initial radial effective stress, radial effective stress evolution throughout cycling, and the effect of pile diameter, on the number of cycles to failure due to the complex stress conditions in the field and to the fact that the transfer of load by the pile shaft is governed by soil localization (Aghakouchak 2015). In addition, there are practical limitations to the number of tests that can be conducted due to mobilization and manufacturing costs. To systematically address the effects of surface roughness, profile asymmetry, boundary stiffness, initial radial effective stress, and static shear stress bias, a laboratory investigation was conducted between sand and six surface types, including reference rough and smooth surfaces as well as four surfaces with asymmetric profiles modeled after the ventral scales of snakes. Laboratory interface tests consider the loss of shaft capacity at a single element along the shaft length without potential effects from the gravitational stress gradient or the redistribution of loads along the pile length (Airey et al. 1992, Tabucanon et al. 1995, Bałachowski 2006, Wang et al. 2017). A schematic illustrating the link between the unit shaft resistance along the pile length and an interface shear test with CNS boundary conditions test are shown in Figure 6.1. The unit shear resistance, τ, that may be achieved by a pile shaft at the element level is described by:

$$\tau = \sigma_n' tan\delta' \hspace{4cm} \text{Eq. 1}$$

where δ' is the interface friction angle between a soil and structural material and σ'_n is the effective normal stress acting against the pile shaft. Numerous factors have been found to influence δ' both at peak and residual or critical state conditions, with the surface roughness (Brumund and Leonards 1973, Paikowsky et al. 1995, Dove and Jarrett 2002), particle shape (Uesugi and Kishida 1986, Rousé 2008, Vangla and Latha Gali 2016, Han et al. 2018), and relative density (DeJong and Westgate 2009) playing the most important roles.

The normal effective stress acting against the pile shaft may change as the pile shaft is displaced. Boulon and Foray (1986) proposed that the constant normal stiffness boundary condition based on cavity expansion theory to link the changes in σ'_n to the contraction or dilation of the soil around a pile. An estimate of the boundary stiffness, k, is given by:

$$k = \frac{4G}{D}$$
Eq. 2

where G is the operational soil shear modulus and D is the pile diameter. The stiffness is then linked to the changes in normal effective stress ($\Delta\sigma'_n$) and dilation or contraction (δ_v) by:

$$\Delta\sigma'_n = \sigma'_{no} - k(\delta_v)$$
Eq. 3

where dilation is denoted with a negative δ_v value and contraction with a positive δ_v value. Under CNS boundary conditions, dilation leads to increases in normal effective stress and contraction leads to a corresponding decrease, affecting shear stress by Eq. 1. The stress path and evolution of δ_v of an interface soil element subjected to loading under CNS conditions can be represented in $\tau - \sigma'_n$ and $\delta_v - \sigma'_n$ space (DeJong et al. 2006), where the path in $\delta_v - \sigma'_n$ space is constrained to a line with a slope of $1/k$. During monotonic loading, dense of critical samples will dilate and move along the $1/k$ line to the critical state condition, whereas during cyclic loading, cumulative contraction between cycles occurs leading to a loss of normal effective stress along the $1/k$ line. This effect has been observed in cyclic interface shear testing (Fakharian and Evgin, 1997,

Oumarou and Evgin 2005, Mortara et al. 2007) and is considered the mechanism underlying the friction fatigue effect observed as loss of pile shaft friction (Heerema 1980, Bond and Jardine 1991, Lehane and White 2005).

The role of surface roughness on the interface friction angle and contribution to unit shaft capacity has been studied extensively, where δ' increases with surface roughness, reaching a maximum value limited by the internal friction angle of the soil, φ'. It has been shown that the specific geometric profile of a surface may result in apparent δ' values greater than φ' when there are tall asperities which are well-spaced (Hryciw and Irsyam 1993, Martinez and Frost 2017, Samanta et al. 2018, Nardelli et al. 2019). Certain applications may benefit from this effect in one direction of loading compared to the other, such a reaction pile with lower installation resistance compared to high pullout resistance. To create profiles with such an effect, a bioinspired approach was used to create structural surfaces with profiles modeled after the ventral scales of snakes (Palumbo 2018, Martinez et al. 2019). Such surfaces were shown to mobilize higher resistances in the direction against the asperities (i.e., cranial) compared to the direction along the asperities (i.e., caudal). The geometric profile was applied to pile shafts, and it was found that such profiles were able to reduce the installation resistances compared to pullout resistances (O'Hara and Martinez 2020, O'Hara and Martinez 2022, Ch. 4 of this work). The results from cyclic pile load tests showed that the cyclic stability under tensile bias loading depended on the mean and cyclic loads applied at the pile head, leading to pullout displacements.

Due to difficulty in measuring both the radial effective and shear stress along a shaft section in the field or centrifuge (Zhu et al. 2009), the failure condition of piles is often analyzed at a global scale using interaction diagrams defined in terms of the normalized mean ($Q_m/Q_{tot.}$) and cyclic (Q_{cyc}/Q_{tot}) load applied at the pile head (Figure 6.1c). Based on the absolute displacement

or displacement rate, contours of number of cycles to failure (Nf) are defined. Interaction diagrams typically define three zones of stability, with $N_f = 100$ and $N_f = 1000$ contours defining the boundaries. A failure occurring before $N_f = 100$ is considered Unstable, no observed failure up to $N_f = 1000$ is considered Stable, and any intermediate condition is considered Metastable. The values of $Q_m/Q_{tot.}$ and $Q_{cyc}/Q_{tot.}$ in the interaction diagram are analogous to the lab condition where normalized mean shear stress (τ_m/τ_{max}) and cyclic stress (τ_{cyc}/τ_{max}) are applied, where τ_{max} is the monotonic shear resistance of the element.

This paper presents the results from a series of cyclic interface shear tests, summarizes those results in the context of a cyclic stability framework, and presents a simplified method for estimating the failure condition of a pile shaft element.

MATERIALS AND METHODS

Interface shear testing. A series of load- and displacement-controlled cyclic direct interface shear tests were conducted with a modified Geotac Direct Shear device (Trautwein, Houston, TX). Testing surfaces are affixed to a base platform, and a rectangular shear box containing the soil specimen overlays the surface. Normal and shear forces are measured with vertically and horizontally mounted load cells, and the shear and horizontal displacements are measured with linear potentiometers. The device is described in detail in Martinez et al. (2019) and Martinez and Stutz (2019) and in Chapter 2. The tests were conducted with k of 160, 320, and 1060 kPa/mm. In order to allow the control system to maintain the CNS condition, the displacement rate was adjusted to allow the vertical actuator to adjust the vertical force corresponding to the measured change in vertical displacement. The shearing rate ranged from 1mm/min at 160 kPa/mm to

0.1mm/min at 1060 kPa/mm, which has been shown to have a minimal effect on the mobilized interface shear strength of dry sands (Al-Mhaidib 2006).

A reference rough and smooth surface were used to capture failure interface behaviors dominated by shearing within the soil mass or interfacial sliding between the sand and surface, respectively. Four snakeskin-inspired surfaces were used to investigate the effect of surface geometry on cyclic stability, with ratios of asperity length (*L*) to height (*H*) of 20 and 40. Previous studies have shown a relationship between the *L/H* ratio and the interface friction angle of interfaces with the snakeskin-inspired surfaces. Therefore, two pairs of equivalent *L/H* surfaces with different *L* and *H* values were used to assess potential differences in the cyclic behavior. The surfaces with *L/H* = 20 had *L* = 12 mm and *H* = 0.60 mm and *L* = 6 mm and *H* = 0.30 mm, while the surfaces with *L/H* = 40 had *L* = 12 mm and *H* = 0.30 mm, and *L* = 24 mm and *H* = 0.60 mm. The surfaces are referred to throughout the text with the length and height of the asperities coded with *L* and *H* and the associated dimension, such as L12H0.3 (i.e., length of 12 mm and height of 0.3 mm). Directionality is denoted with CR for the cranial direction and CD for caudal direction. A schematic of the snakeskin-inspired surfaces is included in Figure 6.1b, shown to scale with the D_{50} of the sand used in this study. For the cyclic tests, the initial shearing direction is referred to first, followed by the opposite direction. For example, a test conducted where the surface is displaced in the CR direction in the first half cycle and in the CD direction in the second half cycle is be referred to as CR – CD. A summary of the tests conducted is presented in Table 6.1.

Medium dense specimens of Ottawa 20-30 (50 < Dr <60%) were used in all tests to ensure that cyclic failure would occur in a reasonable number of cycles. Ottawa 20-30 was used in all tests. This is a poorly graded subrounded sand with a minimum void ratio (e_{min}) of 0.49, maximum void

ratio (e_{max}) of 0.71, and median particle size (D_{50}) of 0.72 mm. Values of e_{min} and e_{max} were taken from Martinez and Frost (2017) and verified through the methods presented in Carey et al. (2020).

The failure condition for each test was evaluated based on a modified version of the stability criteria defined by Rimoy et al. (2013) where only the rate of accumulated axial deformation as a function of cycle number is considered since there is no direct method to estimate the pile diameter from boundary stiffness k since the operational shear modulus G is not well defined (Chow 1997). In the lab test, the corresponding condition is the rate of accumulated horizontal deformations as a function of cycle number. Therefore, the failure conditions are considered as follows:

- Stable: Low and stabilizing accumulated horizontal displacements with small rates of displacement accumulation smaller than 0.01 mm/cycle, with failure requiring more than 1000 cycles (N).

- Metastable: Rates of horizontal displacement accumulation between 0.01 mm/cycle and 0.1 mm/cycle, with failure requiring more than 100 cycles.

- Unstable: Cyclic failure within 100 cycles, with sustained rates of horizontal displacement accumulation greater than 0.1 mm/cycle.

All tests were conducted such that failure occurred in the Unstable and Metastable zone and a unique N_f value was assigned to each test. Following failure, a monotonic post – cyclic phase occurred in tests where the load limit was not met. The results are summarized in the Supplementary Table S6.1 for completeness.

RESULTS

The results from the displacement-controlled cyclic interface shear tests give insight of the stress path behavior of the different soil-surface combinations. The load-controlled cyclic tests indicate

that each surface type resulted in a unique failure response based on the cyclic shear and mean

shear stress and boundary stiffness. In addition, it was found that the initial normal stress (σ'_{no})

had an effect on the number of cycles to failure. The cyclic amplitude of shear stresses for all tests

is reported as a ratio of the cyclic stress to the maximum shear stress (τ_{max}) under constant normal

stress conditions at the given initial normal stress. For example, a test conducted on a rough surface

at $\tau_{cyc} = 27.6$ kPa and $\sigma'_{no} = 106$ kPa would have $\tau_{max} = 63.8$ kPa based on a $\delta' = 31.4°$, leading to

$\tau_{cyc}/\tau_{max} = 0.43$. The maximum interface friction angles used in this normalization were interpreted

from the tests presented in Ch. 5 and are presented in Table 6.2. For the snakeskin-inspired

surfaces, the peak interface friction angle in the CD direction was used since under symmetric

loading conditions it was found that failure always occurred in the CD direction. Although the

tests from Ch. 5 were conducted at a higher relative density, it is expected that a peak stress

behavior occurs for a medium dense sample. If the steady state friction angle is used, then τ_{cyc}/τ_{max}

would be greater than 1, which is not possible by the definition of the ratio.

Displacement-controlled stress – displacement and stress path response. A series of

displacement-limited interface shear tests was conducted, and it was found that each surface

exhibited a unique response in terms of the change from contractive to dilative behavior (phase

transformation), and loss of normal stress after an equivalent number of cycles. All displacement-

controlled tests were conducted at $\sigma'_{no} = 106$ kPa and k = 320 kPa/mm for 10 cycles with a double

amplitude displacement of 2 mm.

The stress – displacement and stress paths from tests conducted on the rough and smooth

surfaces are presented in Figure 6.2a-d. The test on the rough surface shows dilative behavior on

the first cycle, indicated by the slight upward inflection on the stress – displacement plot in Figure

6.2a. This is seen clearly in the stress path in Figure 6.2b, where the effective stress initially decreases, then increases once a certain stress condition is met. Based on the point of change from a decrease to an increase in effective stress each cycle, a phase transformation line was interpreted and included in Figure 6.2b along with the steady state interface friction angle estimated in Chapter 5. By the end of 10 cycles, the normal stress decreases from 106kPa to 37kPa due to a net contraction of 0.225 mm. The test on the smooth surface shows an initial peak and softening behavior in the first cycle with no apparent phase transformation. By the end of cycling, there is a small increase in effective stress near the maximum and minimum displacement limits. These points were used to define the phase transformation angle (θ) for the smooth surface, which is close to the steady state interface friction angle determined in Chapter 5. By the end of 10 cycles, the normal stress decreases from 106 kPa to 82 kPa due to a net contraction of 0.073 mm. These results highlight the greater shear strength that the rough surface can mobilize compared to the smooth surface, although the differences in phase transformation angle leads to a greater loss of effective stress for the rough surface compared to the smooth surface.

The stress – displacement paths from the tests conducted on the L12H0.3, L6H0.3, L12H0.6, and L24H0.6 surfaces at $\sigma'_{no} = 106$ kPa and $k = 320$ kPa/mm are presented in Figure 6.3. Depending on the direction of surface displacement (i.e., CR or CD), the stress response exhibits a response similar to the smooth or rough surface for all surfaces regardless of the initial shearing direction. When the surfaces are displaced in the CR direction, there is a clear upward inflection of shear stress, highlighting the dilatant response associated with soil shearing. When displacement occurs in the CD direction, the stress response is more similar to that of the smooth surface, although the upward inflection indicating dilatancy is slightly more pronounced, especially in the final cycles. The L12H0.6 mobilizes the greatest maximum shear stress throughout cycling in the

CR direction, while the other surfaces mobilize a similar maximum shear stress throughout cycling.

The stress paths from tests conducted on the L12H0.3, L6H0.3, L12H0.6, and L24H0.6 surfaces at σ'_{no} = 106 kPa and k = 320 kPa/mm are presented in Figure 6.3. The tests were conducted in both CD-CR and CR-CD sequences to investigate any potential differences in behavior based on initial shearing direction. All tests indicate similar phase transformation behavior and losses in effective stress regardless of the initial shearing direction. In the CR direction, all tests from each surface shows a characteristic phase transformation angle between 19.0° and 20.1° degrees. However, there is no clear trend in phase transformation angle based on the asperity height or L/H. In the caudal direction, the surfaces with H = 0.3 mm asperities exhibit a higher phase transformation angle compared to the surfaces with H = 0.6 mm asperities. All surfaces lead to similar losses in normal stress at the end of 10 cycles, with a final normal stress ranging between 60 kPa and 75 kPa with the exception of the test on the L24H0.6 test in the cranial first direction (Figure 6.3d) which has a final normal stress of 81 kPa. This may be due to slight variations in initial sand relative density.

Shear – normal stress model for directionally dependent surfaces. The results of the displacement-controlled cyclic interface shear tests indicate that interfaces with the rough surface had a phase transformation angle significantly smaller than their interface friction angle. In contrast, interfaces with the smooth surface had a phase transformation angle similar to their interface friction angle. For the snakeskin-inspired surfaces, $\theta < \delta'$ in the CR direction and $\theta \sim \delta'$ in the CD direction. Pra-ai and Boulon (2017) presented cyclic stress path behavior in terms of stress ratios defining critical state and phase transformation. The results herein support the use of

such a framework, where surfaces of varying roughness and profile geometry have different relative magnitudes of stress ratio at critical state, peak, and phase transformation as presented in Figure 6.4a-c. It was found that among the surfaces, the rough surface had a higher critical stress ratio than the other surface types tested, and a phase transformation line lower compared to its peak stress ratio line. The smooth surface had the lowest critical stress ratio, with a phase transformation line similar to the steady state line. For the snakeskin-inspired surfaces, the magnitude of the steady state stress ratio and stress ratio corresponding to phase transformation was different depending on the surface profile geometry, but it was found that in the CR direction, the phase transformation line was lower than the steady state line, whereas in the CD direction the lines are similar.

Load controlled stress – displacement and stress path response. The results from the symmetric load-controlled tests (i.e., $\tau_m = 0$ kPa) indicate that N_f depends on the magnitude of τ_{cyc} and τ_m, surface roughness and profile geometry of the surface, and boundary stiffness. The stress – displacement and stress paths from tests conducted on the rough surface at $\sigma'_{no} = 106$ kPa, $k = 320$ kPa/mm, and τ_{cyc}/τ_{max} of 0.40 0.44, and 0.53 are presented in Figure 6.5a-f. The results are shown until the N_f criterion is met. Figure 6.4a shows the stress – displacement response for the test conducted at $\tau_{cyc}/\tau_{max} = 0.40$. There is an initial large drop in normal effective stress during the first cycle as the first shear stress limit is achieved, then the displacement continues to accumulate until the displacement rate criteria is met at $N = 12.5$. In the stress path (Figure 6.5d) it can be seen that the effective stress degrades throughout cycling, and the stress condition corresponding to phase transformation is met prior to failure, which corresponds to the onset of rapid displacement accumulation. A similar trend is observed in the tests conducted at $\tau_{cyc}/\tau_{max} = 0.44$ and 0.53 but

with more rapid onset of accumulation of horizontal displacements, larger drops in effective stress per cycle, and fewer cycles to failure.

The stress displacement response and stress paths from tests conducted on the smooth surface at $\sigma'_{no} = 106$ kPa, $k = 320$ kPa/mm, $\tau_{cyc}/\tau_{max} = 0.65$, 0.73 and 0.74 are presented in Figure 6.6a-f. For the tests conducted at $\tau_{cyc}/\tau_{max} = 0.65$ and 0.73, there is minimal accumulation of horizontal displacement prior to failure, while at $\tau_{cyc}/\tau_{max} = 0.74$ small horizontal displacements are accumulated prior to failure. Failure is marked by a sudden loss of shear stress and continued displacement. In the stress path, each test exhibits a small initial decrease in effective stress during the first cycle as some initial soil contraction occurs, followed by subsequent small decreases in effective stress per cycle. The smooth surface does not exhibit a clear phase transformation prior to failure, but rather a sudden failure occurs when the stress state reaches the condition associated with the peak interface friction angle interpreted from monotonic tests on the smooth surface in Chapter 5 and presented in Table 6.2. This failure is more indicative of pure interfacial sliding, where a brittle failure occurs after reaching a peak shear stress (Figure 6.6d-f). N_f decreases by an order of magnitude at each τ_{cyc}/τ_{max} condition presented in Figure 6.6a-c, with N_f decreasing from 125 to 1.5 over an increase of τ_{cyc}/τ_{max} from 0.65 to 0.74.

Similar trends are observed for both rough and smooth surfaces in tests conducted at $k = 160$ kPa/mm terms of stress – displacement and stress path evolution, except for an increase in N_f at any given τ_{cyc}/τ_{max} compared to the tests conducted at $k = 320$ kPa/mm. Figure 6.7a-d shows the stress – displacement and stress paths for tests on smooth and rough surfaces conducted at $k = 160$ kPa/mm at $\tau_{cyc}/\tau_{max} = 0.51$ (rough) and 0.80 (smooth). For the rough surface, horizontal displacements begin to accumulate during the first cycle, and the stress path shows that the phase transformation line is crossed for two cycles prior to N_f. Compared to the test at $k = 320$ kPa/mm

with $\tau_{cyc}/\tau_{max} = 0.53$ (Figure 6.5c,f), N_f is greater with the smaller k which highlights the effect of CNS boundary condition on the degradation of effective stresses under cyclic interface loading conditions, in alignment with Eq. 3. The effects are even more pronounced for the test on the smooth surface, where $\tau_{cyc}/\tau_{max} = 0.80$ results in $N_f = 134.5$, in comparison to the test at $k = 320$ kPa/mm where $\tau_{cyc}/\tau_{max} = 0.74$ results in $N_f = 1.5$.

The stress – displacement and stress paths from symmetric tests on the snakeskin-inspired surfaces exhibit behavior that combines characteristics of the rough and smooth surfaces. CD-CR tests conducted on the L12H0.3 ($L/H = 40$) and L6H0.3 ($L/H = 20$) surfaces at $\sigma'_{no} = 106$ kPa, $k = 300$ kPa/mm, $\tau_{cyc}/\tau_{max} = 0.74$ and 0.72, respectively, are presented in Figure 6.8a-d. The test with the L12H0.3 surface results in accumulation of small horizontal displacements in either direction prior to failure in the caudal direction. The stress path shows a reduction in effective stress as cycling continues. Failure occurs at 3.5 cycles near the caudal peak interface friction stress ratio with no additional increase in shear stress after failure. The test on the L6H0.3 surface exhibits a smaller decrease in normal effective stress per cycle, leading to failure in 21.5 cycles; however, this test exhibits larger accumulated displacements by the end of cycling than the L12H0.3 surface. Prior to the failure, displacements begin to accumulate in both the CR and CD direction, with failure occurring in the CD direction. The stress path of the L6H0.3 surface surpasses the line corresponding to the CD peak interface friction angle, indicating dilation induced increases in shear stress. At failure, a clear phase transformation is observed, with the mobilized shear stress remaining at smaller magnitudes than the target τ_{cyc}, resulting in continuing displacements in the CD direction.

Figure 6.9a-d shows the accumulated horizontal displacements as a function of N for the rough and smooth surfaces at $k = 160$ and 320 kPa/mm. N_f is indicated with a large symbol in each

graph and τ_{cyc}/τ_{max} is specified for each test. For both the rough and smooth surfaces, the number of cycles to failure decreases with increasing boundary stiffness. For the rough surface, displacements begin to accumulate prior to N_f, and continue to accumulate after N_f until the stress limit fails to be met. In contrast, minimal displacements accumulate prior to N_f for the smooth surface, and once N_f is met, a loss of strength occurs, and the surface continues to displace.

The tests on snakeskin-inspired surfaces exhibit similar trends as the tests on the smooth surface. Figure 6.10a-f presents the accumulated horizontal displacements as a function of cycle number for all tests on the four snakeskin-inspired surfaces. The number of cycles to failure decreases as the boundary stiffness increases. All tests eventually fail in the CD direction, although in some cases displacements begin to accumulate in the CR direction prior to failure. Specifically, this occurs in two tests on the L12H0.3 surface (Figure 6.10a) and two tests on the L24H0.6 surface (Figure 6.10e). It is noted that this effect is only observed on tests with $L/H = 40$, which tend to have a smaller difference between the CD interface friction angle and the CR phase transformation angle. This may indicate an "intermediate" failure condition where displacements begin to accumulate in the CR direction, but loss of strength occurs in the CD direction. However, the tests that exhibit this behavior do not correspond to a specific τ_{cyc}/τ_{max} value, and thus may be a result of a bias in the testing apparatus. Tests on the L12H0.3, L12H0.6, and L24H0.6 surfaces show there is minimal accumulation of displacements in the CD direction prior to failure, and once failure is reached the surfaces continue to displace in the caudal direction without meeting the shear stress limit. The tests on the L6H0.3 surface indicate a similar brittle failure, but in 4 of 6 tests an additional cycle occurred before the interface fails to mobilize τ_{cyc}. This result may indicate that the L6H0.3 surface is more dilative when displaced in the CD direction than the other surfaces.

Influence of initial effective normal stress. Symmetric cyclic interface shear tests (i.e., $\tau_m = 0$ kPa) were performed on the rough surface at $\sigma'_{no} = 53$ kPa with similar τ_{cyc}/τ_{max} ratios as the tests conducted at $\sigma'_{no} = 106$ kPa. Tests were conducted at both $k = 160$ kPa/mm and 320 kPa/mm to assess the effect of boundary stiffness and σ'_{no}. The results indicate that at the same k, σ'_{no} has a significant effect on the number of cycles to failure. The stress paths from tests conducted at $\sigma'_{no} = 53$ kPa and $k = 320$ kPa/mm are presented in Figure 6.11a-c in order of increasing τ_{cyc}/τ_{max}. The effective stresses for the test with $\tau_{cyc}/\tau_{max} = 0.41$ decrease, causing the stress path to cross the phase transformation line and then reach failure. Similar results are observed in the tests conducted at $\tau_{cyc}/\tau_{max} = 0.47$ and 0.61, where failure occurs within a single or half cycle after the phase transformation line is crossed. The accumulated horizontal displacements with cycle number are presented in Figure 6.12a,b for tests with $\sigma'_{no} = 53$ kPa at $k = 160$ and 320 kPa/mm. For tests at $k = 160$ kPa/mm, displacements continue to accumulate after failure for an additional 1 to 2 cycles, with larger total accumulated displacements before the target τ_{cyc} was no longer met. In contrast, displacements continued to accumulate after failure for up to a single cycle for the tests at $k = 320$ kPa/mm, with lower accumulated displacements compared to tests at $k = 160$ kPa/mm before the target τ_{cyc} was no longer met. In addition, for comparable values of τ_{cyc}/τ_{max}, tests conducted at $k = 320$ kPa/mm failed in fewer cycles than tests conducted at $k = 160$ kPa/mm. For either boundary stiffness, tests with similar τ_{cyc}/τ_{max} values failed in fewer cycles at $\sigma'_{no} = 53$ kPa compared to $\sigma'_{no} = 106$ kPa. These results highlight the effect of the initial normal stress on the number of cycles to failure under CNS boundary conditions as described by Eq. 3.

Effect of stress bias, τ_m/τ_{max}. The effect of a shear stress bias on the number of cycles to failure has been characterized with respect to randomly structured surfaces such as the rough surface used

herein (Tsuha et al. 2012). Previous studies show that for a given cyclic load τ_{cyc}/τ_{max}, N_f decreases as τ_m/τ_{max} is increased accompanied by a more rapid onset of accumulation of displacement. In contrast, the effect of τ_m/τ_{max} has not been investigated for snakeskin-inspired surfaces, where the CR and CD directions have different failure envelopes, phase transformation lines, and stress – displacement responses (i.e., Figures 6.4 and 6.8). Broadly, the results show that when a mean shear stress of high enough magnitude is introduced in the CR direction, the stress paths clearly show that the failure limit (δ'_{peak}) is not met in the CD direction prior to failure. Tests were conducted on the L12H0.3 surface with $k = 320$ kPa/mm, $\sigma'_{no} = 106$ kPa, at $\tau_{cyc}/\tau_{max} = 0.53 – 0.55$ and $\tau_m/\tau_{max} = 0.14$, $\tau_m/\tau_{max} = 0.20$, $\tau_m/\tau_{max} = 0.27 – 0.28$ in either the CR or CD direction first, with the bias applied in the CR direction regardless. The horizontal displacement – shear stress and stress paths for each test conducted are shown in 13a-i. The tests conducted at $\tau_m/\tau_{max} = 0.14$, the test conducted in the CR – CD sequence (Figure 6.13b) fails in 28 cycles in the CR direction, while the test conducted in the CD – CR direction fails in 19.5 cycles in the CR direction. For both tests, the failure occurred from the displacement rate criteria, which is indicated in Figures 6.13a-c, but after displacements begin to accumulate, the stress criteria is not able to be met in the CD direction which results in continued displacement. For the tests conducted at $\tau_m/\tau_{max} = 0.20$, the test conducted in the CR-CD sequence (Figure 6.13e) fails in 35 cycles in the CR direction, while the CD-CR test (Figure 6.12f) fails in 7.5 cycles also in the CR direction. Based on the stress path of the test conducted in the CR first direction, the target τ_{cyc} is met for a significant number of cycles after reaching the phase transformation line as well as the steady state failure envelope. This may indicate that some box friction was accumulated during this test. Once displacements begin to accumulate, the displacement rate criteria is met within 6 cycles. A similar trend is observed in the test conducted at $\tau_m/\tau_{max} = 0.20$ in the CD-CR sequence, where initially there are small

displacements per cycle, and then a rapid onset of displacement accumulation occurs near failure. In both tests, the phase transformation line is crossed, but there is not a significant dilative response. In the CD-CR test (Figure 6.13f) failure occurs as the CR failure envelope is crossed. For a $\tau_m/\tau_{max} = 0.27 - 0.28$, the CR-CD test (Figure 6.13h) fails in 4 cycles in the CR direction, while the CD-CR test (Figure 6.13i) fails in 2 cycles, also in the CR direction. Although the phase transformation line is crossed in both tests, there is not a significant dilative response observed and the failure criteria is met as the failure envelope is reached.

The failure behavior as a function of stress bias for the L12H0.3 surface had the following characteristics:

- For the tests conducted herein, increases in τ_m/τ_{max} resulted in a decrease in N_f (Figure 6.14).

- For tests conducted at $\tau_m/\tau_{max} = 0.14$ failure occurred in the CR direction, but the failure direction reversed within 4 cycles to the CD direction.

- Displacements continued to accumulate in the CR direction following N_f to the displacement limit of the device (Figure 6.13) for tests conducted $\tau_m/\tau_{max} = 0.20$ or larger, with the final cycle before the limit ranging from 4 mm to 6mm.

It is possible that displacements may continue to accumulate in the CR direction while still meeting the target τ_{cyc}, and total loss of shear strength may occur in the CD direction in a similar manner as the tests conducted at $\tau_m/\tau_{max} = 0.14$. Such a large deformation problem would benefit from lab testing using a ring shear apparatus.

DISCUSSION

Cycles to failure and interaction diagrams. The number of cycles to failure from each load controlled cyclic test can be interpreted to define the bounds of the Stable, Metastable, and Unstable zones in an interaction diagram. The number of cycles to failure from each test is plotted in Figure 6.15a-e as a function of τ_{cyc}/τ_{max}. This condition is equivalent to the symmetric loading line along the y-axis in an interaction diagram, where $\tau_m/\tau_{max} = 0$. The tests on the rough surface resulted in the fewest cycles to failure for a given τ_{cyc}/τ_{max} ratio, followed by the L24H0.6, L6H0.3, L12H0.3, and L12H0.6 surfaces, respectively, and the smooth surface resulted in the greatest number of cycles to failure. To assess the effect of profile geometry on the cyclic stability achieved by each surface, the data was fitted with the following equation:

$$\tau_{cyc}/\tau_{max} = aN^{-b} \hspace{6cm} \text{Eq. 4}$$

where *a* and *b* are fitting parameters. τ_{cyc}/τ_{max} was calculated at $N = 100$ and 1000, which define the Unstable – Metastable and Metastable – Stable boundaries, respectively, for the symmetric load condition where failure always occurred in the CD direction. The values from this analysis are presented in Figure 6.16a-c where τ_{cyc}/τ_{max} is shown as a function of *L/H* at $N_f = 100$ and 1000, and as the difference in τ_{cyc}/τ_{max} between $N_f = 100$ and 1000 ($\Delta\tau_{cyc}/\tau_{max}$). The rough surface is plotted at $L/H = 1$ and the smooth surface is plotted at $L/H = 50$ for visualization purposes. The interpolation of the trend to $N_f = 1000$ assumes that failure within this limit is governed by a similar process of decreases in normal stress due to cumulative contraction. For both $N_f = 100$ and 1000 (Figure 6.16a,b), the rough surface has the lower τ_{cyc}/τ_{max} regardless of the boundary stiffness. The smooth surface at $k = 160$kPa/mm has the largest τ_{cyc}/τ_{max} value for both $N_f = 100$ and $N_f = 1000$, while at $k = 320$ kPa/mm the L6H0.3 surface resulted in the largest τ_{cyc}/τ_{max} value at $N_f = 100$. While the specific values of τ_{cyc}/τ_{max} are informative of the limits of stability, the difference between τ_{cyc}/τ_{max} at $N_f = 100$ (Unstable/Metastable) and $N_f = 1000$ (Metastable/Stable) ($\Delta\tau_{cyc}/\tau_{max}$)

provides a relative measure of the brittleness of the cyclic failure (Figure 6.16c). Large $\Delta\tau_{cyc}/\tau_{max}$ values indicate a gradual transition between the Unstable and Stable zones, while small $\Delta\tau_{cyc}/\tau_{max}$ values indicate a sudden, brittle transition from the Stable to Unstable zones. For all surface types, $\Delta\tau_{cyc}/\tau_{max}$ is greater for higher values of k. This difference is least pronounced for the rough surface likely due to the ability for the surface to meet the load limit through dilation induced increases in shear stress compared to the other surfaces. In addition, the $L/H = 20$ surfaces lead to the greatest $\Delta\tau_{cyc}/\tau_{max}$, while the $L/H = 40$ surfaces have a similar value as the rough surface. The smooth surface resulted in the smallest $\Delta\tau_{cyc}/\tau_{max}$, indicating the most brittle failure behavior.

The results from the symmetric cyclic interface shear tests may be compared to stability of piles from load tests under symmetric loading conditions. Jardine et al. (2005) and Jardine and Standing (2012) assert that cyclic stability of pile shafts may be interpreted in terms of either unit shaft resistance or global shaft resistance in the same interaction diagram (as presented in Figure 6.1c). The L12H0.3 surface presented herein may be compared to the RI-DP0.30 pile used in Ch. 4 as both the surface and pile were subjected to failure in the CD direction. In addition, the results from the rough surface may be compared to results presented in Jardine and Standing (2012) for a rough pile shaft tested in the field. In order to provide a reasonable comparison between field, laboratory, and centrifuge experiments, the values of τ_{cyc}/τ_{max} were plotted for the symmetric loading condition as a function of the boundary stiffness, k, in Figure 6.17. For the results from Jardine and Standing (2012), k was estimated to be 60 kPa/mm based on the pile diameter (0.457 m) and typical values for the small strain shear modulus, G_o, (30 MPa), and assuming an operational G of $0.25G_o$. Similarly, k was estimated to be approximately 1500 kPa/mm in the centrifuge experiment based on a 19.5 mm pile diameter, $G_o = 30$ MPa, and $G = 0.25G_o$. For the rough pile shaft and lab tests, the τ_{cyc}/τ_{max} for $N_f = 100$ boundary tends to decrease with increasing

196

boundary stiffness, while the τ_{cyc}/τ_{max} for $N_f = 1000$ boundary is similar for the field results ($k \sim 60$ kPa/mm) as the lab results at $k = 160$kPa/mm, and then decreases at $k = 320$ kPa/mm. Similar results are seen for the L12H0.3 surface and RI-DP0.30 pile, where both the τ_{cyc}/τ_{max} values at $N_f = 100$ and $N_f = 1000$ decreases with increasing boundary stiffness. The lab results at $k = 1060$ kPa/mm are in reasonable agreement with the results from the centrifuge test, although the τ_{cyc}/τ_{max} value at $N_f = 100$ from the centrifuge experiments is larger than the value from the lab tests (0.58 compared to 0.46). It is noted that this comparison is greatly affected by the value of the operational shear modulus. Namely, a value of $0.25G_o$ was used herein to estimate k, whereas if $0.10G_o$ was used then k would be 600 kPa/mm and the values from the centrifuge and laboratory tests would be in closer agreement.

Normalized stress ratio and initial normal stress. The use of a normalized load combination (i.e., τ_{cyc}/τ_{max} or τ_m/τ_{max}) as a unique parameter to describe the stability of pile shaft elements may lead to either an under or overestimation of the actual stability (i.e., $N_f = 100$ for a specific τ_{cyc}/τ_{max} and τ_m/τ_{max} combination). This can be seen be comparing the interpreted τ_{cyc}/τ_{max} values for $N_f = 100$ and $N_f = 1000$ from tests conducted at different σ'_{no}. The results from the tests on rough surfaces at $\sigma'_{no} = 53$ kPa are presented in Figure 6.18a in terms of τ_{cyc}/τ_{max} and N_f. For similar values of τ_{cyc}/τ_{max}, there are more cycles to failure at $\sigma'_{no} = 106$ kPa than at 53 kPa. These results are summarized in Figure 6.18b, where the interpreted τ_{cyc}/τ_{max} values for $N_f = 100$ and $N_f = 1000$ values are shown as a function of σ'_{no} and k. These results indicate three important aspects of the mechanics governing the failure of soil-structure interfaces: (i) at a lower stress, the number of cycles to failure is lower than at a higher stress, which necessarily follows from Eq. 3 and the space defined in Figure 6.4, and is discussed further in the following sections, (ii) at a lower normal

stiffness, N_f increases more rapidly as the initial normal stress increases, and (iii) regardless of the normal stiffness or initial effective stress, the difference between the cyclic stress at $N_f = 100$ and $N_f = 1000$ is negligible for the rough surface even if the absolute values are different.

Stress path failure analysis. The interaction diagram is useful for mapping failure in terms of a displacement rate given a combination of cyclic and mean loads, but provides little flexibility for estimating the number of cycles to failure for individual elements along a pile shaft or exploring the effects of soil state and boundary condition. Here, a simplified model was employed to estimate the cumulative contraction to failure by introducing a definition of the cyclic load and a failure condition.

Based on these failure envelopes, the CNS model can be used to directly estimate the cumulative volumetric contraction required to meet a failure criterion. If a failure is described using a stress ratio (τ/σ'_n) criterion, and the failure shear stress (τ_f) is the sum of τ_{cyc} and τ_m, then the following equation expresses the shear stress at which failure will occur:

$$\tau_f = \frac{\tau_{cyc} + \tau_m}{\tau_{max}} * tan\delta' * \sigma'_{no} \qquad \text{Eq. 5}$$

The value of δ' may be any appropriate interface friction angle based on the failure criterion (i.e., steady state or an effective stress-dependent peak value). It may be most appropriate to use the peak, which determines the maximum shear strength that may be realized by any shaft element. The normal stress at failure is then defined by:

$$\sigma'_{nf} = \frac{\tau_f}{(\tau/\sigma'_n)_f} \qquad \text{Eq. 6}$$

where $(\tau/\sigma'_n)_f$ is a chosen stress ratio defining failure. For the rough surface, the stress ratio corresponding to the phase transformation line agrees well with the onset of displacement

198

accumulation, whereas for the smooth surface the peak friction angle better aligned with the failure condition. Using the initial effective stress and the computed effective stress at failure, the CNS model gives the cumulative vertical displacement to that failure condition:

$$\Delta\delta_v = \frac{\sigma'_{no} - \sigma'_{nf}}{k}$$ Eq. 7

Figure 6.19a-g shows theoretical curves for cumulative contraction to failure for each surface predicted from Eq. 6 and 7, with $(\tau/\sigma'_n)_f$ noted in each figure. Two curves were calculated for each surface from the maximum and minimum τ_{cyc}/τ_{max} tested on each surface to envelope the possible behavior. The datapoints plotted in Figure 6.19a-g correspond to the cumulative contraction at the failure condition N_f defined by the displacement rate criteria of 0.1mm/cycle for all tests conducted on each surface.

The experimental results agree well with the CNS model, although the model tends to underpredict the vertical contraction to failure. For the tests on the rough surface at $\sigma'_{no} = 53$ and 106 kPa, the model captures the trends well, with the tests at k = 160 kPa/mm in Figure 6.19a showing more contraction to the failure criterion compared to the model. Similar results are seen in Figure 6.19b. This underprediction is due to the nature of the failure, where phase transformation occurs and displacements begin accumulating at a more rapid rate, while vertical contraction continues to occur. On the other hand, the model assumes immediate failure and does not account for continued contraction. In Figure 6.19c and 19d, the results from the smooth and L12H0.3 are presented, respectively. Compared to the rough surface, the results agree better with the envelopes calculated from the model. This is due to the brittle nature of the failures for the smooth and L12H0.3 surface, where failure occurs with no dilation induced increases in shear stress following. Figure 6.12e presents the data from the L12H0.6 surface, showing a similar trend as the rough surface, with the datapoints showing greater contraction at failure compared to the model. This

agrees with the behavior of the L12H0.6 which is more dilative compared to the L12H0.3 or smooth surfaces. Figure 6.19f shows the results from the L6H0.3 surface, and it can be seen that the experimental results do not agree with the predicted values, although the range in values is similar between the experimental and predicted results. As noted in the stress – displacement response and the accumulated horizontal displacement – cycle response, the L6H0.3 surface has more dilative tendencies than the other snakeskin-inspired surfaces. This may lead to a similar over-prediction of the estimated contraction to failure as the rough surface. Figure 6.19g shows the results from the L6H0.3 surface, and shows a similar trend as the rough surface, with the datapoints showing greater contraction at failure compared to the model indicating a less brittle failure than the L12H0.3 and smooth surfaces.

The CNS model provides a reasonable estimate of cumulative contraction to failure defined by a stress ratio compared to failure defined by a displacement rate criteria. In general the model underpredicts the cumulative contraction, which would correspond to predicting fewer cycles to failure. It is noted that the experimental results indicate a log-linear relationship between cumulative contraction to failure and number of cycles to failure, which is presented in Figure S6.1 of the Supplementary material. The experimental and theoretical results are in best agreement when the failure is brittle, such as for the smooth and L12H0.3 surfaces. Further work is recommended to create a direct relationship between the contraction to failure and the number of cycles to failure.

The results presented herein indicate that cyclic interface behavior between sand and a structural surface has similarities which are consistent the mechanics of sand under direct simple shear loading at constant volume. Tests on the rough surface and snakeskin-inspired surfaces displaced in the CR direction have the most directly transferrable similarities since the they induce

shearing in the soil mass. In terms of the phase transformation line, qualitatively the rough and CR surfaces have a similar phase transformation line relative to the failure envelope. In addition, the τ_{cyc}/τ_{max} vs N_f plots for the tests on the rough surface show converging similarities to typical *CRR* vs. N_f relationships for clean sand as the boundary stiffness is increased. Specifically, the exponential term, *b*, from Eq. 4 increases from 0.09 at $k = 160$ kPa/mm to 0.13 at $k = 320$ kPa/mm, where $b = 0.34$ would be a typical value for clean sand at a constant volume condition, or infinite *k*. Tests on the smooth and CD displaced surfaces do not have the same direct similarities as the behavior is dominated by sliding. For example, the tests on the smooth surface do not have pronounced volumetric change behavior, with sliding at the surface dominating the response. It would be useful to conduct direct simple shear tests under CNS boundary conditions to directly evaluate the soil behavior. In addition, constant volume interface shear tests at a larger range of initial normal stresses as well as constant volume conditions would be beneficial in assessing the similarities to soil behavior.

CONCLUSIONS

A series of laboratory cyclic interface shear tests were conducted to assess the effect of surface roughness, profile geometry, boundary stiffness, cyclic shear stress magnitude, static shear stress bias, and initial effective stress the on accumulation of deformations and cyclic stability of surfaces subjected to cyclic loads. Experiments were performed on four snakeskin-inspired surfaces, a reference rough surface, and a reference smooth surface.

The boundary stiffness had the greatest effect on the number of cycles to failure for a given initial effective stress, where tests conducted with higher boundary stiffnesses resulted in fewer

cycles to failure at the same cyclic shear stress magnitude. The surface roughness and profile geometry also had an important effect on the accumulation of displacement and number of cycles to failure. The rough surface accumulated the largest displacements prior to failure, followed by the snakeskin inspired surfaces, and the smooth surface with the least. The smooth surface exhibited brittle failure accompanied by a sudden loss of shear strength. In symmetric loading conditions, the interfaces with snakeskin-inspired surfaces always failed in the CD direction, although in certain cases some displacements accumulated in the CR direction. When a shear stress bias greater than 20% of the interface strength was introduced in the CR direction, failure changed from a sudden loss of strength in the CD direction to continued displacements in the CR direction.

The results from tests conducted on all surfaces were summarized in terms of the cyclic stress to reach failure in 100 and 1000 cycles. $N_f = 100$ $N_f = 1000$ conditions correspond to the zones between Unstable and Metastable and between Metastable and Stable, respectively, under symmetric loading conditions. The rough surface had the lowest values of τ_{cyc}/τ_{max} for the boundary between Unstable and Metastable conditions, the smooth surface had the greatest corresponding τ_{cyc}/τ_{max} values, and the snakeskin inspired surfaces have intermediate values.

The magnitude of initial effective stress was shown to have a governing effect on the number of cycles to failure for the rough surface, where smaller initial effective stresses led to failure in a smaller number of cycles. This effect is a result of the imposed CNS boundary conditions. A framework for estimating failure based on cumulative contraction was expanded, and it was shown that the experimental results matched the theoretical results. These results indicate that the cyclic stability of a pile shaft element in terms of the cumulative contraction to failure may be robustly represented by accounting for the boundary stiffness, effective normal stress, and shaft surface geometry through the use of a stress ratio defining failure.

Data. All data from the tests conducted at the UC Davis CGM are available on DesignSafe under PRJ-3320.

ACKNOWLEDGEMENTS

REFERENCES

Aghakouchak, A., W. W. Sim, and R. J. Jardine. 2015. "Stress-path laboratory tests to characterise the cyclic behaviour of piles driven in sands." *Soils and Foundations*, 55 (5): 917–928. https://doi.org/10.1016/j.sandf.2015.08.001.

Airey, D., R. Al-Douri, and H. Poulos. 1992. "Estimation of Pile Friction Degradation from Shearbox Tests." *Geotech. Test. J.*, 15 (4): 388. https://doi.org/10.1520/GTJ10253J.

Al-Mhaidib, A. I. 2006. "Influence of shearing rate on interfacial friction between sand and steel." *Engineering Journal of the University of Qatar*, 19: 1–16.

Bałachowski, L. 2006. "Scale effect in shaft friction from the direct shear interface tests." *Archives of Civil and Mechanical Engineering*, 6 (3): 13–28. https://doi.org/10.1016/S1644-9665(12)60238-6.

Bond, A. J., and R. J. Jardine. 1991. "Effects of installing displacement piles in a high OCR clay." *Géotechnique*, 41 (3): 341–363. https://doi.org/10.1680/geot.1991.41.3.341.

Brumund, W., and G. Leonards. 1973. "Experimental Study of Static and Dynamic Friction Between Sand and Typical Constuction Materials." *J. Test. Eval.*, 1 (2): 162. https://doi.org/10.1520/JTE10893J.

Carey, T. J., N. Stone, and B. L. Kutter. 2020. "Grain Size Analysis and Maximum and Minimum Dry Density Testing of Ottawa F-65 Sand for LEAP-UCD-2017." *Model Tests and Numerical Simulations of Liquefaction and Lateral Spreading*, B. L. Kutter, M. T. Manzari, and M. Zeghal, eds., 31–44. Cham: Springer International Publishing.

Chan, S.-F., and T. H. Hanna. 1980. "Repeated Loading on Single Piles in Sand." *J. Geotech. Engrg. Div.*, 106 (2): 171–188. https://doi.org/10.1061/AJGEB6.0000920.

Chow, F. C., 1997. "Investigations into the behaviour of displacement piles for offshore structures." Doctoral dissertation, University of London Imperial College.

Dove, J. E., and J. B. Jarrett. 2002. "Behavior of Dilative Sand Interfaces in a Geotribology Framework." *J. Geotech. Geoenviron. Eng.*, 128 (1): 25–37. https://doi.org/10.1061/(ASCE)1090-0241(2002)128:1(25).

Fakharian, K., and E. Evgin. 1997. "Cyclic Simple-Shear Behavior of Sand-Steel Interfaces under Constant Normal Stiffness Condition." *J. Geotech. Geoenviron. Eng.*, 123 (12): 1096–1105. https://doi.org/10.1061/(ASCE)1090-0241(1997)123:12(1096).

Han, F., E. Ganju, R. Salgado, and M. Prezzi. 2018. "Effects of Interface Roughness, Particle Geometry, and Gradation on the Sand–Steel Interface Friction Angle." *J. Geotech. Geoenviron. Eng.*, 144 (12): 04018096. https://doi.org/10.1061/(ASCE)GT.1943-5606.0001990.

Heerema, E. P. 1978. "Predicting Pile Driveability: Heather As An Illustration Of The 'Friction Fatigue' Theory." *All Days*, SPE-8084-MS. London, United Kingdom: SPE.

Hryciw, R. D., and M. Irsyam. 1993. "Behavior of Sand Particles Around Rigid Ribbed Inclusions During Shear." *Soils and Foundations*, 33 (3): 1–13. https://doi.org/10.3208/sandf1972.33.3_1.

Jardine, R. J., and J. R. Standing. 2012. "Field axial cyclic loading experiments on piles driven in sand." *Soils and Foundations*, 52 (4): 723–736. https://doi.org/10.1016/j.sandf.2012.07.012.

Jardine, R., F. Chow, R. Overy, and J. Standing. 2005. *ICP design methods for driven piles in sands and clays*.

Lehane, B. M., and D. J. White. 2005. "Lateral stress changes and shaft friction for model displacement piles in sand." *Can. Geotech. J.*, 42 (4): 1039–1052. https://doi.org/10.1139/t05-023.

Mortara, G., A. Mangiola, and V. N. Ghionna. 2007. "Cyclic shear stress degradation and post-cyclic behaviour from sand–steel interface direct shear tests." *Can. Geotech. J.*, 44 (7): 739–752. https://doi.org/10.1139/t07-019.

Nardelli, A., P. P. Cacciari, and M. M. Futai. 2019. "Sand–concrete interface response: The role of surface texture and confinement conditions." *Soils and Foundations*, 59 (6): 1675–1694. https://doi.org/10.1016/j.sandf.2019.05.013.

Oumarou, T. A., and E. Evgin. 2005. "Cyclic behaviour of a sand steel plate interface." *Canadian geotechnical journal*, 42 (6): 1695–1704. NRC Research Press Ottawa, Canada.

Paikowsky, S., C. Player, and P. Connors. 1995. "A Dual Interface Apparatus for Testing Unrestricted Friction of Soil Along Solid Surfaces." *Geotech. Test. J.*, 18 (2): 168. https://doi.org/10.1520/GTJ10320J.

Pra-ai, S., and M. Boulon. 2017. "Soil–structure cyclic direct shear tests: a new interpretation of the direct shear experiment and its application to a series of cyclic tests." *Acta Geotech.*, 12 (1): 107–127. https://doi.org/10.1007/s11440-016-0456-6.

Rousé, P. C., R. J. Fannin, and D. A. Shuttle. 2008. "Influence of roundness on the void ratio and strength of uniform sand." *Géotechnique*, 58 (3): 227–231. https://doi.org/10.1680/geot.2008.58.3.227.

Samanta, M., P. Punetha, and M. Sharma. 2018. "Influence of surface texture on sand–steel interface strength response." *Géotechnique Letters*, 8 (1): 40–48. https://doi.org/10.1680/jgele.17.00135.

Tsuha, C. H. C., P. Y. Foray, R. J. Jardine, Z. X. Yang, M. Silva, and S. Rimoy. 2012. "Behaviour of displacement piles in sand under cyclic axial loading." *Soils and Foundations*, 52 (3): 393–410. https://doi.org/10.1016/j.sandf.2012.05.002.

Uesugi, M., and H. Kishida. 1986. "Influential Factors of Friction Between Steel and Dry Sands." *Soils and Foundations*, 26 (2): 33–46. https://doi.org/10.3208/sandf1972.26.2_33.

Vaid, Y. P., and S. Sivathayalan. 1996. "Static and cyclic liquefaction potential of Fraser Delta sand in simple shear and triaxial tests." *Can. Geotech. J.*, 33 (2): 281–289. https://doi.org/10.1139/t96-007.

Vangla, P., and M. Latha Gali. 2016. "Effect of particle size of sand and surface asperities of reinforcement on their interface shear behaviour." *Geotextiles and Geomembranes*, 44 (3): 254–268. https://doi.org/10.1016/j.geotexmem.2015.11.002.

Wang, J., S. Liu, and Y. P. Cheng. 2017. "Role of normal boundary condition in interface shear test for the determination of skin friction along pile shaft." *Can. Geotech. J.*, 54 (9): 1245–1256. https://doi.org/10.1139/cgj-2016-0312.

Zhu, B., R. Jardine, and P. Foray. 2009. "The Use of Miniature Soil Stress Measuring Cells in Laboratory Applications Involving Stress Reversals." *Soils and Foundations*, 49 (5): 675–688. https://doi.org/10.3208/sandf.49.675.

Table 6.1. Summary of tests conducted, including surface type, initial normal effective stress, boundary stiffness, and cyclic stress amplitude. *Indicates τ_{cyc}/τ_{max} and τ_m/τ_{max}.

Surface	σ'_{no} (kPa)	k (kPa/mm)	τ_{cyc}/τ_{max}	Surface	σ'_{no} (kPa)	k (kPa/mm)	τ_{cyc}/τ_{max}
Rough	106	160	0.43	L12H0.3 CR	106	1060	0.55
Rough	106	160	0.51	L12H0.3 CR	106	1060	0.46
Rough	106	160	0.60	L12H0.3 CR	106	1060	0.64
Rough	106	320	0.40	L12H0.3 CD	106	1060	0.55
Rough	106	320	0.53	L12H0.3 CD	106	1060	0.47
Rough	106	320	0.44	L12H0.3 CD	106	1060	0.64
Rough	53	160	0.38	L12H0.6 CR	106	160	0.88
Rough	53	160	0.63	L12H0.6 CR	106	160	0.82
Rough	53	160	0.51	L12H0.6 CR	106	160	0.73
Rough	53	320	0.41	L12H0.6 CD	106	160	0.81
Rough	53	320	0.61	L12H0.6 CD	106	160	0.73
Rough	53	320	0.47	L12H0.6 CR	106	320	0.73
Smooth	106	160	0.80	L12H0.6 CR	106	320	0.65
Smooth	106	160	0.87	L12H0.6 CR	106	320	0.57
Smooth	106	160	0.84	L12H0.6 CD	106	320	0.72
Smooth	106	320	0.74	L12H0.6 CD	106	320	0.65
Smooth	106	320	0.65	L12H0.6 CD	106	320	0.57
Smooth	106	320	0.73	L24H0.6 CR	106	320	0.75
L12H0.3 CR	106	160	0.75	L24H0.6 CR	106	320	0.76
L12H0.3 CR	106	160	0.75	L24H0.6 CR	106	320	0.85
L12H0.3 CR	106	160	0.67	L24H0.6 CD	106	320	0.85
L12H0.3 CD	106	160	0.68	L24H0.6 CD	106	320	0.96
L12H0.3 CD	106	160	0.73	L6H0.3 CR	106	320	0.88
L12H0.3 CD	106	160	0.76	L6H0.3 CR	106	320	0.82
L12H0.3 CR	106	320	0.74	L6H0.3 CR	106	320	0.71
L12H0.3 CR	106	320	0.65	L6H0.3 CD	106	320	0.85
L12H0.3 CR	106	320	0.68	L6H0.3 CD	106	320	0.78
L12H0.3 CD	106	320	0.74	L6H0.3 CD	106	320	0.69
L12H0.3 CD	106	320	0.59				
L12H0.3 CR	106	320	0.53/0.27*				
L12H0.3 CR	106	320	0.53/0.20*				
L12H0.3 CR	106	320	0.54/0.14*				
L12H0.3 CD	106	320	0.53/0.28*				
L12H0.3 CD	106	320	0.55/0.20*				
L12H0.3 CD	106	320	0.54/0.14*				

Table 6.2. Interface friction values used to calculate τ_{max}. Phase transformation angles interpreted from displacement-controlled tests.

Surface	δ' for calculation of τ_{max}	Phase transformation angle, θ
L24H0.6 CD	14.8°	13.0°
L6H0.3 CD	16.8°	15.4°
L12H0.3 CD	16.2°	15.4°
L12H0.6 CD	17.1°	13.5°
Smooth	16.7°	15.1°
Rough	31.4°	21.7°
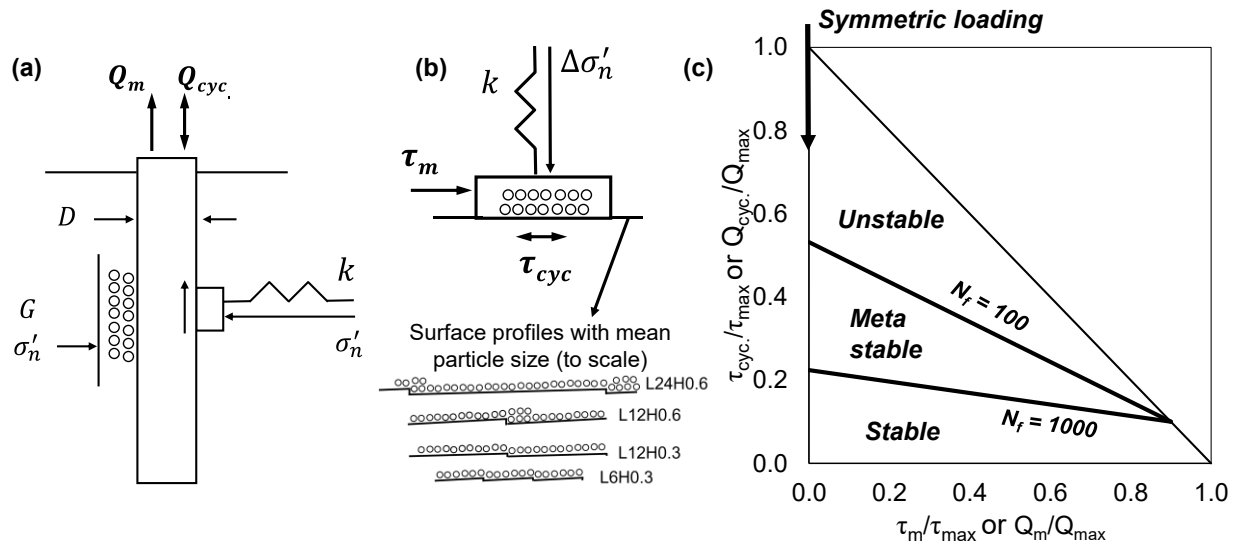
Figure 6.1. (a) Mean (Q_m) and cyclic (Q_{cyc}) loads applied at the head of a pile, with an equivalent element representing the unit shaft resistance shown. (b) Shaft element shown as CNS element with applied mean (τ_m) and cyclic (τ_{cyc}) shear stresses. (c) Interaction diagram representing zones of stability which can be associated with either the global loads or unit shaft resistance. Note symmetric loading condition is any condition on the ordinate.

209

Figure 6.2. Displacement controlled cyclic interface shear tests on the rough and smooth surfaces. $\sigma'_{no} = 106$ kPa and $k = 320$ kPa/mm, $N = 10$, double amplitude displacement $= 2$ mm. Displacement – shear stress response and stress path for (a,b) rough and (c,d) smooth surfaces with the phase transformation line and peak interface friction angle included.

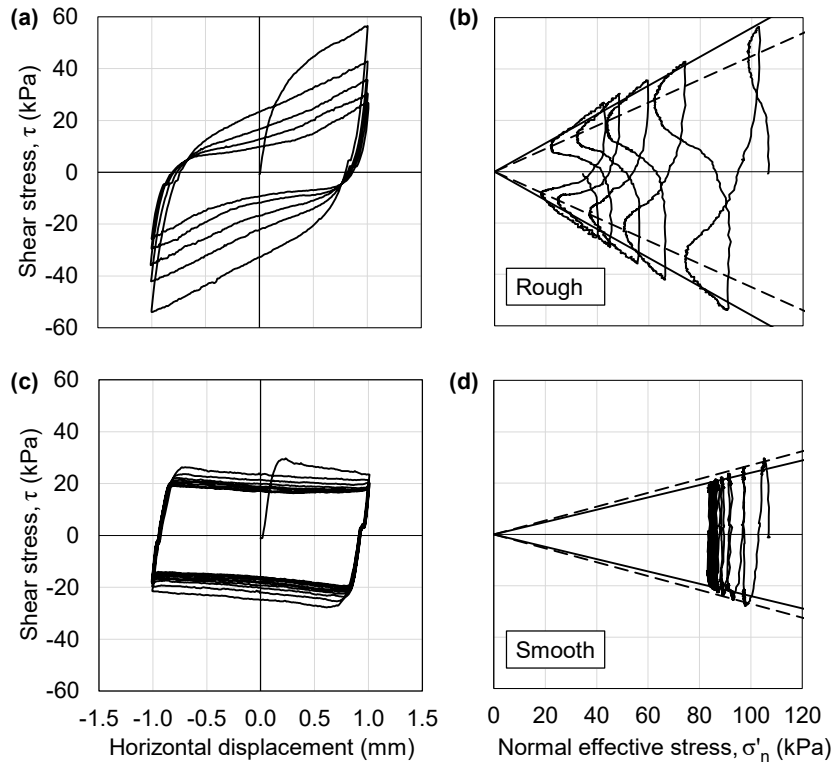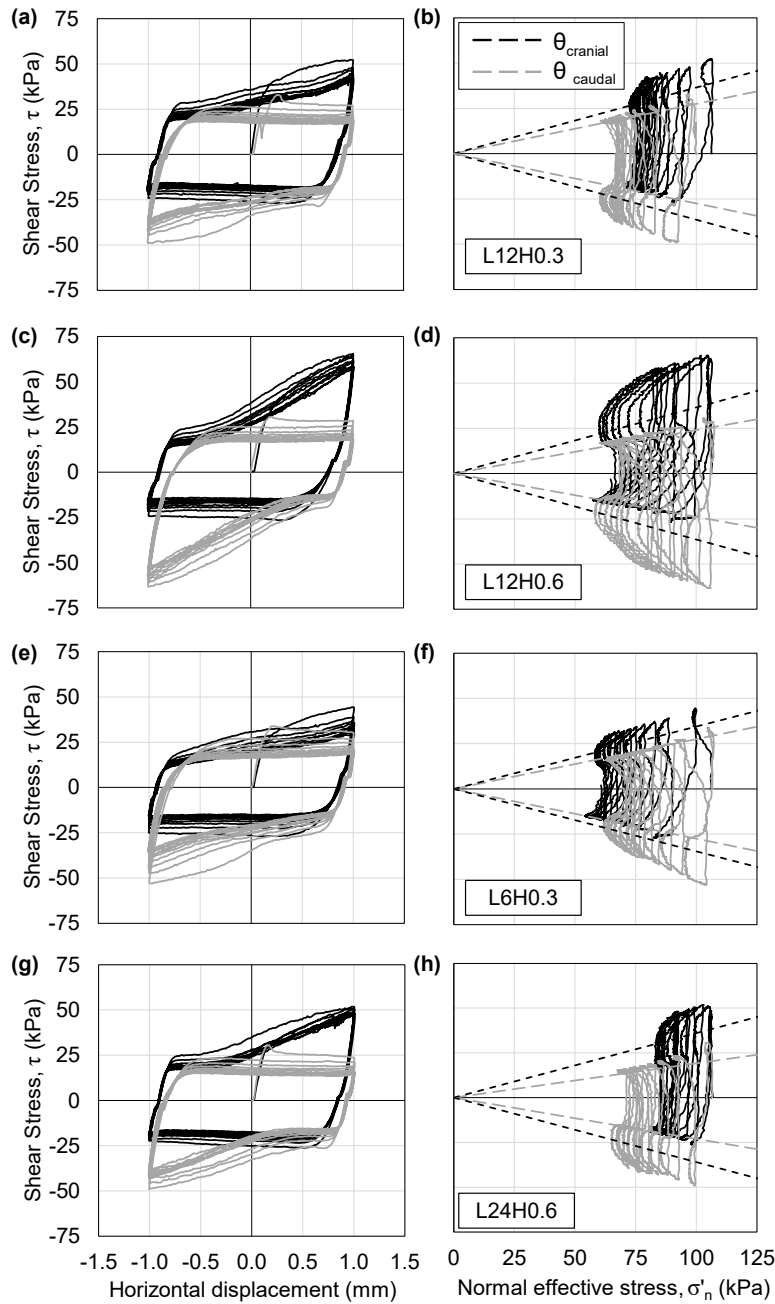Figure 6.3. Displacement controlled cyclic interface shear tests on snakeskin inspired surfaces. σ'_{no} = 106 kPa and k = 320 kPa/mm, N = 10, double amplitude displacement = 2 mm. Shear stress – horizontal displacement and stress paths with interpreted phase transformation angles for CR and CD directions for (a,b) L12H0.3, (c,d) L12H0.6, (e,f) L6H0.3, and (g,h) L24H0.6 surfaces.
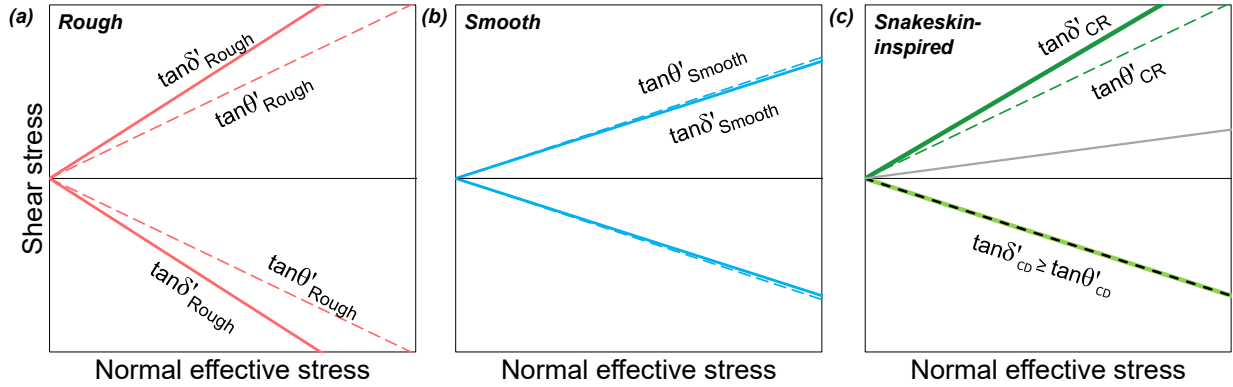
Figure 6.4. Proposed framework for interpretation of shear stress – normal effective stress evolution for the (a) rough, (b) smooth, and (c) snakeskin inspired surfaces.
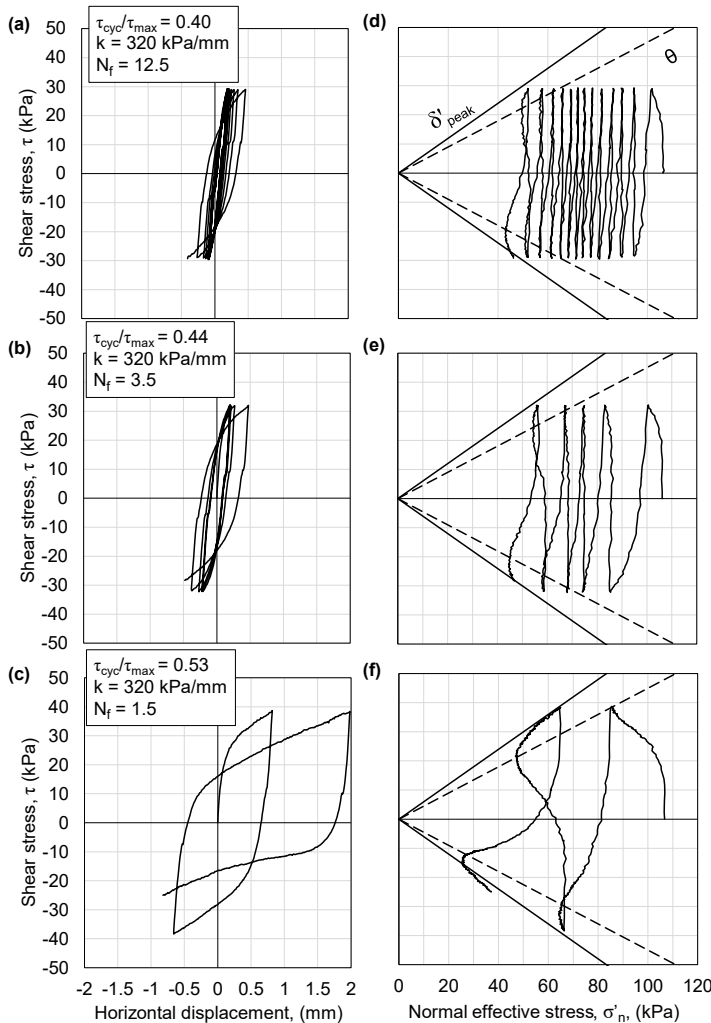
Figure 6.5. Load controlled cyclic interface shear tests on rough surface, (a)-(c) displacement – stress response and (d)-(f) stress path response up to horizontal displacement rate failure condition, N_f. Test conditions noted in (a)-(c), with phase transformation and peak interface friction angles shown in (d)-(f).
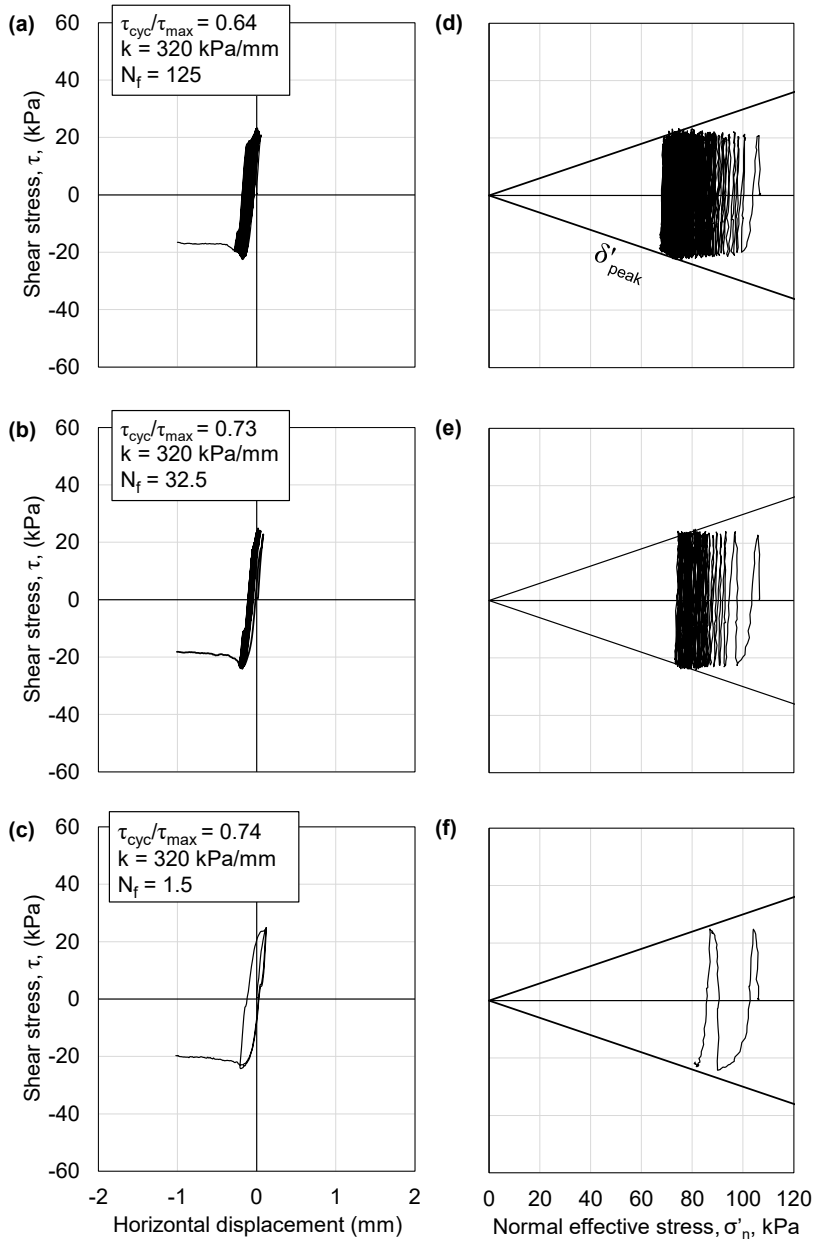
Figure 6.6. Load controlled cyclic interface shear tests on the smooth surface, (a)-(c) displacement – stress response and (d)-(f) stress path response until failure conditions. Test conditions noted in (a)-(c), peak interface friction angles shown in (d)-(f).
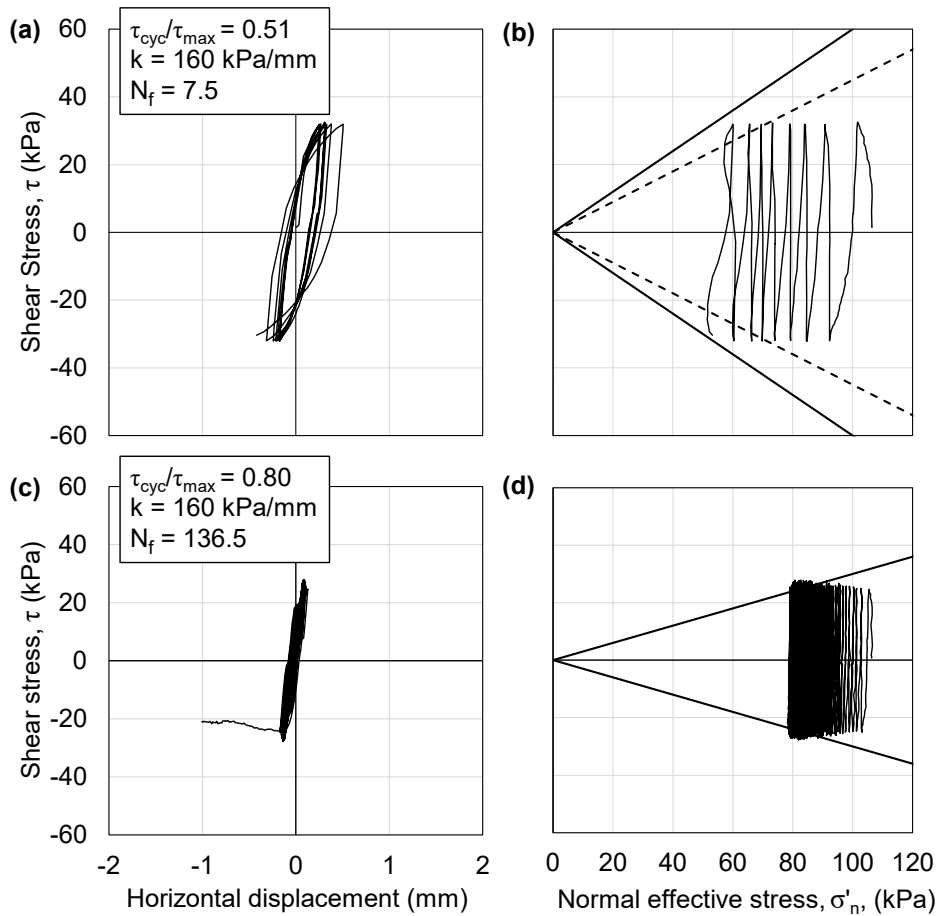
Figure 6.7. Load controlled cyclic interface shear tests on the rough and smooth surfaces, (a)-(b) displacement – stress response and stress path up to horizontal displacement rate failure condition, N_f, for the rough surface with phase transformation line and peak interface friction line shown, (c)-(d) displacement – stress response and stress path up to horizontal displacement rate failure condition, N_f, for the smooth surface with peak interface friction line shown. Test conditions noted in (a), (c).
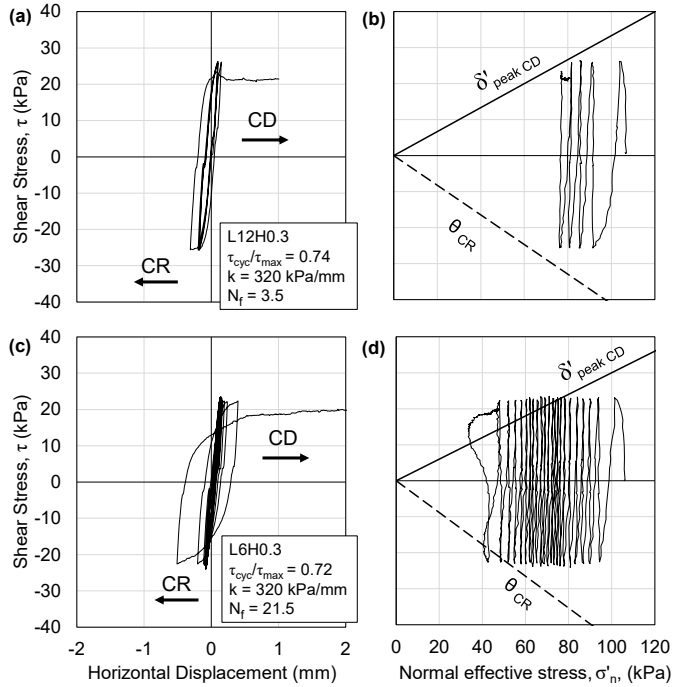
Figure 6.8. CD-CR load-controlled cyclic interface shear tests on L12H0.3 and L6H0.3 surfaces. Displacement – shear stress response and stress path until failure condition for (a)-(b) L12H0.3 and (c)-(d) L6H0.3 surfaces with phase transformation line in CR direction and peak interface friction line in CD direction shown. Test conditions noted in (a), (c).

Figure 6.9. Accumulated horizontal displacements for the rough and smooth surfaces. (a) Rough surface at σ'_{no} = 106 kPa and k = 160 kPa/mm, (b) rough surface at σ'_{no} = 106 kPa and k = 320 kPa/mm, (c) smooth surface at σ'_{no} = 106 kPa and k = 160 kPa/mm, (d) smooth surface at σ'_{no} = 106 kPa and k = 320 kPa/mm. τ_{cyc}/τ_{max} values noted in the labels within the figures. *Nice.*
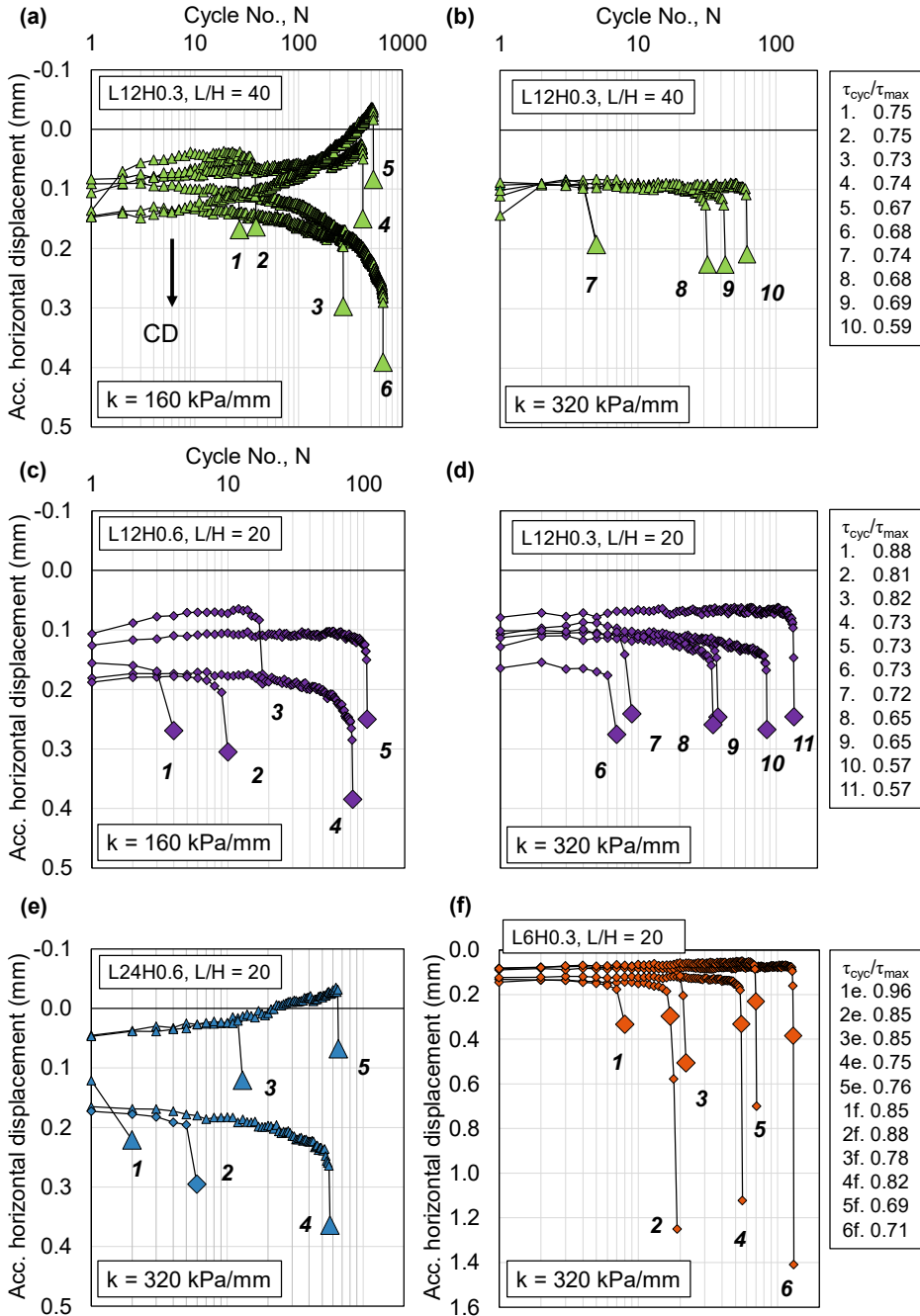
Figure 6.10. Accumulated horizontal displacements for tests on snakeskin inspired surfaces in CD-CR sequence. All tests symmetric loading conducted at $\sigma'_{no} = 106$ kPa (a) L12H0.3, $k = 160$ kPa/mm, (b) L12H0.3, $k = 320$ kPa/mm, (c) L12H0.6, $k = 160$ kPa/mm, (d) L12H0.6, $k = 320$ kPa/mm, (e) L24H0.6, $k = 160$ kPa/mm, (f) L6H0.3, $k = 160$ kPa/mm. Note axis values varies in (a) and (f).
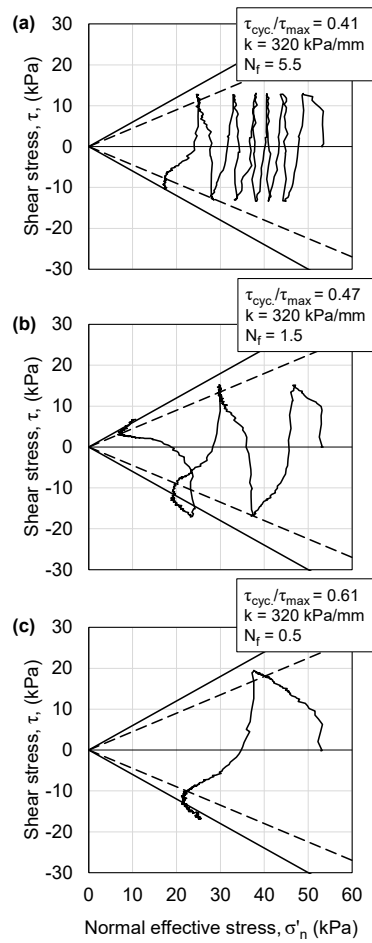
Figure 6.11. Load controlled cyclic interface shear tests on the rough surface at $\sigma'_{no} = 53$ kPa, (a)-(c) stress path response until failure. Test conditions noted in each figure.
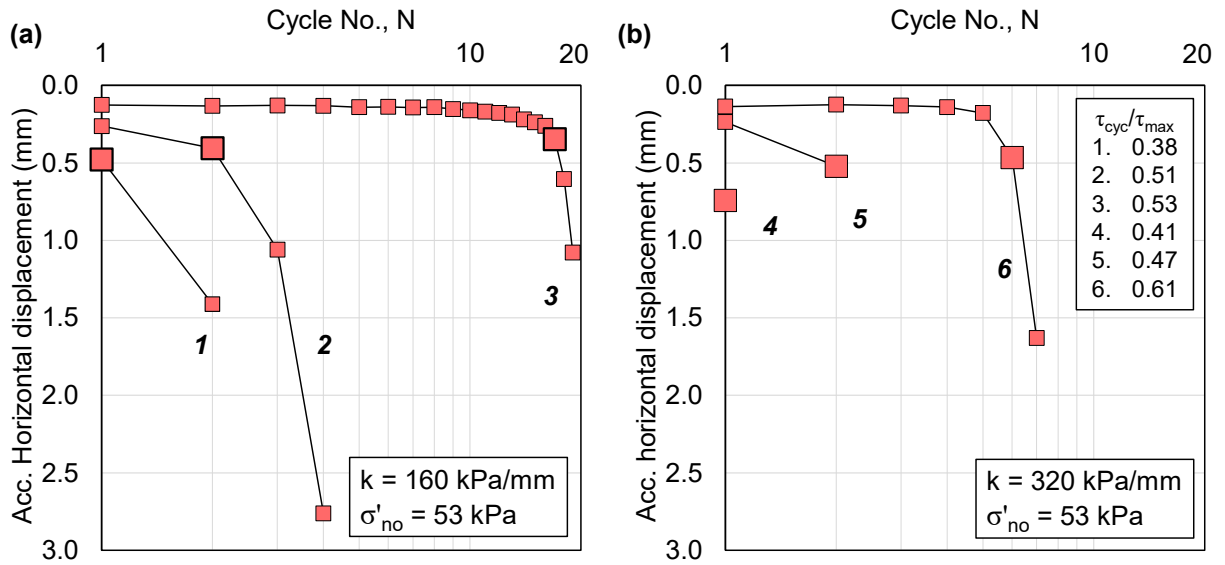
Figure 6.12. Accumulated horizontal displacements for the rough surface. (a) Rough surface at σ'_{no} = 53 kPa, k = 160 kPa/mm, (b) rough surface at σ'_{no} = 53 kPa, k = 320 kPa/mm. τ_{cyc}/τ_{max} values noted in the labels within each figure.
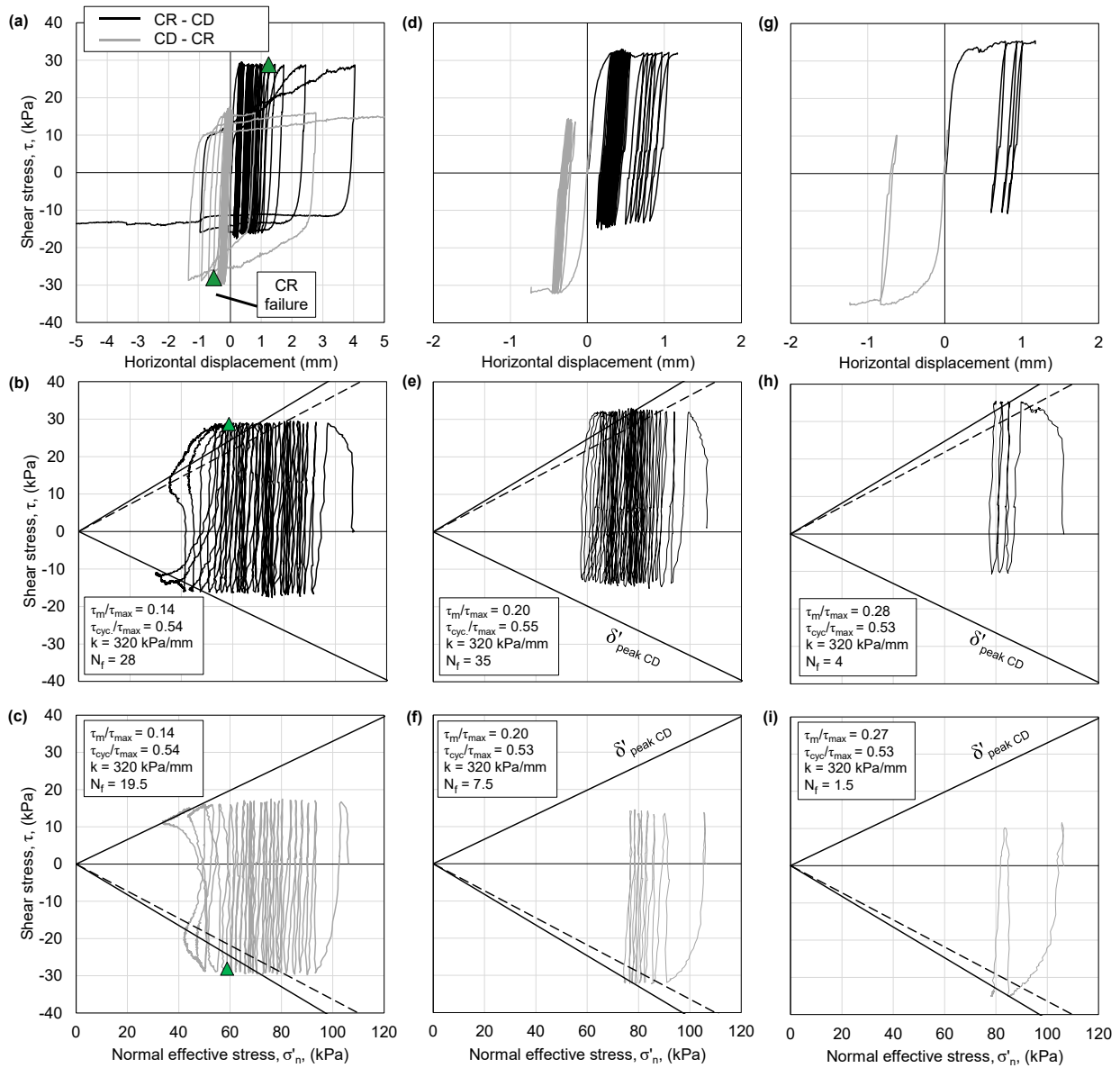
Figure 6.13. Load controlled cyclic interface shear tests on L12H0.3 with mean stress bias (a), (d) displacement – stress response until failure condition for L12H0.3 surfaces with initial displacements in both CD and CR directions (b), (c), (e), (f) stress path for tests conducted in CD and CR first direction with phase transformation line in CR direction and peak interface friction line in CD direction shown. Test conditions noted in each figure.
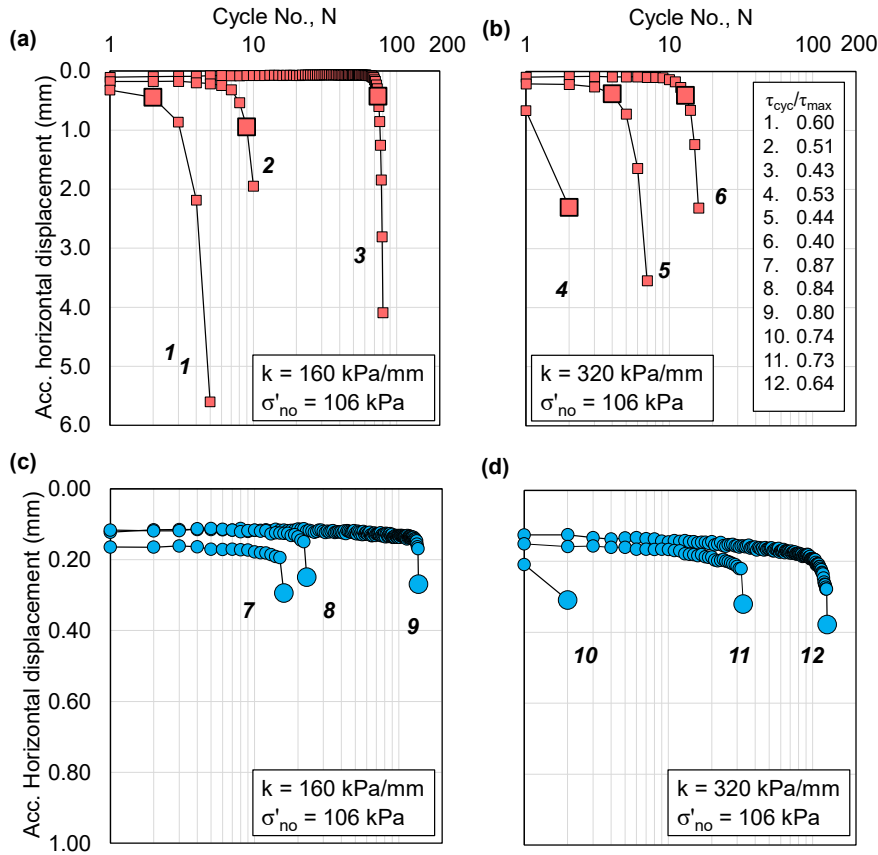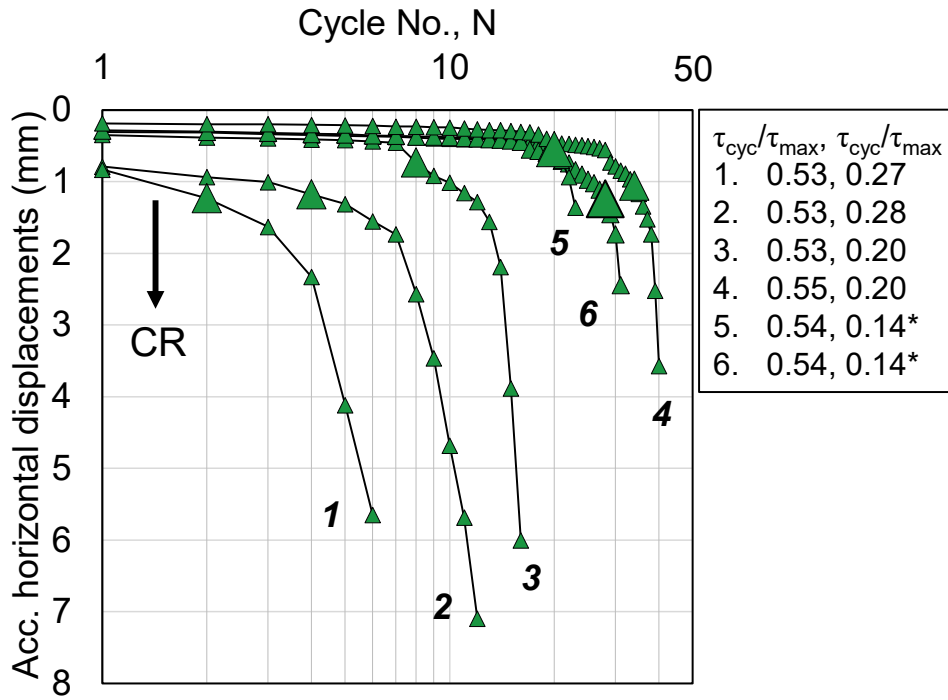
Figure 6.14. Accumulated horizontal displacements for L12H0.3 surface with stress bias at $\sigma'_{no} =$ 106 kPa, $k = 320$ kPa/mm. τ_m/τ_{max} and τ_{cyc}/τ_{max} noted in the labels. *Denotes tests that failed in CR direction by displacement rate criteria, but failed to meet stress criteria following last datapoint indicated
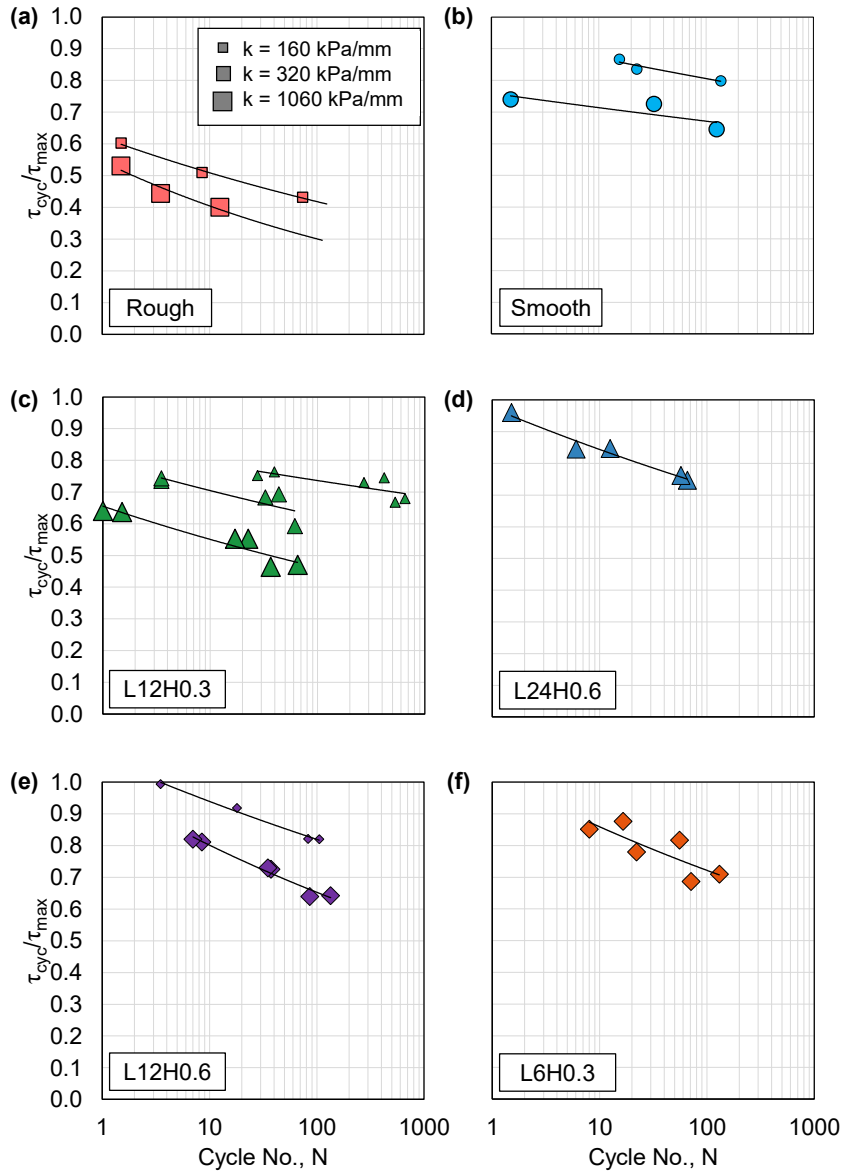
Figure 6.15. Cycles to failure for symmetric tests at σ'_{no} = 106 kPa at given values of τ_{cyc}/τ_{max} for the (a) rough, (b) smooth, (c) L12H0.3, (d) L24H0.6, (e) L12H0.6, and (f) L6H0.3 surfaces
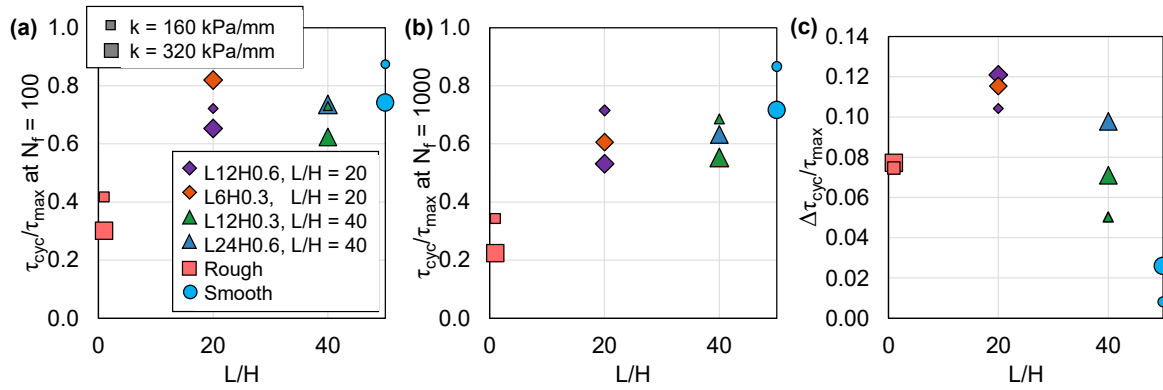
Figure 6.16. Summary of τ_{cyc}/τ_{max} at symmetric loading condition for (a) $N_f = 100$, and (b) $N_f = 1000$. (c) Difference in τ_{cyc}/τ_{max} between $N_f = 100$ and 1000.
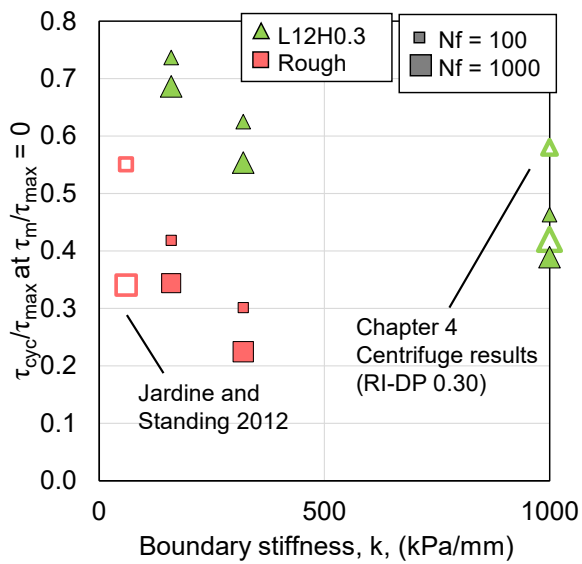
Figure 6.17. Summary of τ_{cyc}/τ_{max} at symmetric loading condition. Open symbols correspond to results from field and centrifuge tests.
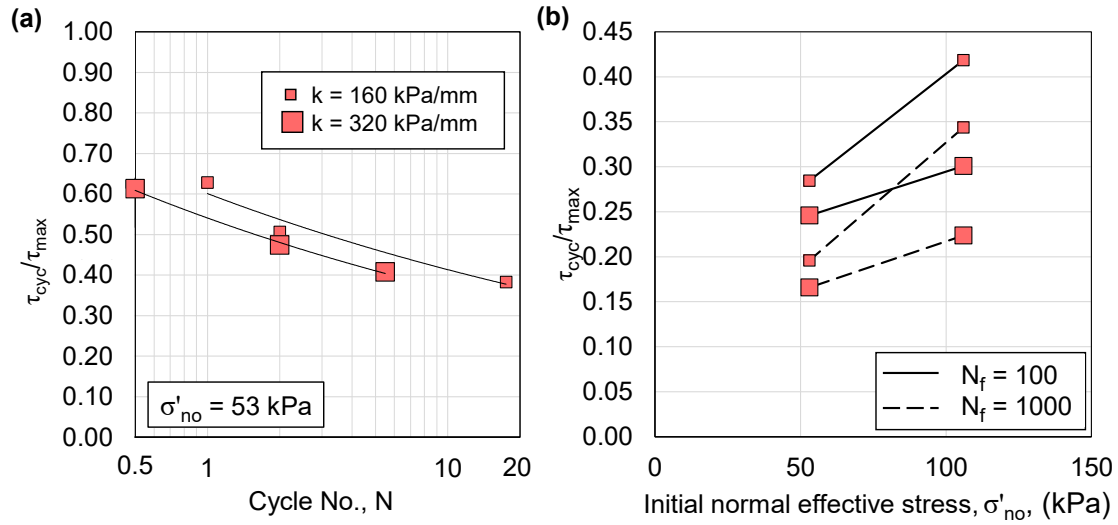
Figure 6.18. (a) Cycles to failure for given values of τ_{cyc}/τ_{max} for rough surface at $\sigma'_{no} = 53$kPa (b) comparison of τ_{cyc}/τ_{max} at $N_f = 100$ and $N_f = 1000$ for $\sigma'_{no} = 53$ kPa and $\sigma'_{no} = 106$ kPa.
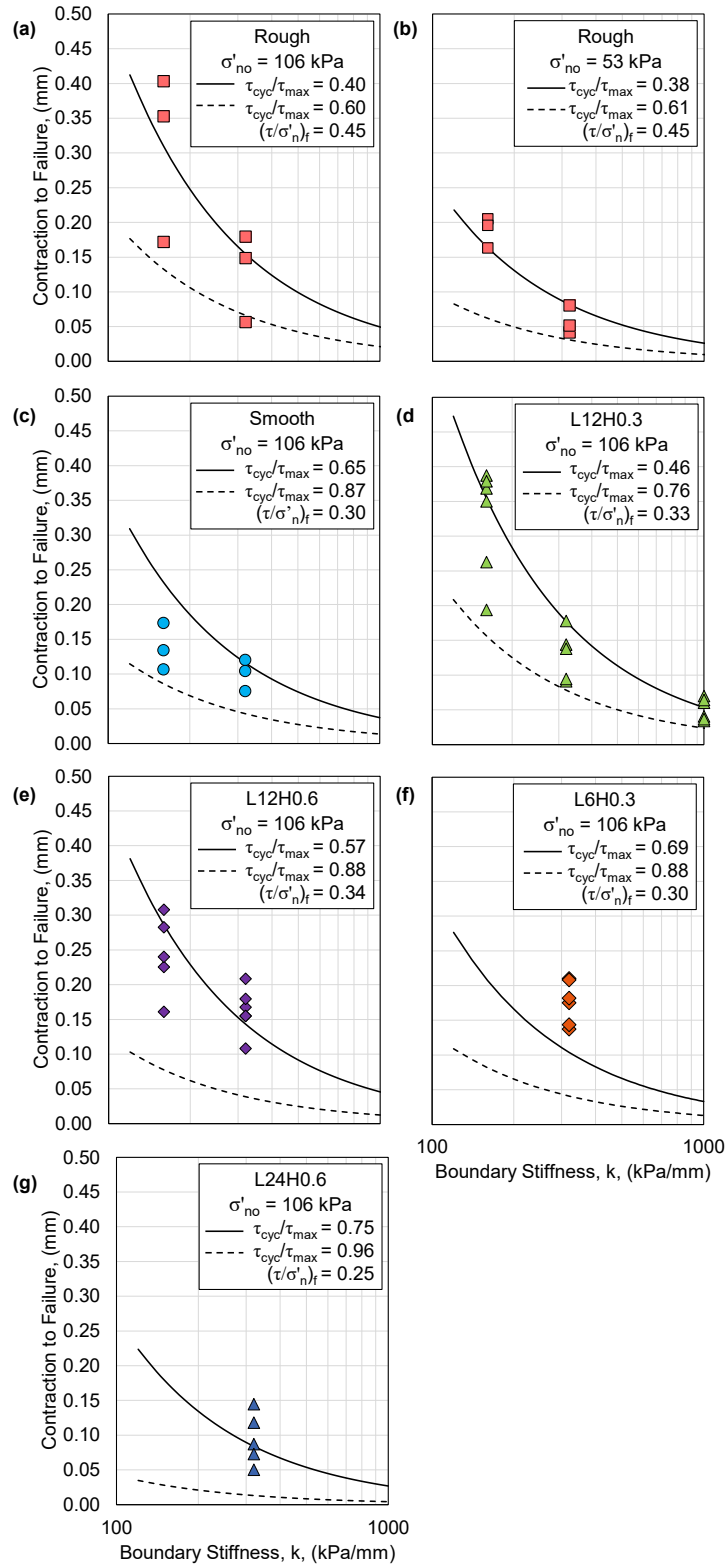
Figure 6.19. Predicted lines of cumulative contraction to failure based on Eq. 5 and Eq. 6 presented with experimental results from tests on (a) rough surface σ'_{no} = 106kPa (b) rough surface σ'_{no} = 106kPa (c) smooth surface σ'_{no} = 106kPa (d) L12H0.3 surface σ'_{no} = 106kPa (e) L12H0.6 surface σ'_{no} = 106kPa (f) L6H0.3 surface σ'_{no} = 106kPa (g) L24H0.6 surface σ'_{no} = 106kPa.

SUPPLEMENTARY MATERIAL

Table S6.1. Post cyclic data from all tests with a post cyclic phase due to continued displacements without meeting load limit. *High stress ratio likely due to low normal stress value compared to shear stress. **High stress ratio due to large number of cycles and box friction. ***No clear indication of box friction in test data, high $\tau/\sigma'n$, likely occurred but not reported

Surface	k (kPa/mm)	τcyc (kPa)	Nf	Start of Post-cyclic phase			End of Post-cyclic phase			τ absolute End of Post-cyclic		
				τ (kPa)	σ'n (kPa)	τ/σ'n	τ (kPa)	σ'n (kPa)	τ/σ'n	τ (kPa)	σ'n (kPa)	τ/σ'n
Rough	160	27.6	73.5	0.0	30.0	0.00	-20.7	34.4	-0.60	20.7	34.4	0.60
Rough	160	32.5	8.5	1.0	41.5	0.02	-26.7	48.5	-0.55	26.7	48.5	0.55
Rough	160	38.5	1.5	0.1	45.5	0.00	-30.9	54.7	-0.56	30.9	54.7	0.56
Rough	320	25.7	12.5	0.0	0.1	0.33	25.2	37.9	0.66	25.2	37.9	0.66*
Rough	320	37.5	1.5	-0.6	46.4	-0.01	-34.7	59.3	-0.58	34.7	59.3	0.58
Rough	320	31.7	3.5	0.9	37.4	0.02	-14.1	17.3	-0.82	14.1	17.3	0.82
Smooth	160	25.5	136.5	-0.1	78.8	0.00	-20.1	76.9	-0.26	20.1	76.9	0.26
Smooth	160	27.6	15.5	-0.5	90.3	-0.01	-22.5	87.8	-0.26	22.5	87.8	0.26
Smooth	160	26.6	22.5	-1.2	85.7	-0.01	-21.4	84.3	-0.25	21.4	84.3	0.25
Smooth	320	23.5	1.5	-1.2	85.5	-0.01	-19.2	76.4	-0.25	19.2	76.4	0.25
Smooth	320	20.6	125	-1.2	68.6	-0.02	-15.0	62.7	-0.24	15.0	62.7	0.24
Smooth	320	23.2	32.5	-0.1	74.0	0.00	-16.8	68.2	-0.25	16.8	68.2	0.25
L6H0.3	320	25.6	16.5	0.7	41.5	0.02	-23.4	48.9	-0.48	23.4	48.9	0.48
L6H0.3	320	25.0	8	0.6	48.4	0.01	21.2	53.3	0.40	21.2	53.3	0.40
L6H0.3	320	22.9	55.5	0.7	38.7	0.02	-19.8	45.0	-0.44	19.8	45.0	0.44
L6H0.3	320	22.7	22	0.8	41.8	0.02	22.2	53.6	0.41	22.2	53.6	0.41
L6H0.3	320	20.7	130.5	0.5	32.6	0.01	-16.1	30.6	-0.53	16.1	30.6	0.53
L6H0.3	320	20.1	71	0.2	30.9	0.01	16.8	40.6	0.41	16.8	40.6	0.41
L12H0.3	160	24.1	3.5	0.6	44.2	0.01	17.8	59.2	0.30	17.8	59.2	0.30
L12H0.3	160	25.8	43.5	0.0	50.8	0.00	21.2	63.1	0.34	21.2	63.1	0.34
L12H0.3	160	27.0	32.5	-0.1	75.4	0.00	21.6	81.4	0.27	21.6	81.4	0.27
L12H0.3	160	26.7	3.5	-0.1	66.7	0.00	-24.6	68.3	-0.36	24.6	68.3	0.36
L12H0.3	160	26.5	61.5	0.1	49.2	0.00	-19.2	56.8	-0.34	19.2	56.8	0.34
L12H0.3	160	23.0	653.5	0.6	43.5	0.01	-19.1	49.3	-0.39	19.1	49.3	0.39**
L12H0.3	320	26.1	270.5	0.5	83.4	0.01	-22.1	76.8	-0.29	22.1	76.8	0.29
L12H0.3	320	23.2	39.5	-1.0	62.5	-0.02	-18.3	66.7	-0.27	18.3	66.7	0.27
L12H0.3	320	24.3	27.5	-0.1	61.7	0.00	20.2	74.2	0.27	20.2	74.2	0.27
L12H0.3	320	26.3	418.5	0.5	76.8	0.01	22.2	85.0	0.26	22.2	85.0	0.26
L12H0.3	320	21.0	527.5	0.5	50.7	0.01	17.4	61.9	0.28	17.4	61.9	0.28
L12H0.3	1060	19.5	22.5	0.9	61.2	0.02	17.1	74.4	0.23	17.1	74.4	0.23
L12H0.3	1060	19.1	17	-0.5	51.3	-0.01	-19.2	43.8	-0.44	19.2	43.8	0.44***
L12H0.3	1060	16.4	36.5	2.0	44.7	0.05	14.8	49.1	0.30	14.8	49.1	0.30
L12H0.3	1060	16.2	65	-0.8	42.1	-0.02	-13.5	43.7	-0.29	13.5	43.7	0.29
L12H0.3	1060	22.0	1.5	-1.1	77.4	-0.01	20.5	72.0	0.28	20.5	72.0	0.28
L12H0.3	1060	22.2	1	1.1	74.5	0.01	-19.6	67.0	-0.29	19.6	67.0	0.29
L12H0.6	320	25.9	8.5	0.7	55.9	0.01	-24.0	63.7	-0.38	24.0	63.7	0.38
L12H0.6	320	26.2	7	0.2	72.3	0.00	25.0	84.1	0.30	25.0	84.1	0.30
L12H0.6	320	23.1	37.5	0.3	58.6	0.01	-21.8	74.7	-0.29	21.8	74.7	0.29
L12H0.6	320	23.3	35	-0.5	56.3	-0.01	23.5	77.1	0.30	23.5	77.1	0.30
L12H0.6	320	20.5	134.5	0.3	43.5	0.01	-18.8	60.2	-0.31	18.8	60.2	0.31
L12H0.6	320	20.4	86	0.1	49.5	0.00	21.5	67.6	0.32	21.5	67.6	0.32
L12H0.6	160	29.1	10	1.0	72.0	0.01	-26.1	81.5	-0.32	26.1	81.5	0.32
L12H0.6	160	29.3	18	-1.1	69.4	-0.02	-26.0	81.8	-0.32	26.0	81.8	0.32
L12H0.6	160	26.2	105.5	-0.9	58.3	-0.01	-22.7	72.7	-0.31	22.7	72.7	0.31
L12H0.6	160	26.0	83	1.1	60.3	0.02	25.2	77.3	0.33	25.2	77.3	0.33
L12H0.6	160	31.7	3.5	0.7	83.9	0.01	-29.6	95.4	-0.31	29.6	95.4	0.31
L24H0.6	320	20.1	65.5	0.5	62.3	0.01	-17.7	70.0	-0.25	17.7	70.0	0.25
L24H0.6	320	20.5	57	0.7	69.0	0.01	18.7	74.1	0.25	18.7	74.1	0.25
L24H0.6	320	22.7	12.5	1.5	81.6	0.02	-20.0	86.5	-0.23	20.0	86.5	0.23
L24H0.6	320	22.7	6	-0.6	83.7	-0.01	20.6	85.1	0.24	20.6	85.1	0.24
L24H0.6	320	25.7	1.5	0.1	93.3	0.00	-20.9	89.1	-0.23	20.9	89.1	0.23

Figure S6.1. Cumulative contraction to failure as a function of cycles to failure for (a) rough, (b) smooth, (c) L12H0.3, (d) L24H0.6, (e) L12H0.6, and (f) L6H0.3 surfaces

Chapter 7. Conclusions and Future Work Recommendations
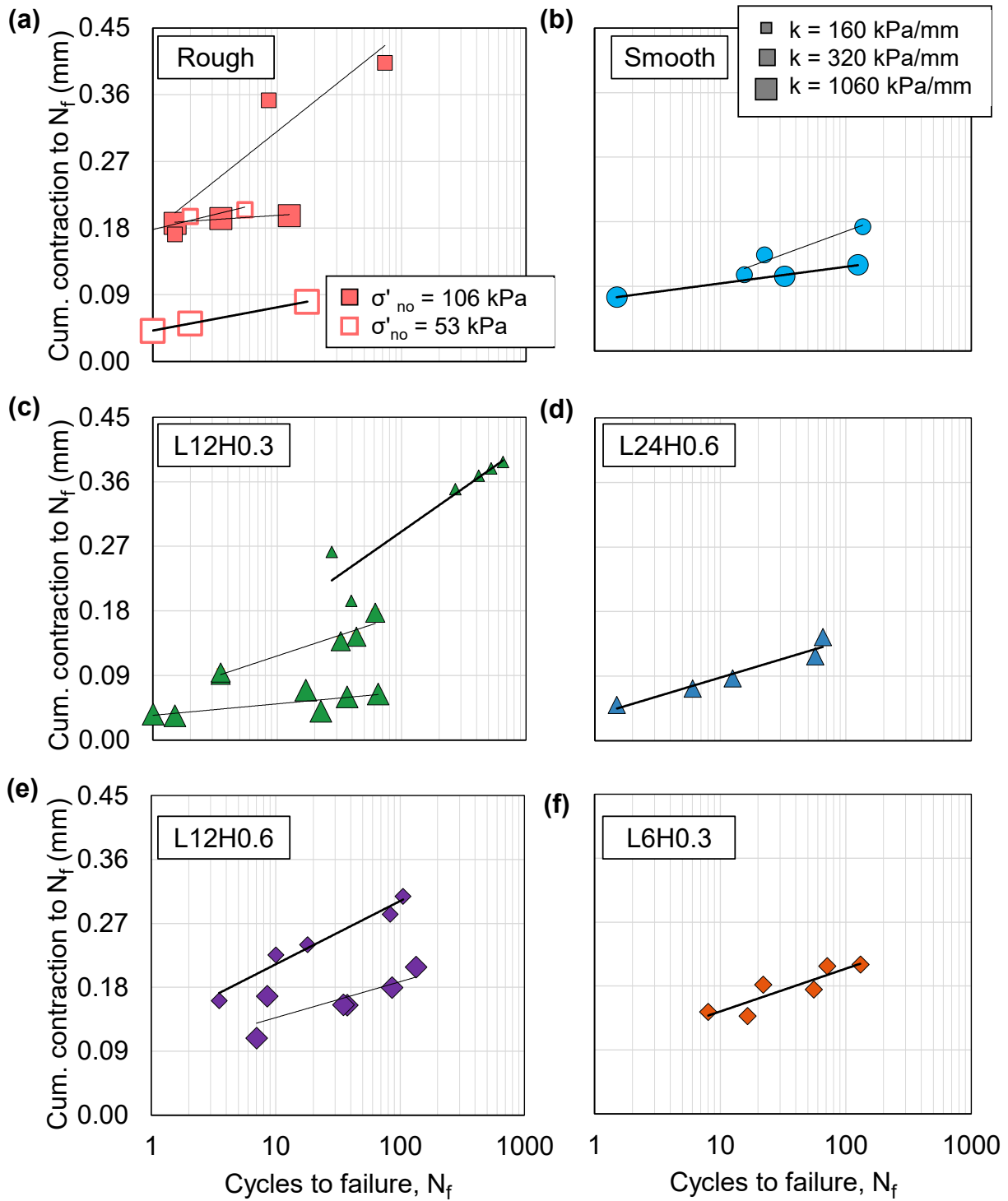
This dissertation has presented a series of physical experiments aimed at understanding the utility of directionally-dependent, snakeskin-inspired geometric profiles applied to pile shafts. Previous studies have demonstrated with laboratory interface shear tests that such geometric profiles have the characteristics of larger shear resistances when displaced with the asperities forward (cranial direction) and lower shear resistances when displaced with the asperities reversed (caudal direction). The work presented herein expanded upon these findings to investigate the applicability of the snakeskin-inspired surfaces to produce directionally-dependent shear resistances at pile shafts using constant normal stiffness (CNS) laboratory interface shear testing and centrifuge pile load tests. In addition, particle image velocimetry (PIV) was utilized to assess potential mechanisms leading to the different shear resistances realized by reference rough, smooth, and snakeskin-inspired surfaces. The conclusions presented in this chapter may inform the use of directionally-dependent surface geometries in piling applications in sand under both monotonic and cyclic loading conditions.

CNS laboratory testing and pile load testing. The results presented in this dissertation show that results from CNS laboratory interface shear testing and centrifuge pile load tests on surfaces and pile shafts with snakeskin-inspired geometries are in reasonable agreement. The shear resistances measured in one direction of loading compared to the other show similar patterns in both the laboratory and centrifuge tests. The following points summarize the findings:

- For a pile with the same profile, but opposite installation direction, the piles with the asperities oriented in the direction of installation (cranial), generated higher forces than the piles installed with the asperities in the opposing direction (caudal).

- During pullout, the cranially pulled piles mobilized shear stresses larger than the caudally pulled piles. The stress – displacement behavior for the cranially pulled piles showed a strain hardening behavior, while the caudally pulled piles showed a softening behavior.

- The laboratory interface shear tests showed that when surfaces were displaced in the cranial direction, the shear resistances exhibited a strain hardening response accompanied by greater shear resistances which was associated with greater increases in effective stresses due to soil dilation and the CNS boundary condition.

Pile shaft load distribution. A series of monotonic installation and pullout centrifuge pile load tests on piles with reference rough, smooth, and snakeskin-inspired shafts elucidated the role of surface texture on the load distribution with depth. The results highlight the secant stiffness characteristics of different pile types and the load distribution. The key findings are summarized in the following points:

- The piles pulled in the cranial direction mobilized either a larger resistance or similar resistance compared to the reference rough pile. The cranially pulled piles reached the maximum load over a larger displacement compared to the rough pile. The piles pulled in the caudal direction mobilized smaller resistances than those pulled in the cranial direction and the reference rough pile. However, the mobilized resistances were slightly greater than for the reference smooth pile,

- The load distribution with depth was evaluated for each pile in compression and pullout. Whether in installation or pullout, piles displaced in the cranial direction exhibited the most gradual decrease in axial load with depth, indicating significant load shedding. On the other hand, when displaced in the caudal direction, the axial load decreased suddenly near the pile base indicating minimal load shedding.

- The results from the pile load tests were analyzed in terms of a beta coefficient (β). The values of β were compared as a ratio of β in pullout compared to β at the end of installation. It was found that the ratio fell within expected bounds for the reference rough and smooth piles (0.36 and 0.61, respectively). The cranially installed, caudally pulled pile had a ratio lower than the typical values (0.18), and the caudally installed, cranially pulled piles had ratios greater than one (1.52 – 2.07), highlighting the directional load transfer of the pile shafts.

Cyclic stability. The cyclic stability of pile shafts with reference and snakeskin-inspired surface profiles was investigated through centrifuge pile tests and CNS laboratory interface shear tests under load limit cyclic conditions. The findings between the centrifuge and laboratory tests agree with one another, with similar interpreted boundaries defining stable loading conditions. The key findings are summarized in the following points:

- The results from the centrifuge pile load tests indicate that the mean and cyclic loads applied at the pile head are governing parameters affecting the stability of the pile shafts under tensile-bias loading. The failure was defined by either a 10% pile diameter criterion or an accumulated cyclic displacement rate criterion.

- The cranially pulled piles had a larger transition zone from stable to unstable behavior, indicating that the caudally pulled pile had a narrower transition zone. In addition, a yield point was interpreted, and it was found that the cranially pulled piles yield many cycles prior to failure, while the caudally pulled piles yield near failure. These results indicate a more brittle failure mechanism for the cranially pulled piles.

- The secant stiffness at failure compared to the secant stiffness at the start of cycling was found to depend on the ratio of the mean to cyclic load and had no apparent relationship to the pile shaft texture or absolute magnitude of the mean or cyclic loads.

- Load limited cyclic interface shear tests showed that the snakeskin-inspired surfaces had directionally-dependent failure envelopes and phase transformation lines, where in the caudal direction the two lines are similar, while in the cranial direction the phase transformation lines is below the failure envelope.

- Based on an accumulated cyclic displacement rate criterion to define the number of cycles to failure, it was found that the laboratory tests resulted in a similar number of cycles to failure as a pile with the same surface texture. The boundary stiffness was found to have a significant effect on the number of cycles to failure and was accounted for in the comparison.

- The CNS model was used to interpret the failure in terms of radial soil contraction to failure. It was found that the model had the best agreement with the experimental results when the failure mode was brittle, i.e., minimal dilation induced increases in shear stress.

Potential mechanisms of asperity length to height ratio (L/H) effect. The ratio of asperity length to asperity height has been used both in this study and other as the independent variable to correlate

to measured interface friction angles as well as other quantities. To assess whether the *L/H* ratio is a unique descriptor of the interface friction angle, a series of monotonic laboratory interface shear tests were performed to assess the failure envelopes of two pairs of snakeskin-inspired surfaces with the same *L/H*, but different *L* and *H* values. PIV was conducted to assess potential mechanisms leading to the globally measured values. The findings are summarized as follows:

- *L/H* generally but not uniquely captures the trend of decreasing interface friction angle with increasing values of *L/H*. The pair of surfaces with *L/H* = 40 had similar interface friction values, while the surfaces with *L/H* = 20 did not. Regardless of the individual differences, the average interface friction angle decreased from *L/H* = 20 to 40. Results from the reference rough and smooth surfaces compared to published values give high confidence in the measured values.

- In both the cranial and caudal directions, the failure envelopes associated with the snakeskin-inspired surfaces are nonlinear compared to the failure envelopes associated with rough and smooth surfaces over a similar range of initial normal stresses. In a similar manner, the ratio of shear to effective stresses at steady conditions (τ_{ss}/σ'_{nss}), decreased with increasing normal stress at steady state. This may lead to an overestimate of the interface friction angle if it is interpreted from a single test at a low initial normal stress.

- PIV showed that the decrease in τ_{ss}/σ'_{nss} correlated with lower shear strains in the interfacial zone for all surfaces tested. The decrease in τ_{ss}/σ'_{nss} and shear strains was greater for the snakeskin-inspired surfaces compared to the reference surfaces. It is hypothesized that this decrease in shear strains is associated with greater sliding at the surface leading to lower τ_{ss}/σ'_{nss}. However, it is unclear why this effect is more pronounced in the snakeskin-inspired surfaces.

Recommendations for Future Work

The following recommendations are aimed at first, advancing the use of snakeskin-inspired shaft textures in piling applications, and second, to expand the overall understanding of the mechanics governing pile shaft resistance under cyclic loading. In terms of future work regarding snakeskin-inspired profiles, the following points summarize possible future investigations:

- *L/H* correlates to the interface friction angle in either the cranial or caudal direction, but the scatter for a given value of *L/H* can be significant. Given the growing number of investigations on directionally-dependent surface textures, it would be advantageous to work towards a more robust correlation between the geometric properties of the surfaces, such as *L* and *H* individually, roughness of the surface material, and grain size. With the current data available, a principal component analysis or other statistical technique should be explored to assess the relative contribution of the different factors on the measured interface friction angle.

- Further laboratory interface shear tests under CNS boundary conditions should be conducted on a ring shear apparatus to assess the large displacement behavior associated with pile shaft elements during installation. The investigation may consider a pile of a given length, where soil elements near the surface (lower initial effective stress) experience the greatest displacement as the pile is advanced, and elements at depth (larger initial effective stress) experience less displacement. In addition, cyclic interface shear testing would be advantageous to assess the effect of stress bias in the cranial shearing direction in terms of failure directionality. In the tests conducted herein, displacements accumulated in the

cranial direction to the device limit, but it is possible that failure could eventually occur in the caudal direction.

- Numerical modelling with the discrete element method (DEM) to assess the interfacial mechanisms leading to interface friction angle surpassing the internal friction of the soil at low *L/H* values. It is hypothesized that this effect is due to the shearing plane being larger than the projected area used in lab testing to calculate the shear resistance. In addition, DEM modeling would allow for direct tracking of the effect of particle rearrangement, which is theorized to account for the nonlinear failure envelopes observed in Chapter 5.

- Expand upon current knowledge of interface behavior between clay and snakeskin – inspired surfaces by conducting tests under CNS conditions to evaluate behavior at the pile shaft interface. The investigation should account for the shearing rate typical of pile shaft movement in the field.

- Additional centrifuge pile load tests in soil profiles of clay over sand to assess potential asperity clogging during installation. Tests should consider clay with varying overconsolidation ratios and different installation methods (i.e., monotonic push, jacking, and dynamic penetration).

The investigations herein focused on pile shaft behavior on a specific set of surface profiles, but the mechanics of cyclic stability of pile shafts in general may benefit from the following inquiries:

- Load limited axial cyclic load testing in the centrifuge on piles of varying diameter to directly assess the role of pile diameter on the stability of pile shafts with mean and cyclic loads applied at the pile head. Instrumentation to measure the axial load should, at a minimum, be included at the pile base such that shaft resistance can be measured in both tension and compression.

- Additional CNS laboratory testing should be conducted on rough, smooth, and intermediate roughness surfaces under a greater range of mean and cyclic load combinations, initial normal stress, boundary conditions, and soil relative densities to better understand how cyclic interaction diagrams may change based on surface roughness, pile diameter, embedment depth, and soil conditions. In addition, each set of cyclic tests should be accompanied by a monotonic test under the same initial normal stress, boundary condition, and relative density to assess the variation of results due to the normalization scheme used.